学位論文

Studies on development of three-dimensional magnetohydrodynamic turbulence reconnection

（三次元磁気流体乱流リコネクションの発展の研究）

平成 **29** 年 **12** 月博士（理学）申請

東京大学大学院理学系研究科

地球惑星科学専攻

王　爍洋

Contents

Abstract

Magnetic reconnection is considered to be one of the most important fundamental processes due to its wide application. It converts ubiquitously existing magnetic energy into heating and accelerating plasma thus explains various astronomical events that relate to the efficient energy release. Numerous works that tried to solve the fast reconnection problems started from more than 50 years ago. However, there still remains a big issue that how the reconnection is accelerated to reach the fast energy output shown by the observations. In this dissertation, we executed numerical simulations of a current sheet with a finite guide field to understand the basic physics for reconnection inside a self-generated turbulent state.

Since the coexistence of multiple tearing layers was found in many numerical studies for a current sheet with non-zero guide field under random perturbation, the coupling between these layers might lead to a solution for fast reconnection. So first in Chap.2, we applied a pair of rotational-symmetric eigenmodes of tearing instability to understand the local mechanism of the coupling. We found that the coupling, namely the inflow-outflow coupling between diffusion regions that are not aligned with each other, increases the inflow as well as the local reconnection rate from the coupling side and triggers secondary tearing instability in the original diffusion regions.

In Chap.3, the consequences of the initial inflow-outflow coupling were examined both in the local and the global scales. With the partition of the diffusion region, a vent is open across the sheet that magnetic fields are ejected out to collide with the free field lines. The collision creates new diffusion regions outwardly. In the global view, the new diffusion regions form new reconnection layers that correspond to new energy modes,

which have larger wavenumbers along the global guide field direction than the original modes. The creation of the new energy modes come from the nonlinear coupling of initial modes with the higher order harmonics of their counterparts. These new reconnection layers are close to the asymptotic magnetic fields, so they transport free energy into the turbulent sheet. Meanwhile, the old and new reconnection layers also build up inflow-outflow coupling across the sheet. It is found that the global reconnection rate increases.

In order to generalize our sheet-crossing coupling model, we re-examined the reconnection in the current sheet under random perturbation in Chap.4. As many tearing layers emerge together, they build up inflow-outflow coupling across the current sheet, while activating new energy modes outwardly. As the overall reconnection rate increases, the same story as the eigenmodes coupling simulation is retrieved.

We made a parameter survey on the layer distance to check the dependence of the inflow-outflow coupling model, as well as the nonlinear coupling that produces new energy modes in Chap.5. We found that when two layers are far apart, no coupling is built that each layer grows independently. When two layers are close, they efficiently build up inflow-outflow coupling and cascade the energy into energy modes with larger wavenumbers thus follow the sheet-crossing coupling picture. On the other hand, decreasing the global guide field will sufficiently shrink the distance between tearing layers. We thus also tested a simulation with a very weak guide field and found that the coupling is broken soon and substituted by a series of transient and local reconnection.

In Chap.6, we summarized our results first and discussed several different issues. We compared our reconnection rate with other measurements and found that the reconnection in our system can be as fast as the other spontaneous 3D reconnection simulations. As the bi-directional flow pattern is often observed in the astronomical events, we examine the interaction between 2D and 3D modes. We notice that even in the environment dominated by 3D modes, 2D modes can grow and coalesce into longer 2D modes that produce global bi-directional flow and large 2D flux tube. In addition, the contribution of our results to the turbulence reconnection studies and the possible extension to the particle regime were

discussed. Future prospects were presented that many works can be done, such as the model dependence on the diffusivity, the boundary condition and the sheet structure, to make a wholesome theory.

In conclusion, we have developed a well-defined model on the fast 3D reconnection. We followed the development of the diffusion regions and found that the universal existing coupling between tearing layers across the whole current sheet is the essential part in the acceleration of the global reconnection. The coupling does not only increase the local reconnection for each reconnection layer but also produces the new reconnection layers that expand further into the magnetic reservoir where free energy is provided.

Acknowledgments

I would like to present my greatest gratitude to my supervisor Yokoyama Takaaki for his earnest instructions during these five and a half years. I obtained not only the knowledge on the plasma physics, but also the way of thinking and presenting opinions. I am always feeling very lucky to be here and will cherish the memory of my stay forever.

Since our supervisor is a very unique person, all of my seniors and juniors have lots of personality. It was my pleasure to spend years with them, discussing the researches while having silly conversations sometimes. Iida Yusuke and Kitagawa Naomasa are my eldest seniors. Their gentleness is a great comfort. Hotta Hideyuki and Toriumi Shin are both kind and severer to the juniors. They always answer the help without any complaints and never hesitate to point out my problems for my own good. Matsui Yuki gave me advices that I owned him a thanking. Iijima Haruhisa is patient to everyone and I learnt a lot from him in many aspects. His smartness is something that I envy much. Nasuda Tetsuya and Kono Shunya are a pleasure to talk with as they are capable to provide enlighted comments. Shoda Munehito help me a lot on my research, both in soft and hard ways. Although it was tough when my problems were exposed by him, I appreciate it very much that he never gives me up. The cheerful personality of Ichimura Chiaki and the plainspoken manner of Oi Yoshiaki are nice things to see. They never make me feel the age gap between us, which is good for old people like me. Wang Yikang has a broad range of knowledge. I absorb lots of new things from the conversation with him. Bekki Yuto is a so talented student to look up to. His existence encourages me to work harder to not to be lagged behind. By sharing the interests in anime, I enjoyed the talk with Mineta Ryuji very much. I would like to give special thanks to Kaneko Takafumi, who was working as

my tutor during my first year in Master course. He helped me with many things, studies and living, while showing strong responsibility and patience. I felt extremely guilty when I heard that he did not make a fortune by doing my tutor.

In addition to my lab members, I really appreciate the kindness from all people I met in The University of Tokyo. There are several people who helped me a lot on my research that I would like to give special thanks. First of all, I would like to thank Isobe Hiroaki for providing the numerical codes that run our simulation. I would like to thank Professor Shibata Kazunari, Professor Yokoi Nobumitsu, Dr. Janvier Miho, Dr. Takasao Shinsuke and Dr. Hirabayashi Kouta for giving advice and comments on our work. During my stay in Princeton Plasma Physics Laboratory (PPPL), Professor Amitava Bhattacharjee, Professor Yamada Masaaki, Dr. Yi-Min Huang and Dr. Luca Comisso also spared their precious time to discuss with me on the research. Also, I would like to thank Professor Ono Ryo who always supports my academic travels.

Our research presented in this dissertation was partly conducted using the Fujitsu PRIMEHPC FX10 System (Oakleaf-FX,Oakbridge) in the Information Technology Center, The University of Tokyo. Numerical computations were [in part] carried out on Cray XC30 at Center for Computational Astrophysics, National Astronomical Observatory of Japan.

Finally, I would like to appreciate my parents for the long-standing support, mainly the economical support. I also feel gratitude for all the food I ate in the past 31.5 years, as they eternally sacrificed their lives for me. Great gratitude goes to the idol group Arashi, especially Mr. Sakurai Sho. Words fail me on this point (I apologize if my future husband or children feel uncomfortable).

Chapter 1

General Introduction

In this chapter, we will review the historical and up-to-date understanding of our research topic, magnetic reconnection, and our motivation for the study, which is the leading point of this dissertation.

1.1 Magnetic reconnection

In one-fluid magnetohydrodynamics (MHD) regime, in which the collision between ions and electrons are sufficiently effective, the magnetic field development is described by the induction equation

$$\begin{aligned} \frac{\partial \mathbf{B}}{\partial t} &= -c\nabla \times \mathbf{E} \\ &= \nabla \times (\mathbf{v} \times \mathbf{B}) - c\nabla \times (\eta \mathbf{J}) \end{aligned} \tag{1.1}$$

where $\mathbf{B}, \mathbf{E}, \mathbf{v}, \mathbf{J}, c$ are the magnetic field, the electric field, the velocity field, the current density and the speed of light respectively. Resistivity η is the reverse of conductivity σ. When the magnetic field changes the orientation in the direction perpendicular to the local magnetic field, a current layer is built. This is described by

$$\mathbf{J} = \frac{c}{4\pi}\nabla \times \mathbf{B}. \tag{1.2}$$

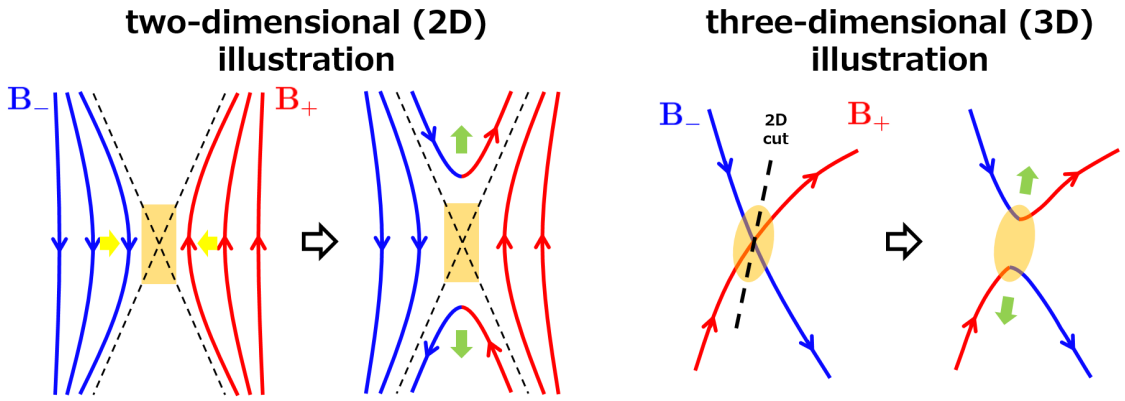

Figure 1.1: Illustration of magnetic reconnection in 2D and 3D (3D figure is the revision of Yamada et al. (2010) FIG.2). Blue and red lines with arrows are the magnetic field lines. Orange regions are diffusion regions. Inflows and outflows are represented by yellow and green arrows. Thin black dashed lines are separatrices.

When the velocity $\mathbf{v}$ is negligible or uniformly acting on the magnetic field along $\mathbf{B}$ direction, the diffusion term (the second term on the R.H.S. of Eq.(1.1)) becomes dominant. The magnetic structure is diffusing as a whole and described by a diffusion equation

$$\frac{\partial \mathbf{B}}{\partial t} = \widetilde{\eta}\nabla^2\mathbf{B}. \tag{1.3}$$

where $\widetilde{\eta} = \eta c^2/(4\pi)$ is the uniform magnetic diffusivity. It is clear that no new component of magnetic fields is created due to the diffusion itself. The sheared components gradually annihilate until the whole magnetic structure relaxes into a uniform field. Non-uniformity of $\mathbf{v}$ or $\mathbf{B}$ will introduce new physics by enhancing the significance of the advection term (first term on the R.H.S. of Eq.(1.1)). This is the topic of our interest, namely magnetic reconnection, which was first introduced by Dungey (1961).

An illustration of two-dimensional (2D) magnetic reconnection is shown in the left panel of Fig.1.1. The anti-parallel magnetic fields enter the diffusion region, where diffusion dominates, and literally reconnect. The newly ”reconnected” field line has a strong bent that the tension force drags the magnetic field together with the plasma away from the diffusion region to release the bent. As flow converges into the diffusion region then diverges out in the perpendicular direction, there exists a stagnation point of flow that

$\mathbf{v} = 0$ when no global background flow is introduced.

In reconnection picture, the magnetic field changes the connectivity by exchanging parts of the field lines when passing through a separatrix. The separatrix separates the inflow region, where field lines are approaching the diffusion region, and the outflow region, where field lines are leaving the diffusion region. The crossing point of two separatrices is called an X-point, where reconnection happens.

In general, magnetic reconnection happens when the diffusion term becomes localized. Similar scenario happens in three-dimensional (3D) reconnection (right panel of Fig.1.1). When field lines with arbitrary orientations meet in the diffusion region, they reconnect by annihilating the anti-parallel components while holding other components. After exchanging parts of the field lines, reconnected field lines form bents and eject the plasma out by tension force. If a cut along the thick black dashed line is made, 2D-like reconnection scenario is retrieved.

The explanation above just gives the basic information and a rough image of magnetic reconnection. Introducing asymmetry, a guide field (the magnetic field that is perpendicular to the local reconnection plane), open/closed boundary can change the story considerably. On the other hand, including other effects, such as the ionization degree, the kinetic scale physics, special relativity and so on are also essentially important for a profound understanding of magnetic reconnection physics and further extension of its application. Since this dissertation concentrates on the reconnection physics that is treated in one-fluid MHD regime, in the following sections and chapters, we will only touch these effects no further than necessary.

1.2 Application

By consuming the anti-parallel magnetic fields, local diffusion in magnetic reconnection generates heat, which originally comes from the collisions between ions and electrons. The work done by the tension force in the outflow region accelerates plasma particles. So from the energy point of view, magnetic reconnection converts magnetic energy into

kinetic and thermal energy of plasma. Additionally, magnetic fields reconnect and build up new magnetic structures. Since magnetic fields are considered to be existing ubiquitously in the universe, it is believed that reconnection can explain various energy releasing astronomical events; especially those ones that create new magnetic topology.

Being the closest star to the Earth, the Sun is the best laboratory for plasma physics studies. Many solar activities can be captured by telescopes and examined in detail. Among all solar activities, the solar flare is the most frequently addressed in magnetic reconnection studies, as the first quantitative understanding of magnetic reconnection was targeting to solve the fast energy release from the solar flare (Sweet, 1958; Parker, 1957). The solar flare is a sudden brightening in a large range of observation during a short time (in the order of minutes or hours). A 2D standard model (Carmichael, 1964; Sturrock, 1966; Hirayama, 1974; Kopp & Pneuman, 1976) was proposed by integrating many features that are observed during the flare events, such as the candle-light cusp structure (Tsuneta et al., 1991), hard and soft X-ray emission (Masuda et al., 1994). As tube-like structures are often created with flare (e.g., Sakurai, 1976), a 3D standard model of flare was founded by introducing an extra magnetic component along the direction that is perpendicular to the reconnection plane (Shibata et al., 1995). Eventually, more complicated features were caught by various observations. Therefore, advanced models which incorporate complex magnetic structures were built. For example, the slipping reconnection model (e.g., Janvier et al., 2013) is applied to explain the S-shaped sigmoids (e.g., Gibson et al., 2002) and the slipping motion of the coronal loop footpoints (e.g., Aulanier et al., 2007); the tether-cutting model (e.g., Moore et al., 1997) and the model with emerging flux near the polarity inversion line (e.g., Kusano et al., 2012) explain the onset of reconnection and the flux tube production. Other phenomena such as solar jets (e.g., Takasao et al., 2013), filament production (e.g., Kaneko & Yokoyama, 2017), coronal mass ejection (e.g., Hassanin & Kliem, 2016), corona heating (e.g., Parker, 1972), Ellerman bomb (e.g., Watanabe et al., 2011) are also highly related to reconnection.

The extension of the solar atmosphere that reaches the interplanetary space is called

the solar wind. The reconnection events are prevalent in the solar wind (Phan et al., 2009), thus it is believed to be important in explaining the intermittent turbulence and the creation of coherent structures in different scales (Osman et al., 2014), the acceleration of the solar wind (Fisk et al., 1999) and so on.

Magnetic fields of the Sun extend and inevitably contact with the magnetosphere of the Earth and other planets in solar system. Regarding the tilting angle difference and the time-dependent orientation of the magnetic fields from the Sun, the magnetic fields of the Sun and the Earth are not necessary to be always aligned at the magnetosphere. Meanwhile, the unceasing solar wind compresses the magnetic fields towards the Earth's side, which triggers reconnection naturally. Reconnection happens at the magnetopause transfers the solar plasma into the Earth (e.g., Lee & Fu, 1985). At the geotail, reconnection is also considered to happen (e.g., Eastwood et al., 2010) while producing flux tubes (Hughes & Sibeck, 1987) and the earthward busty bulk flows (Birn et al., 2011).

Magnetic fields from different stars, protostars or accretion disks fill in the interstellar space. Sometimes the fields tangle with each other and create spectacular views, such as the Galactic Ridge X-ray Emission (Tanuma et al., 1999). Reconnection is also supportive in explaining the transportation of angular momentum bi-directionally in the accretion disk (Hoshino, 2015), the non-thermal particle acceleration (Hoshino, 2012) and so on.

The system size of the astronomical events is always too large compared to a single reconnection event, whose size is determined by the particle scale. Therefore, one of the most significant purposes of the reconnection theoretical studies is to prepare a firm foundation for the more realistic models in the future.

1.3 Classical models and theory

First theoretical studies of magnetic reconnection intended to solve the fast energy release observed in the solar flares. Assumptions and approximations were used for simplicity in building up these models. They construct solid bases for the proceeding advanced studies on the topic of reconnection. Meanwhile, analysis of current sheet physics also signifi-

cantly deepens the understanding of reconnection dynamics. In this section, we overview two classical time-independent models and the spontaneous instability of a current sheet in detail.

1.3.1 The Sweet-Parker model and Petschek's model

The first time-independent analytical study on reconnection was proposed by Sweet (1958) and refined by Parker (1957) to understand the fast energy release from the solar flare. They assumed that a large current sheet in the same size of the solar flare is formed by a pair of approaching magnetic dipoles under the footpoint motion. The compressed region between the two dipole fields becomes a 2D slab-like sheet. The whole current sheet participates reconnection that the diffusion region is as large as the current sheet itself (left panel of Fig.1.2). By considering the conservation law (total mass and magnetic flux) inside a diffusion region with a half-width d and a half-length l, a simple scaling law is deduced that

$$\frac{d}{l} \sim \frac{v_{\rm in}}{v_{\rm out}} \sim \frac{v_{\rm in}}{v_{\rm A}} \tag{1.4}$$

where $v_{\rm in}$, $v_{\rm out}$ and v_A represent the inflow, outflow and the Alfvén velocity of the system asymptotic magnetic field. The outflow becomes Alfvénic that $v_{\rm out} \sim v_{\rm A}$, as the global asymptotic fields are supposed to be sufficiently converted.

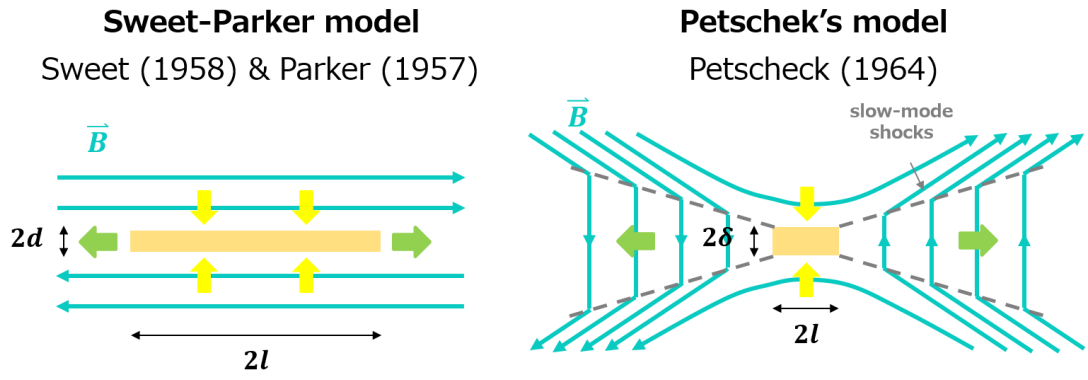

Figure 1.2: Illustration of magnetic reconnection in the Sweet-Parker model and Petschek's model. Turquoise lines are magnetic field lines. Yellow and green arrows are inflow and outflow. Orange regions represent diffusion regions. Grey dashed lines are slow-mode shocks in Petschek's model.

The most important issue in the reconnection modeling is the capability of fast energy release. In another word, fast reconnection is always required. In the Sweet-Parker model, the inflow v_{in} is estimated by the diffusion equation that

$$v_{\text{in}} \sim \frac{\tilde{\eta}}{d} \tag{1.5}$$

which is dependent on the diffusivity. The diffusion strength in a system can be evaluated by the Lundquist number, S, which is defined by

$$S \equiv \frac{v_c L_c}{\tilde{\eta}} \tag{1.6}$$

where v_c and L_c are the characteristic velocity and the length scale that change with problems. When S is large, the system slowly diffuses. In the context of global reconnection,

$$S = \frac{v_A L}{\tilde{\eta}} \tag{1.7}$$

where L is the system size. By relating Eq.(1.4), Eq.(1.5) and Eq.(1.7) and take $l \sim L$, we have the reconnection rate of the Sweet-Parker reconnection as

$$M_A = \frac{v_{\text{in}}}{v_A} \sim S^{-\frac{1}{2}}. \tag{1.8}$$

The environment of most astronomical events usually has large S. For instance, the solar corona, where the solar flare happens, has $S \sim 10^{12} - 10^{14}$. It indicates that in a large current sheet in the same size as the flare itself, the reconnection rate is in the order of tens or hundreds of days. This result is far slower than the observation (minutes or hours), so another model with a higher reconnection efficiency is needed.

From Eq.(1.4), the reconnection rate is inversely proportional to the diffusion region length l. So one way to increase the reconnection rate is to shrink the diffusion region size. Petschek (1964) argued that if the diffusion region has $d \sim l \propto \tilde{\eta}$, the reconnection rate is enhanced. In addition, two pairs of slow-mode shocks are created as the reconnec-

tion produces a discontinuity between the inflow and the outflow regions (right panel of Fig.1.2). By combining solutions in the diffusion region, the inflow and outflow regions, the reconnection rate is tuned up to

$$M_A \sim \frac{\pi}{8 \log S}, \tag{1.9}$$

which is less dependent on the diffusivity. For solar flare case, the reconnection rate is raised to $M_A \sim 0.01$, which seems to be consistent with the global observation on the reconnection inflow (Yokoyama et al., 2001a; Takasao et al., 2012a).

Petschek's model was regarded as an effective model that can be implemented into the solar flare model. However, it was noticed that unless localized diffusivity is applied (e.g., Ugai & Tsuda, 1977; Baty et al., 2006), Petscheck's model cannot last long. Rather, it degenerates into the Sweet-Parker type reconnection (Biskamp, 1986), which seems to be a common scaling law for a single diffusion region.

These two classical models are time-independent models. It means that they can explain the physics when the system reaches a quasi-steady state. Then here comes a question that how the reconnection starts. There are roughly two types of initiations, driven reconnection and spontaneous reconnection. Driven reconnection corresponds to the reconnection that is controlled by the external force (e.g., Sato & Hayashi, 1979; Kowal et al., 2009). In comparison, spontaneous reconnection exhibits the potential of a current sheet in reconnection. The latter one is often related to the tearing instability, which is an inherent instability of the current sheet itself.

1.3.2 The tearing instability

The tearing instability is a spontaneous instability of the current sheet, which extracts free energy from currents. A simple picture of the tearing instability could be explained as the following (Fig.1.3). When a current sheet is perturbed, at some points the current enhances locally. Due to the Ampère's law, the enhanced current will absorb more current

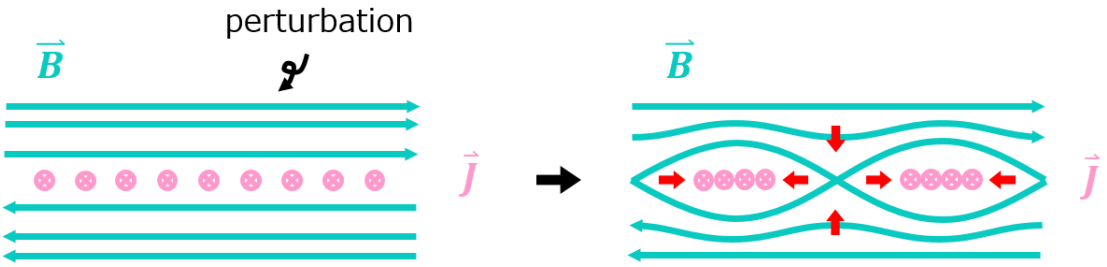

Figure 1.3: Illustration of the tearing instability (2D). Turquoise lines are magnetic fields while pink circle-with-cross labels are currents running into the paper. Red arrows represent plasma flows.

to itself, which triggers the instability. Since the currents are the counter-flowing electrons and ions streams, the motion of currents along the tearing layer represents the motion of plasma. The position where currents are depleted needs external plasma to fill in. Meanwhile, the external magnetic fields are bent into the tearing layer to fit the new configuration of current distribution. The converging flow across the current sheet will further ensure the bent of the field lines. As the magnetic field across the current sheet gets more and more compressed under the push of flow and the current reorganization, current density is gradually enhanced locally. When the diffusion term in the induction equation Eq.(1.1) becomes dominant in the local region, reconnection starts and the position with enhanced current density develops into an X-point. In between X-points, currents are collected inside a confined structure formed by reconnected magnetic fields, namely a plasmoid (or a magnetic island).

The tearing instability can be triggered on any layers where current density is high. So Fig.1.3 is a 2D cut along the propagation direction of the tearing instability in a 3D system. The more general illustration of the tearing instability is given in Fig.1.4 for a current sheet formed by sheared magnetic fields, which could be decomposed into anti-parallel magnetic fields with a global guide field. For simplicity, we assume a uniform global guide field. Current runs along the guide field and reaches a peak at the current sheet center. If the perturbation wave vector propagates along the direction of the anti-parallel fields (2D perturbation), the tearing instability grows at the current sheet center

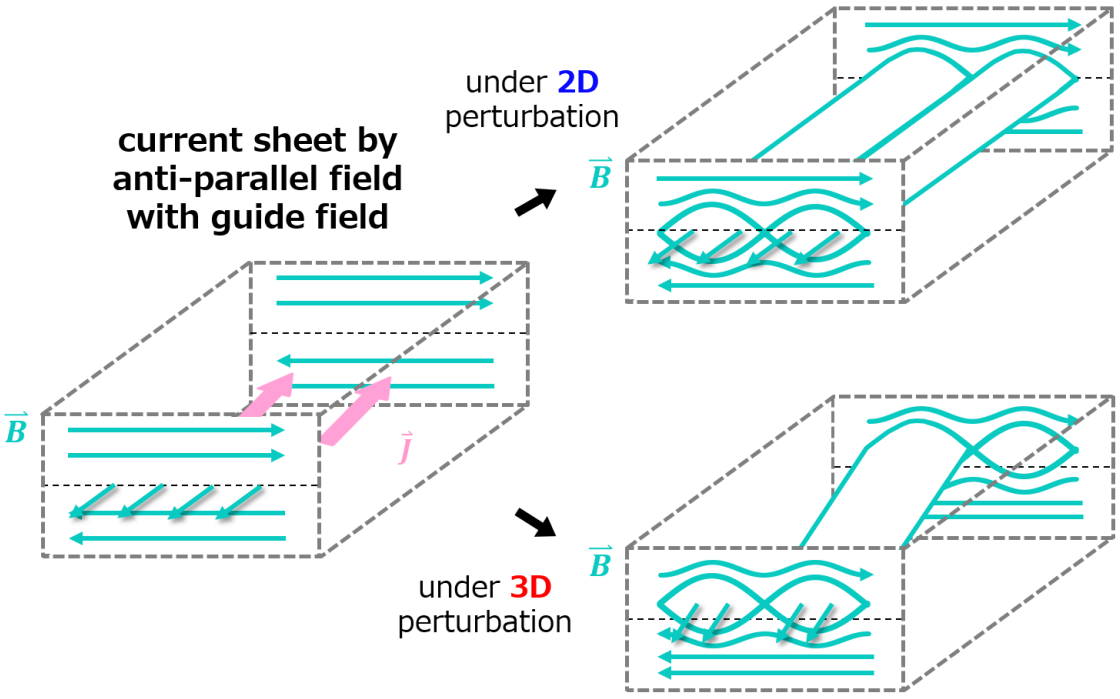

Figure 1.4: Illustration of the tearing instability in a current sheet formed by anti-parallel fields (turquoise lines) with a uniform guide field (turquoise lines with shadows on the left panel). The current sheet center is shown as horizontal dashed lines on fore and rare surfaces. Current (pink arrows) runs along the guide field. Orientation of tearing-produced flux tubes depends on the perturbation wave vector. Turquoise lines with shadows represent the local field on the right panels.

and generates a line of X-points (X-line) with flux tubes in between. This structure is 2D-like as each cut across the guide field direction is the same. When the perturbation wave vector is tilted to the guide field (3D perturbation), the tearing instability grows on a layer that is away from the current sheet center. Flux tubes and X-lines that are parallel to the local field are formed. The position of the tearing layer is chosen by the criteria:

$$\mathbf{k} \cdot \mathbf{B} = 0 \tag{1.10}$$

(Furth et al., 1963) that the tearing instability grows on the layer where the local magnetic field is perpendicular to the perturbation wave vector $\mathbf{k}$.

In reality, it is rare the case that the perturbation contains only one single $\mathbf{k}$. Random perturbation which is a mixture of numerous wave vectors with a continuous spectrum is generally expected. Each wave vector will select its preferable magnetic layer and plant seed for the tearing instability. As a result, the current sheet is packed with tearing layers that each one of them corresponds to a certain wave vector (Galeev & Zelenyi, 1977). But the fastest growing ones will govern the physics of the global current sheet.

The growth rate of the tearing instability can be obtained by analytical study. Furth et al. (1963) were the first to quantitatively examine the tearing instability in a sheared magnetic field with a current sheet half-width a. By neglecting viscosity and assume incompressibility ($\nabla \cdot \mathbf{v} = 0$) for simplicity, the full set of MHD equations are left with two coupled equations of the perturbed fields. The tearing is effective in a thin layer near the resonance layer, in which diffusion dominates. Thus the linearized equations become a boundary-layer problem that solutions inside the diffusion layer and the outer region should be connected. The connection is done by equating the tearing parameter Δ' inside and outside of the tearing layer.

There are many ways of linearizing equations, so different forms of Δ' are given. We will follow the process in Biskamp (1997) here as an example. Since incompressibility is often assumed in many linear studies, the coupled equations of $\mathbf{B}$ and $\mathbf{v}$ can be rewritten as equations of coupled magnetic flux function ψ and plasma flow function ϕ. General

definitions of flux function ψ and flow function ϕ are:

$$\mathbf{B} = \mathbf{e_z} \times \nabla\psi \tag{1.11}$$

$$\mathbf{v} = \mathbf{e_z} \times \nabla\phi \tag{1.12}$$

where the fields along the direction perpendicular to the tearing plane ($\mathbf{e_z}$) are neglected. For a tearing mode that is growing on $x = x_s$, the tearing parameter is expressed as

$$\Delta' \sim \frac{\psi_1'(x_s^+) - \psi_1'(x_s^-)}{\psi_1(x_s)} \tag{1.13}$$

(Biskamp, 1997, Eq.(4.87)) where $\psi_1'(x_s^\pm) = \partial\psi_1(x_s^\pm)/\partial x$ represent the first derivative of the perturbed magnetic flux on either side of the tearing layer x_s. It reflects how much magnetic field piles up just outside the diffusion layer across the X-point. When $\Delta' > 0$, magnetic field compresses into the X-point and encourages the tearing instability to grow. When $\Delta' < 0$, there exists no bi-directional compression thus the tearing is stopped. By comparing all terms in the coupled equations, the tearing instability with a long wavelength has a growth rate γ and a diffusion layer half-width δ_η:

$$\gamma^{\text{FKR}} \sim (64\pi)^{-1/5}\widetilde{\eta}^{3/5}(\Delta')^{4/5}(kB_0')^{2/5} \propto k^{-2/5}\widetilde{\eta}^{3/5} \tag{1.14}$$

$$\delta_\eta \sim \frac{\widetilde{\eta}\Delta'}{2\gamma} \sim (2\pi)^{1/5}\widetilde{\eta}^{2/5}(\Delta')^{1/5}(kB_0')^{-2/5} \propto k^{1/5}\widetilde{\eta}^{2/5} \tag{1.15}$$

(Biskamp, 1997, Eq.(4.90)(4.91)), where B_0' measures the current sheet pinch.

A Harris sheet (Harris, 1962) is often implemented in the reconnection study as the background current sheet. The magnetic field has a structure of

$$B_\parallel(x) = B_0 \tanh\left(\frac{x}{a}\right) \tag{1.16}$$

where B_0 is the asymptotic value for the anti-parallel magnetic fields in the infinity $x \to \infty$ and a is the current sheet half-width. Then the analytical solution of the tearing instability can be obtained by considering the boundary condition $\psi_1(x = \pm\infty) = 0$

that

$$\psi_1 = e^{-k|x|}\left[1 + \frac{1}{ka}\tanh\left(\frac{|x|}{a}\right)\right]. \tag{1.17}$$

(Biskamp, 1997, Eq.(4.97)). Therefore, the tearing parameter Δ' is calculated as

$$\Delta' = \frac{2}{a}\left(\frac{1}{ka} - ka\right) \tag{1.18}$$

(Biskamp, 1997, Eq.(4.98)).

A cut-off wavelength of the tearing exists that

$$k_{\text{cut}}a \sim 1 \tag{1.19}$$

so only the perturbed mode with a wavelength longer than 2π of the current sheet half-width can grow ($ka < 1$). The mode with a shorter wavelength will be sufficiently suppressed by the magnetic tension force.

From Eq.(1.18), there exists a monotonically increasing dependence of the growth rate on the tearing wavelength. However, when Δ' becomes too large, say $\Delta'\delta_\eta \sim 1$, the local reconnection at the X-point cannot consume the piling-up magnetic field fast enough. So reversely, the growth of the tearing reduces with longer wavelengths (Coppi et al., 1976). Therefore, the growth rate of longer tearing modes is following a scaling law that

$$\gamma^{\text{Coppi}} \propto k^{2/3}\widetilde{\eta}^{1/3}. \tag{1.20}$$

For a short current sheet, the available modes are always FKR modes. So the most unstable modes k_{max} are the longest modes in the system. When the sheet becomes long enough, the most unstable modes are determined by the junction of the two regimes, FKR and Coppi (Fig.1.5), that

$$k_{\text{max}} \propto \widetilde{\eta}^{1/4} \tag{1.21}$$

with a growth rate of

$$\gamma_{\text{max}} \propto \widetilde{\eta}^{1/2}. \tag{1.22}$$

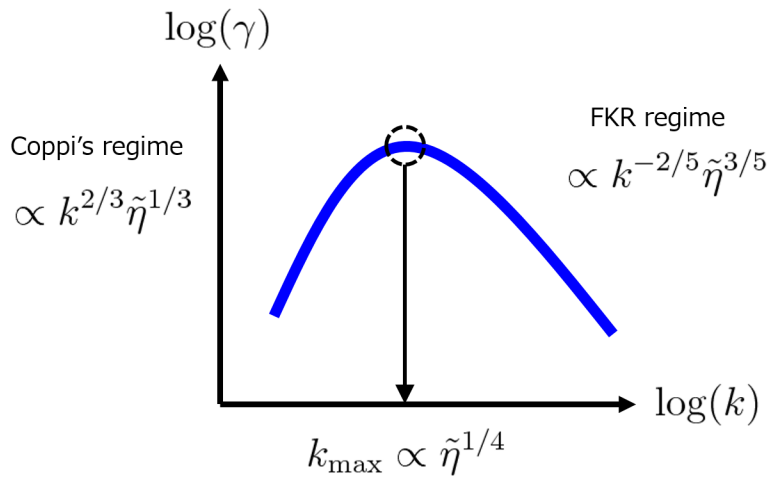

Figure 1.5: Two regimes of the tearing instability growth in the log-log scale.

As it can be clearly seen from Eq.(1.14), Eq.(1.20) and Eq.(1.22), the growth rate of the tearing instability is decreasing with smaller diffusivity. Therefore, the linear stage of the tearing instability alone is incapable to explain the fast reconnection. Further stages should be investigated to understand the spontaneous reconnection.

1.3.3 Other classical models

In Sec.1.3.1, we reviewed two classical steady solutions of reconnection. Although the Sweet-Parker reconnection is slow, it presents a common scaling law in diffusion regions since only the conservation laws are applied in the deduction. In comparison, the requirement for achieving Petschek's reconnection is much more severe. The localized diffusivity can be regarded as a boundary condition from the inner side. The inflow and outflow characteristics are determined by the information propagating outwardly from the diffusion region. Also, the boundary condition onto the whole system changes the central physics inwardly (Biskamp, 1986). It was found by Priest & Forbes (1986) that Petschek's reconnection is one of a group of solutions that react to different boundary conditions. The solution by Sonnerup (1970), which considered slow-mode expansion waves propagating towards the diffusion region, is also included as one of these solutions.

In addition to these models, another model declared that the slow-mode shocks as

that in Petschek's model cannot be stationary. Rather, they propagate with the moving plasmoid (Biernat et al., 1987). During the propagation, the plasmoid boundary also consumes the magnetic energy so it creates a bursty reconnection during the propagation phase (Semenov et al., 1998). A 3D extension of this model was shown in Linton & Longcope (2006). The bursty feature also starts from the discontinuity near the X-point. So essentially, this model depends on the boundary condition applied by the diffusion region as well.

All reconnection models above are applied to a slab-like current sheet. Since the magnetic field is rather complicated in the universe, this assumption is not always held. The magnetic fields on the solar surface sometimes expand into the form of a dome instead of an extended loop (e.g., Jiang et al., 2015). The reconnection therefore becomes different from the slab-like type as the symmetry changes from flat into cylindrical. The model of fan-spine reconnection is raised (e.g., Priest & Pontin, 2009) and serves different geometries.

1.4 Advanced models

As the steady solutions are either too slow to explain the observed astronomical events or highly dependent on the boundary condition, it is worth considering more dynamic reconnection pictures to overcome these problems.

1.4.1 The 2D plasmoid instability reconnection model

Strong and continuous external forces that sustain driven reconnection cannot be always guaranteed. Therefore, whether spontaneous reconnection has a potential to be fast is important to cover all possibilities.

The tearing instability cannot grow exponentially eternally. As no flux can be ejected from the system, the growth of plasmoids in between X-points will eventually suppress the reconnection outflow from X-points. When the plasmoid width grows as large as the

diffusion layer width $2\delta_\eta$, the lateral fields do not diffuse as the central fields do. So the magnetic island is trying to contract across the current sheet direction, which also slows down the instability growth. Then the tearing layer enters the nonlinear phase. The island width grows linearly with time ($w \propto t$) during this stage (Rutherford, 1973). Rutherford's regime gradually stops when the island width approaches $1/\Delta'$ (Uzdensky & Loureiro, 2016), when the magnetic island configuration exceeds the provided potential change from the initial magnetic pinch. Further island growth is quenched by the background magnetic pressure from the lateral.

In summary, the magnetic island width w grows from a small amplitude supplied by the initial perturbation and goes through 2 classical phases that

$$w(t=0) \xrightarrow{\text{linear tearing}} 2\delta_\eta \xrightarrow{\text{nonlinear Rutherford}} 1/\Delta'. \tag{1.23}$$

It is clear that for shorter FKR modes ($\Delta'\delta_\eta \ll 1$), there exists a long term Rutherford's stage. But for Coppi's modes with long wavelength, Rutherford's stage is considerably shortened and enters another regime. When the tearing parameter Δ' is sufficiently large, the continuous supply of magnetic fields compresses the X-point along the tearing layer and forms an elongated diffusion region (Jemella et al., 2003), which thereafter enters the Sweet-Parker phase (Loureiro et al., 2005).

As the reconnection continues in the Sweet-Parker type diffusion region, the diffusion region is elongated and gets thinner as the outflow push the plasma away from the X-point (Shibata & Tanuma, 2001). It is found that a 2D Sweet-Parker sheet is unstable to secondary tearing (Biskamp, 1986). So the elongated diffusion region collapses again into smaller pieces (Loureiro et al., 2005). It is expected that the collapsing continues before the diffusion region width reaches the ion gyroradius (Shibata & Tanuma, 2001; Uzdensky et al., 2010). Secondary tearing grows in the local Sweet-Parker type diffusion region when the diffusion region aspect ratio $d/l < 0.01$ (Biskamp, 1986; Uzdensky et al., 2010; Huang & Bhattacharjee, 2010). Therefore, the whole system is determined by the smallest thus fastest diffusion region and obtains a global reconnection rate $M_A \sim d/l \sim$

0.01 (Bhattacharjee et al., 2009; Huang & Bhattacharjee, 2010; Loureiro et al., 2012; Shibayama et al., 2015).

This 2D fast reconnection model is called the 2D plasmoid instability reconnection or the 2D hierarchical reconnection. As the reconnection rate becomes independent of S when $S \gtrsim 10^4$ (Bhattacharjee et al., 2009; Huang & Bhattacharjee, 2010; Loureiro et al., 2012; Shibayama et al., 2015), this model seems to be applicable to a system with a considerably large Lundquist number, such as the solar flare. Also, it builds up a bridge between the large system scale with the small particle scale by continuous collapsing (Shibata & Tanuma, 2001; Uzdensky et al., 2010; Bárta et al., 2011).

However, a strong limitation exists in this model. As shown by 3D simulations, the 2D structures are easy to be disturbed by the 3D perturbation, even though the initial seeded 3D modes (wave modes propagate along the current sheet with non-zero wave vectors perpendicular to the anti-parallel magnetic fields) energy is much smaller than the seeded 2D modes (wave modes propagate only along the anti-parallel magnetic fields) (Dahlburg et al., 1992; Dahlburg & Einaudi, 2002). When no global guide field is applied, the produced 3D flux tubes that are perpendicular to the reconnection plane are easy to be distorted by kink-like instability. Therefore, the 2D plasmoid instability reconnection model seems to be unfeasible in a 3D system without guide fields. It has been confirmed that the reconnection in a 3D simulation box with no guide field becomes turbulent that no clear coherent structures can be identified (Oishi et al., 2015). It is straightforward to think that the 3D perturbation can be suppressed by implementing a strong guide field in the current sheet. In this case, the turbulence still emerges. Meanwhile, coherent flux tubes that are not parallel to the global guide field can be observed (Landi et al., 2008; Huang & Bhattacharjee, 2016)

It seems that the 3D reconnection enters a different regime compared to the 2D reconnection. Thus a new model in 3D reconnection, especially the fast 3D reconnection, is required.

1.4.2 3D turbulence reconnection model

A reconnecting current sheet spontaneously generates turbulence, both in 2D (Lapenta, 2008; Bárta et al., 2011) and in 3D (Huang & Bhattacharjee, 2016; Beresnyak, 2017; Kowal et al., 2017). The understanding of the interaction between turbulence and reconnection starts from how turbulence changes the reconnection rate. It was found that by introducing a strong random perturbation onto a 2D current sheet, multiple X-points emerge and increase the global reconnection rate (Matthaeus & Lamkin, 1985). Also in a 3D current sheet, a driven turbulence increases the global reconnection rate which becomes independent of diffusivity (Kowal et al., 2009). However, since the self-generated turbulence couples with the reconnection in spontaneous reconnection, how turbulence accelerates the reconnection in a free system is still not sufficiently understood.

One turbulence reconnection model theoretically describes the reconnection development in a 3D current sheet when a statistical steady turbulent state has reached (Lazarian & Vishniac, 1999). In the global scale, which corresponds to the energy input scale, the magnetic fields are absorbed into the current sheet as the turbulent area expands across the current sheet. In the local scale, which corresponds to the dissipation scale, reconnection happens and blends the field lines into the pool of magnetic fields. A fast global reconnection rate is deduced by coupling to the MHD turbulence theory (Goldreich & Sridhar, 1995) that each diffusion region is diffusing fast.

Fast overall reconnection is found in 3D spontaneous reconnection. In a current sheet with no guide field, the reconnection rate is in the magnitude of 0.001, while a non-monotonic change of reconnection rate with diffusivity is found (Oishi et al., 2015). In a current sheet with a guide field that varies from half to twice of the anti-parallel fields strength, the overall reconnection rate is consistently high that $M_A \sim 0.01$, which is also independent of diffusivity. The reconnection rate remains high even when the guide field is reduced to 10% of the anti-parallel field (Kowal et al., 2017). Judging by the up-to-date results, it seems that 3D reconnection has a potential to be fast even in the system with a large Lundquist number. On the other hand, the physics changes between the current

sheet with and without a guide field.

Unlike the global features such as the global reconnection efficiency, the validation of the local reconnection process predicted by the turbulence theory has not been confirmed in the 3D reconnection due to the structural complexity. Moreover, the present MHD turbulence theories all consider a strong background field (e.g., Goldreich & Sridhar, 1995; Boldyrev & Loureiro, 2017; Mallet et al., 2017). In the language of reconnection, this setup roughly corresponds to a current sheet with a strong guide field. In that sense, the application of the present turbulence reconnection model is very limited. When the guide field is weak, this model can be applied only to a thin layer near the current sheet center where anti-parallel fields are much weaker than the guide field. When the guide field becomes zero, the present theory is not feasible. As the energy spectrum from different studies varies (e.g., Huang & Bhattacharjee, 2016; Beresnyak, 2017; Kowal et al., 2017), it indicates that a new fast 3D reconnection model is needed to explain more general behaviors of the current sheet.

1.5 Motivation

Although magnetic reconnection is one of the basic processes in plasma physics, the understanding is still far from sufficient, especially the spontaneous reconnection in a three-dimensional (3D) current sheet.

As turbulence is always observed in the reconnecting current sheet, many studies solve the reconnection issue from the turbulence theory viewpoint. However, the understanding of the MHD turbulence in sheared magnetic fields has not been substantially developed. Therefore, the coupling of turbulence-enhanced-reconnection and reconnection-generated-turbulence needs a careful treatment. We are going to approach the 3D fast reconnection problem by analyzing the diffusion region development, where reconnection happens and produces turbulence. We expect that our result could support the turbulence reconnection theory by connecting the diffusion region creation and distribution with the energy spectrum study in the future.

Because we are interested in the spontaneous fast reconnection regime, we start the consideration from a 3D current sheet with a finite guide field under perturbation. From the physics picture of the tearing instability, it is natural to expect that the most unstable tearing instability to be always growing on the layer where the current density is the strongest in a static current sheet (see also Appendix.A). Many linear studies on the tearing instability showed that 2D modes, which are growing along the current sheet center, are always the most unstable tearing modes compared to 3D modes that are growing away from the current sheet center (Onofri et al., 2004; Landi et al., 2008; Dahlburg et al., 1992; Baalrud et al., 2012). Interestingly, nonlinear simulations show a different result. After applying the random perturbation to a 3D current sheet with a finite guide field, it is often the case that multiple reconnection layers emerge and sustain even in the nonlinear phase (Onofri et al., 2006; Landi et al., 2008; Wang et al., 2015; Beresnyak, 2017; Kowal et al., 2017). Although the present researches cannot explain this fact, we will make use of the coexistence of multiple tearing layers in our argument.

In our previous study on the development of 3D tearing layers (Wang et al., 2015, master thesis), we found that when two diffusion regions on neighboring tearing layers are shifted from each other along the current sheet direction, the outflow from one diffusion region diverts into the inflow region of the counterpart diffusion region. This inflow-outflow coupling, or "positive-feedback system" as we called, is observed ubiquitously inside the simulation box. It seems that this coupling between diffusion regions, namely the coupling between tearing layers, is correlating with the global reconnection enhancement, as the simulation with single tearing layer does not show the same eruptive phase of reconnection. Because of the anisotropic turbulence in our simulation, it is difficult to analyze the detailed physics in the inflow-outflow coupling. Thus the concrete reasoning between the coupling and the global reconnection efficiency was not sufficiently deduced.

The first question we should solve is the basic properties of the inflow-outflow coupling. The apparent structure of the 3D tearing layer coupling resembles the double tearing instability (DTM) in which two reconnection layers in two adjacent current sheets

couple with each other. The local reconnection in an individual diffusion region is enhanced due to the coupling (Pritchett et al., 1980) and resultantly enhances the global reconnection (Yan et al., 1994). Whether the same argument is true in the 3D tearing layer coupling needs to be verified.

Although multiple layers also coexist in the current sheet during the turbulent state, it is not proved yet that whether the inflow-outflow coupling is universally existing along time. If the inflow-outflow coupling is limited in some certain areas or even missing in the later phase, other mechanisms should be employed to understand the global fast reconnection. In addition, if the inflow-outflow coupling is always confined near the current sheet center, the global reconnection cannot be fast as the annihilated anti-parallel magnetic components are limited.

The inflow-outflow coupling is formed by diffusion regions. Before investigating the existence and distribution of the coupling, the temporal and the spatial development of diffusion regions should be checked first. A large coverage of diffusion regions, or an extended reconnection layer along the current sheet direction is essential for 3D fast overall reconnection (Fig.1.6). In 2D reconnection, a translational invariance is assumed along the direction perpendicular to the reconnection plane (local guide field direction). Magnetic fluxes are transported into participating reconnection uniformly. A fast global reconnection is achieved as long as the reconnection is efficient on the 2D plane. If the diffusion regions are scattered along the local guide field direction, the whole magnetic sheet is partly absorbed into the current sheet. The global reconnection is slower than the 2D counterpart because not all magnetic fluxes are consumed. Therefore, a uniform distribution of diffusion region along the sheet direction is required for a sufficient reconnection.

We propose a hypothesis by considering all arguments above: the 3D reconnection in a current sheet with a finite guide field is accelerated by the ubiquitously existing coupling between sheet-wise extending reconnection layers that span across the whole current sheet. The motivation of our study is the confirmation of our fast 3D reconnection

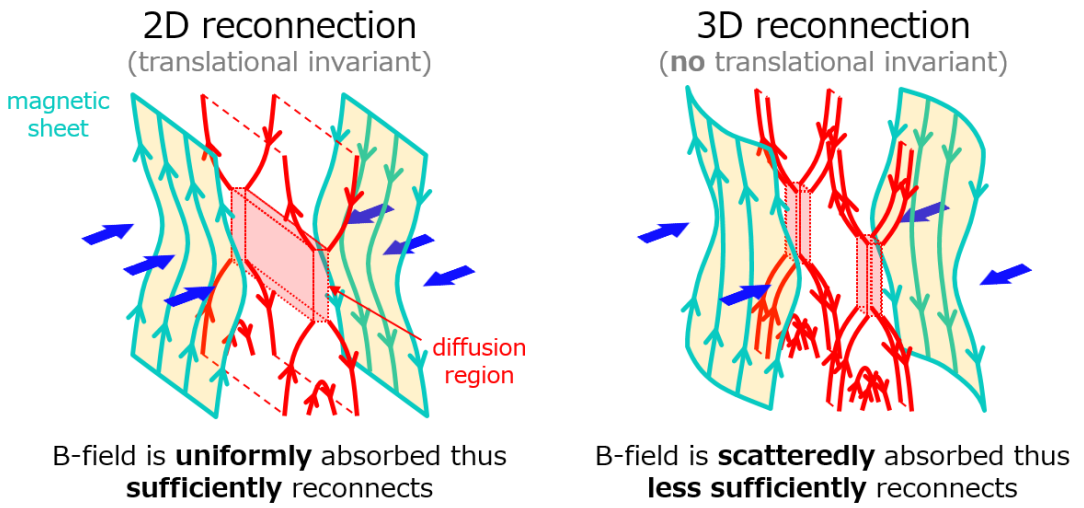

Figure 1.6: Comparison of uniform 2D-like reconnection and non-uniform 3D reconnection. Turquoise lines with orange surfaces are magnetic sheets under inflow (blue arrows). Translucent red boxes represent diffusion regions, while red lines with arrows are reconnected magnetic field lines.

hypothesis.

The structure of this dissertation is summarized as the following (Fig.1.7). In Chap.2, we examine in detail the coupling effect in a typical case to understand the basic physics from a local point of view. In Chap.3, extended from the previous result, we expand our view into global features to check whether sheet-wise reconnection layers are created, whether the coupling links the asymptotic magnetic fields across the whole current sheet and whether overall reconnection rate increases. In Chap.4, we re-examine the random perturbation simulation result to find the same features shown in Chap.2 and Chap.3. In Chap.5, we generalize our model further by changing the initial perturbation and background magnetic field. In Chap.6 and Chap.7, we summarize our findings and discuss the extension of our model by considering more realistic setups.

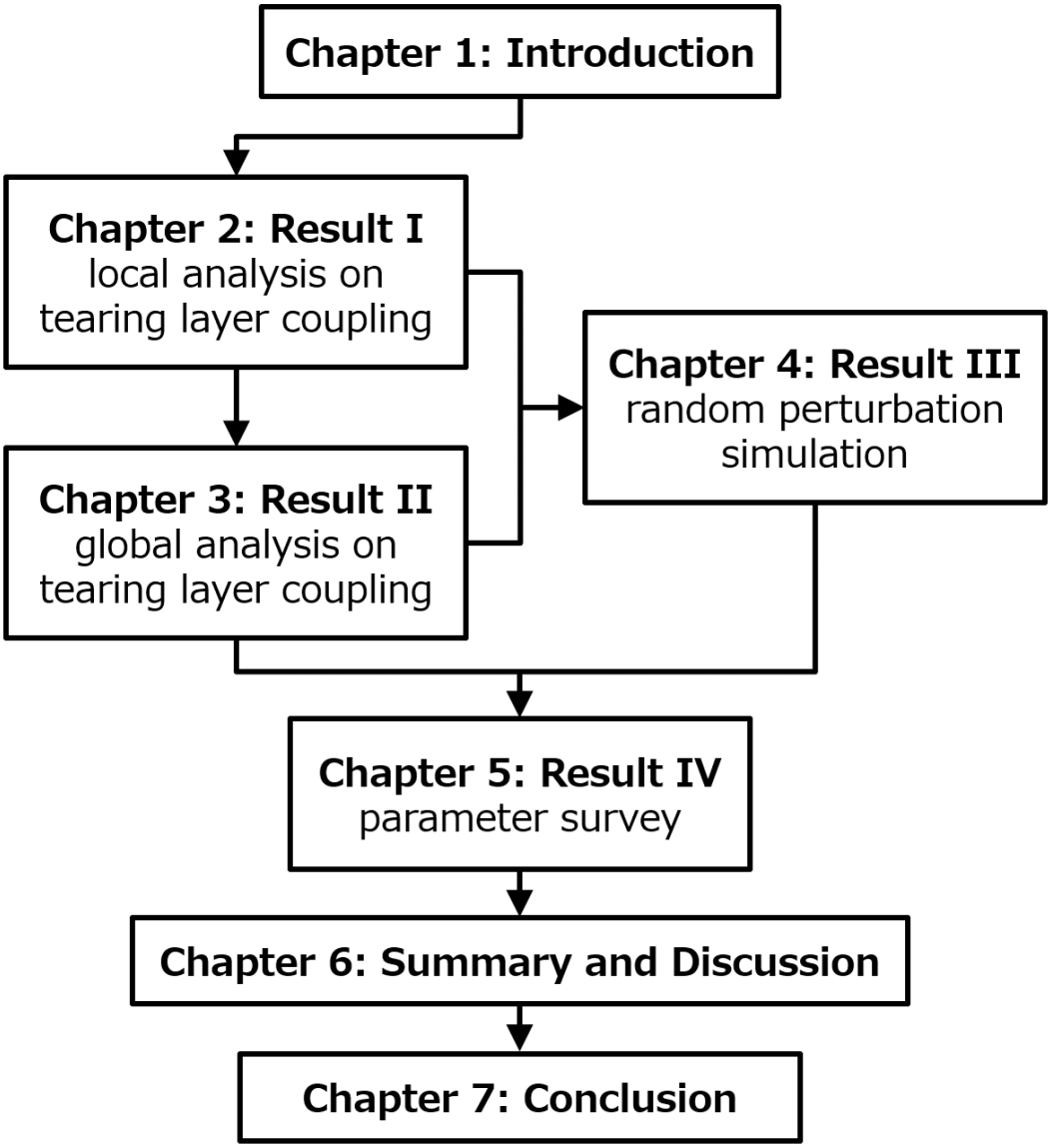

Figure 1.7: Organization of this thesis.

Chapter 2

Result I: local analysis of the typical case

We expect that the understanding of the tearing layer coupling approaches the final understanding of the fast 3D reconnection in sheared magnetic fields. We are going to attack this question from the detailed analysis on the local diffusion region development.

2.1 Introduction

The tearing layer grows inside the current sheet with increasing amplitude, which can be measured by the half-width of the produced flux tube. When flux tubes on two adjacent tearing layers grow large enough, say the total amplitudes of two tearing modes is larger than the distance between the layers, these two tearing layers are potential to interfere with each other. As the tearing modes grow along the current sheet in different directions, a variance of the phase difference between two tearing modes can be observed along the sheet direction. When there is a phase difference of $\pi, 3\pi, ...$ between two tearing modes on a certain plane cut across the sheet, a diffusion region grows on one tearing mode is aligned with a flux tube on the other mode across the sheet direction. If the flux tube grows wide enough, the outflow region inside the flux tube is capable to merge with the inflow region of the aligned diffusion region on the other tearing layer. Therefore, the inflow,

namely the reconnection, is mediated by the locally Alfvénic outflow from the other side across the sheet. We define this merging of the inflow and outflow regions from different diffusion regions as the inflow-outflow coupling of diffusion regions. Furthermore, the two tearing modes are said to be coupled when diffusion regions growing on them are coupled somewhere.

If the configuration of a system is simple, especially when the symmetry is introduced, the local analysis is easy to be done. However, this is a strong limitation compared to the realistic astronomical events. Real systems contain waves with arbitrary frequencies and propagation directions. These waves are considered to be the possible seeds for triggering reconnection, such as solar flares. Consequently, no simple structure is expected. Many numerical simulations on reconnection studies implement a random perturbation initially to mimic the real circumstance thus successfully generalize their results. The disadvantage of such application is that it toughens the local analysis which depicts the fundamental reconnection process. Because the global reconnection can be regarded as a collection of local reconnection, the answer to the global reconnection enhancement is therefore also difficult to make clear. Each diffusion region is thought to be efficiently processing reconnection by itself from the theoretical prediction (Lazarian & Vishniac, 1999). However, no concrete proof is shown in the 3D simulation. Therefore, we will start the simulation with a simple setup to meet our need for the local analysis. Afterwards, the generalization should be applied in a more chaotic system to make the conclusion firm.

This simple setup should be carefully chosen, based on the random perturbation simulation result. The random perturbation will give birth to numerous tearing layers, while each layer follows the tearing criteria Eq.(1.10) with the correspondent wavenumber $\mathbf{k}$. It is widely accepted that 2D modes (wave modes propagate along the anti-parallel magnetic fields) should dominate from the beginning as they are always the most unstable modes in linear studies (e.g., Dahlburg et al., 1992). So a system predominantly described by 2D modes with a mediation of 3D modes (wave modes propagate along the current sheet with non-zero wave vectors perpendicular to the anti-parallel magnetic fields) seems to be

reasonable. In contrast, as shown in many numerical studies, unless a continuous ejection of 2D energy is provided (Huang & Bhattacharjee, 2016), one is more likely to retrieve a system initially dominated by 3D modes that are growing on both sides of a symmetric current sheet (e.g., Landi et al., 2008). Unfortunately, this controversy is still unclear. However, we will use this *a priori* argument that we consider first the coupling between 3D modes in a system, as they develop the fastest in the studies by far.

It is straightforward to expect an efficient coupling between layers when they are close, while similar argument has been concluded in the study of double tearing mode (DTM, Wang et al., 2007; Janvier et al., 2011). If we pick up one tearing layer and consider its adjacent coupled layer, there exist two possibilities. First, if the distance between these two layers is much smaller than the magnetic shear, namely how far it takes for the magnetic field to rotate a full π across the current sheet, these two modes are roughly parallel to each other. Second, if the distance between these two layers is comparable to the magnetic shear, the three-dimensionality in the coupling construction is strong as the tilting angle between these two modes is large.

In our previous study, we identified the coupling of the flow pattern in a current sheet with a finite guide field along time. By taking a closer look, it reveals that the coupling exists between the layers on the same side of the current sheet, as well as between the layers across the current sheet center. The tearing modes on the same side of the current sheet have a smaller tilting angle with each other compared to the modes across the center in our case. Meanwhile, no 2D modes dominate until the late phase of the simulation. When 2D modes grow sufficiently large, they are highly possible to couple with 3D modes and contribute to the global reconnection.

At this moment, we will concentrate on the coupling across the current sheet center in a current sheet with a finite guide field due to the following arguments.

First of all, the coupling of 3D tearing modes across the center exhibits a stronger character of three-dimensionality which is not well understood. The coupling between layers on the same side has a weaker three-dimensionality. The two tearing modes are

likely to merge into one single mode when they are in-phase or develop a DTM-like coupling when they are off-phase. So the coupling system across the whole current sheet can be roughly regarded as a coupling of two thick layers before 2D modes grow large.

Secondly, for the coupling limited on one side, it takes longer time for the fast rarefaction wave in the inflow region of the coupled layers to travel across the whole current sheet to influence the magnetic field on the other side. It is important to connect the anti-parallel magnetic fields on either side of the sheet to have a sufficient global reconnection. Therefore, the coupling across the current sheet center seems to be more efficient as the fast-mode wave has a shorter distance to go. In this sense, 2D modes right at the center also function in the same way. As we argued above, 2D modes are growing slowly compared to the 3D modes from the results of different simulations. So the coupling between 2D modes and 3D modes emerges only from the later phase.

By the considerations above, in this chapter, we will examine the local physics in the tearing layer coupling across the current sheet center first by conducting numerical simulation of a single current sheet. We will apply a finite guide field to this current sheet to have a strong three-dimensionality. Since simple configuration is preferred for the local analysis, we will perturb the current sheet with a pair of rotational-symmetric tearing modes that two tearing layers coexist at the beginning of the simulation. The generalization of the result will be checked in the later chapters.

2.2 General setup

We apply ordinary one-fluid resistive (uniform diffusivity) MHD equations which neglect viscosity, gravity and heat conduction for simplicity:

$$\frac{\partial \rho}{\partial t} + (\mathbf{v}\cdot\nabla)\rho = -\rho(\nabla\cdot\mathbf{v}) \tag{2.1}$$

$$\rho\frac{\partial \mathbf{v}}{\partial t} + \rho(\mathbf{v}\cdot\nabla)\mathbf{v} = -\nabla p + \frac{\mathbf{J}\times\mathbf{B}}{c} \tag{2.2}$$

$$\rho\frac{\partial e}{\partial t} + \rho\,(\mathbf{v}\cdot\nabla)\,e = -p\nabla\cdot\mathbf{v} + \eta\mathbf{J}^2 \tag{2.3}$$

$$\frac{\partial \mathbf{B}}{\partial t} = \nabla\times(\mathbf{v}\times\mathbf{B} - c\eta\mathbf{J}) \tag{2.4}$$

$$\mathbf{J} = \frac{c}{4\pi}\nabla\times\mathbf{B} \tag{2.5}$$

in which ρ and p are plasma mass density and pressure, $\gamma = 5/3$ is the adiabatic index and e is the internal energy per unit mass that $e = p/[(\gamma-1)\rho]$. Together we consider the equation of state for ideal gas that

$$p = \frac{\rho}{\bar{m}}k_B T \tag{2.6}$$

where k_B is the Boltzmann constant, $\bar{m}$ is the mean particle mass, T is temperature.

All quantities are normalized by the typical parameters. The length scale is in the unit of the initial current sheet width δ. The time scale is normalized by $t_A = \delta/v_{A0}$, where v_{A0} is the asymptotic Alfvén velocity. Initial uniform mass density ρ_0 is used for mass density, $\bar{m}$ is taken in the case of fully ionized hydrogen gas that $\bar{m} = 0.5m_p$, where m_p is the proton mass. Normalization of the magnetic field is implemented by $B_0 = v_{A0}\sqrt{\rho_0}$. Current density is normalized by $J_0 = B_0/\delta$ while plasma pressure is normalized by $p_0 = B_0^2$. Cartesian coordinate is used for the linear analysis as well as the nonlinear simulation.

Our background magnetic field is composed of anti-parallel components $B_y(x)$ with

a uniform finite guide field B_z:

$$\begin{aligned}\mathbf{B} &= B_y\hat{\mathbf{y}} + B_z\hat{\mathbf{z}} \\ &= B_{y0}\tanh\left(\frac{x}{a}\right)\left\{\frac{1}{2}\left[\tanh\left(\frac{\mid x \mid -x_{\rm sec}}{a}\right)-1\right]\right\}\hat{\mathbf{y}} + \alpha B_{y0}\hat{\mathbf{z}} \qquad (2.7)\end{aligned}$$

where $B_{y0} = \sqrt{4\pi}B_0$ and $a = 0.5\delta$. The magnetic field is plotted in Fig.2.1. This modified Harris sheet has two secondary current sheets near $\pm x_{\rm sec} = \pm 4\delta$, which do not participate in reconnection essentially. We have shown in our previous paper that the existence of these secondary current sheets near the boundary along the x-direction does not change the result within our simulation time (Wang et al., 2015). Since we are interested in the highly 3D structure in the tearing mode coupling, we apply $\alpha = 0.1$ which is the same as our previous study. The dependence of the coupling on the guide field strength will be further examined later. A uniform magnetic diffusivity is set as $\widetilde{\eta} \sim 3 \times 10^{-4}\delta^2/t_A$. Our typical simulation box size $L_x \times L_y \times L_z$ is $10\delta \times 24\delta \times 6\delta$, while periodic boundary condition is applied on all surfaces for simplicity. As we have explained in Sec.1.3.2, shrinking the current sheet length may change the most unstable tearing mode from a long wave mode into a short wave mode which is determined by

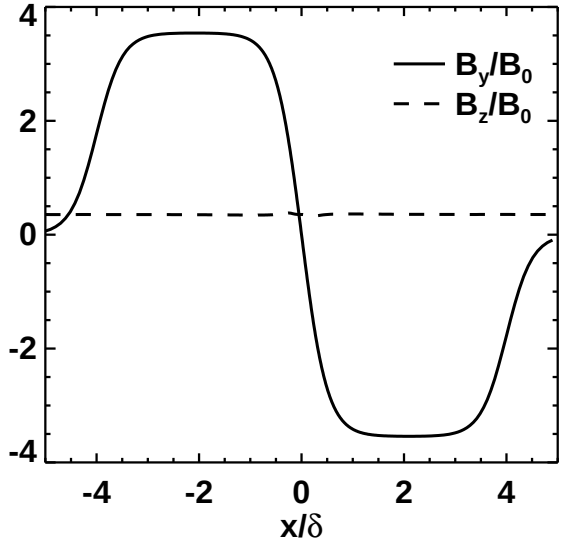

Figure 2.1: Initial magnetic field structure.

the box size. As the boundary condition can have a strong influence during the nonlinear stage, the dependence of the coupling on the box size will be also considered in the future.

2.3 Linear analysis of the tearing instability

Because we want to study how tearing layers couple with each other, a "clean" coupling can be reserved if we apply eigenfunctions of several selected tearing modes onto a static current sheet as an initial condition. So as a start, we solve the eigenfunctions of the tearing instability in our current sheet from linear resistive MHD equations.

In most of the tearing instability linear analysis, compressibility and background diffusivity are neglected for simplicity (e.g., Furth et al., 1963; Steinolfson, 1983; Landi et al., 2008; Baalrud et al., 2012). Incompressibility gives $\nabla \cdot \mathbf{v} = 0$. By assuming a uniform density, the mass equation and the energy equation are excluded from the dynamics. The remained equations are the coupled velocity field and magnetic field in Eq.(2.2), Eq.(2.4) and Eq.(2.5).

We are trying to solve the eigenfunctions of the tearing instability on a plane that is along the wave vector $\mathbf{k}$, since all variables are assumed to be uniform in the direction perpendicular to this plane (left panel of Fig.A.1). We rotate the coordinate into a new one, which is constructed by three new unit orthogonal vectors

$$(\hat{\mathbf{x}}, \hat{\mathbf{k}}, \hat{\mathbf{h}}) \tag{2.8}$$

where $\hat{\mathbf{x}}$ is the unit vector across the current sheet, $\hat{\mathbf{k}}$ is the unit vector along the wave vector $\mathbf{k} = k_y\hat{\mathbf{y}} + k_z\hat{\mathbf{z}}$ that $\hat{\mathbf{k}} = \mathbf{k}/k$ which has an angle θ to the y-axis that $\theta = \arccos\left(\hat{\mathbf{k}} \cdot \hat{\mathbf{y}}\right)$. Third unit vector $\hat{\mathbf{h}}$ is perpendicular to the analysis plane that $\hat{\mathbf{h}} = \hat{\mathbf{x}} \times \hat{\mathbf{k}}$. We expand the variables as the background part (the zeroth order $f^{[0]}$) and the perturbation part (the first order $f^{[1]}$) as

$$f = f^{[0]} + f^{[1]} \tag{2.9}$$

then the linearized equations Eq.(2.2), Eq.(2.4) and Eq.(2.5) can be written as

$$\frac{\partial \mathbf{v}^{[1]}}{\partial t} = -\nabla p_1 - \frac{\mathbf{B}^{[0]} \times (\nabla \times \mathbf{B}^{[1]}) + \mathbf{B}^{[1]} \times (\nabla \times \mathbf{B}^{[0]})}{4\pi} \tag{2.10}$$

$$\frac{\partial \mathbf{B}^{[1]}}{\partial t} = \nabla \times \left(\mathbf{v}^{[1]} \times \mathbf{B}^{[0]} - \widetilde{\eta} \nabla \times \mathbf{B}^{[1]} \right) \tag{2.11}$$

where we assume a stationary plasma $\mathbf{v}^{[0]} = 0$ and a uniform density $\rho = 1$. As we have neglected the compressibility, global diffusion $\tilde{\eta}\nabla^2 \mathbf{B}^{[0]}$, together with

$$\nabla \cdot \mathbf{B} = 0 \tag{2.12}$$

the velocity field and the magnetic field can be written as gradients of potential scalar fields on the analysis plane

$$\mathbf{v}^{[1]} = \nabla_\perp \phi \times \hat{\mathbf{h}} + v\hat{\mathbf{h}} \tag{2.13}$$

$$\mathbf{B}^{[1]} = \nabla_\perp \psi \times \hat{\mathbf{h}} + b\hat{\mathbf{h}} \tag{2.14}$$

where v and b are values along the normal component $\hat{\mathbf{h}}$. The gradient $\nabla_\perp$ is defined on the analysis plane that

$$\nabla_\perp \equiv \hat{\mathbf{k}}\partial_k + \hat{\mathbf{x}}\partial_x. \tag{2.15}$$

We rewrite the variables in the form of

$$\phi(\mathbf{r}, t) = i\phi(x) e^{i\mathbf{k}\cdot\mathbf{r} + \gamma t} \tag{2.16}$$

$$\psi(\mathbf{r}, t) = \psi(x) e^{i\mathbf{k}\cdot\mathbf{r} + \gamma t} \tag{2.17}$$

where $\mathbf{r}$ is the displacement. Then the linearized tearing instability equations are

$$\frac{d^2\phi}{dx^2} = \left(\frac{1}{4\pi\gamma} \frac{d^2 F}{dx^2} - \frac{F}{4\pi\widetilde{\eta}} \right) \psi + \left(\frac{F^2}{4\pi\gamma\widetilde{\eta}} + k^2 \right) \phi \tag{2.18}$$

$$\frac{d^2\psi}{dx^2} = \left(\frac{\gamma}{\widetilde{\eta}} + k^2 \right) \psi - \frac{F}{\widetilde{\eta}} \phi \tag{2.19}$$

while

$$F \equiv \mathbf{B}^{[0]}(x) \cdot \mathbf{k}. \tag{2.20}$$

The method of solving linear equations is described in Appendix.B.

The possible tearing modes in our simulation box are limited by the box size and the periodic boundary condition. For convenience, we label each tearing mode as (m, n). Integers m and n are defined as

$$m = k_y \frac{L_y}{2\pi} \tag{2.21}$$

$$n = k_z \frac{L_z}{2\pi} \tag{2.22}$$

where k_y is always taken as positive while k_z can be positive or negative. Thus the sign of n is determined by the propagating direction of the tearing mode. In our system, the mode growing on the $-x$-side is labeled as $n < 0$ while the mode growing on the $+x$-side is labeled as $n > 0$. One example of an x-plane on which $(m, n) = (3, -1)$ grows is

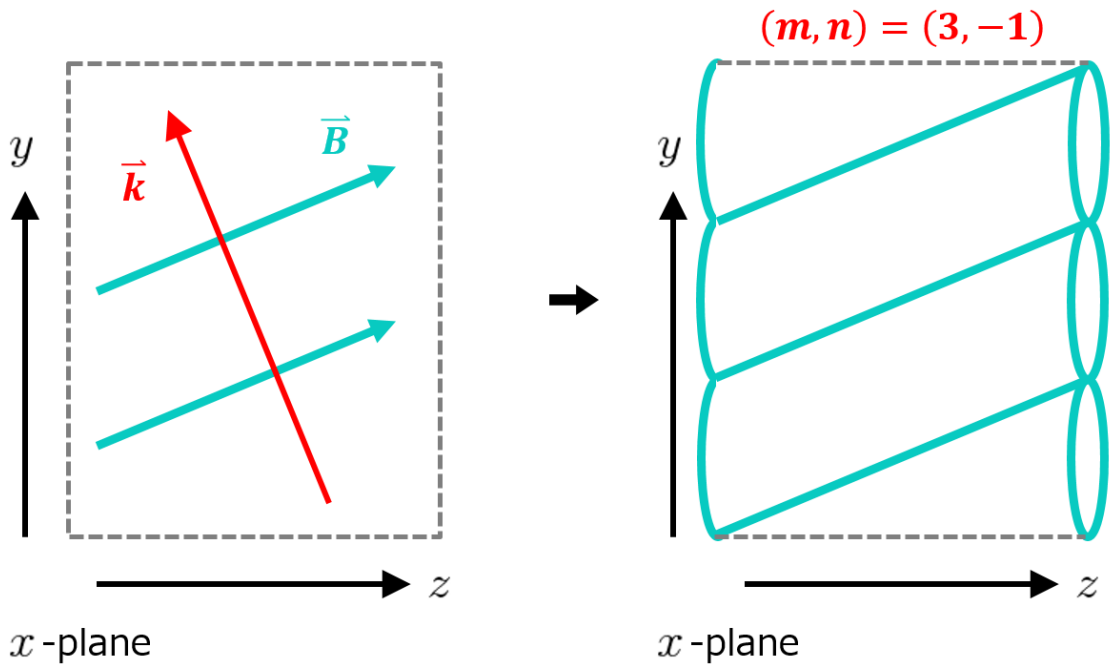

Figure 2.2: Example of an x-plane on which $(m, n) = (3, -1)$ grows. Turquoise lines are magnetic field lines (left panel) and flux tubes (right panel). Red vector represents wave vector $\mathbf{k}$.

shown in Fig.2.2. The tearing mode produces a chain of diffusion regions with flux tubes in between, then integer number m and n can be also understood by counting how many flux tubes are encountered along y- and z-direction. Since the tearing instability grows on the tearing layer where Eq.(1.10) is satisfied, we define a resonance factor q that

$$q = \frac{B_y}{B_z} \tag{2.23}$$

which mimics the safety factor used in tokamak and reversed-field pinch (RFP). The resonance condition $\mathbf{B} \cdot \mathbf{k} = 0$ can be rewritten as

$$q = -\frac{L_y}{L_z}\frac{n}{m}. \tag{2.24}$$

On a resonance layer with a certain q, a series of harmonics grows with the same ratio of n/m. The maximum value of $|q|$ regarding the initial condition is

$$|q| \leq |q|_{\max} = \frac{1}{\alpha} \tag{2.25}$$

which implies a maximum ratio of wavenumber that

$$\frac{|n|}{m} \leq \frac{1}{\alpha}\frac{L_z}{L_y}. \tag{2.26}$$

Considering the cut-off wavelength by Eq.(1.19), the maximum wavenumber that is allowed in our initial setup is

$$k \leq k_{\text{cut}} \sim 2/\delta. \tag{2.27}$$

So the available spontaneous tearing modes in our initial current sheet are limited by $m \leq 7$ for 2D modes with $n = 0$, while the available 3D tearing modes are limited by $m \leq 6$ and $|n| = 1$. The resonance layer position x_s along the x-direction is determined

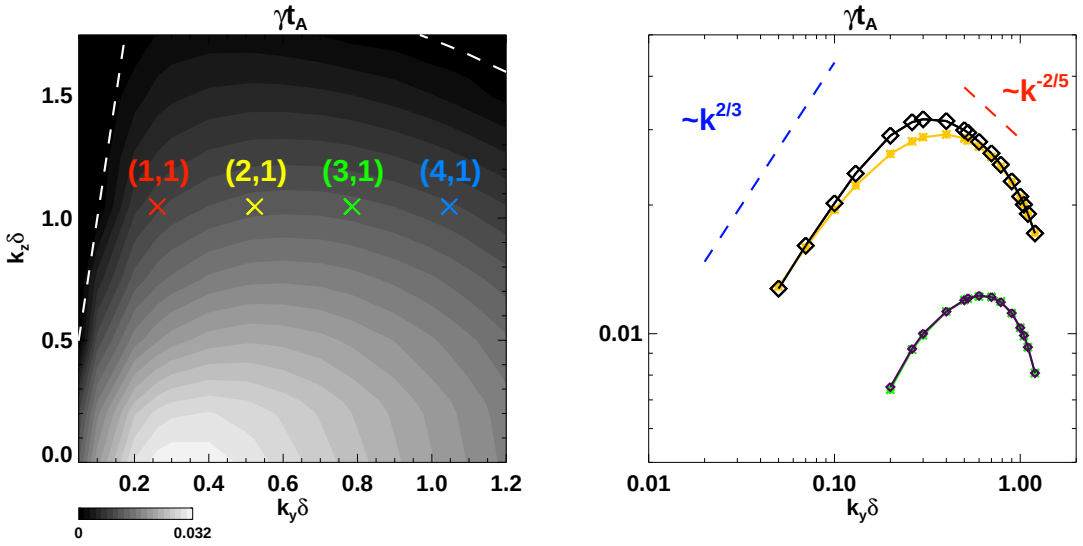

Figure 2.3: Left panel: contour plot of the tearing instability growth rate calculated from the linear analysis. Colored crosses locate the positions of our selected 3D tearing modes. Right panel: the growth rate of the 2D tearing modes ($n = 0$) in our modified Harris sheet (black line with diamonds) and in a Harris sheet with $L_x = 80\delta$ (orange line with asterisks). The growth rate of 3D modes ($n = 1$) in the modified Harris sheet (purple line with diamonds) and in a Harris sheet (green line with asterisks) are also plotted. Analytical solutions of a Harris sheet is shown as dashed lines. Blue dashed line is of Coppi's regime, while red dashed line is of FKR's regime.

by the initial sheared magnetic fields with $F(x_s) = 0$ that

$$x_s \sim \alpha a \frac{L_y}{L_z} \frac{n}{m}. \tag{2.28}$$

Then a 3D oblique resonance layer with a higher value of m is closer to the current sheet center when n value is fixed. We only solve eigenfunctions of modes with $m \leq 4$ due to the limitation on the numerical cost.

The summarized growth rate contour plot is shown in the left panel of Fig.2.3 with the available 3D modes in our simulation box as colored crosses. The growth rates of the selected modes satisfy $\gamma\tau_{\text{diff}} > 1$, where $\tau_{\text{diff}} \sim a^2/\tilde{\eta} \sim 770 t_A$, thus the neglect of global diffusion in our linear analysis is justified. It can be seen that the most unstable mode in our configuration is around $(1, 0)$, while the growth rate of 3D modes have a peak in between $(2, 1)$ and $(3, 1)$. The growth rate of 2D modes and $n = 1$ 3D modes are plotted in the right panel of Fig.2.3, while the theoretical scaling laws (longer waves in Coppi's

regime and shorter waves in FKR's regime) are also shown.

It is noted that the tearing mode is highly influenced by the boundary condition (Steinolfson, 1983). The longer the tearing mode wavelength is, the more its inflow region expands thus more sensitive to the boundary condition. Setting the inflow boundary closer to the current sheet practically changes the tearing mode into a shorter wave mode, therefore shifts the most unstable modes into longer wave modes. If our closed system is too small across the current sheet direction, the most unstable modes are highly controlled by the boundary, not to mention how much the boundary is acting onto the inner system during the nonlinear stage. In order to show how much the boundary is interfering the tearing instability, we also calculate the 2D tearing mode growth rate in a Harris sheet Eq.(1.16) with a box size of $L_x = 80\delta$, which is much wider than our box. The tearing instability growth rate in the wider Harris sheet is peaking at $k_y\delta = 0.4$ that the most unstable 2D mode is around a wavelength of 15.7δ. This peak is shifted into the longer wave mode in our modified Harris sheet as the peak is now around $k_y\delta = 0.3$ which corresponds to a wavelength of 20.9δ. Generally speaking, the growth rate is not significantly changed, which is within 11% only near $(1, 0)$ and falls inside 5% when the wavelength is shorter than 12.6δ. This is because that the longer waves are always easy to be influenced by the boundary, while the shorter waves are not affected at all. In our system, the only mode that is longer than the threshold (12.6δ) is $(1, 0)$. In another word, the boundary effect is not important for any mode, except $(1, 0)$ mode. This fact is also reflected in the comparison of the growth rate of 3D modes with $n = 1$ in Harris sheet and the modified Harris sheet. Although the most unstable 2D mode changes from $(2, 0)$ to $(1, 0)$ in our system due to the boundary effect, since the growth rate itself does not significantly change, moreover the dominant modes are proved to be 3D modes with smaller wavelengths in the nonlinear simulations, we argue that the boundary effect across the current sheet can be ignored until plasmoids in the current sheet center becomes comparable to the box size.

2.4 Nonlinear simulation setup

We solve the whole set of resistive MHD equations as shown in Eq.(2.1) to Eq.(2.6). Normalization factors are the same as that are introduced in Sec.2.2. The background magnetic field is shown as Eq.(2.7). The initial mass density is uniform in the whole box, while the initial pressure balance is maintained that the total uniform pressure is:

$$P_{\text{tot}} = \frac{B_0^2}{2}(1+\alpha^2)(1+\beta) \tag{2.29}$$

in which $\beta = 0.2$ is taken as the ratio between the plasma pressure and the magnetic pressure at asymptotic field just outside of current sheet. The Lundquist number S in our system is defined by the total Alfvén speed $v_A = v_{A0}\sqrt{1+\alpha^2}$ then $S = v_A L/\tilde{\eta} \sim 7\times 10^4$.

Since we are mostly interested in how tearing layers interact with each other across the current sheet and how they increase the global reconnection rate, we perturb the initial static current sheet with eigenfunctions of the tearing modes we have solved in the previous section. In order to make the analysis simpler, we apply a pair of rotational-symmetric modes to the current sheet. The notation we use for this type of simulation with double tearing layers is, for example $(3, \pm 1)$. Meanwhile, in order to show that the existence of coupled layers changes the current sheet development substantially, a single-layer simulation with only one tearing mode is also executed. This type of simulation is denoted as, for example $(3, 1)$. So in the double-layer simulation, two layers of tearing modes with the same wavelength exist on either side of the current sheet. In the single-layer simulation, only one tearing layer exists on the positive side of x.

In our double-layer simulation, the initial condition is similar to that in Grasso et al. (2007). The perturbed magnetic and velocity fields are applied as the superposition of tearing modes with wave vector of $\mathbf{k_L}$ and $\mathbf{k_R}$ on the negative and the positive side of x

respectively. The total fields which are applied initially to the double-layer simulation are

$$\mathbf{B}(t=0) = \mathbf{B}^{[\mathbf{0}]} + \mathbf{B}_{\mathbf{L}}^{[\mathbf{1}]} + \mathbf{B}_{\mathbf{R}}^{[\mathbf{1}]} \tag{2.30}$$

$$\mathbf{v}(t=0) = \mathbf{v}_{\mathbf{L}}^{[\mathbf{1}]} + \mathbf{v}_{\mathbf{R}}^{[\mathbf{1}]} \tag{2.31}$$

while the initial fields in the single-layer simulation are

$$\mathbf{B}(t=0) = \mathbf{B}^{[\mathbf{0}]} + \mathbf{B}_{\mathbf{R}}^{[\mathbf{1}]} \tag{2.32}$$

$$\mathbf{v}(t=0) = \mathbf{v}_{\mathbf{R}}^{[\mathbf{1}]}. \tag{2.33}$$

The detailed formulae are listed in Appendix.C. Amplitude of the initial perturbation is determined that

$$\max(|v_x|, |v_y|, |v_z|) = 0.01 v_{A0}. \tag{2.34}$$

The amplitude is small enough to start from the linear stage but rather large compared to many other studies. What we are interested in is the nonlinear coupling between the two tearing layers. So by applying appropriately large initial amplitude, the system enters the nonlinear stage earlier that the simulation resource is saved.

The simulation box has periodic boundary condition on all sides. The box size is $L_x \times L_y \times L_z = 10\delta \times 24\delta \times 6\delta$. The length of the current sheet is much smaller than many big simulations. Suppose that the most unstable linear mode (2D mode) emerges after the perturbation is applied onto a much larger sheet than our present one along the anti-parallel fields. As we have shown in Sec.2.3, the most unstable 2D mode in our field pinch is $(2, 0)$, regardless of the box size along the current sheet direction. Then what we obtain in a bigger sheet is a chain of X-points with plasmoids in between, while each plasmoid is in the size of our present simulation box. Therefore, we are solving a part of a big sheet before inverse cascade works efficiently into the structures that are larger than the present box size. On the other hand, if the emerging modes are 3D modes as many simulations have shown, they are also determined by the sheet size along the global guide

field. How the dynamics changes with the box size should be checked in the future.

The system is resolved by $640 \times 1000 \times 250$ grids. Across the x-direction, we apply non-uniform grids to resolve the current sheet that $\Delta x \geqslant 0.005\delta$. Resolution check is done by applying different widths of current sheet in solving 1D diffusion equation. The grid size we apply here could resolve the current sheet with a width of at least $a = 0.02\delta$. Uniform grids along y- and z-direction are adjusted with $\Delta y = \Delta z = 0.024\delta$. We test the convergence check by changing the grid size into $\Delta y = \Delta z = 0.04\delta$ for the double-layer simulation $(1, \pm 1)$. At $t = 100t_A$, the reconnection rate increases by 3%. The typical structures are not essentially changed, only the local reconnection is reduced moderately in higher resolution simulation. So we argue that the resolution does not have a strong impact on our model, but the scaling can be changed when an even higher resolution is applied. We use CIP-MOCCT code (Kudoh et al., 1999) with artificial Lapidus-type viscosity (Lapidus, 1967) developed by H. Isobe from Kyoto University.

2.5 Local analysis of the inflow-outflow coupling

We specifically study the development of the double-layer simulation $(3, \pm 1)$. The resonance layer of $(3, 1)$ is located close to the current sheet center. So it is likely that $(3, 1)$ can build up an efficient coupling with its counterpart $(3, -1)$ across the sheet. Moreover, $(3, 1)$ is one of the most unstable 3D tearing modes. Once we perturb the current sheet with a random perturbation, we are expecting the most unstable 3D modes to emerge and dominate the whole system.

The local analysis is studied first on the characters of diffusion region when the inflow-outflow coupling is built. The consequence of this coupling will be examined afterwards.

As we have specified in the previous section, the three-dimensionality is strong when the guide field is finite that the system loses the translational invariance in any direction. This argument is exhibited in Fig.2.4. The isosurface of current density J is plotted, which separates diffusion regions and flux tubes by different values of J thus different colors. The diffusion regions form lines, which are parallel to the local $\mathbf{B}$ and perpendicular to $\mathbf{k}$

of the correspondent tearing mode.

Since the tilting angles of the tearing modes θ on either side of the current sheet are different, the alignment of diffusion regions changes on different 2D-plane across the guide field direction (z-direction). Two examples are shown in panels C) and D) for $z = 0$ and $z = -1.5\delta$, respectively. In panel C), diffusion regions (bright features with concentrated current density) shift from each other along the current sheet direction (y-direction). On the other hand, diffusion regions align with each other across the sheet in panel D). We notice that the inflow-outflow coupling can exist only in the case as panel C), but never for the case as panel D). A similar conclusion was made in the study of DTM (Yan et al., 1994). It means that the reconnection in each diffusion region is enhanced on planes similar to $z = 0$ plane in panel C) but not on planes similar to $z = -1.5\delta$ plane in panel D).

The variance of reconnection along the sheet direction is nicely presented in panel A) by observing the change in the thickness of diffusion lines. On the plane where the inflow-outflow coupling exists, diffusion lines are thicker which implies a higher current density thus faster local reconnection. While on the plane where no inflow-outflow coupling exists, diffusion lines are thinner that slower local reconnection is expected. Also in panel B), flux tubes are larger on $z = 0$ plane but smaller on $z = -1.5\delta$ plane. Considering the position of diffusion regions, we denote the plane similar to $z = 0$ plane as the anti-symmetric plane, while the symmetric plane for planes similar to $z = -1.5\delta$. In this section, we will study in detail on the local reconnection in diffusion regions on the anti-symmetric plane. Diffusion regions on the symmetric plane will be taken as a comparison.

A typical inflow-outflow coupling in $(3, \pm 1)$ is shown in the left panel of Fig.2.5. Only one wavelength is presented along the y-direction. It is clear to see that the outflow from one diffusion region on one tearing mode diverts into the inflow region of another diffusion region lies on the counterpart tearing layer. To understand the inflow-outflow coupling more quantitatively, we measure the velocity and the magnetic fields along the boundary of a coupled diffusion region and its external region where the frozen-in condi-

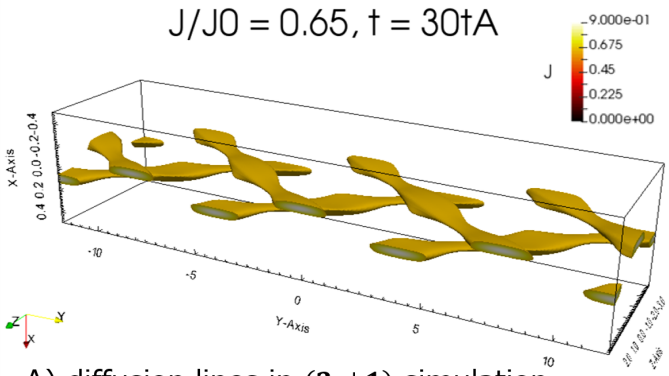

A) diffusion lines in $(\mathbf{3}, \pm\mathbf{1})$ simulation

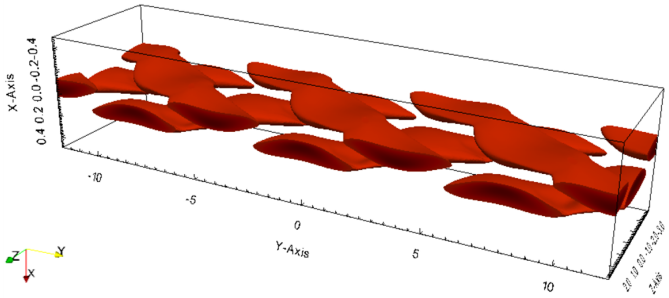

B) flux tubes in $(\mathbf{3}, \pm\mathbf{1})$ simulation

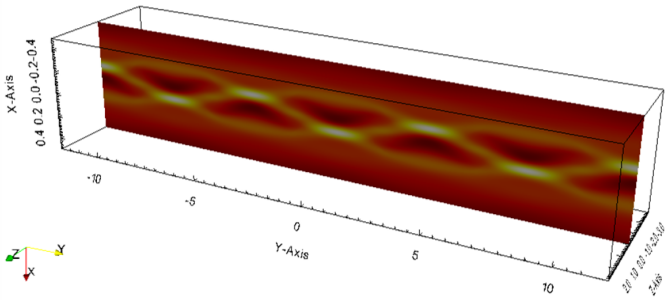

C) current density J on $z = 0$ plane

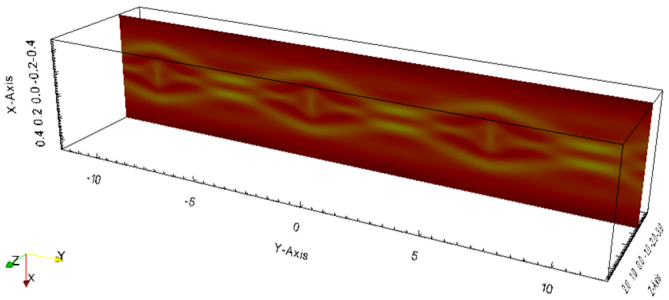

D) current density J on $z = -1.5\delta$ plane

Figure 2.4: 3D magnetic structure of $(3, \pm 1)$ at $t = 30t_A$.

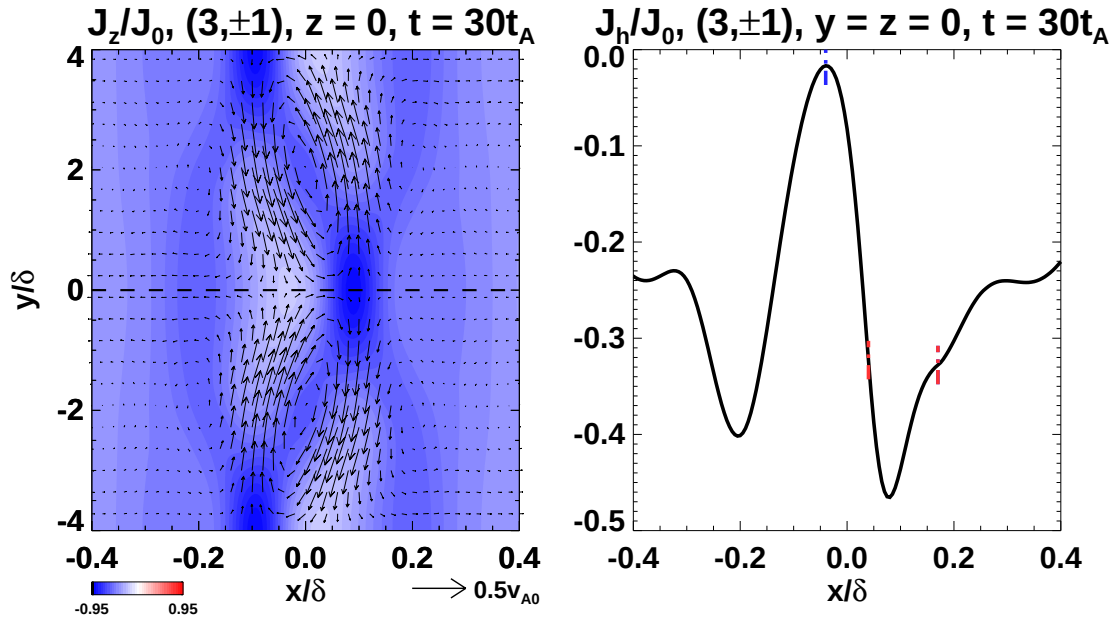

Figure 2.5: Left panel: the inflow-outflow coupling in $(3, \pm 1)$ at $t = 30t_A$. The velocity field on $z = 0$ anti-symmetric plane is plotted as vectors over the contour plot of current density J_z/J_0. Right panel: one example of showing the diffusion region boundary and the external region in our measurement. The 1D plot is the current density J_h on the reconnection plane, right across the center of diffusion region on $(3, 1)$ tearing layer (dashed line in the left panel). Diffusion region boundaries are labeled by red dot-dash lines, while the external regions are labeled by blue dot-dash lines. Vector scale is plotted at the bottom.

tion is roughly maintained. The determination of diffusion region and its external region is shown in Appendix.D. One example is plotted in the right panel of Fig.2.5, in which the current density perpendicular to the reconnection plane J_h across the diffusion region from the tearing mode $(3, 1)$ in the double-layer simulation $(3, \pm 1)$ is plotted. The external region boundaries are labeled as blue dot-dash lines, while the diffusion region boundaries are labeled as red dot-dash lines. We measure the quantities along the inflow boundaries (along $\mathbf{k}$).

The summarized result is shown in Fig.2.6. Averaged values along the inflow boundary near the current sheet center (inside the coupling) are applied that $\langle v_{\text{in}} \rangle$ is denoted as the averaged values for instance. We show the values in the time range when diffusion regions can be identified and maintain intact. In panel A), local inflow normalized by the global Alfvén velocity for diffusion region on the anti-symmetric plane (red), the

symmetric plane (blue) and in the single-layer simulation (black) from $(3, 1)$ are plotted together, thus represents the global reconnection efficiency. It is obvious that the inflow is enhanced by roughly 6 times due to the coupling on the anti-symmetric plane compared to the single-layer simulation. The inflow of diffusion region on the symmetric plane is at first almost the same strength as that in the single-layer simulation, but decreases with time and falls to almost one-quarter of the single-layer simulation around $t = 50t_A$. This is because, when diffusion regions align with each other on the symmetric plane, they extract magnetic energy from the region in between. This region is then gradually depleted thus chokes the reconnection and the inflow grows weaker and weaker.

Another effect of the inflow-outflow coupling is shown in panel B). As the outflow from one diffusion region is ejected into another, the inflow approaches local Alfvén speed. The magnetic field is transported fast into the diffusion region thus piles up in front of the inflow region. It is shown that the inflow magnetic field in the external region is roughly twice of that in the single-layer simulation at $t = 50t_A$. In the single-layer simulation, the inflow magnetic field gets weaker as the reconnection saturates. Reversely, the inflow magnetic field in front of the diffusion region on the symmetric plane is growing. It is probably because that the reconnection in the diffusion region saturates so fast that it cannot consume all magnetic fields that are transported into it previously. Thus a piling up of magnetic flux is observed.

Local reconnection rate is plotted in the lower panels. Panel C) shows the inflow normalized by the Alfvén velocity in the external region. It shows a similar trend as that in panel A), but the magnitude is one order larger. It means that at this stage, although the coupling increases the reconnection efficiency in the coupled diffusion regions, it is still not enough to influence the whole current sheet. Panel D) shows the reconnection rate measured by the electric field (perpendicular to the reconnection plane) difference measured at the X-point and the O-point (see also Appendix.D). It is normalized by local quantities thus can be compared with panel C). The normalized reconnection rate in the diffusion region on the anti-symmetric plane is 30% smaller than that in panel C).

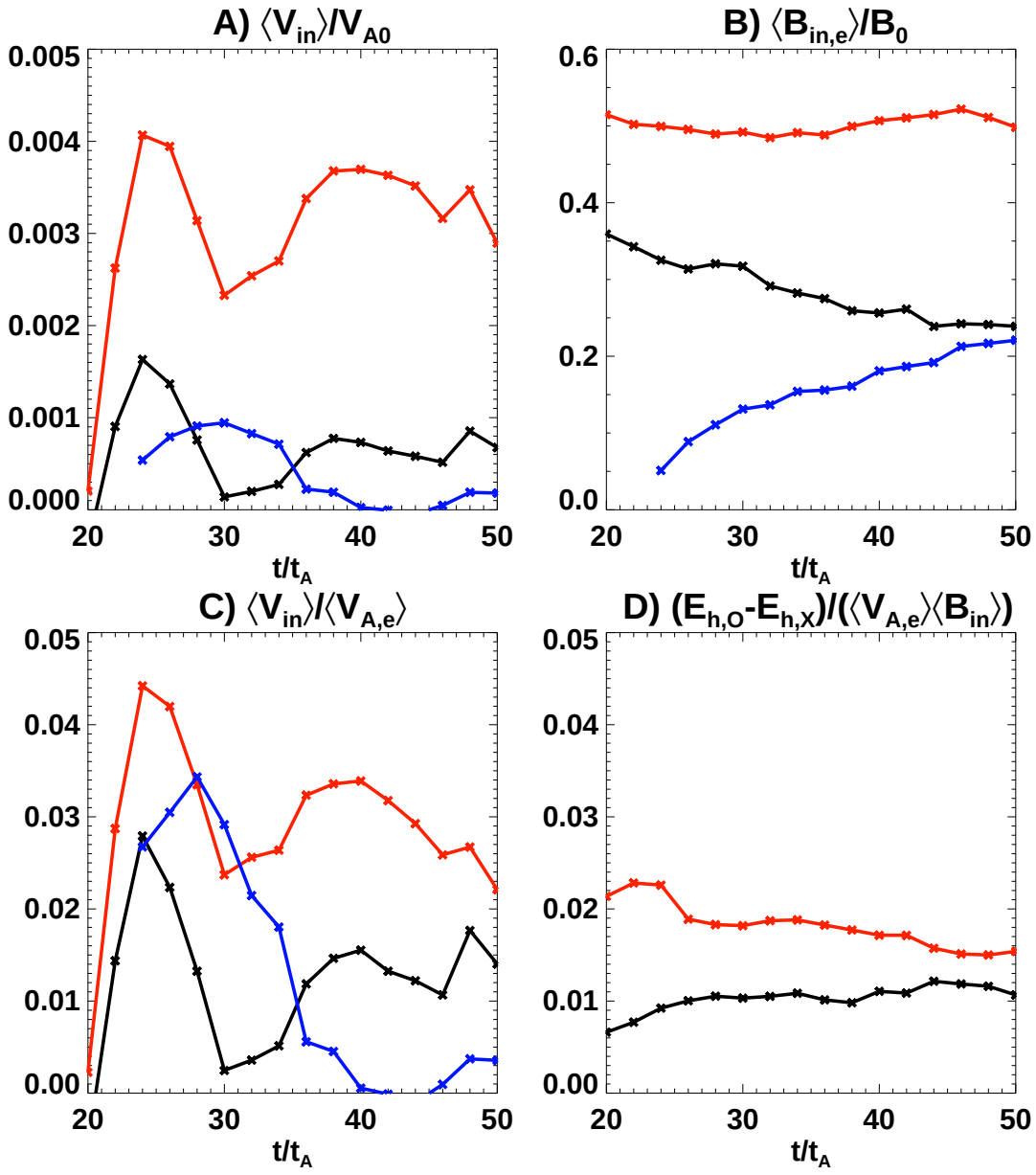

Figure 2.6: Panel A): averaged inflow into diffusion region of $(3, 1)$ measured from the inner side of the current sheet. Panel B): averaged magnetic field in the external region from the inner side of the current sheet. Panel C): averaged inflow normalized by the Alfvén velocity from the inner side of the current sheet. Panel D): electric field (perpendicular to the reconnection plane) difference in X-point and O-point along $(3, 1)$, normalized by the external Alfvén velocity and the inflow magnetic field. Red line with crosses is the measurement from the anti-symmetric plane, blue line with crosses is the measurement from the symmetric plane and black line with crosses is the measurement from the single-layer simulation.

This is because that the inflow-outflow coupling only increases the inflow from the inner side directly. This information propagates outwardly across the sheet then increases the inflow from the outside gradually. Therefore, the reconnection becomes asymmetric as the inflow from the outside is smaller than the inner one. For asymmetric reconnection, the effective inflow is taken as the geometric mean of the inflow from either side (Cassak & Shay, 2007). So the reconnection rate in panel C), which measures only the inner faster inflow, is larger than that in panel D), which measures the effective inflow. The measurement of the single-layer simulation is basically consistent in both panels, since the local reconnection is symmetric across the diffusion region. No measurement on the symmetric plane is shown as it is affected by the reconnection right at the current sheet center that the measurement includes not only the $(3, 1)$ mode.

The inflow-outflow coupling also increases the diffusion region width, which is a positive contribution to the local reconnection increase. The detail is given in Appendix.E.

As we have shown in panel B) of Fig.2.6, magnetic field piles up in front of the diffusion region. Theoretically, secondary tearing is triggered when Δ' is large (Jemella et al., 2003; Loureiro et al., 2005), which means a strong piling-up magnetic field in front of the diffusion layer. Therefore, secondary tearing is expected to grow when the inflow-outflow coupling is effective, as the external magnetic field gets strong. The diffusion region development is tracked in Fig.2.7. The upper panels show current density J_z on the anti-symmetric plane in the double-layer simulation $(3, \pm 1)$. Initially in one period of wavelength, only one intact diffusion region can be found (left panel). With time goes on, the diffusion region splits into two and the current density gets much enhanced due to the coupling (right panel). No strong growth of secondary tearing is identified in the single-layer simulation at the same time (lower left panel). In contrast, the diffusion region on the symmetric plane saturates (lower right panel). Secondary tearing is an indication of a further violent change of current sheet, as shown in the plasmoid instability. But unlike the plasmoid instability, which comes from the interaction between diffusion regions and plasmoids along the current sheet, the inflow-outflow coupling in 3D is in the direction

across the current sheet and can be only built when there exists phase shift of tearing mode that are growing along the sheet. It reflects the importance of understanding the three-dimensionality in the reconnection study, which will be further developed in the next chapter.

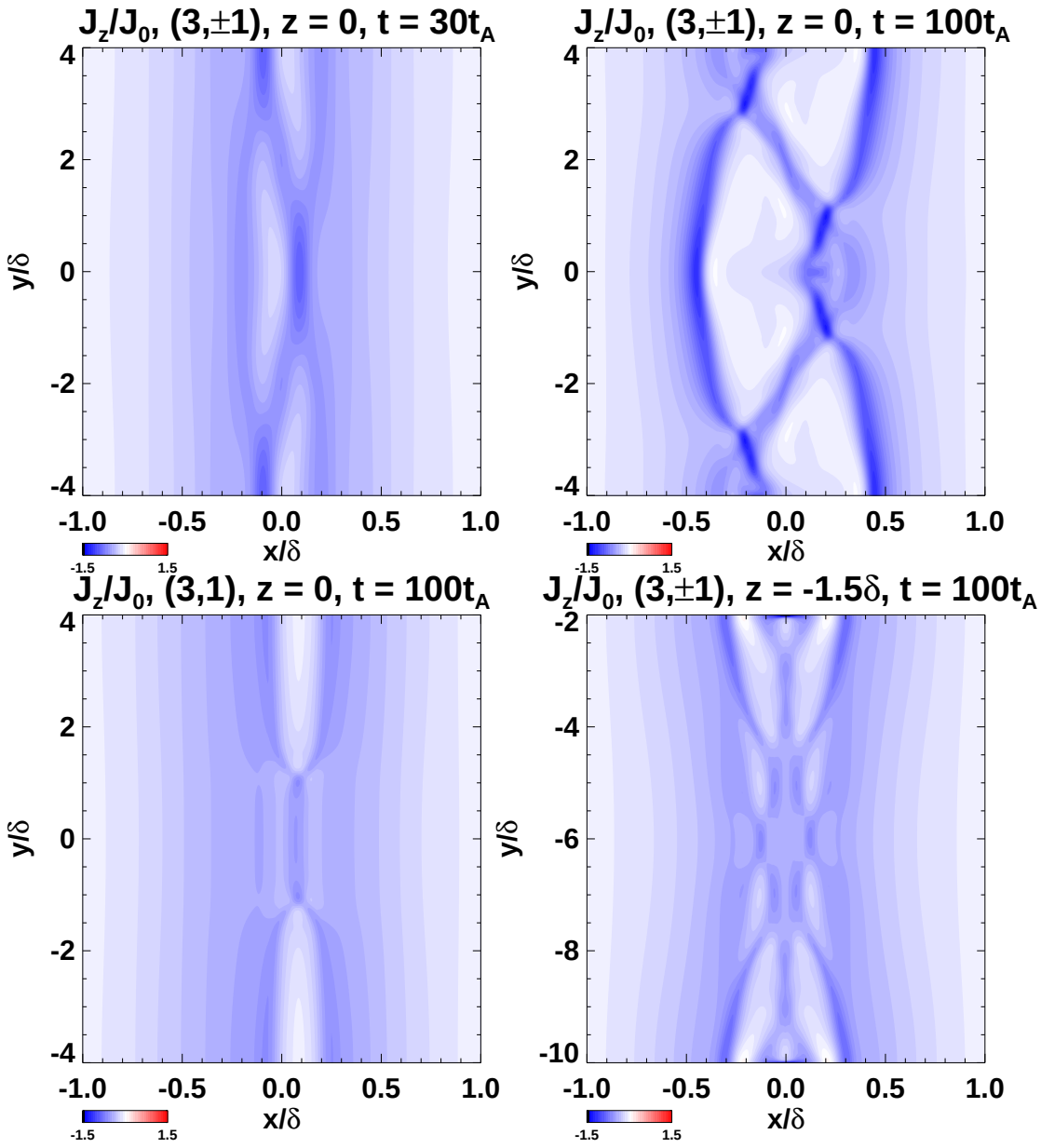

Figure 2.7: Current density contour plot in the double-layer and the single-layer simulations at different times.

2.6 Discussion

2.6.1 Comparison with DTM

In the previous section, we found that the inflow-outflow coupling exists on some planes but not on the others due to the three-dimensionality of the current sheet. This is one of the main differences from DTM, as shown in Fig.2.8. In DTM, a uniform distribution of inflow-outflow coupling is well built along the global guide field direction. But when two 3D tearing modes couple with each other, they show a transition from coupling to non-coupling character periodically. If the inflow-outflow coupling is just a localized phenomenon, no further global contribution is expected. So we check the global distribution of the coupling along the guide field in our simulation at $t = 100t_A$, which is shown in Fig.2.9. As we have already noted that secondary tearing grows when the inflow-outflow coupling is effective, we can use this fact to detect the coupling efficiency. We check carefully $\mathbf{v}$ and $\mathbf{B}$ then pinpoint diffusion regions in the figure as dashed line boxes. It can be seen that secondary tearing is triggered in half of the box along the sheet. Although the coupling is not 100% covering as that in DTM, it is already substantially widely distributed. In our present simulation, only one pair of tearing layers are applied. Once the random perturbation is applied, multiple tearing modes with arbitrary phases are expected to grow simultaneously. In that case, a mixed inflow-outflow coupling all along the guide field is expected. This will be checked in the later chapter.

Another distinguished difference of the 3D tearing mode coupling from the DTM is the consideration of the flow along the global guide field direction. Since DTM is essentially translational-invariant along the global guide field, the effect of the global flow along this direction is often ignored. Although we have shown the inflow-outflow connection on the anti-symmetric plane where two adjacent tearing modes have a π phase difference, we did not take into account of the flow along the global guide field. The flow we plot, such as that shown in Fig.2.5, is the projection of 3D flow pattern onto this plane. Precisely speaking, the two diffusion regions on the anti-symmetric plane do not directly

couple with each other. However, this does not jeopardize our argument.

The tearing mode grows lines of diffusion regions with flux tubes in between. Inside each flux tube, the reconnection outflow is accelerated towards the flux tube center while being carried along the tube direction, which is also the direction along the lines of diffusion regions. The tube oriented flow is thought to be formed due to the gas pressure difference between the reconnecting field lines (Nakamura et al., 2012). Therefore, the acceleration of the outflow into Alfvénic is like a relay race by different diffusion regions along the tube direction. The flux tube holds inside two trains of Alfvénic flows from the diffusion regions on either end of the tube. When the flow passes near the anti-symmetric plane where a diffusion region is on the other side, the flow train can divert into it and accelerate the local reconnection, although the Alfvénic flow was not originated from the diffusion region on this plane.

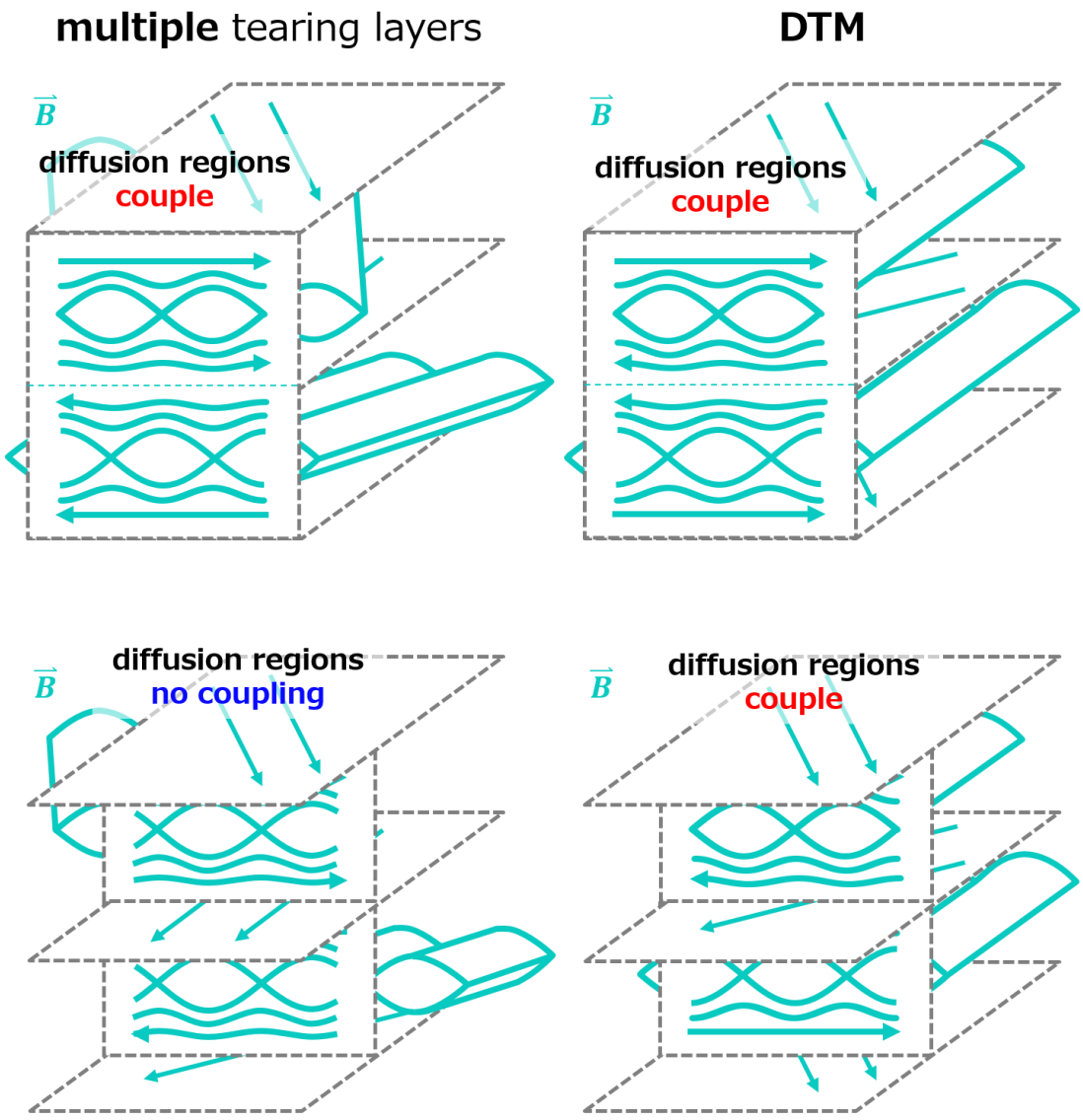

Figure 2.8: Spatial dependence of the tearing layer coupling in our simulation and the DTM. Two-dimensional cuts are taken at different positions along the global guide field.

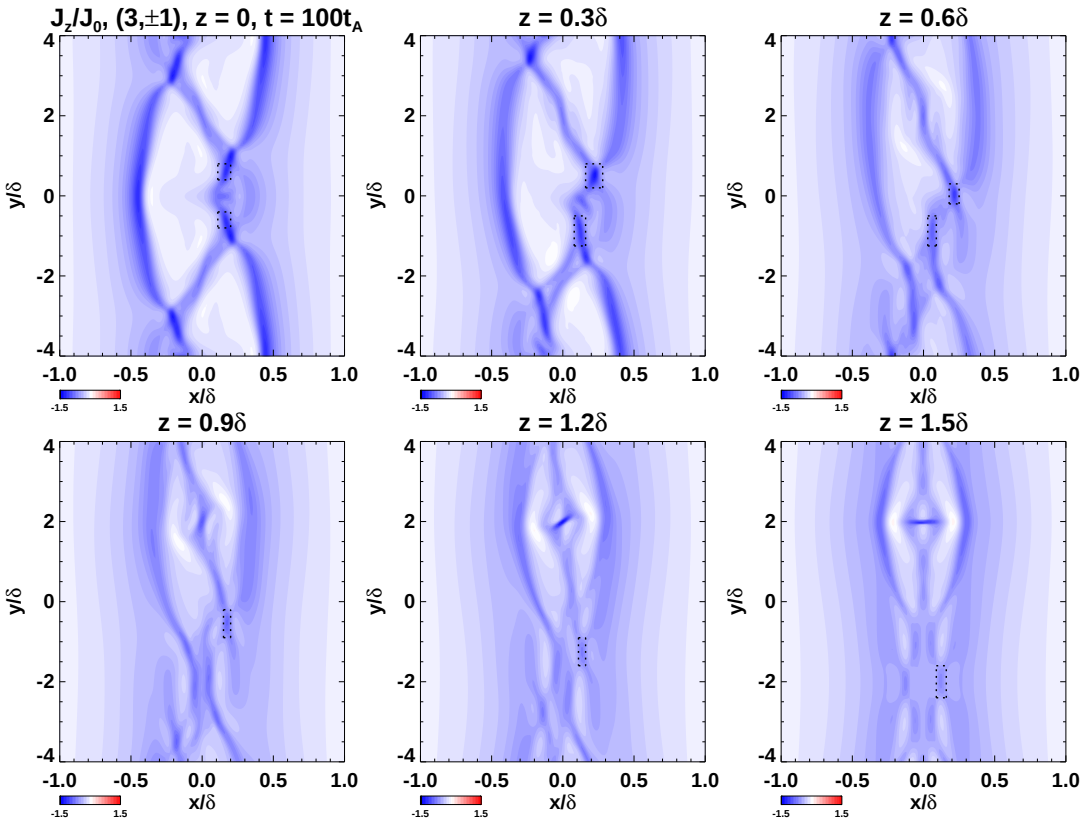

Figure 2.9: Scan of current density J_z along the global guide field direction. Diffusion regions are labeled as dashed line boxes.

2.6.2 Suppression of 2D modes by 3D modes

As it can be observed in Fig.2.5, on the anti-symmetric plane, outflows along the y-direction from diffusion regions on either side of the current sheet are moving in opposite directions. Shear flow along the current sheet can sufficiently suppress the tearing instability as it approaches Alfvénic (Chen et al., 1997). Therefore, it indicates that the tearing instability right at the current sheet center, namely the 2D tearing modes, are likely to grow slowly when the outflows from 3D modes are strong.

In our system, 2D modes are growing inside the region bounded by two 3D tearing layers. It means that their asymptotic magnetic fields are determined by the resonance layers of these two modes. In another word, they cannot be informed by the magnetic fields outside. So the asymptotic Alfvén velocity for 2D modes $v_{A,\mathrm{2D}}$ at the center is approximately:

$$v_{A,\mathrm{2D}} \sim v_{A0}\frac{x_s}{a}. \tag{2.35}$$

where $x_s > 0$ is the position of the 3D tearing mode on the positive x-side by applying Eq.(2.28). As multiple tearing layers coexist in the current sheet, the asymptotic magnetic field for each layer is changed by the adjacent layers on either side. In our double-layer simulation, the asymptotic magnetic field for the 3D tearing layer on the sheet center side is approximately:

$$B_{y,e} \sim B_{y0}\frac{2x_s}{a} \tag{2.36}$$

which is the difference of $B_y(x_s)$ and $B_y(-x_s)$. For the double-layer simulation $(3, \pm 1)$, this value is $\sim 0.95B_0$, which meets our detected value of $\langle B_{in,e}\rangle$ in panel B) of Fig.2.6 very well ($B_{in,e} = B_{y,e}\cos\theta \sim 0.57B_0$ from the estimation since the reconnection is proceeding on a rotated coordinate perpendicular to $\mathbf{k}$, while the measured $B_{in,e} \sim 0.5B_0$). So the estimated maximum Mach number $M_{a,y}$ of this shear flow is

$$M_{a,y} = \frac{v_{y,o}}{v_{A,\mathrm{2D}}} \sim 2 \tag{2.37}$$

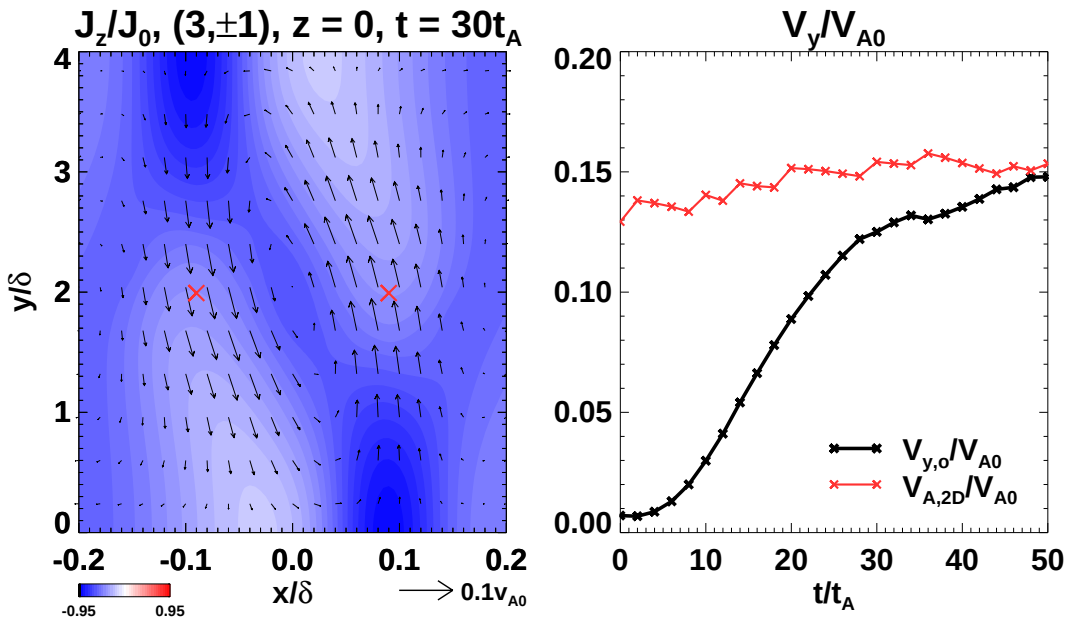

Figure 2.10: Left panel: the local coupling flow in $(3, \pm 1)$ by showing velocity fields on $z = 0$ plane as vectors over current density J_z. Red crosses locate the positions of detection on outflow $v_{y,o}$ from diffusion regions on 3D tearing layers $(3, -1)$ (left) and $(3, 1)$ (right). It is also the location for the detection of 2D mode Alfvén velocity $v_{A,2D}$. Vector scale is plotted at the bottom. Right panel: 1D plot of detected $v_{y,o}$ and $v_{A,2D}$ along time.

where the outflow on y-plane is $v_{y,o} \sim B_{y,e}/\sqrt{4\pi\rho}$. Therefore, 2D modes are highly possible to be suppressed at the current sheet center because of the shear flow on the anti-symmetric plane.

We show an example of this argument in Fig.2.10. The left panel is the zoom-in view of the left panel in Fig.2.5. Since the vortex center is on $(x, y, z) = (0, 2\delta, 0)$, we check the outflow $v_{y,o}$ and $v_{A,2D}$ across $y = 2\delta$. As we argued that the growing environment for 2D modes is closed by 3D modes $(3, -1)$ and $(3, 1)$, we detect the flow on the resonance layers of these two modes. The positions are identified on the left panel as red crosses. Due to the rotational symmetry on $z = 0$ plane, the detection at these two points is the same. The development of $v_{y,o}$ and $v_{A,2D}$ are shown in the right panel before secondary tearing explicitly emerges. Similar to our expectation, the outflow on y-plane grows up to the local Alfvén velocity that $M_{A,o} \sim 1$. This value is half of our maximum estimation in Eq.(2.37), as the outflow is roughly half of the Alfvén velocity for the 3D tearing modes.

This trend suggests that the 2D tearing modes which are sandwiched in between the 3D tearing modes on either side are more and more suppressed by the accelerating shear flow from these 3D modes.

For a more quantitative proof, we examine the magnetic energy for dominant 2D and 3D modes as the following. In addition to our typical double-layer simulation, we execute a new set of simulations which includes the 3D tearing modes in our typical case, as well as a selected 2D mode. We label this new set as the three-layer simulation, because it contains two 3D tearing layers and a 2D tearing layer at the current sheet center. In our double-layer simulation, only 3D modes are perturbed initially. Other modes eventually get activated due to nonlinear processes, which will be discussed in the next chapter. The 2D mode $(6, 0)$ is the strongest 2D mode produced by nonlinear processes before $t = 50t_A$, while other 2D modes have much smaller amplitudes. Therefore, the 2D modes we choose for the three-layer simulations are $(6, 0)$, which seems to be a preferable 2D mode by the double-layer simulation, and $(1, 0)$, which is the most unstable 2D mode in our unperturbed current sheet. While keeping the same energy input for the 3D tearing modes as that in our typical case from the beginning, we apply 2D modes with different amplitudes in different simulations. The amplitude is controlled by the outflow speed from the 2D tearing mode. For example, for a three-layer simulation, in which the 2D mode $(6, 0)$ ejects outflows in the magnitude of $0.01v_{A0}$ initially, the simulation is labeled as $(3, \pm 1) + (6, 0)_{-2}$.

We calculate the magnetic energy of each mode (m, n) in the Fourier space by converting the magnetic field

$$\tilde{\mathbf{B}}(x, m, n) = \frac{1}{L_y L_z} \int_{-\frac{L_z}{2}}^{\frac{L_z}{2}} \int_{-\frac{L_y}{2}}^{\frac{L_y}{2}} \mathbf{B}(x, y, z) e^{-i(k_y y + k_z z)} dy dz \tag{2.38}$$

into magnetic energy spectrum and integrate along the x-direction that

$$\tilde{E}_m(m, n) = \int_{-\frac{L_x}{2}}^{\frac{L_x}{2}} \frac{|\tilde{\mathbf{B}}(x, m, n)|^2}{8\pi} dx. \tag{2.39}$$

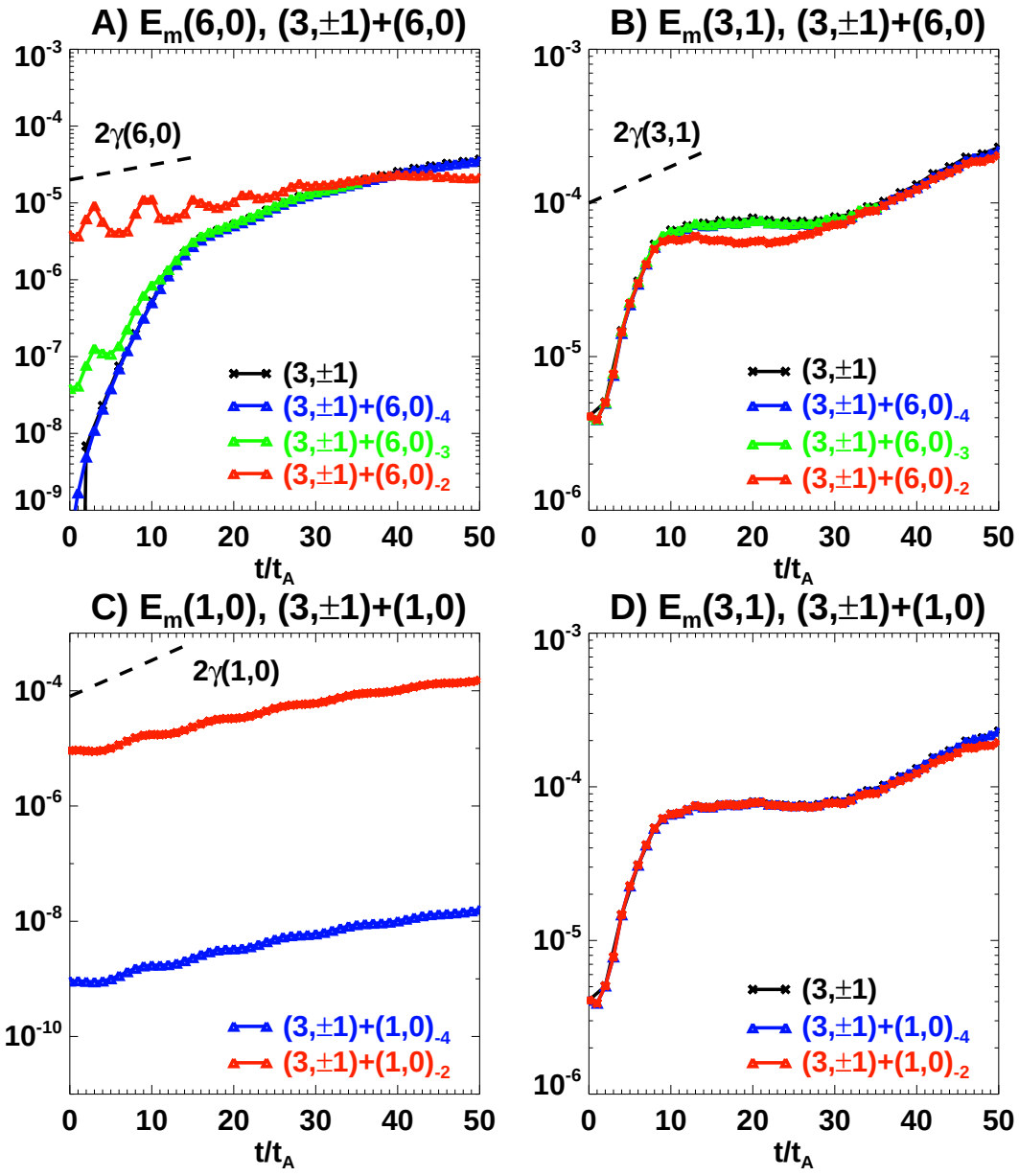

Figure 2.11: Panel A): magnetic energy of the 2D mode $(6, 0)$ growing in the double-layer simulation $(3, \pm 1)$ and the three-layer simulations. Panel B): magnetic energy of the 3D mode $(3, 1)$ growing in the double-layer simulation $(3, \pm 1)$ and the three-layer simulations. Panel C): magnetic energy of the 2D mode $(1, 0)$ growing in the three-layer simulations. Panel D): magnetic energy of the 3D mode $(3, 1)$ growing in the double-layer simulation $(3, \pm 1)$ and the three-layer simulations.

The result of dominant 2D and 3D modes is plotted in Fig.2.11.

In the upper panels of Fig.2.11, the implemented 2D mode is $(6,0)$. When the initial energy of $(6,0)$ is weak, as shown in $(3,\pm1)+(6,0)_{-4}$ and $(3,\pm1)+(6,0)_{-3}$ in panel A), the growth of $(6,0)$ quickly approaches that in the double-layer simulation. It means that the growth of $(6,0)$ is predominantly controlled by nonlinear processes in this phase, rather than the spontaneous tearing instability. The growth rate of $(6,0)$ is much faster than its theoretical linear growth rate (black dashed line in panel A)) before $t\sim15t_A$, when the outflow from 3D modes are weak. Meanwhile, the growth of 3D modes $(3,1)$ and $(3,-1)$ are barely affected as shown in panel B). After $t\sim15t_A$, the growth of $(6,0)$ apparently decelerates and approaches its theoretical linear growth rate. The amplitudes of $(6,0)$ are always one order of magnitude smaller than $(3,1)$. On the other hand, when the initial energy of $(6,0)$ is strong and comparable to the initial energy of 3D modes, $(6,0)$ grows linearly as fast as its theoretical linear growth before $t\sim35t_A$ but reversely decreases after that. The strong input of $(6,0)$ changes $(3,1)$ and $(3,-1)$ growth from $t\sim8t_{A0}$ to $t\sim35t_A$, even when its magnitude is one order of magnitude smaller than the 3D modes. However, 3D modes recover and grow in the similar manner as the other simulations afterwards.

In the lower panels, the implemented 2D mode is $(1,0)$, which is growing in the double-layer simulation with a strength of several orders of magnitude weaker than any of our implemented energy in the three-layer simulations. Regardless of the initial input energy, $(1,0)$ is always growing linearly. However, the growth rate is half of its theoretical linear growth (black dashed line). We also execute 2D simulation with $(1,0)_{-2}$ in a static current sheet. It is found that $(1,0)$ in the 2D nonlinear simulation grows similar to our linear prediction (only 6% reduced), which indicates that the growth change of $(1,0)$ in the three-layer simulation should come from 3D modes. In comparison, the 3D mode $(3,1)$ is not effectively affected when the amplitude of $(1,0)$ is small and only reduced by 16% in $(3,\pm1)+(1,0)_{-2}$ at $t=50t_A$ compared to the double-layer simulation. The growth of $(1,0)$ also decelerates by 34% in $(3,\pm1)+(1,0)_{-4}$ and 36% in $(3,\pm1)+(1,0)_{-2}$

roughly from $t \sim 25t_A$ compared to their initial growth.

As we argued, the growing environment of 2D modes is determined by 3D modes on either side. The position of 3D modes cut off the asymptotic magnetic fields for 2D modes into the fields on 3D modes resonance layers. We then calculate the theoretical linear growth rate of $(1, 0)$ in a much narrower current sheet. The width of this narrow sheet is $1/5$ of our typical static sheet and the asymptotic field is also $1/5$ of our typical case. This narrow sheet covers the 3D tearing layers in our typical double-layer case, as can be seen from Fig.2.10. The growth rate of $(1, 0)$ reduces by 6% in this narrow sheet compared to the growth rate in our typical static sheet. Therefore, the reduction of the growth rate of $(1, 0)$ in the three-layer simulations is more likely due to the dynamics of 3D modes rather than the background field.

From the results above, it can be seen that 3D modes change the growth of 2D modes in between when 3D modes are close to each other. For the most unstable mode $(1, 0)$, the growth rate is suppressed into half while being even slower when 3D modes grow stronger. The 2D mode $(6, 0)$, which is preferred by the system built up by 3D modes, is also regulated by 3D modes. It is encouraged to grow with small amplitude, but suppressed when the amplitude gets large (one order of magnitude smaller than $(3, 1)$).

If 3D modes are far away from each other, in another word, no inflow-outflow coupling is built, the argument above is not valid. As 3D modes are growing independently, the effective asymptotic magnetic field which determines the outflow for 3D modes gets smaller than the prediction by Eq.(2.36). Meanwhile, the asymptotic Alfvén velocity of 2D modes is less constrained by 3D modes as it increases with the position of 3D modes x_s. Then the effective Mach number for 2D modes in Eq.(2.37) gets smaller. So when the two tearing layers are far from each other, their influence on 2D modes reduces. Thus 2D modes are capable to grow freely and regain their initiative.

It is found that 3D modes dominate from the initial phase (Landi et al., 2008). It is possible that they are close to each other across the sheet center thus form a shearing flow sheet in between and prevent the growth of 2D modes. Then 2D modes can only grow

fast when the layers are far apart, which needs further investigation.

2.7 Summary

In this chapter, we studied the 3D tearing mode coupling, specifically the inflow-outflow coupling, across the current sheet center by investigating the local velocity and magnetic fields change.

We first solved the eigenfunctions of the tearing instability (Sec.2.3) then applied the eigenfunctions into the nonlinear simulation to see further development (Sec.2.4 and so on). We noticed that although the most unstable mode in our system is the longest 2D mode (Fig.2.3), it does not emerge nor dominate in our previous random perturbation simulation, which is consistent with many other studies. When two 3D tearing modes start to grow in a current sheet together, they exhibit a system with high three-dimensionality (Fig.2.4). On the plane where one diffusion region from a tearing layer is aligned with a flux tube on another tearing layer across the current sheet, the inflow and outflow from different tearing layers couple with each other (Fig.2.5). The direct result of the inflow-outflow coupling is the local increase of the inflow, local reconnection rate enhancement and a piling up of reconnecting magnetic field in the coupling region (Fig.2.6). As the incoming magnetic field increases due to the inflow-outflow coupling, secondary tearing is triggered in the coupled diffusion region (Fig.2.7), which is not found in the non-coupling cases.

Although the three-dimensionality makes the 3D tearing mode coupling less efficient than the DTM in the global sense (Fig.2.8), the coupled region covers about half of the box along the guide field direction (Fig.2.9) which is sufficiently large. This large coverage of the inflow-outflow coupling system also implies a large coverage of shear flow sheet across the current sheet center, where 2D tearing modes can emerge. The shear flows produced by the two 3D tearing modes across the sheet center is locally Alfvénic that it is highly possible that they suppress the growth of 2D modes (Fig.2.10). The suppression of 3D modes onto 2D modes are proved by the three-layer simulations which contain

two coupled 3D modes and one 2D mode at the current sheet center. The growth rate of the most unstable 2D mode $(1, 0)$ is roughly half compared to the case when no 3D modes exist. The system preferred 2D mode $(6, 0)$ is initially encouraged to grow but later suppressed by the 3D modes.

Up to now, we have examined the initial phase of the tearing mode coupling (before $t = 50t_A$). The coupled reconnection has not grown strong enough to influence the whole current sheet. The trigger of secondary tearing indicates an upcoming violent change of the whole current sheet, as the story of the plasmoid instability tells. In the next chapter, we are going to check how the local inflow-outflow coupling affects the faraway magnetic fields across the current sheet then gives faster reconnection as a whole.

Chapter 3

Result II: global analysis of the typical case

In this chapter, we pursue further the consequences of the inflow-outflow coupling of the tearing layers in order to relate it to the 3D global fast reconnection in a turbulent state.

3.1 Introduction

In the previous chapter, we examined in detail the basic physics of the 3D tearing mode coupling across the current sheet. We noticed that secondary tearing is triggered when the inflow-outflow coupling exists. In the 2D simulation of a well evolved Sweet-Parker current sheet, the emergence of secondary tearing is followed by an eruptive energy release. In this case, the reconnection, to be specific the production and development of diffusion regions, is limited to the current sheet center where anti-parallel magnetic field components annihilate. However, in the 3D reconnection, the three-dimensionality introduces an extra degree of freedom that diffusion regions are not only allowed along the sheet center but can sprout anywhere in the sheet.

There are two possibilities after secondary tearing emerges in our system. One is that each layer develops into a hierarchical reconnection layer by itself. Overall, these hierarchical layers build up the inflow-outflow coupling and accelerate the global reconnection.

The other possibility is that the 3D cascade dominates in the system. In the induction equation Eq.(1.1), the cross term of $\mathbf{v}$ and $\mathbf{B}$ will give new energy mode into the magnetic field. By the chain effect, more and more modes are created.

The previous study has shown that the energy is pouring into the modes not only along the initial unstable modes but also across these modes on the Fourier space (Landi et al., 2008). Some of these new modes are residing in between the original modes near the current sheet center, while some are growing outside which could explain why the current sheet gets thicker with time (Onofri et al., 2006; Huang & Bhattacharjee, 2016; Beresnyak, 2017). The outside modes are closer to the magnetic reservoir where free energy is abundant. So we believe that a fast global reconnection can be achieved when the inflow-outflow coupling is built across the whole sheet. This picture is similar to the turbulent reconnection theory, which explains the global fast reconnection as an integrated result from successive fast local reconnection as field lines are wandering across the sheet (Lazarian & Vishniac, 1999).

In this chapter, we will study where and how new diffusion regions are created after secondary tearing develops in the initial diffusion region, both locally (Sec.3.2.1) and globally (Sec.3.2.2). In the local analysis, we are concentrating on the area very close to a certain diffusion region. In the global analysis, we are tracking the development of diffusion regions in the range of the whole simulation box. In addition, in order to confirm our hypothesis of the global fast reconnection, we will check whether the inflow-outflow coupling exists globally and continuously (Sec.3.5).

3.2 Diffusion region creation

The simulation setup is the same as that in Sec.2.4 that the double-layer simulation $(3, \pm 1)$ is studied.

3.2.1 Local view

We first investigate the local production of diffusion regions. As we have shown in Fig.2.9, the system varies from the coupling plane to the non-coupling plane periodically due to our initial perturbation. The regions in between the anti-symmetric and the symmetric planes are possessing the characters from both of these planes, while the dominant character is determined by the closer one. So in the following part, we concentrate on the change of these two characteristic planes and treat the other planes as the mixture.

In Fig.3.1, we track the diffusion region development on the anti-symmetric plane $z = 0$ along time. At $t = 100t_A$, clear secondary tearing feature is observed. Later, a vertical diffusion region, which is perpendicular to the current sheet direction, is created in between these two pieces, as indicated in the plot of $t = 120t_A$. During the growth of this vertical diffusion region, there also grows an overlying diffusion region just in front. This overlying diffusion region, which is growing outside of the initial diffusion region, gradually takes over the reconnection instead of the partitioned diffusion regions and becomes the dominant diffusion region on this anti-symmetric plane.

A zoom-in view of the region near the diffusion region is selected, together with the velocity field overplotted, as shown in Fig.3.2. Due to the partition of the original diffusion region, the flow pattern has been changed. As two smaller diffusion regions that result from secondary tearing grow, they eject outflows into $y = 0$ plane bidirectionally. The outflows collide along the y-direction with each other then divert along the x-direction. In this way, they open up a vent that the reconnected magnetic field is transported out to touch the free field. The free field is under the global Lorentz force that is always pointing to the current sheet center. Thus an overlying diffusion region is created as the magnetic fields with different characters meet.

We want to make a caution here that the vertical diffusion region is created due to the perfect symmetry across y-plane. It accelerates the flow outwardly that the overlying diffusion is created fast. We are arguing that the opening of the outward flow that comes from the partitioned diffusion regions is an essential point in creating the new diffusion

region across the current sheet direction. When a random perturbation is applied, the symmetry is lost. Then it is highly possible that overlying diffusion regions are formed without the emergence of vertical diffusion regions. The detailed analysis of the magnetic field lines is shown in Appendix.F.

Next, we turn our focus to the diffusion region creation on the symmetric plane, which is shown in Fig.3.3. As we have shown in the previous chapter, the diffusion regions from the initial tearing modes saturate on this plane. It can be seen that the diffusion regions gradually disappear. Instead, a new elongated diffusion region starts to grow in front of the original one.

The understanding of the building up of the new diffusion region is shown in Fig.3.4. We select a bunch of field lines (blue lines) in between the original and the new diffusion region. Structural non-uniformity is observed along these lines. They bend to the $+x$-direction when passing through the symmetric planes ($z = \pm 1.5\delta$) by comparing panels A) and C), while expanding out to the $-x$-direction when passing through the anti-symmetric planes ($z = \pm 3\delta$ and $z = 0$ planes).

The non-uniformity comes from the different reconnection efficiency on these two characteristic planes. In Chap.2, we have shown that the reconnection is fast on the anti-symmetric plane but slow on the symmetric plane. So when the free field lines approach the tearing layer, the parts near the anti-symmetric planes reconnect first while the parts near the symmetric planes have not reconnected. As a result, the lines have some parts inside the flux tubes but other parts still remain free as shown in panel D). Since the flux tubes are growing outwardly, the bents are created along the field lines. As the reconnection in the original tearing mode saturates on the symmetric plane, the free field line parts will subject to the tension force that comes from the bent. The tension force drags the field lines in the $-x$-direction, which is opposite to the inflow for the original diffusion region. It does not only kill the reconnection in the original tearing mode faster but also helps the field lines to collide with the outer field lines that are going into the current sheet under the global Lorentz force. Therefore, a new diffusion region is created.

In both cases, the coupling planes and the non-coupling planes, we found how new diffusion regions are created outwardly. Since we believe that the process on other layers along the z-direction is the mixture of the mechanisms on these two characteristic planes, the production can be global but needs to be proved. Furthermore, a new set of inflow-outflow coupling is expected to build up between the old diffusion regions and the new ones, which accelerates the reconnection locally in both old and new diffusion regions. This argument is checked in the latter section.

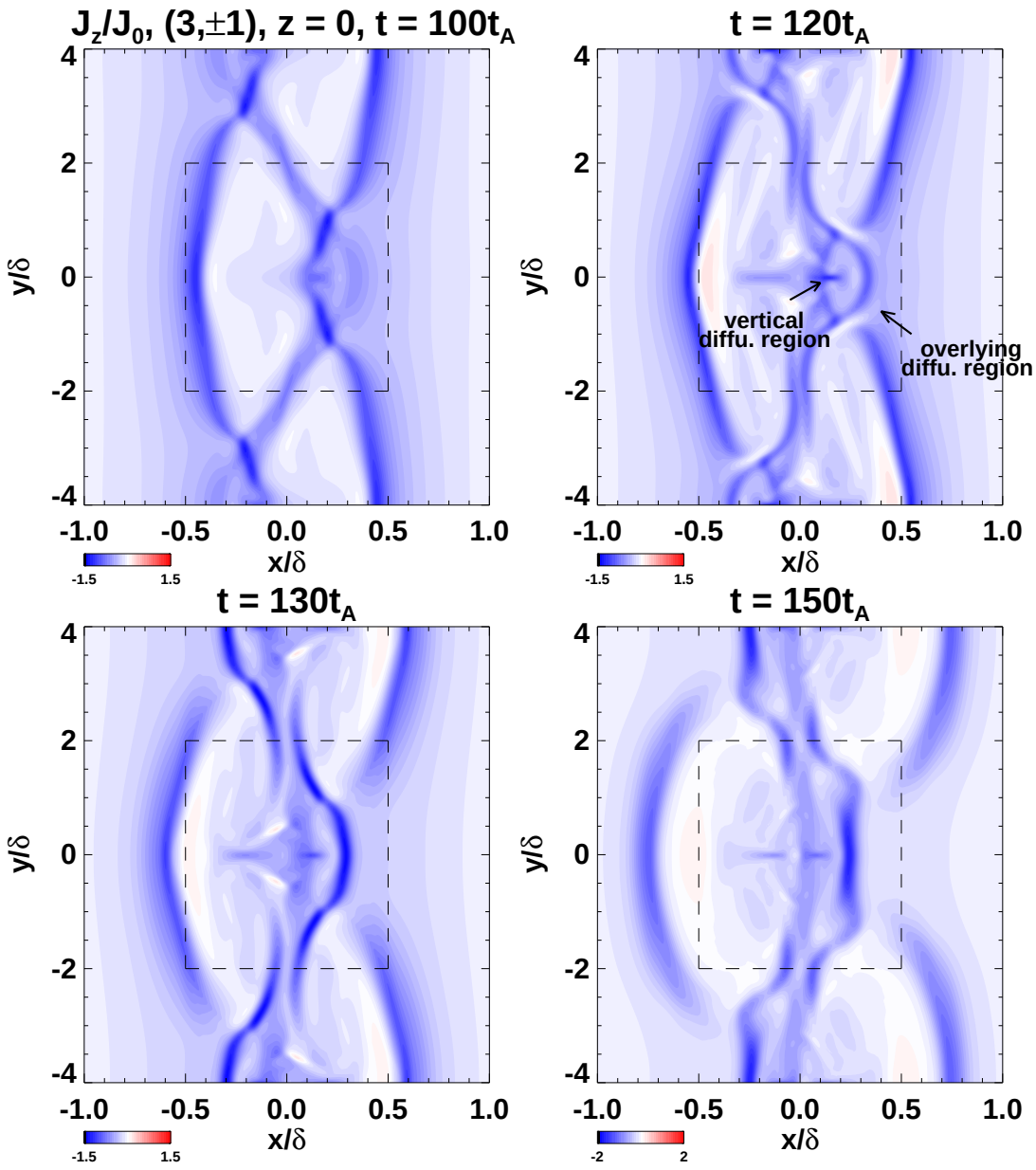

Figure 3.1: Diffusion region development along time by showing the current density J_z contour plot on the anti-symmetric plane $z = 0$. The big dashed line box confines the zoom-in region shown in Fig.3.2.

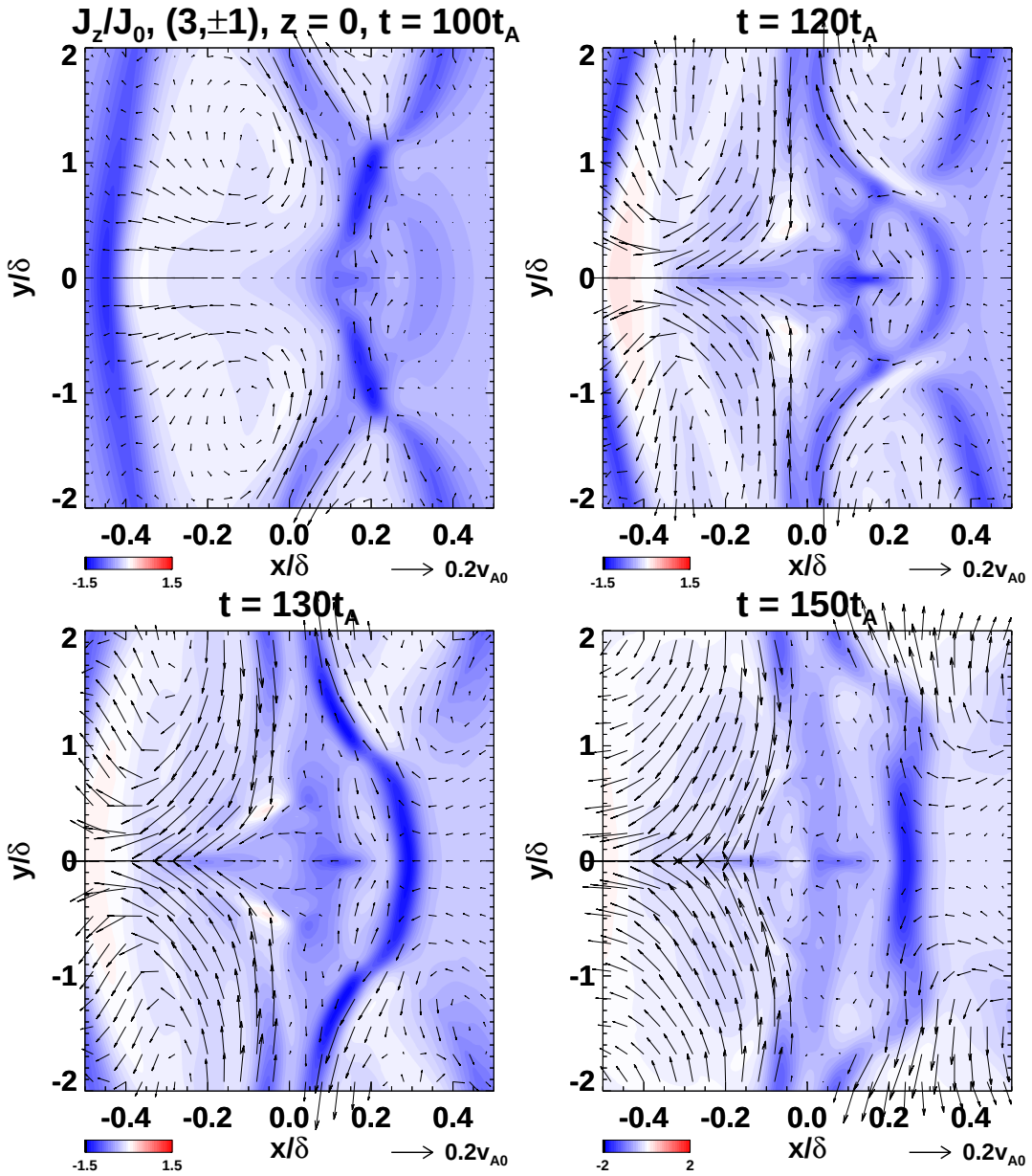

Figure 3.2: Velocity fields overplotted on the current density J_z contour plots as vectors, which are the zoom-in views of the dashed line boxes in Fig.3.1. Vector scales are plotted at the bottom.

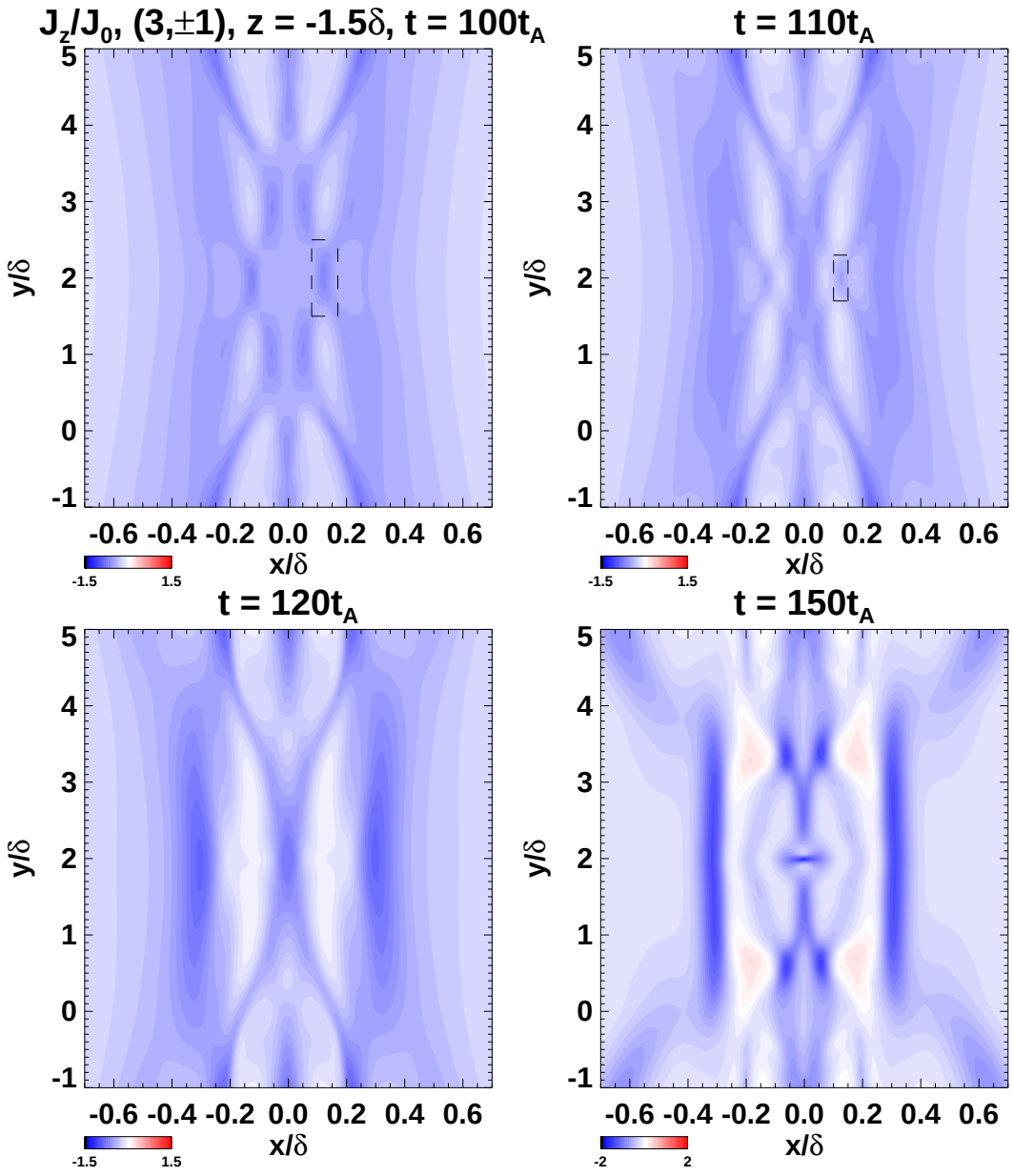

Figure 3.3: Diffusion region development along time by showing the current density J_z contour plot on the symmetric plane $z = -1.5\delta$. The dashed line boxes locate the diffusion regions on initial 3D tearing mode $(3, 1)$.

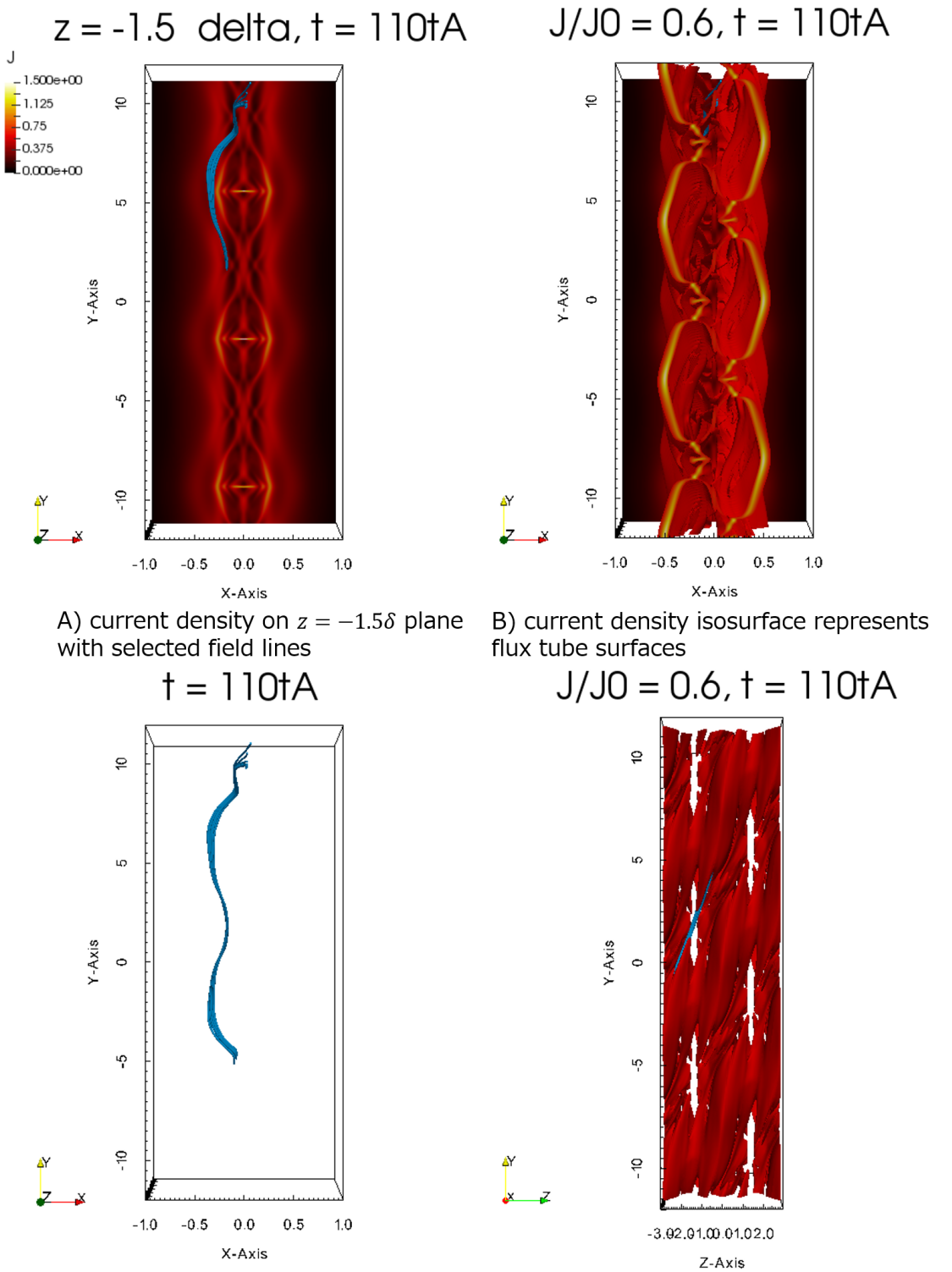

A) current density on $z = -1.5\delta$ plane with selected field lines

B) current density isosurface represents flux tube surfaces

C) selected field lines

D) current density isosurface represents flux tube surfaces with selected field lines

Figure 3.4: Field lines that are correspondent to the creation of the overlying diffusion region, together with current density structures at $t = 114t_A$.

3.2.2 Global view

As we have already identified the local creation of diffusion regions on two characteristic planes, it is necessary to examine whether these mechanisms are only affecting limited region or they are capable to influence the whole current sheet that diffusion regions emerge systematically. The global creation of diffusion regions along the current sheet is required for the global fast reconnection. On the other hand, the global coverage of diffusion regions can be understood as the growth of new modes, which explains the energy cascade on the spectrum. Therefore, we will check the 3D diffusion region distribution, as well as the mode energy along time to confirm the global creation of new diffusion region.

In the early phase, the current sheet is dominated by the two initial perturbed modes that form two reconnection planes along the current sheet before secondary instability grows (Fig.3.5). In panel A), diffusion regions and flux tubes can be clearly identified. Field lines inside the tubes braid and form coherent structures, as shown in panels B) and C). Later at $t = 150t_A$, when new diffusion regions sufficiently grow, three flux tube cross-sections can be counted along the anti-parallel magnetic field direction (y-direction), while five flux tube cross-sections exist along the global guide field direction (z-direction) on either side of the current sheet. Since these flux tubes cover the whole box, they indicate the growth of new modes $(3, \pm 5)$. We also plot the diffusion regions above $x = -0.15\delta$ plane, which is away from the resonance layers of the initial perturbed modes, as shown in panel B). Together we plot the magnetic field lines that root on the resonance layer $(3, -5)$. Clearly, diffusion regions form diffusion lines that appear to be the new modes $(3, -5)$ and fully extend along the sheet direction thus form a new reconnection layer. Meanwhile, the magnetic field lines that compose the flux tubes in panel A) are nicely confined in between two diffusion lines above this plane as shown in panel B). It proves that the flux tubes are the result of the reconnection proceeding on this plane. Judging by the findings here, we argue that new diffusion regions are created globally and they form an extended reconnection layer on either side of the current sheet, which is essentially helpful for the global fast reconnection.

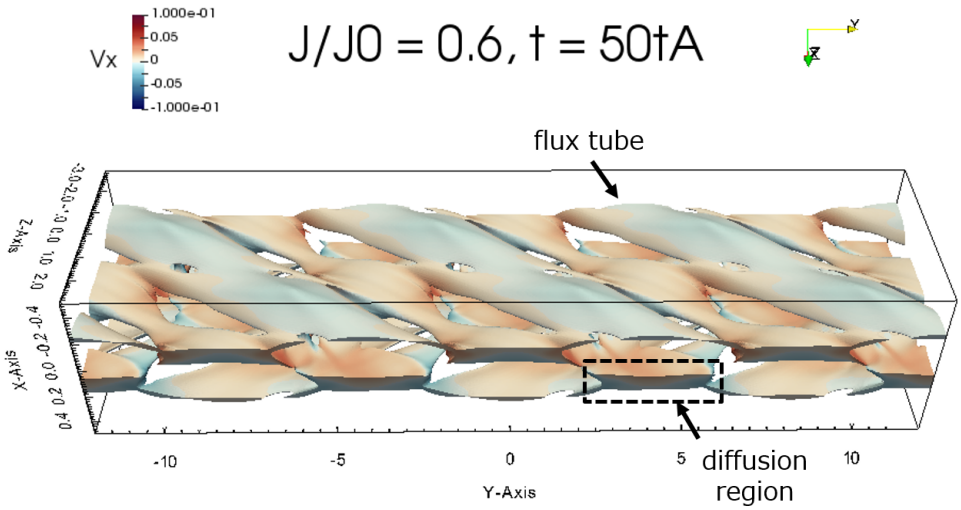

A) flux tube surfaces and diffusion regions in $(\mathbf{3}, \pm\mathbf{1})$ simulation

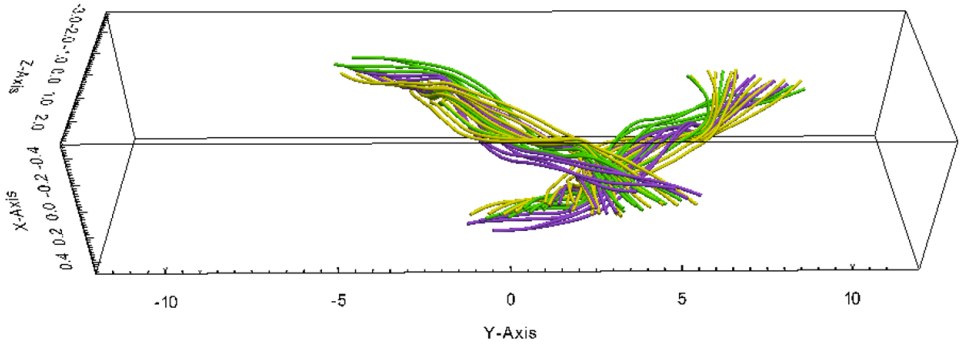

B) flux tube magnetic field lines

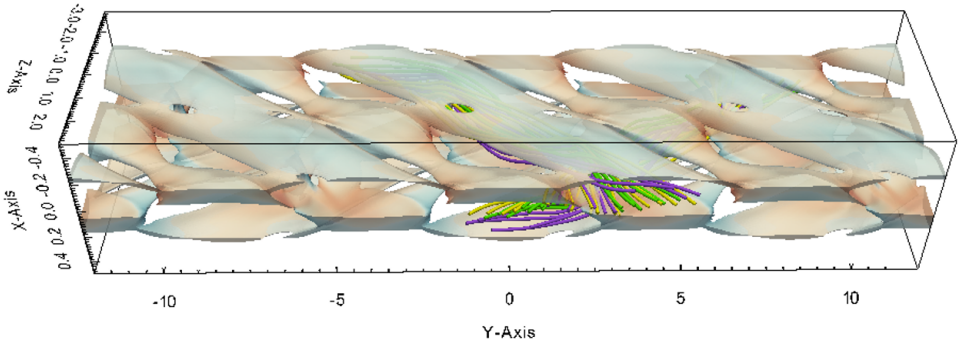

C) flux tube surfaces with field lines

Figure 3.5: Current density isosurface represents flux tube surfaces and diffusion regions, together with magnetic field lines. Yellow, purple and green lines are selected field lines from $z = 0$, -1.5δ and 1.5δ plane and root along the resonance layers $(3, 1)$ and $(3, -1)$ respectively.

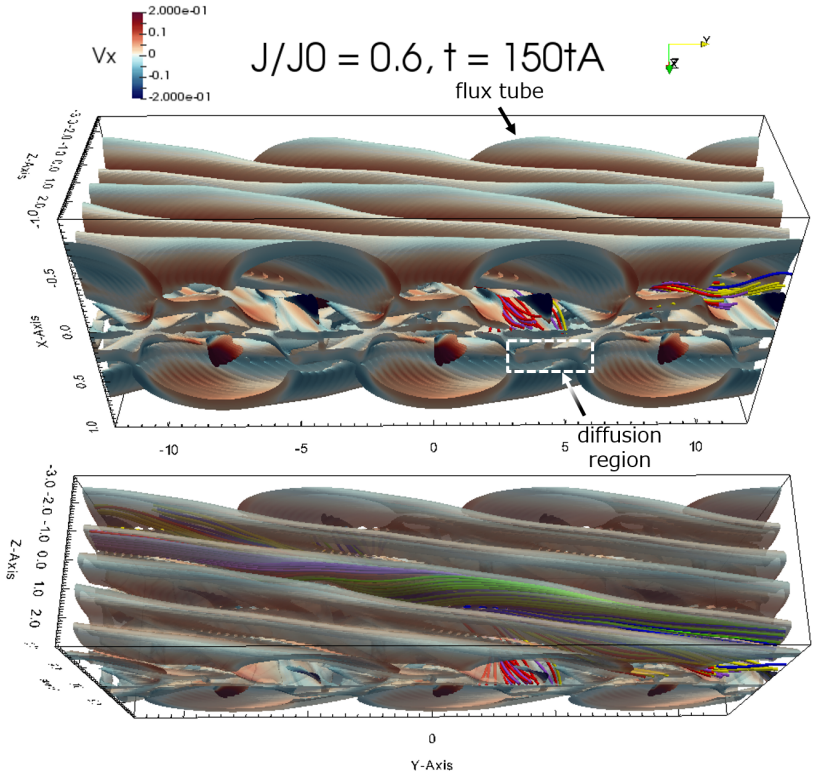

A) flux tube surfaces and diffusion regions, with magnetic field lines

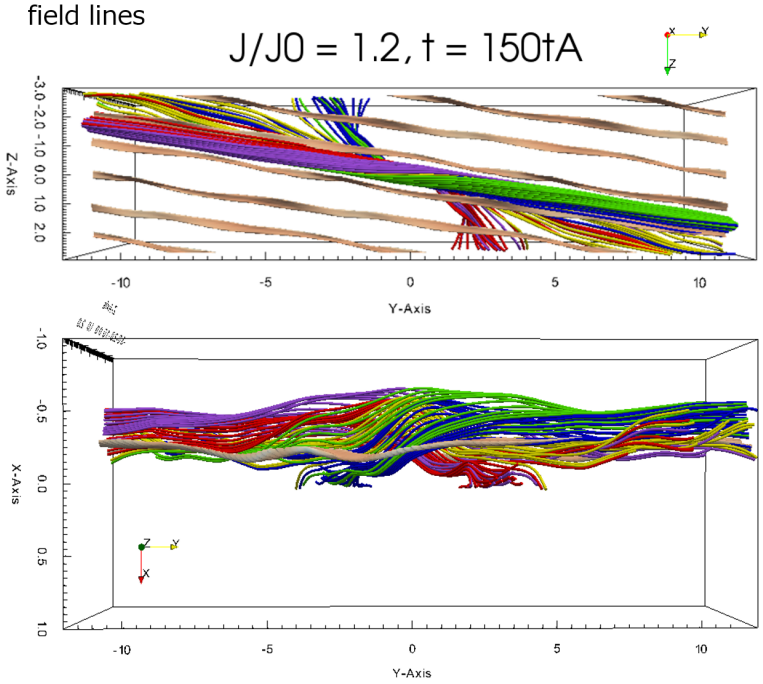

B) diffusion regions with magnetic field lines

Figure 3.6: Current density isosurface represents flux tube surfaces and diffusion regions, together with magnetic field lines. Yellow, purple and green lines are selected field lines from $z = 0$, -1.2δ and 1.2δ planes, while red and blue lines are selected field lines on $z = -0.6\delta$ and 0.6δ planes. All lines root along the resonance layer $(3, -5)$.

As the initial tearing modes grow stronger, the nonlinear terms such as the second-order terms cannot be ignored anymore. For example, in the induction equation Eq.(1.1), the nonlinear term comes from the cross term of $\mathbf{v}$ and $\mathbf{B}$ of the initial modes, later all existing modes when they sufficiently grow. The detailed equations describe this process are shown in Appendix.G. We refer to this mechanism as the nonlinear coupling of tearing modes. The inflow-outflow coupling in the previous discussion describes the enhancement of the field amplitude across the current sheet. The nonlinear coupling of the tearing modes we are going to investigate in the following part produces new modes growing along the current sheet, while the new modes have different wavenumbers compared to the original modes (e.g., Kusano & Sato, 1987).

Initially, the system is provided with only two 3D modes. As it is described in Appendix.G, the nonlinear coupling between two modes (m_1, n_1) and (m_2, n_2) produces

$$(m_1, n_1) + (m_2, n_2) \rightarrow (m_1 \pm m_2, n_1 \pm n_2) \tag{3.1}$$

in general. Higher order harmonics of the initial modes and new modes on other resonance layers, such as $(3, 1) + (3, -1) \rightarrow (6, 0)$, are created.

Chain effect of successive nonlinear coupling afterwards between new and old energy modes will form an extended energy spectrum. We thus study the magnetic energy of each mode as shown in Fig.3.7. We calculate the energy of each mode (m, n) in the Fourier space as that shown in Eq.(2.38) and Eq.(2.39). Since we are applying the rotational-symmetric setup, we average all energy modes into the form of

$$\tilde{E}_m(m, |n|) = \frac{1}{2}\left[\tilde{E}_m(m, +|n|) + \tilde{E}_m(m, -|n|)\right] \tag{3.2}$$

for convenience. The maximum mode energy at each time step is plotted as the thick black dashed line in Fig.3.7. In the left panel, we plot the most energetic modes before $t = 200t_A$. It can be seen that 3D modes (i.e., modes with $n \neq 0$) always dominate during this time. The most energetic mode changes from the initial perturbed $(3, 1)$ to $(3, 3)$ first,

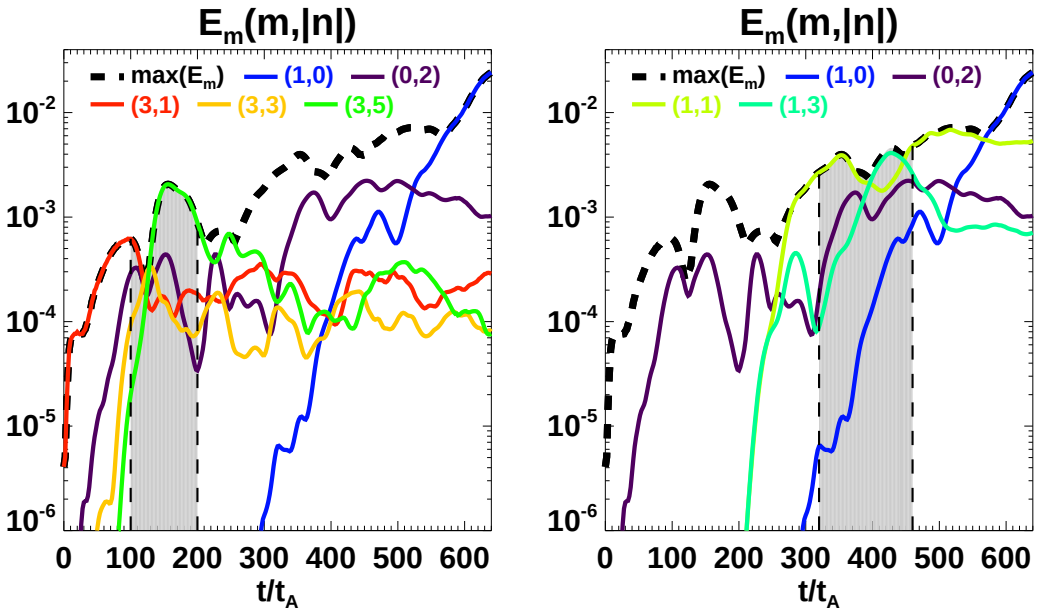

Figure 3.7: Magnetic mode energy in the selected periods (shaded by gray colors) which correspond to the overall reconnection rate boosts in Fig.3.10. Black dashed line is the maximum mode energy at each time step. Colored lines are the most energetic modes during each boost. In addition, the energy mode $(0, 2)$ and $(1, 0)$ are also plotted as purple and blue lines.

then finally $(3, 5)$ in the shaded region, which shows an energy transfer from a smaller $|n|$ mode to a larger $|n|$.

By checking the position of diffusion regions and the resonance layers, it can be confirmed that the new reconnection layers are the mixture of the modes $(3, \pm 3)$ and $(3, \pm 5)$. In Fig.3.8, we plot the current density J on different y-planes across a quarter of the whole box along the y-direction, where bright features represent diffusion regions. We concentrate on the $-x$-side of the current sheet and the highly enhanced diffusion regions along $x = -0.3\delta$. They are the newly created diffusion regions outside of the original tearing layers (red dashed lines) thus the reconnection plane is reaching outwardly from the current sheet center. On all planes, five diffusion regions with enhanced current density can be identified. We overplot the resonance layer of $(3, -5)$, but find that it does not always co-locate with the diffusion regions. Instead, the mode $(3, -3)$ are close to these diffusion regions on all y-plane. So it seems that the diffusion lines are from both $(3, -3)$ and $(3, -5)$. Although further cascade into $(3, \pm 7)$ can be found very close to the current

sheet boundary, they are too weak to be important to the whole system.

In summary, from the analysis above, we show that how diffusion regions are created locally and globally, which are necessary to explain the overall fast reconnection. New diffusion regions correspond to new energy modes which come from the nonlinear coupling. In addition, some diffusion regions along the original perturbed modes remain and coexist with the new reconnection layer formed by the new diffusion regions (Fig.3.8). Whether the inflow-outflow coupling also exists between them will be checked in Sec.3.5.

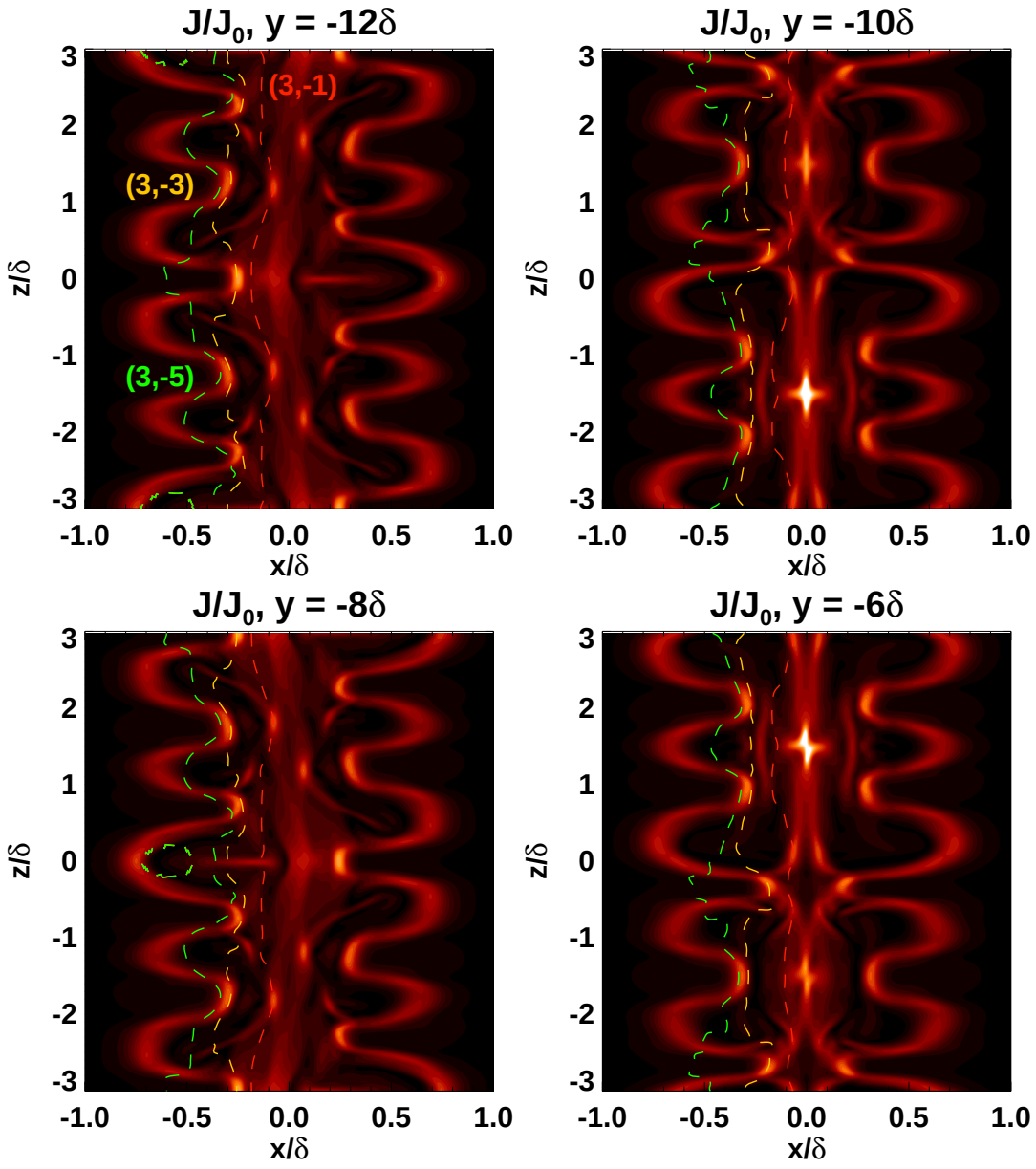

Figure 3.8: Current density contour plot at different y-planes at $t = 150t_A$. Red, orange and green dashed lines correspond to the position of the resonance layers of $(3, -1)$, $(3, -3)$ and $(3, -5)$ respectively.

3.3 Dominant energy transfer path

We have observed that new energy modes are created and participate reconnection. Since there develop numerous possible energy transfer paths as Eq.(3.1) that lead to activate a certain mode, we need to calculate the energy transfer rate along each path to find the most contributing one that explains the emergence of new energy modes. The calculation of the energy transfer rate is based on the study by Dahlburg et al. (1992), which is the extension of the work in hydrodynamics (Orszag & Patera, 1983).

The velocity field and the magnetic field are decomposed into:

$$\mathbf{v}(x,y,z) = \mathbf{v}^{(1)}(x) + \mathbf{v}^{(2)}(x,y) + \mathbf{v}^{(3)}(x,y,z) \tag{3.3}$$

$$\mathbf{B}(x,y,z) = \mathbf{B}^{(1)}(x) + \mathbf{B}^{(2)}(x,y) + \mathbf{B}^{(3)}(x,y,z) \tag{3.4}$$

while being explicitly

$$\begin{aligned}\mathbf{v}(x,y,z) = \mathbf{v}^{(1)}(x) &+ \sum_{m=-M}^{M} \tilde{\mathbf{v}}^{(2)}_{m0}(x)\exp(ik_y y) \\ &+ \sum_{|n|=1}^{N}\sum_{m=-M}^{M} \tilde{\mathbf{v}}^{(3)}_{mn}(x)\exp(ik_y y + ik_z z)\end{aligned} \tag{3.5}$$

$$\begin{aligned}\mathbf{B}(x,y,z) = \mathbf{B}^{(1)}(x) &+ \sum_{m=-M}^{M} \tilde{\mathbf{B}}^{(2)}_{m0}(x)\exp(ik_y y) \\ &+ \sum_{|n|=1}^{N}\sum_{m=-M}^{M} \tilde{\mathbf{B}}^{(3)}_{mn}(x)\exp(ik_y y + ik_z z)\end{aligned} \tag{3.6}$$

where M and N are the largest wavenumbers along y- and z-direction in this system. Rewrite the component into 1D, 2D and 3D modes as:

$$\mathbf{v}^{[1]} = \mathbf{v}^{(1)} + \mathbf{v}^{(2)}_{00} \quad , \quad \mathbf{B}^{[1]} = \mathbf{B}^{(1)} + \mathbf{B}^{(2)}_{00} \tag{3.7}$$

$$\mathbf{v}^{[2]} = \mathbf{v}^{(2)} - \mathbf{v}^{(2)}_{00} \quad , \quad \mathbf{B}^{[2]} = \mathbf{B}^{(2)} - \mathbf{B}^{(2)}_{00} \tag{3.8}$$

$$\mathbf{v}^{[3]} = \mathbf{v}^{(3)} \quad , \quad \mathbf{B}^{[3]} = \mathbf{B}^{(3)}. \tag{3.9}$$

Consider the energy transfer between 1D, 2D and 3D modes energy in the form of

$$\frac{dE_1}{dt} = -\tau_{12} - \tau_{13} + \delta_1 \tag{3.10}$$
$$\frac{dE_2}{dt} = \tau_{12} - \tau_{23} + \delta_2 \tag{3.11}$$
$$\frac{dE_3}{dt} = \tau_{13} + \tau_{23} + \delta_3 \tag{3.12}$$

where τ_{ij} represents the energy transfer rate from the i-th dimensional mode to the j-th dimensional mode, δ_i is the dissipation rate of the i-th dimensional mode. Applying the momentum equation Eq.(2.2) and the induction equation Eq.(2.4) into Eq.(3.10) to Eq.(3.12), the energy transfer rate between 1D, 2D and 3D modes can be written as

$$\tau_{12} = \int \frac{\mathbf{B}^{[1]}}{4\pi} \cdot \nabla \times \left(\mathbf{v}^{[2]} \times \mathbf{B}^{[2]}\right)^* d^3x \tag{3.13}$$
$$\tau_{13} = \int \frac{\mathbf{B}^{[1]}}{4\pi} \cdot \nabla \times \left(\mathbf{v}^{[3]} \times \mathbf{B}^{[3]}\right)^* d^3x \tag{3.14}$$
$$\tau_{23} = \int \left[\rho \mathbf{v}^{[3]} \cdot (\mathbf{v} \times \omega)^{[3]*} + \frac{\mathbf{v}^{[3]}}{c} \cdot (\mathbf{J} \times \mathbf{B})^{[3]*} + \frac{\mathbf{B}^{[3]}}{4\pi} \cdot \nabla \times (\mathbf{v} \times \mathbf{B})^{[3]*}\right] d^3x$$
$$-\tau_{13} \tag{3.15}$$

where the cross terms are in the form of

$$(\mathbf{v} \times \omega)^{[3]} = \mathbf{v}^{[2]} \times \omega^{[3]} + \mathbf{v}^{[3]} \times \omega^{[2]} \tag{3.16}$$

while the dissipation rates are

$$\delta_i = \int -\frac{\eta}{(4\pi)^2} \left|\nabla \times \mathbf{B}^{[i]}\right| d^3x. \tag{3.17}$$

We assume an incompressive plasma that ρ is treated as a uniform constant.

We are interested in the individual energy transfer path, namely how a certain mode

(m,n) is produced. By expanding Eq.(3.15) for each path, it gives

$$\begin{aligned}\tau_{mn} &= \int 2\rho\Re\left(\tilde{\mathbf{v}}^{[3]}_{mn}\cdot(\tilde{\mathbf{v}}\times\tilde{\omega})^{[3]*}_{mn}\right)\frac{(2\pi)^2}{L_yL_z}dx \\ &+ \int 2\frac{1}{c}\Re\left(\tilde{\mathbf{v}}^{[3]}_{mn}\cdot\left(\tilde{\mathbf{J}}\times\tilde{\mathbf{B}}\right)^{[3]*}_{mn}\right)\frac{(2\pi)^2}{L_yL_z}dx \\ &+ \int 2\Re\left(\frac{\tilde{\mathbf{B}}^{[3]}_{mn}}{4\pi}\cdot\nabla\times\left(\tilde{\mathbf{v}}\times\tilde{\mathbf{B}}\right)^{[3]*}_{mn}\right)\frac{(2\pi)^2}{L_yL_z}dx. \end{aligned} \tag{3.18}$$

The cross terms contain the information of the parent modes. Regarding Eq.(3.1), the cross terms can be written in the form of

$$(\tilde{\mathbf{v}}\times\tilde{\omega})^{[3]*}_{mn} = \tilde{\mathbf{v}}^{[3]*}_{m_1n_1}\times\tilde{\omega}^{[3]*}_{m_2n_2} + \tilde{\mathbf{v}}^{[3]*}_{m_2n_2}\times\tilde{\omega}^{[3]*}_{m_1n_1}. \tag{3.19}$$

Summation of all possible (m_1,n_1) and (m_2,n_2) will give a total energy transfer to a certain mode (m,n).

The eigenfunction of energy mode becomes less well defined in the highly nonlinear system. Therefore the calculation above is not applicable in the late phase. We then only concentrate on the early phase. That is, to understand how $(3,3)$ and $(3,5)$ are produced. The energy transfer rate and the dissipation rate before the end of the first boost are shown in Fig.3.9. The dissipation rate in panel A) shows a very similar trend as the mode energy in Fig.3.7. The dissipation by the 2D mode $(6,0)$ before $t = 200t_A$ is far slower than 3D modes. In panel B), the total energy transfer rate into $(3,3)$ and $(3,5)$ by summing up all possible combinations of (m_1,n_1) and (m_2,n_2) are plotted. Comparing panel A) and B), it can be observed that both the dissipation rate and the total energy transfer rate start to increase rapidly from $t \sim 80t_A$. From $t \sim 80t_A$ to $130t_A$, the dissipation rate and the total energy transfer rate are rapidly increasing for $(3,3)$, which correspond to the increase of the total magnetic energy of $(3,3)$ in Fig.3.7. The dissipation rate increases fast until almost $t \sim 190t_A$ for $(3,5)$, but the total energy transfer rate has a peak around $140t_A$. As the dissipation is stronger than the energy $(3,5)$ receives afterwards, the total magnetic energy of $(3,5)$ has a peak around $150t_A$ as shown in Fig.3.7.

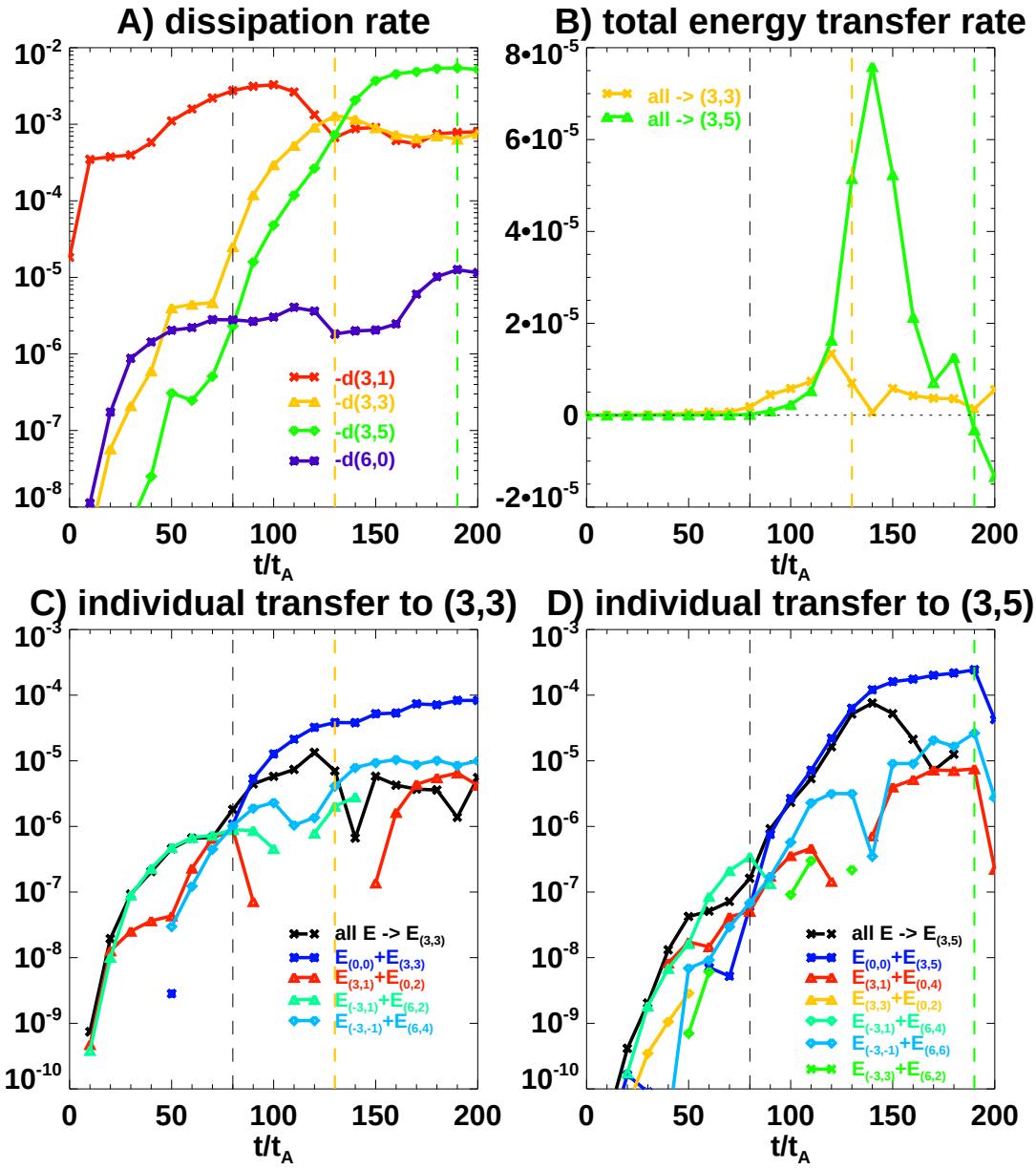

Figure 3.9: Panel A): the dissipation rate of selected modes. Panel B): the total energy transfer rate of $(3,3)$ and $(3,5)$ by summing up all possible combinations of (m_1,n_1) and (m_2,n_2). Panel C) and D): individual energy transfer rate of $(3,3)$ and $(3,5)$ from different paths. Black dashed lines are the starting time for the rapid growth of $(3,3)$ and $(3,5)$. Orange and green dashed lines label the peak times for the dissipation rate of these two modes respectively.

Looking back to Fig.3.2, the new modes $(3,3)$ and $(3,5)$ start to participate reconnection from $t \sim 120t_A$. It implies that these two modes are growing mainly by absorbing energy from the background current during this phase, similar to an ordinary tearing mode. This argument is supported by the individual energy transfer path shown in panels C) and D). The energy transfer from $(0,0)$ mode becomes predominant after $80t_A$ for both modes. It runs over the total energy transfer from $90t_A$ in $(3,3)$ and $140t_A$ in $(3,5)$ as these two modes are pouring energy to other modes as well. However, $(3,3)$ and $(3,5)$ are not preferable tearing modes in the initial current sheet. Thus to understand the energizing phase which activates these two modes is important.

In the case of $(3,3)$, before the rapid growth $\sim 80t_A$, the main energy transfer paths are $(3,1)+(0,2)$, $(-3,1)+(6,2)$ and $(-3,-1)+(6,4)$. The first transfer path can be understood by Sec.3.6.1. The second and the third transfer paths both involve higher wavenumber modes, in which $(6,2)$ is the second harmonic of the original mode, while $(6,4)$ is produced predominantly by $(-3,1)+(9,3)$ (not shown here) and $(9,3)$ is the third harmonic of the original mode. Similar processes happen for $(3,5)$, as the energy transfer path $(-3,1)+(6,4)$ dominates before $(3,5)$ grows rapidly. In addition, the second harmonic of $(3,3)$ is also participating in transferring the energy via $(-3,-1)+(6,6)$.

The dominant energy transfer path seems to be the nonlinear coupling of the initial modes and their higher order harmonics. The growth of higher order harmonics of the original tearing modes is highly related to secondary tearing. As we have explained, secondary tearing is important to produce new diffusion region outwardly. Thus the nonlinear coupling can be linked to the processes shown in Fig.3.1 and Fig.3.2. As secondary tearing grows, the inflow-outflow coupling between diffusion regions gradually shifts to the partitioned diffusion regions. It means that the modes which participate the inflow-outflow coupling is not only limited to the original modes but also their higher order harmonics. As a result, energy modes with higher wavenumbers become more energetic.

By calculating each energy transfer path, we find that the higher order harmonics are important in activating new energy modes outwardly across the current sheet. Our initial

perturbation contains only two modes. When the initial system is perturbed by a broad band of modes, whether the nonlinear coupling is also dominated by the higher order harmonics of the initial modes needs further study.

The efficiently growing higher order harmonics are activated by the inflow-outflow coupling as we described in Sec.2.5. Although they are growing along the sheet, they subsequently participate the nonlinear coupling across the current sheet. When the higher order harmonics become dominant, they break the original diffusion region due to secondary tearing. Therefore, it is suggested here that the nonlinear coupling and secondary tearing are also coupled processes.

3.4 Global energy change

We have shown the creation of new reconnection layers that expand further into the asymptotic magnetic field. From the rapid growing dissipation rate of these new modes shown in panel A) of Fig.3.9, it is expected that the reconnection is growing fast after $t \sim 80t_A$.

In order to confirm this, we check the total kinetic energy in the box and the magnetic reconnection rate by evaluating the magnetic energy conversion rate. The total kinetic energy is calculated as:

$$E_k = \int_{-\frac{L_z}{2}}^{\frac{L_z}{2}} \int_{-\frac{L_y}{2}}^{\frac{L_y}{2}} \int_{-\frac{L_x}{2}}^{\frac{L_x}{2}} \frac{1}{2}\rho \mathbf{v}^2 dxdydz. \tag{3.20}$$

The magnetic energy conversion rate is calculated by the time derivative of the reduced total magnetic energy, which is calculated by:

$$\Delta E_m = \int_{-\frac{L_z}{2}}^{\frac{L_z}{2}} \int_{-\frac{L_y}{2}}^{\frac{L_y}{2}} \int_{-\frac{L_x}{2}}^{\frac{L_x}{2}} \frac{|\mathbf{B_f}|^2 - |\mathbf{B}|^2}{8\pi} dxdydz \tag{3.21}$$

where $\mathbf{B_f}$ is the magnetic field calculated in a nonlinear simulation without any perturbation. By subtracting $\mathbf{B_f}$, the magnetic change from the global diffusion is removed.

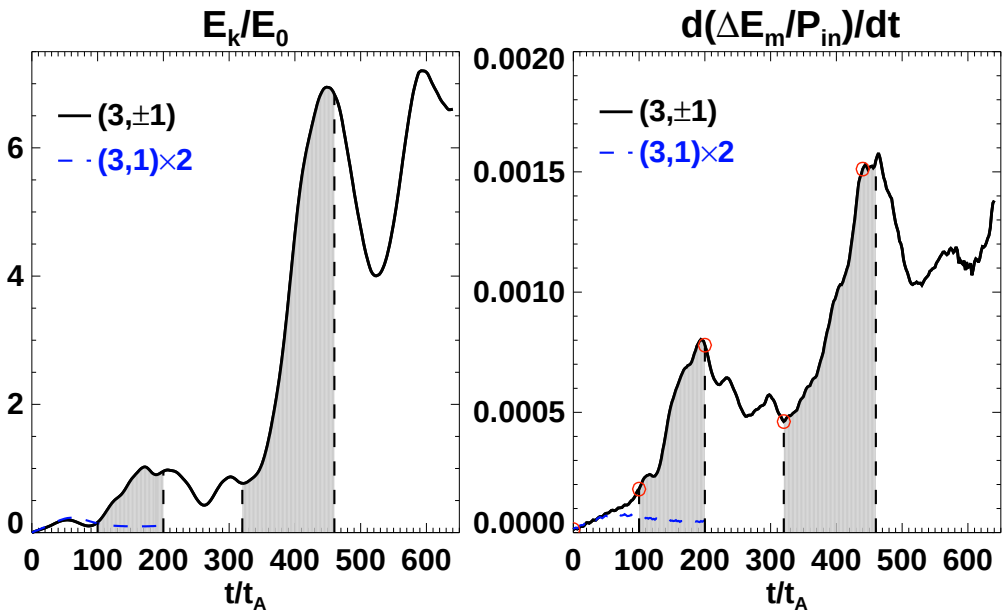

Figure 3.10: The total kinetic energy (left) and the magnetic energy conversion rate (right) of the double-layer simulation $(3, \pm 1)$. Gray shaded regions are the stages where reconnection rate has a boost.

The magnetic energy conversion rate is normalized by P_{in}, which is defined as $P_{\text{in}} = 2L_y L_z v_{A0} B_{y0}^2/(4\pi)$ that represents the total inflow Poynting flux estimated by the global asymptotic magnetic field from both sides of the current sheet.

By observing the magnetic energy conversion rate in Fig.3.10, we notice a clear boost at $t = 100 - 200t_A$ (first gray shaded region), which also corresponds to a boost in the total kinetic energy. We also execute the single-layer simulation $(3, 1)$ until the end of the first boost. However, no such eruptive energy release is found. So the boost must correlate with the 3D effects rather than the 2D-like cascade along the initial tearing layer. We have already identified the creation of new reconnection layers outwardly due to the growth of higher wavenumber modes. They are highly related to the global reconnection efficiency.

After the first boost ($t = 200t_A$), the global reconnection decelerates. The whole system starts to reorganize itself, as the outermost modes $(3, \pm 5)$ get weaker (Fig.3.7) and give out energy to other modes (panel B) in Fig.3.9). In Fig.3.11, we show how existing flux tubes behave in the relaxation phase after $t = 200t_A$. We select flux tubes on the $x > 0$ side of the current sheet. At $t = 240t_A$, five flux tubes are still visible along

the current sheet. If we concentrate on the positions where the red arrows are pointing at, we notice that the field lines gradually untwist and re-twist with the field lines nearby. Eventually, a new big flux tube is formed across the current sheet. Visually, we have found the phenomenon that is similar to the coalescence instability. As this new tube structure extends from one corner of the box to its diagonal corner along the sheet direction, it is probably the tube on the same resonance layer as $(3, 3)$ but produced by lower order harmonics.

As it can be seen from Fig.3.10, both the kinetic energy and the global energy conversion rate have another boost after $t = 320t_A$ until around $460t_A$ (second gray shaded area). From the right panel of Fig.3.7, it is found that during this phase, the lower order harmonic of $(3, \pm 3)$, namely $(1, \pm 1)$, start to grow and subsequently evokes $(1, \pm 3)$. The existence of $(1, 1)$ has been captured by Fig.3.11. So the second boost also correlates with a production of higher wavenumber modes along the guide field direction (an increase of $|n|$ number), the same as the first boost.

We first try to locate $(1, 1)$ and $(1, 3)$ in Fig.3.12 and Fig.3.13. As the resonance layer of $(1, 1)$ is closer to the sheet center compared to $(3, 5)$, $(1, 1)$ is growing from the inside and difficult to be identified from the outermost layer of the current density isosurface, as shown in the panel A). Moreover, it is coexisting with other harmonics of $q = -4$, such as $(3, 3)$. We select the magnetic field lines from the resonance layer of $q = -4$ along one flux tube. The coherency of the field lines is not as good as that in Fig.3.6. However, the structure of $(1, 1)$ tube can be found from the purple and the green lines between two diffusion lines on either side. Later, the new mode $(1, 3)$ start to grow, which has a larger wavenumber along the global guide field than $(1, 1)$. Clearly, three flux tubes that extend along the sheet direction can be seen. The field lines selected from the resonance layer of $(1, 3)$ show a coherent twist inside the flux tube above the reconnection layer which is formed by the diffusion lines. By checking the resonance factor q of the diffusion lines, we find that they are the combination of $(1, 1)$ and $(1, 3)$, consistent with the spectrum. Actually, the modes $(1, \pm 3)$ are not allowed by the original system because

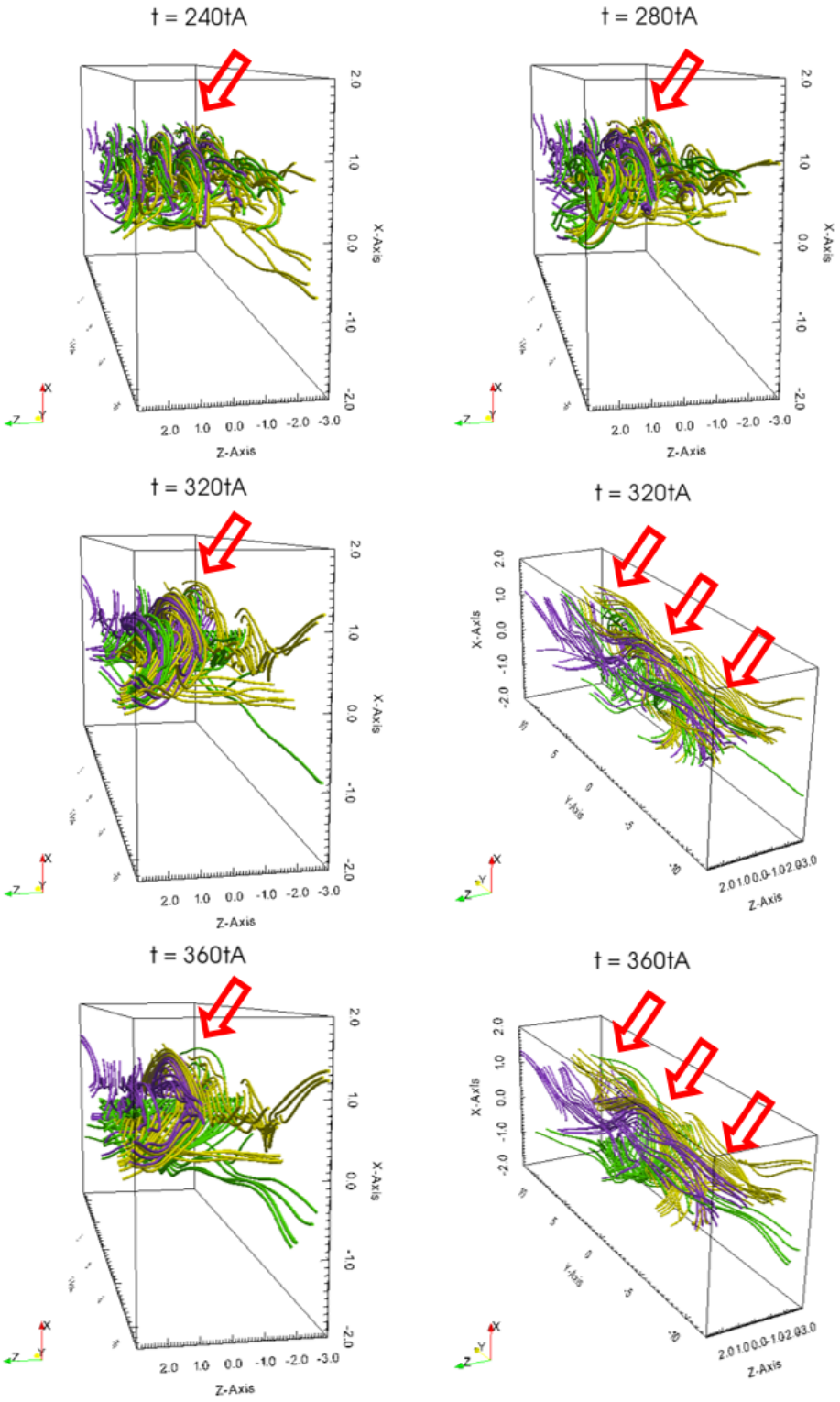

Figure 3.11: Magnetic field lines selected in the double-layer simulation $(3, \pm 1)$ during the relaxation phase. Green, purple and yellow lines are magnetic fields selected from $y = 0, \pm 6\delta$ across $x = 0.5\delta$.

of the limitation by Eq.(2.26). But due to the inflow-outflow coupling across the whole current sheet, magnetic flux is absorbed into the current sheet globally. A piling up of magnetic field exists along the current sheet boundary. It increases the anti-parallel fields more than the global guide field locally thus modes with higher wavenumbers along the guide field can survive.

The local creation of diffusion regions for $(1, \pm 3)$ is shown in Fig.3.14, where the black dashed line box confines. In the upper left panel, a chain of diffusion regions at the current sheet center can be seen, which correspond to the 2D mode $(6, 0)$ that starts to grow from the early phase. Later ($t = 300t_A$), the diffusion region near $y = 6\delta$ disappears, which implies an inverse energy cascade to a longer 2D mode so two diffusion regions remain inside the box. Both diffusion regions reconnect magnetic fields and eject outflows into $y = 6\delta$ thus form a new vertical diffusion region. As we have described in Fig.3.1, the vertical diffusion region pushes the field lines outwardly then forms new diffusion regions, as shown in the lower panels of Fig.3.14. Although no secondary tearing is needed here, the essential mechanism is shared with the previous description that new diffusion regions are created by the re-orientation of the flow and the existence of multiple orders of harmonics.

Therefore, the story in the second boost is consistent with what we have developed in the first boost. They both give the same conclusion that the global reconnection accelerates with the growth of new reconnection layers that correspond to new 3D modes near the asymptotic magnetic field.

As we have shown in the above, new energy modes are created due to the nonlinear coupling. During the coupling, the parent modes energy transfers to the daughter modes which have a larger wavenumber $|n|$ than the original modes. In our simulation which starts from a pair of rotational-symmetric tearing modes, the energy transfer with increasing wavenumber $|n|$ appears twice while each one corresponds to a reconnection boost. The change of the most energetic mode can be clearly observed from the 2D energy spectrum. In Fig.3.15, the 2D magnetic energy spectrum is shown at different times which

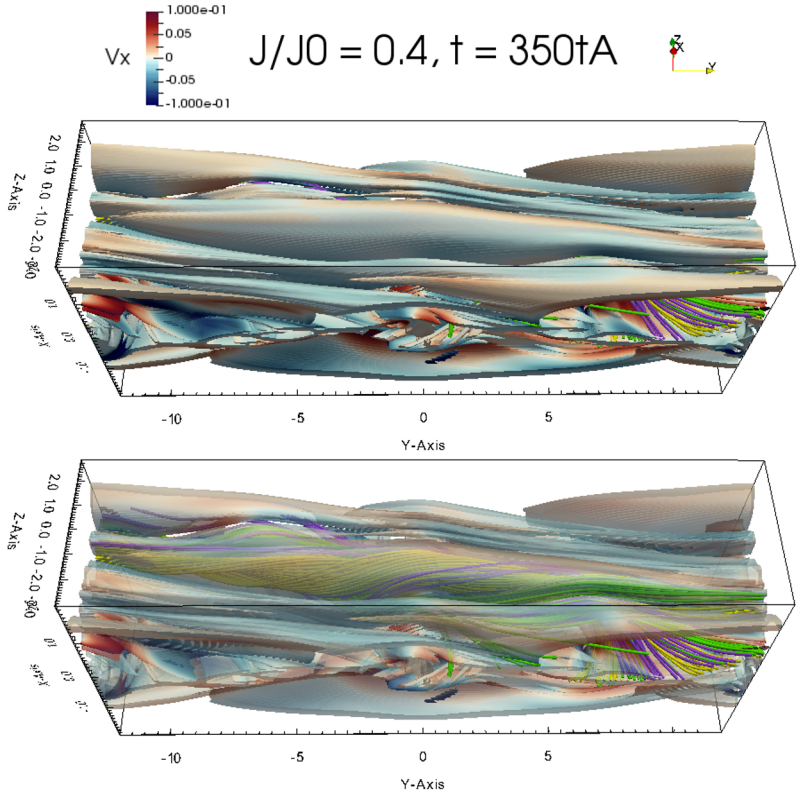

A) flux tube surfaces and diffusion regions, with magnetic field lines

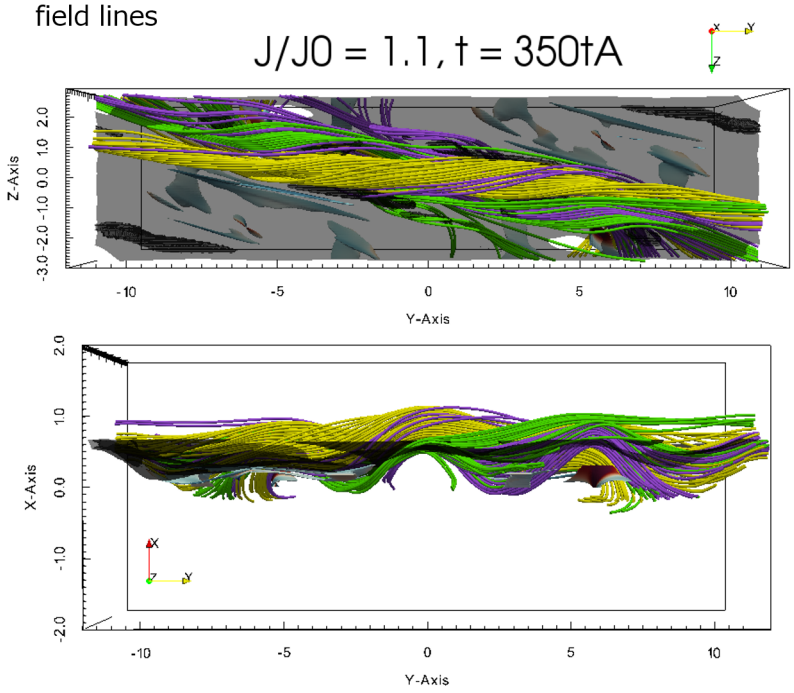

B) diffusion regions with magnetic field lines, translucent black surface is $q = -4$ resonance layer

Figure 3.12: Current density isosurface represents flux tube surfaces and diffusion regions, together with selected magnetic field lines. Yellow, purple and green lines are selected field lines from $z = 0$, -1.5δ and 1.5δ planes. All lines root along the resonance layer $(1, 1)$ (translucent black surface).

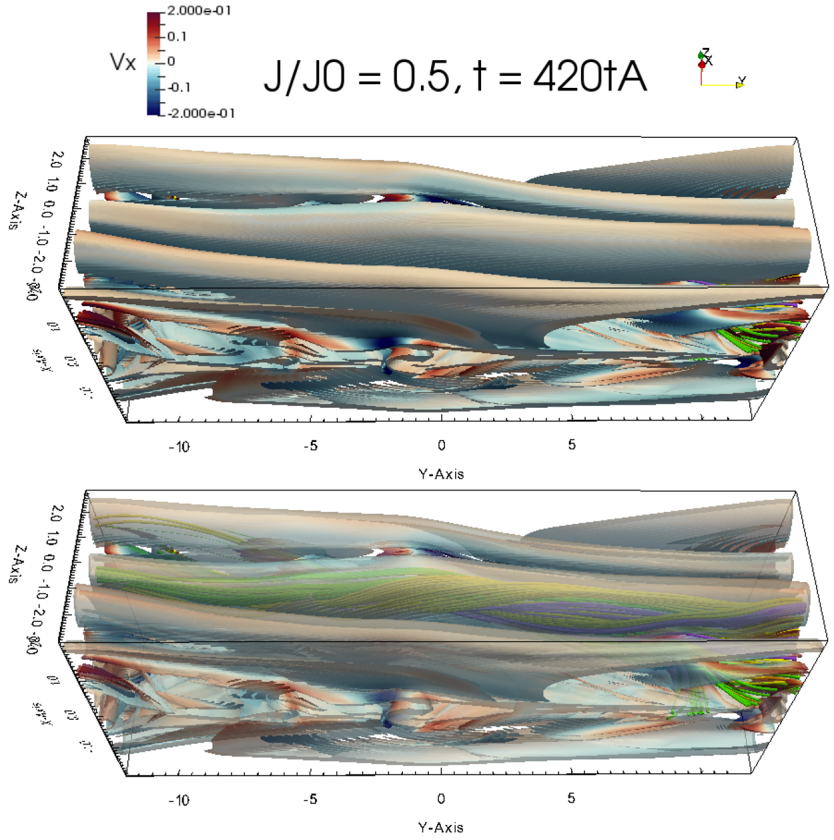

A) flux tube surfaces and diffusion regions, with magnetic field lines

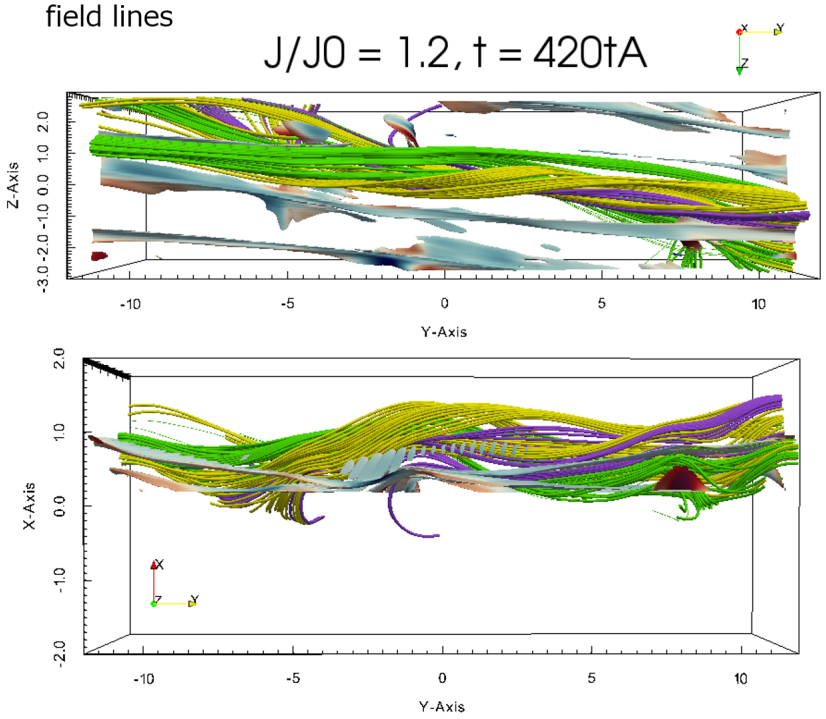

B) diffusion regions with magnetic field lines

Figure 3.13: Current density isosurface represents flux tube surfaces and diffusion regions, together with selected magnetic field lines. Yellow, purple and green lines are selected field lines from $z = 0$, -1δ and 1δ planes. All lines root along the resonance layer $(1, 3)$.

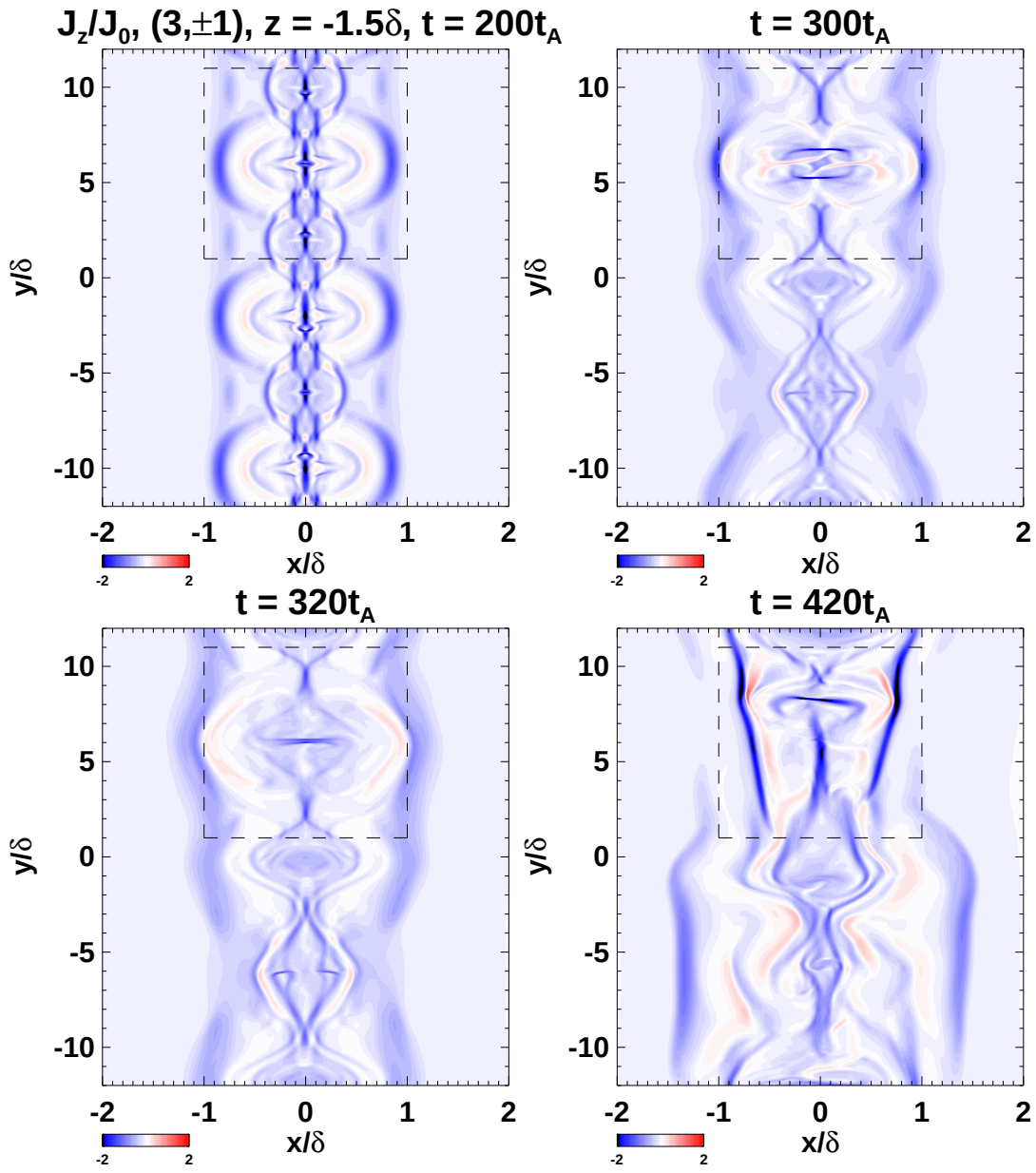

Figure 3.14: Diffusion region development along time by showing the current density J_z contour plot on the symmetric plane $z = -1.5\delta$. The big dashed line box locates the region how new diffusion regions are created.

correspond to the red circles in Fig.3.10. It can be seen that the energy is showing a cascading trend towards the asymptotic magnetic field along the global guide field direction (k_z) in each boost, which is consistent with the previous study (Landi et al., 2008). In between the two boosts, an energy cascade into the longer mode $(1, 1)$ can be seen. The integrated 1D spectrum is shown in Appendix.H.

To consolidate our argument that 3D modes are important in the 3D reconnection, we calculate the spatially averaged current density strength $\langle|\mathbf{J}|\rangle$ that

$$\langle|\mathbf{J}|\rangle = \int_{-L_z/2}^{L_z/2}\int_{-L_y/2}^{L_y/2}\int_{-L_x/2}^{L_x/2}|\mathbf{J}(x,y,z)|dxdydz/(L_xL_yL_z). \tag{3.22}$$

It represents the Joule heating thus the dissipation of the system. The current sheet width is defined as the distance between the positions with a certain current density threshold that equals to the current density at the initial current sheet half-width ($\sim 0.24J_0$). The sheet width is plotted in panel A) of Fig.3.16, Inside the shaded regions which correspond to the reconnection boosts, there exist faster expansions of the current sheet. Meanwhile, $\langle|\mathbf{J}|\rangle$ increases during these phases, which also indicates an acceleration of global dissipation. The total mode energy of 2D and 3D modes are plotted in panel C). During each boost, 3D modes have a sudden increase, while the 2D modes in the second boost is growing almost linearly.

By plotting the distribution of the sheet-wise averaged current density $\langle|\mathbf{J}(x)|\rangle$ that $\langle|\mathbf{J}(x)|\rangle = \int_{-L_z/2}^{L_z/2}\int_{-L_y/2}^{L_y/2}|\mathbf{J}|dydz/(L_yL_z)$ along the x-direction as shown in panels B) and D), we are capable to distinguish the contribution of dissipation from 2D and 3D modes to some extent. In panel B), there is clear boundary with finite current density between the dissipation region and the non-dissipating region. This boundary is the outermost boundary of the 3D flux tubes. Our measurement of the current sheet width is always beyond this region. In the initial phase before $100t_A$, two branches of $\langle|\mathbf{J}(x)|\rangle$ local maximum can be observed inside the flux tube boundaries. By comparing to the 3D distribution of $|\mathbf{J}|$, it is confirmed that they correspond to the diffusion regions of initial perturbed modes $(3, 1)$ and $(3, -1)$. After $100t_A$, the new modes $(3, \pm 3)$ and $(3, \pm 5)$ emerge. The

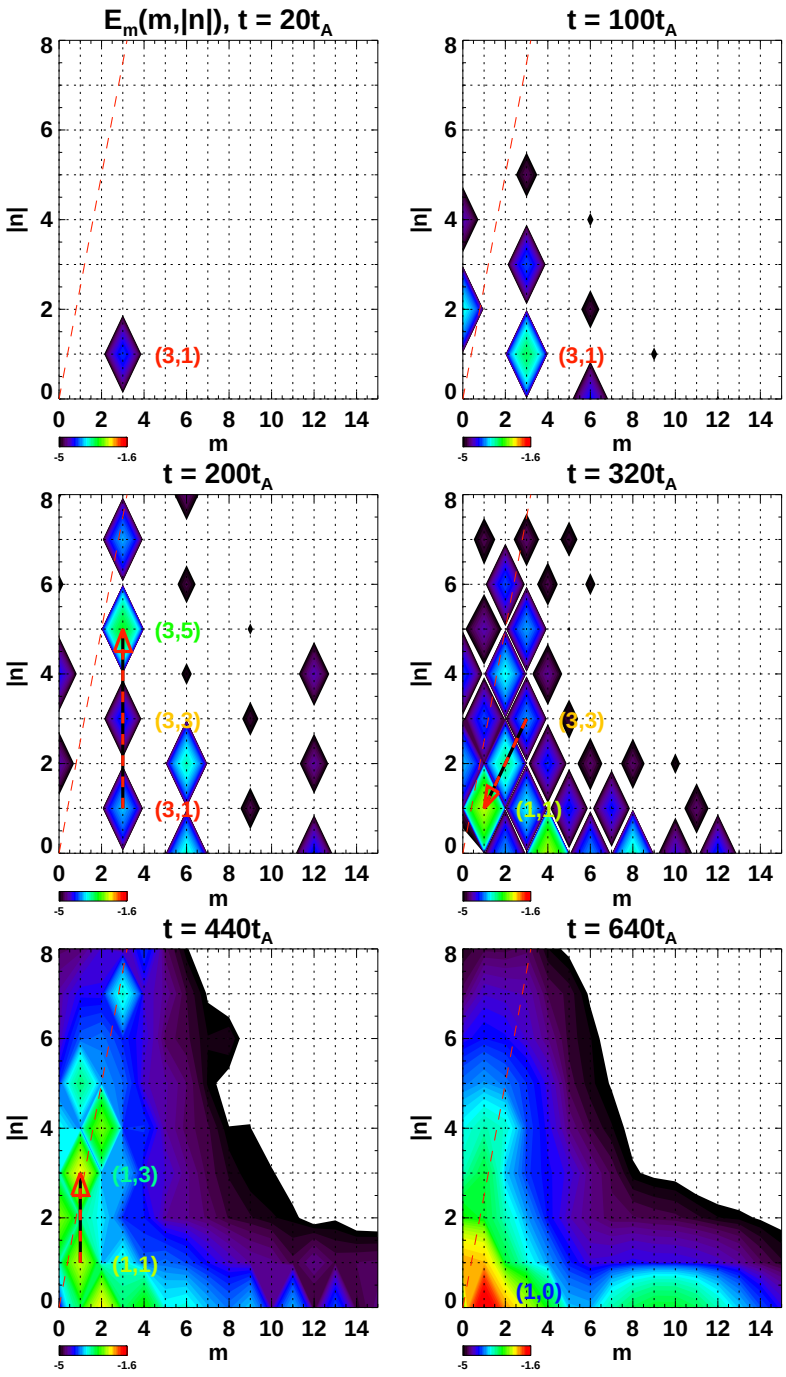

Figure 3.15: The magnetic energy spectrum of Eq.(2.39) at times corresponding to the red circles in Fig.3.10, in addition to the final time of our simulation. The dominant modes are labeled in each panel. Black-red dashed arrows indicate the possible energy transfer paths. The red dashed line represents the asymptotic magnetic field for the current sheet. The region between the red dashed line and k_z axis is the reconnection-incapable region in the original current sheet. Colors are in the logarithmic scale.

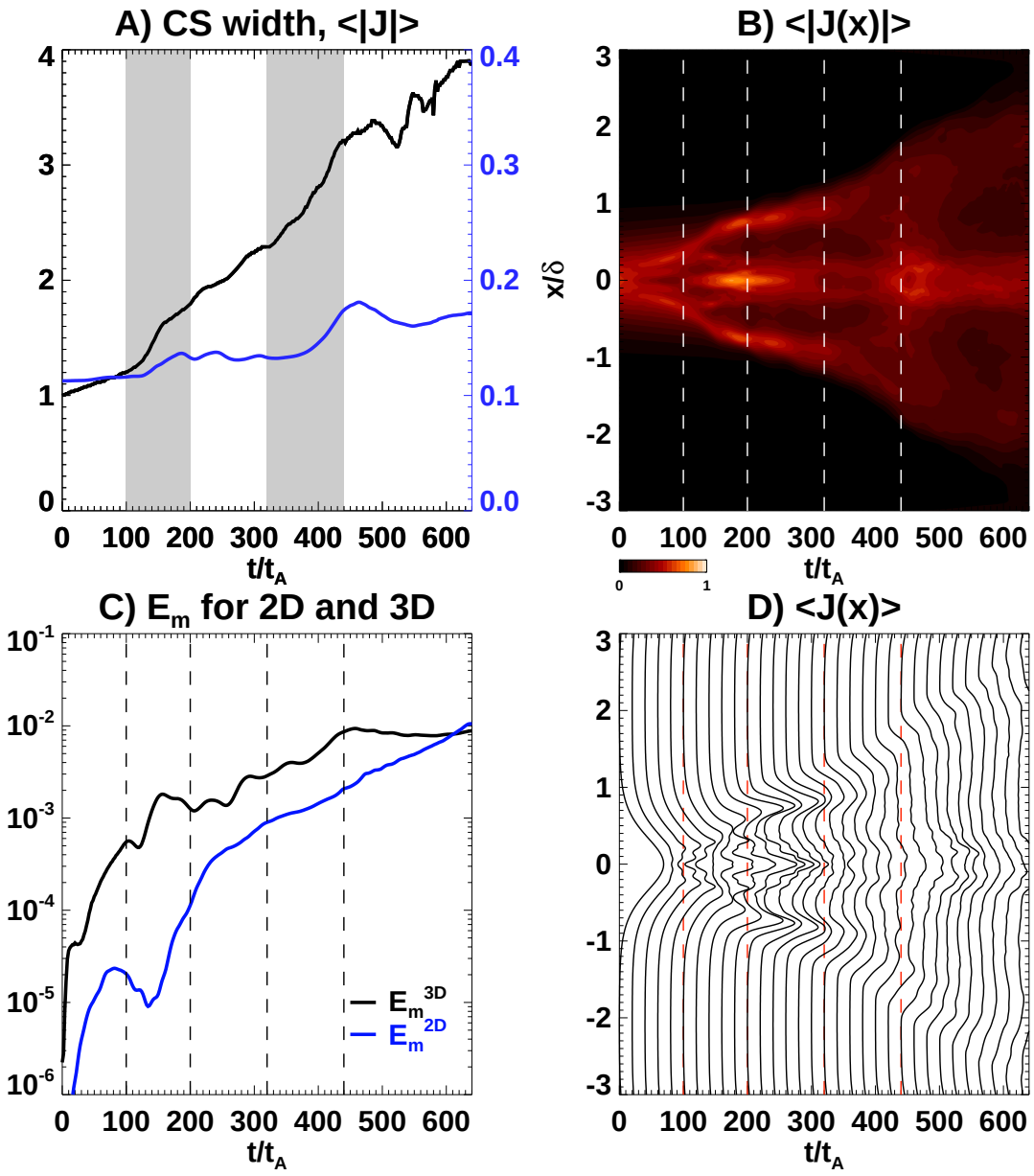

Figure 3.16: Panel A): the current sheet width (black solid line) and the spatially averaged current density in the whole simulation box. Panel B): spatially averaged current density along the x-direction. Panel C): total magnetic energy of all 3D modes (black) and 2D modes (blue). Panel D): stack plot of the spatially averaged current density as panel B). The two boost periods are labeled as the gray shaded regions in panel A), and in between the dashed lines in other panels.

diffusion regions of these modes are identified as two branches of local enhanced current density between the central strong dissipation region and the flux boundary. The strong dissipation region at the sheet center from $100t_A$ to $250t_A$ is the mixture of the remaining diffusion regions from $(3, 1)$ and $(3, -1)$, separatrix of new modes, as well as the growing 2D modes. As the system enters the relaxation period, the central dissipation region gradually fades away. The current sheet slowly expands due to the saturation of the outermost reconnection layer $(3, 5)$ and $(3, -5)$ that flux tubes untwist to relax, as can be seen from Fig.3.11. When new tearing layers grow strong enough and the system enters the second boost, local enhancements of current density near the sheet center are more complicated than the initial phase. They are composed of both 2D and 3D modes that it becomes difficult to differentiate them. As the new 3D modes are created outwardly, the current sheet expands further. The wide current sheet in the later phase has a lower current concentration anywhere across the sheet compared to the initial one (panel D)), but the integration along the x-direction gives a higher total dissipation (panel A)). The enhancement and re-distribution of current density are highly related to the creation and growth of new 3D modes.

3.5 Ubiquitously existing coupling

As we have described in Sec.3.2 and Sec.3.4, new reconnection layers are created away from the current sheet center. From Fig.3.8, some diffusion regions remain along the original resonance layers of $(3, \pm 1)$. As shown in Fig.3.1 and Fig.3.3, the original diffusion regions disappear near the anti-symmetric and the symmetric planes. It means that the coverage of the original reconnection layers shrinks along the sheet direction during the production of new reconnection layers. Moreover, apparently no direct inflow-outflow coupling exists across the sheet between the new layers (Fig.3.2). If the inflow-outflow coupling between new and old layers are piece-like, the global reconnection is highly possible to be slow. So in this section, we will identify whether the inflow-outflow coupling across the sheet globally exists after new layers are created.

In Chap.2, we used the existence of secondary tearing as a tool for detecting the effective coupling along the global guide field direction (z-direction). In this chapter, we concentrate on the local flow pattern that once a coupling of inflow and outflow exists between two modes on a certain z-plane, we label this z-plane as an inflow-outflow coupled plane. This is a more relaxed condition.

We show some examples of the inflow-outflow coupling in Fig.3.17. We identify the coupled diffusion regions on two different z-planes at two different times, selected from the first shaded region (first reconnection boost) in the left panel of Fig.3.7. The upper panels are selected at the time when the mode $(3, \pm 5)$ almost reaches its energy peak. Strong inflows and outflows eject in and out of the outermost layers formed by the new modes. The strong outflows divert and enter some diffusion regions near the center. Meanwhile, the diffusion regions near the center, which are on the original resonance layers of $(3, \pm 1)$, also build up the inflow-outflow coupling with each other across the sheet (zoom-in view in the upper right panel). In comparison, the inflow and outflow are much smaller than the new layers. In the lower panels which correspond to the end time of the first reconnection boost, the inflow-outflow couplings also exist both across the sheet and on the same side of the sheet. At this moment, the outflow from the diffusion regions near the sheet center is having almost the same magnitude as the outflow from the diffusion regions near the current sheet boundary. In the meantime, the overall reconnection efficiency reaches the first peak.

As we have shown, the inflow-outflow coupling still exists after the new layers grow. Next, we examine the distribution of the coupling along the global guide field. We identify the coupling by observing the inflows and outflows into and from the diffusion regions by eye. We trace the velocity vectors, which form streamlines, on different z-plane in and out of the diffusion regions. If the streamlines of outflow from a diffusion region on a certain mode is connected to the streamlines of inflow into another diffusion region on another mode, while the velocity across the sheet direction shows a smooth increase when leaving the diffusion region then a decrease when entering another one along the streamline, as

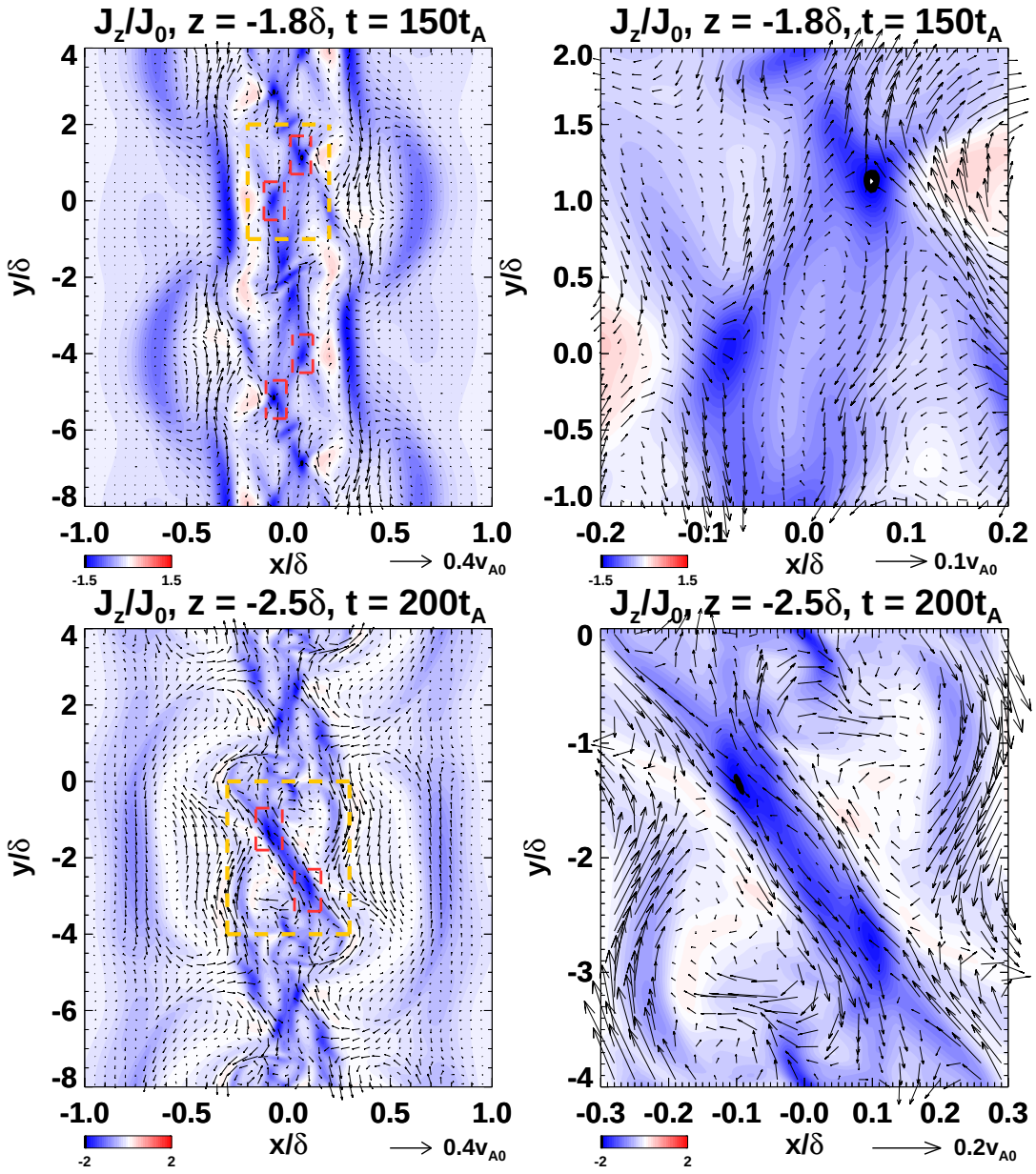

Figure 3.17: Examples of diffusion region couplings at different times. Red dashed boxes represent the coupled diffusion regions near the center. Right panels are the zoom-in view of the orange dashed boxes in the left panels. Velocity fields are overplotted as arrows onto the current density J_z contour plot. Vector scales are plotted at the bottom.

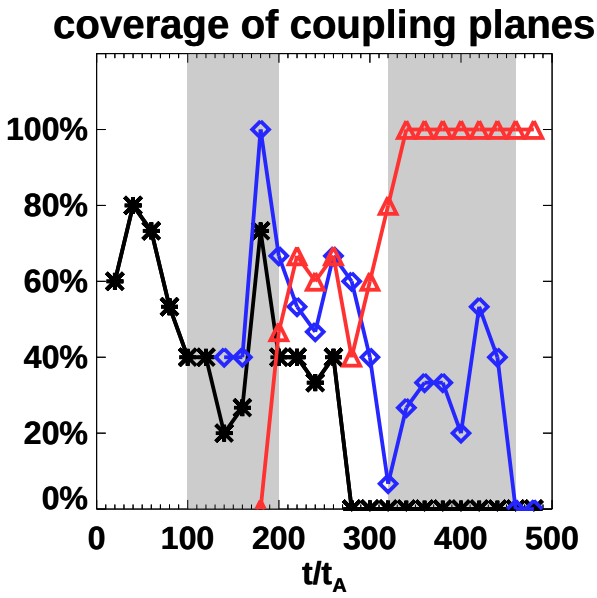

Figure 3.18: The coverage of the inflow-outflow coupling planes inside the simulation box along the global guide field direction. The black line with stars is the coverage of the coupling across the current sheet center. The blue line with diamonds is the coverage of the coupling on the same side of the current sheet. The red line with triangles is the coverage of the coupling between 2D and 3D modes.

that in Fig.2.5, we say that these two modes are coupled with each other. We are detecting the coupling only on the 2D plane instead of 3D volume for simplicity. The validation of this method was argued in Sec.2.6.1 under the assumption that the system maintains symmetric and simple. A more rigorous definition should be applied in the future.

The coverage of the inflow-outflow coupling planes in the whole box along the global guide field is shown in Fig.3.18. It is calculated as the number of z-planes along global guide field on which inflow-outflow coupling is found over the grid number N_z. Initially, the inflow-outflow coupling covers a wide area along the current sheet. It is interesting to notice that the coverage becomes smaller when secondary tearing starts to grow after $t = 50t_A$. When new modes are under production by extracting energy from the original modes, diffusion regions on the original reconnection layers disappear on some z-planes. A direct result is the shrinking of the coverage. However, as new modes have fully grown, the coverage of the inflow-outflow coupling across the center recovers and reaches the same level as the initial state. In addition, new 3D layers build up inflow-outflow couplings with old 3D layers in a considerably large area along the current sheet

during this phase, as they are more parallel to each other.

In Sec.2.6.2, we have shown the potential suppression mechanism onto 2D modes by the shear outflow from 3D modes. During the new diffusion region creation, parts of the original reconnection layers disappear (Fig.3.1 and Fig.3.3) that the suppression mechanism from 3D modes becomes weaker. Meanwhile, the new reconnection layers are too far away from each other that they cannot build up new coupling by themselves (Fig.3.1, the dependence of the coupling on the layer distance will be checked in Chap.5). Therefore, 2D modes are capable to grow. They cut off the direct potential inflow-outflow coupling between 3D modes from either side of the current sheet. So instead, the inflow-outflow coupling gradually shifts to the inflow-outflow coupling between 3D and 2D modes, in addition to the inflow-outflow coupling between 3D modes on the same side. One example of the inflow-outflow coupling between 2D modes and 3D modes are shown in Fig.3.19. In the later phase (from $t \sim 300t_A$), the coupling is dominated by 2D-3D modes inflow-outflow coupling before $t = 500t_A$. After the second boost, the outermost modes $(1, \pm 3)$ saturate. Even though the inflow-outflow coupling is still universally existing, the total reconnection rate decreases by approximately 25% as the free energy supply from the asymptotic fields are stopped.

Regarding the results above, we have confirmed that the inflow-outflow coupling is a common feature of the current sheet at any time, which is supportive for a global fast reconnection.

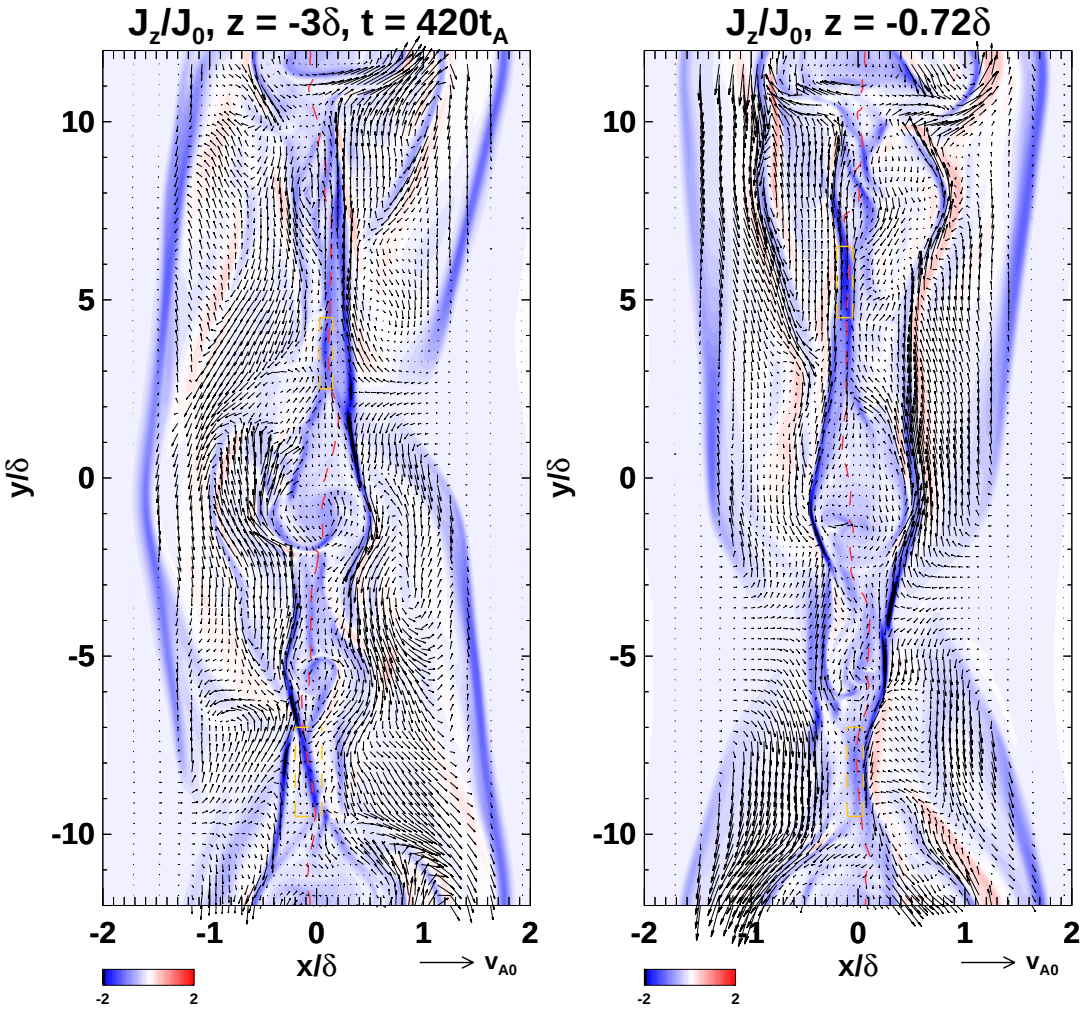

Figure 3.19: The inflow-outflow coupling between 2D and 3D modes shown by velocity vectors over current density contour plot. The resonance layer of 2D modes (B_y = 0) is plotted by red dashed line. The diffusion regions of 2D modes are labeled by orange dashed line boxes. Vector scales are plotted at the bottom.

3.6 Discussion

3.6.1 Mechanism of mode creation

From our result, we explained how new diffusion regions are created both locally and globally. New diffusion regions are growing on new energy modes which have larger wavenumbers along the global guide field than the original modes. In the following part, we will explain why these modes are selected by the system.

As we have elaborated in Chap.2, the anti-symmetric planes, which have a fast reconnection, and the symmetric planes, on which the reconnection is slow, exist along the guide field alternatively. Each type of layers influences approximately half of the box, as shown in Fig.3.18. It means that if a detector is applied onto each z-plane along the global guide field direction, the detected reconnection efficiency will change from efficient on the anti-symmetric plane to inefficient on the symmetric plane, alternatively. Since the initial modes are $(3, 1)$ and $(3, -1)$, one period is provided by each mode along the guide field inside our box. After the coupling, they produce two periods of the reconnection efficiency change along the guide field. This can be directly observed from panel A) of Fig.2.4 that the diffusion line width has two periods of change along the guide field direction. This change of the reconnection efficiency corresponds to the new mode $(0, 2)$, which is along the global guide field.

Next, we consider how magnetic field lines are absorbed into this system, as shown in Fig.3.20. In this case, we only consider the field lines on the $-x$-side due to the rotational-symmetry. As the reconnection proceeds on two initial reconnection layers, field lines in further places are absorbed closer to the sheet center from either side of the current sheet. Meanwhile, the reconnected flows are ejected from the flux tubes and go in the opposite direction of the field lines absorption across the lateral boundary of the flux tube. Therefore, field lines are being absorbed while being rejected, which can be seen from the color of v_x on the surface of the contour plot. Due to the inflow-outflow coupling, field lines just outside of the anti-symmetric planes are absorbed in faster, while field lines

near the symmetric planes are approaching the current sheet more slowly. As a result, the whole system is more or less under the control of the anti-symmetric planes as they provide stronger flow. The summarized flow pattern mainly due to the anti-symmetric planes is shown as the cartoon in the upper panel of Fig.3.20. The stronger inflows (red dots) are along the diffusion lines (thick red lines). The stronger outward flows (blue dots) are along the flux tubes. As a whole, they form a check structure near the sheet surface along the current sheet. It indicates that, if the field lines correspond to a certain mode are uniformly absorbed by the red dots and avoid all blue dots along the current sheet, the correspondent mode can grow due to the resonance. If field lines are absorbed by red dots at some positions but pushed out by the blue dots somewhere else, the correspondent mode cannot grow. Thus generally speaking, the possible modes are categorized into favorable modes and unfavorable modes, as shown in the lower panel. The predicted diffusion line position is the same as the simulation shows (Fig.3.6).

Because new field lines from the outer side are always having larger tilting angles compared to the initial perturbed modes, an increase of the wavenumber along the anti-symmetric field direction (y-direction) is less preferred to an increase of the wavenumber along the guide field direction (z-direction). As the new modes have larger values of $|n|$, the wavelengths of the new modes are monotonically decreasing, which it can be seen from the distance between the diffusion lines. The direct result of the shrinking wavelength is the decreasing diffusion region length on the new reconnection layer, as the diffusion region length is approximately half of the wavelength. The local reconnection rate in a diffusion region is linearly scaled with the diffusion region aspect ratio d/l, where d and l are the diffusion region width and length. So a shrinkage of the wavelength, together with an increase of the diffusion region width due to the coupling (Appendix.E), the local reconnection on the new modes is considered to be fast once the inflow-outflow coupling is built up across the whole sheet.

As we have shown that the selection is mediated by $(0, 2)$ mode, it is expected that the energy transfer path involves $(0, 2)$ is also important. From Fig.3.9, the energy transfer

into $(3,3)$ from the path $(3,1)+(0,2)$ gives a considerable contribution. On the other hand, the energy transfer from $(3,3)+(0,2)$ into $(3,5)$ becomes negative (cannot be shown in the logarithmic scale) from $50t_A$. In comparison, the energy transfer through $(3,1)+(0,4)$ is large, where $(0,4)$ is the second harmonic of $(0,2)$.

Although the dominant energy transfer does not necessarily go through $(0,2)$ or $(0,4)$, the above consideration may be understood as a geometrical constraint that the modes generated by nonlinear mode couplings must satisfy. When the system has an open boundary condition, the selection might change and remains an open issue by far.

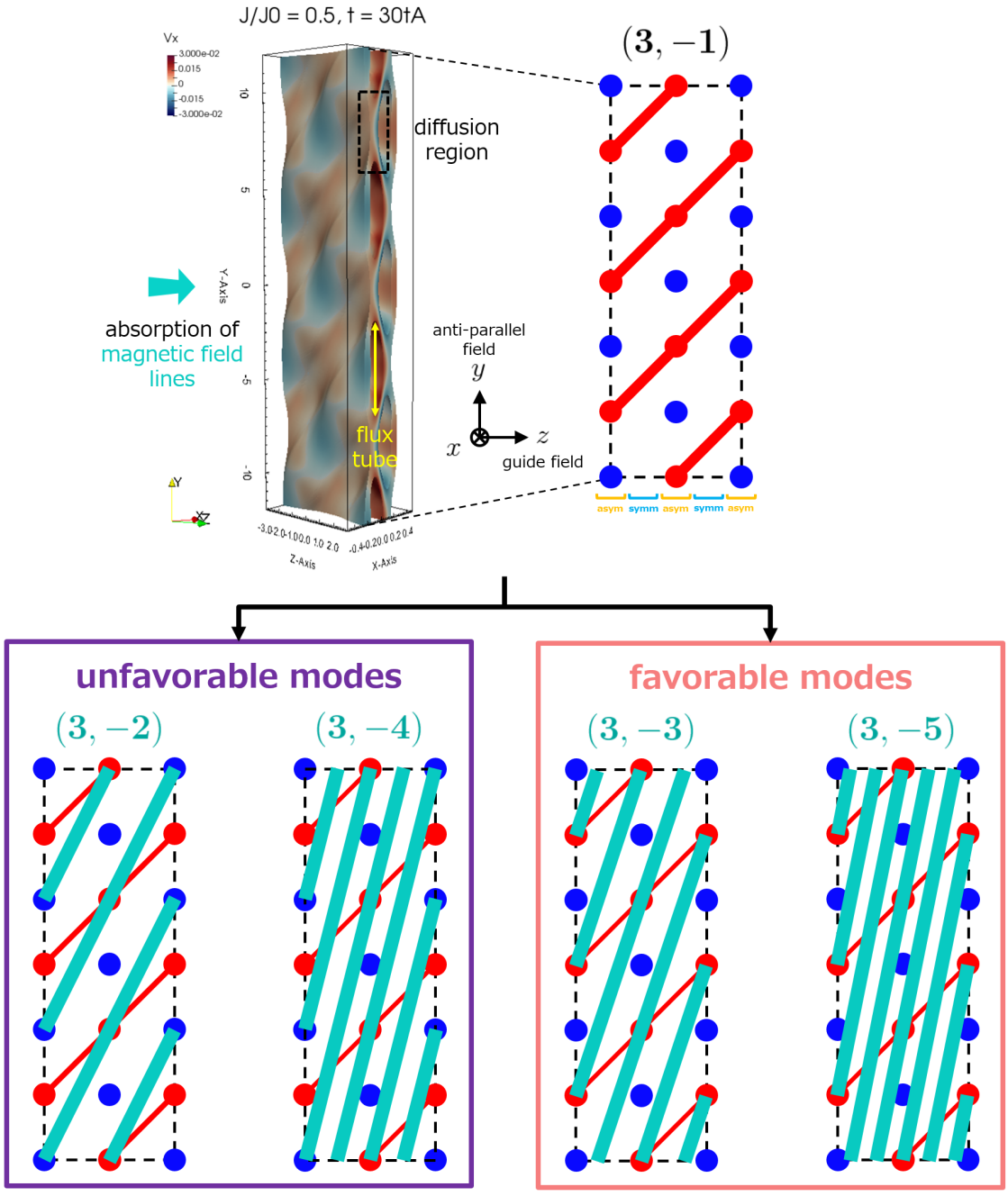

Figure 3.20: Explanation of new modes creation. Upper panel: the current density J isosurface represents the flux tube surfaces with diffusion regions. The color on the surface is the strength of the flow v_x into and out of the surface. The cartoon on the right shows the characteristic pattern of this flow. Red and blue dots are the positive and negative v_x on the surface from the left isosurface plot. Thick red lines are the diffusion lines of tearing mode $(3, -1)$. The enhanced v_x are localized on the anti-symmetric planes. Bottom panel: unfavorable modes and favorable modes of this system. The turquoise lines are the correspondent mode's diffusion lines.

3.7 Summary

In this chapter, we studied how and where new reconnection layers are created, in addition to how the global reconnection rate increases.

We first examined the production of new diffusion regions in the double-layer simulation $(3, \pm 1)$ (Sec.3.2), both locally (Sec.3.2.1) and globally (Sec.3.2.2). In the local view, secondary tearing is triggered due to the inflow-outflow coupling on the anti-symmetric plane. The partitioned diffusion regions open a vent that reconnected field lines are ejected outwardly and collide with free field lines thus create a new diffusion region in front of the original one (Fig.3.1 and Fig.3.2). Since the reconnection is faster on the anti-symmetric planes compared to the symmetric planes, the field lines exhibit a strong non-uniformity along the guide field direction. The parts of field lines that reconnect earlier stretch the other parts that have not participated reconnection outwardly and form new diffusion regions in front of the disappearing original diffusion regions (Fig.3.3 and Fig.3.4). Since the other part of the simulation box possesses both the characters from these two planes, they also produce new diffusion regions that are closer to the asymptotic magnetic fields. So a new sheet-wise extending reconnection layer is created on either side of the current sheet outwardly (Fig.3.6). By checking the energy spectrum (Fig.3.7) and the resonance factor q (Fig.3.8), we found that the new layers are the mixture of new energy modes $(3, \pm 3)$ and $(3, \pm 5)$, which have larger wavenumbers along the global guide field direction compared to the initial perturbed modes $(3, \pm 1)$.

For a better understanding of the creation of new modes, we calculated the energy transfer rate, together with the dissipation rate, of new energy modes in Sec.3.3. It is found that the energy transfer from the initial energy modes and their higher order harmonics are important to produce new energy modes outwardly (Fig.3.9), while the higher order harmonics are related with secondary tearing that is triggered by the inflow-outflow coupling. These energy transfer paths continuously pour energy into new modes which were not preferred by the initial current sheet. After the new modes are forced to grow beyond a certain threshold, they are capable to grow by themselves and consume the energy

from the background current.

By examining the energy change in Sec.3.4, it is confirmed that the reconnection has a boost when there exists a creation of new 3D modes outwardly across the current sheet (Fig.3.10, Fig.3.12, Fig.3.13, Fig.3.14). In between the two energy boosts, the current sheet reorganizes that the previous flux tubes untwist and re-twist to produce new flux tubes, which shows similar feature as the coalescence instability (Fig.3.11). The energy transfer is clear on the 2D magnetic energy spectrum that the energy is transported approaching the asymptotic magnetic field (Fig.3.15). The dissipation of 3D modes dominates in the process while the current sheet expands as 3D modes grow further away from current sheet center (Fig.3.16).

Then we checked whether the inflow-outflow coupling between new and original diffusion regions, namely the coupling between new and original reconnection layers, is always globally existing (Sec.3.5). It can be seen that after new reconnection layers are created, they also build up the inflow-outflow coupling with the original layers, while the original layers maintain the inflow-outflow coupling across the sheet center (Fig.3.17). The coverage of the inflow-outflow coupling becomes sufficiently large along the sheet when new modes are growing, which suggests an increasing global reconnection (Fig.3.18). In the latter phase, the inflow-outflow coupling between 2D and 3D modes becomes dominant (Fig.3.19). The globally existing inflow-outflow coupling supports a fast overall reconnection.

The physical understanding of how the new modes are chosen by the system is given that the original inflow-outflow coupling pattern mediates the absorption of new field lines (Fig.3.20).

The conclusion based on our studies by far is that the globally distributed coupling across the current sheet and the existing of sheet-wise extending reconnection layers near the asymptotic magnetic fields increase the global reconnection rate. However, a rotational-symmetric initial condition is assumed from the beginning. In order to generalize our argument, different initial conditions should be considered. In the next chapter,

we are going to examine the application of our hypothesis by varying the initial setup to make a general conclusion.

Chapter 4

Result III: random perturbation case

Our present understanding of the fast 3D reconnection bases on the development of a current sheet with a specific initiation. In order to approach the realistic system, we change the initial perturbation to a more general form to consolidate our conclusion.

4.1 Introduction

In Chap.2 and Chap.3, we examined in detail the local effect as well as the global consequences from the tearing layer coupling across an extending current sheet with a finite guide field. We found that when the sheet-crossing inflow-outflow coupling is ubiquitously distributing along the current sheet, the global reconnection accelerates. Our conclusion based on the simulation that starts with a pair of rotational-symmetric tearing layers. This simple configuration is convenient for the local analysis but limits the application.

The perturbation in a real system is arbitrary. The introduction of a random initial perturbation mimics the realistic environment, such as the persistent ejection of MHD waves from the photosphere that initiate reconnection in the higher atmosphere on the Sun. In previous studies (Landi et al., 2008; Wang et al., 2015), multiple 3D tearing layers (more than 2) are found in the initial state under random perturbation. Although an increasing reconnection rate was observed, we have not tried to push further the analysis

due to the complicated and chaotic structures in the turbulent state (Wang et al., 2015).

The results from our typical double-layer simulation which starts from a symmetric and simple structure give a clear guideline to the understanding of a more complex system. So in this chapter, we will re-examine the system development in the random perturbation simulation to confirm our arguments in previous chapters. We will continue to concentrate on the development of a slab-like magnetic structure for simplicity.

4.2 Simulation setup

The simulation setup is the same as that in Sec.2.4. The initial perturbation is changed to a random perturbation on the velocity fields, while all components are smaller than $0.01v_{A0}$. Compared to our previous study (Wang et al., 2015), the resolution becomes higher and no wave filter on the initial perturbation is applied in the present study.

4.3 Result

By applying random perturbation on the velocity field, multiple tearing layers grow in the current sheet. We calculate the mode energy density along the x-direction by using Eq.(2.39) that

$$\tilde{E}_m(x,m,n) = \frac{|\tilde{\mathbf{B}}(x,m,n)|^2}{8\pi}. \tag{4.1}$$

The results at $t = 200t_A$ on different x-slices are shown in Fig.4.1. There exist roughly 2 layers on either side of the current sheet, while asymmetry is exhibited in our system. The outer layers are growing with $q = \pm 4$ (black dashed lines) weakly, while the inner layers are dominated by $q = \pm 8/3$ (red dashed lines). Precisely speaking, many modes with different q are growing near $q = \pm 8/3$ in parallel, while having similar tilting angles with each other.

As the modes on the same side are close to each other, they couple more effectively than the modes couple across the current sheet center in the early stage. The coupling has

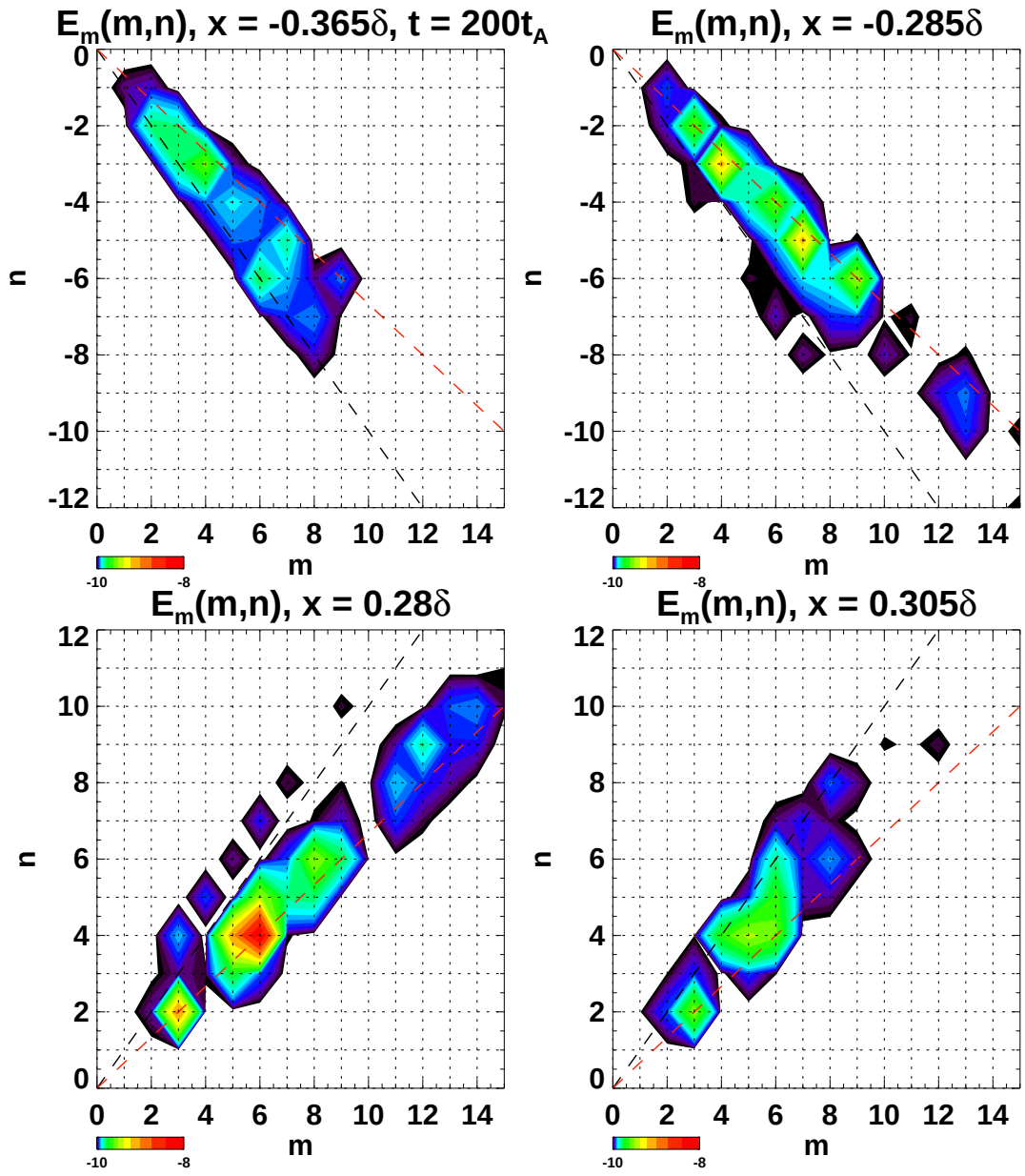

Figure 4.1: Magnetic energy density of modes on different x-slices at $t = 200t_A$. The black dashed lines represent $q = \pm 4$ while the red dashed lines represent $q = \pm 8/3$. Colors are in the logarithmic scale.

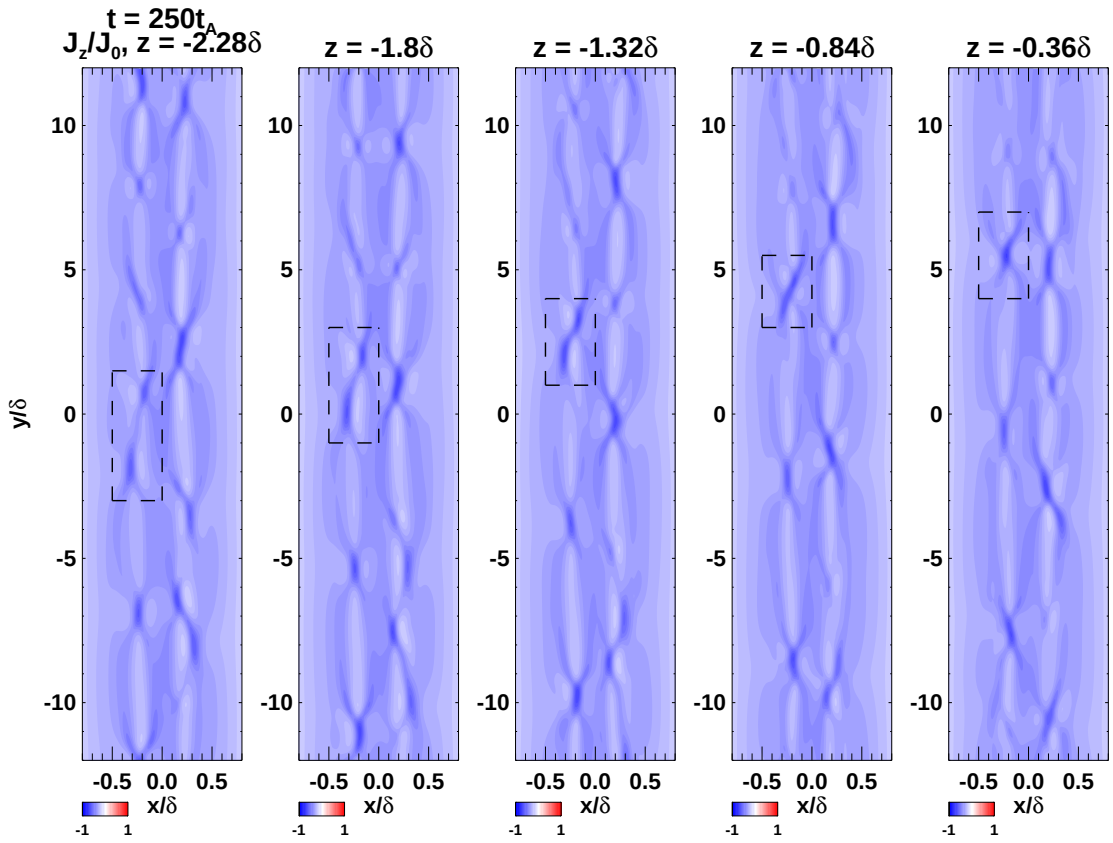

Figure 4.2: Diffusion region distribution on 2D planes across the global guide field in the early phase. Two modes merge into one diffusion region when they are close and in phase, as labeled inside the dashed line box on the current density J_z contour plot.

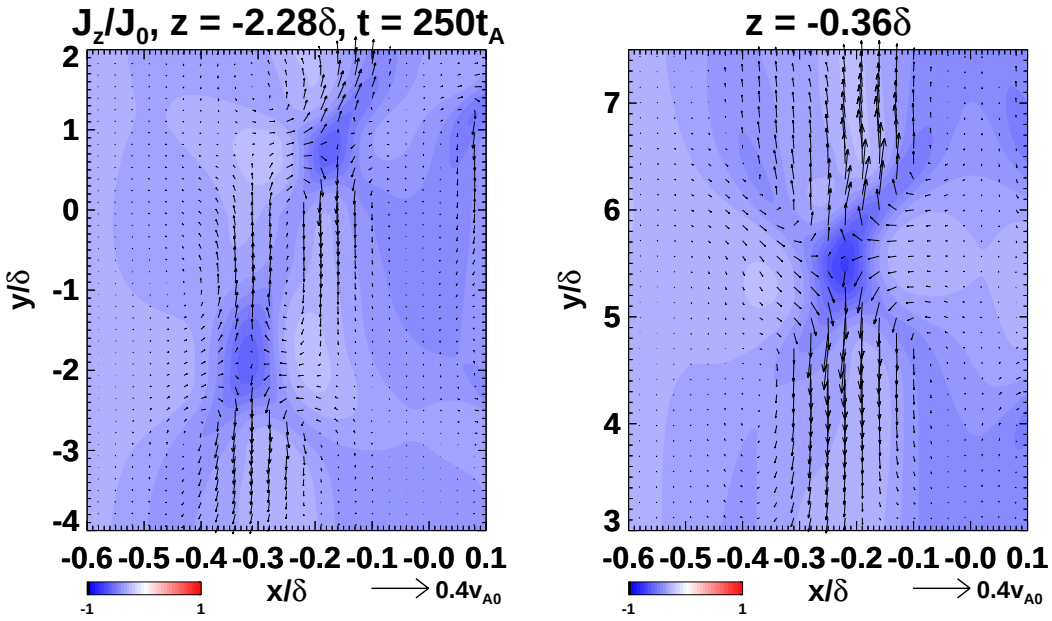

Figure 4.3: The local coupling between modes on different z-planes at $t = 250t_A$ by showing the velocity fields as vectors on the current density J_z contour plot. The left panel is the enlarged view of the box in the left-most panel of Fig.4.2. The right panel is the enlarged view of the box in the right-most panel of Fig.4.2. Vector scales are plotted at the bottom.

two types. One is the inflow-outflow coupling as what we have discussed in Chap.2. It can exist when the two modes have a phase difference on a certain z-plane, such as the left three panels in Fig.4.2. The flow pattern of the box region in the left-most panel of Fig.4.2 is re-plotted in the left panel of Fig.4.3. A clear coupling flow can be observed. Another type of the coupling is the coalescence of diffusion regions. When two diffusion regions are very close to each other side by side, say the distance is smaller than the tearing parameter $1/\Delta'$, they degenerate into one and reconnect fast due to the contribution from two modes simultaneously. In the right panel of Fig.4.3, we show the enlarged view of the box in the right-most panel of Fig.4.2. It can be seen that the localized current density inside the diffusion region in the right panel is even larger than the left panel. Thus as a whole, tearing layers on both sides of the current sheet accelerate the reconnection by coupling.

One direct result of the inflow-outflow coupling is the trigger of secondary tearing. On the other hand, the coalescence of diffusion regions on adjacent tearing modes is

also likely to trigger secondary tearing as the piling-up magnetic fields are roughly doubled. We select two planes and find that the emergence of secondary tearing becomes a common feature in the whole box. Some examples of secondary tearing are selected in Fig.4.4. As we have discussed in Sec.3.2.1, secondary tearing will open a vent for the current sheet and create overlying diffusion regions by changing the flow. Due to the turbulent Alfvénic flows generated by the outflows from diffusion regions, in addition to the existence of multiple layers, it is very difficult to identify a clear picture as we did in Sec.3.2.1. Still, we find a diffusion region that is created when secondary tearing is triggered in this turbulent state that possibly supports our previous result.

In our argument, energy modes with higher wavenumbers along the guide field direction are created due to the nonlinear coupling, during which higher order harmonics of the pre-existing modes are participating actively across the current sheet. As secondary tearing emerges all over the simulation box, it indicates that the higher order harmonics with shorter wavelengths are flourishing. Then the new modes are expected to be created outwardly, but with very complicated processes. In order to identify the correspondent new modes in the reconnection, we calculate pseudo flux function $\psi^*_{(m,n)}$, which mimics the toroidal flux in tokamaks and RFP numerical simulation analysis. We first rotate the coordinate into Eq.(2.8) and consider only B_k, since it is the component that participates the reconnection. Then we calculate the magnetic field $B_{k,(m,n)}$ for a certain mode (m,n) in the Fourier space as

$$\tilde{B}_k(x,m,n) = \frac{1}{L_y L_z} \int_{-\frac{L_z}{2}}^{\frac{L_z}{2}} \int_{-\frac{L_y}{2}}^{\frac{L_y}{2}} B_k(x,y,z) e^{-i(k_y y + k_z z)} dy dz \tag{4.2}$$

then convert it back into real space that

$$B^*_{k,(m,n)}(x,y,z) = \frac{4\pi^2}{\Delta y \Delta z} \int_{-\frac{\pi}{\Delta z}}^{\frac{\pi}{\Delta z}} \int_{-\frac{\pi}{\Delta y}}^{\frac{\pi}{\Delta y}} \tilde{B}_k(x,m,n) e^{i(k_y y + k_z z)} dk_y dk_z. \tag{4.3}$$

The pseudo flux function is calculated by integrating B_k^* along the x-direction that

$$\psi^*_{(m,n)}(x,y,z) = \int_{-\frac{L_x}{2}}^{x} B^*_{k,(m,n)}(x',y,z)dx'. \tag{4.4}$$

In 2D-space, the contour lines of flux function represent the magnetic field lines. In 3D-space, the coherency of the flux surface is not always guaranteed thus the definition of flux function is not precise. However, we will only use this variable as a guideline to find the mode that participates reconnection. We use "X-point" and "O-point" to label the positions where diffusion region and flux tube center are likely to be produced by a certain mode.

In the lower right panel of Fig.4.4, we identified a secondary tearing structure inside the red dashed line box centers at $(x,y,z) = (0.2\delta, 4.5\delta, 0)$. Just on the right of this box, there seems to grow a new diffusion region near $(x,y,z) = (0.4\delta, 4\delta, 0)$. So we track the growth of this new diffusion region along time in Fig.4.5. At $t = 250t_A$, we find that the energy mode $(3,2)$ corresponds to the diffusion region inside the box region. By plotting the contour lines of the pseudo flux function of $(3,2)$ over the current density J_z, the "X-points" and "O-points" match with the positions of diffusion regions and flux tube structures respectively on both the cuts of $y = 0$ and $z = 0$. At $t = 300t_A$, as secondary tearing develops, new diffusion region like features appear near $(x,y,z) = (0.4\delta, 4\delta, 0)$ on the left middle panel and also near $(x,y,z) = (0.4\delta, 0, 0.8\delta)$ on the right middle panel. We notice that they co-locate with "X-point" of a new mode $(3,4)$. The correspondence eventually grows clearer that three and four flux tubes can be observed on $y = 0$ plane (left bottom panel) and $z = 0$ plane (right bottom panel) at $t = 380t_A$.

It seems that new reconnection layer that corresponds to a larger wavenumber along the global guide field is created, which is consistent with our previous result. We next confirm whether it is a common feature in the global view and whether the overall reconnection rate increases. We plot the total kinetic energy by Eq.(3.20) and the total reconnection rate calculated by Eq.(3.21), together with the mode magnetic energy calculated by Eq.(2.39) on either side of the current sheet in Fig.4.6. Similar to the result

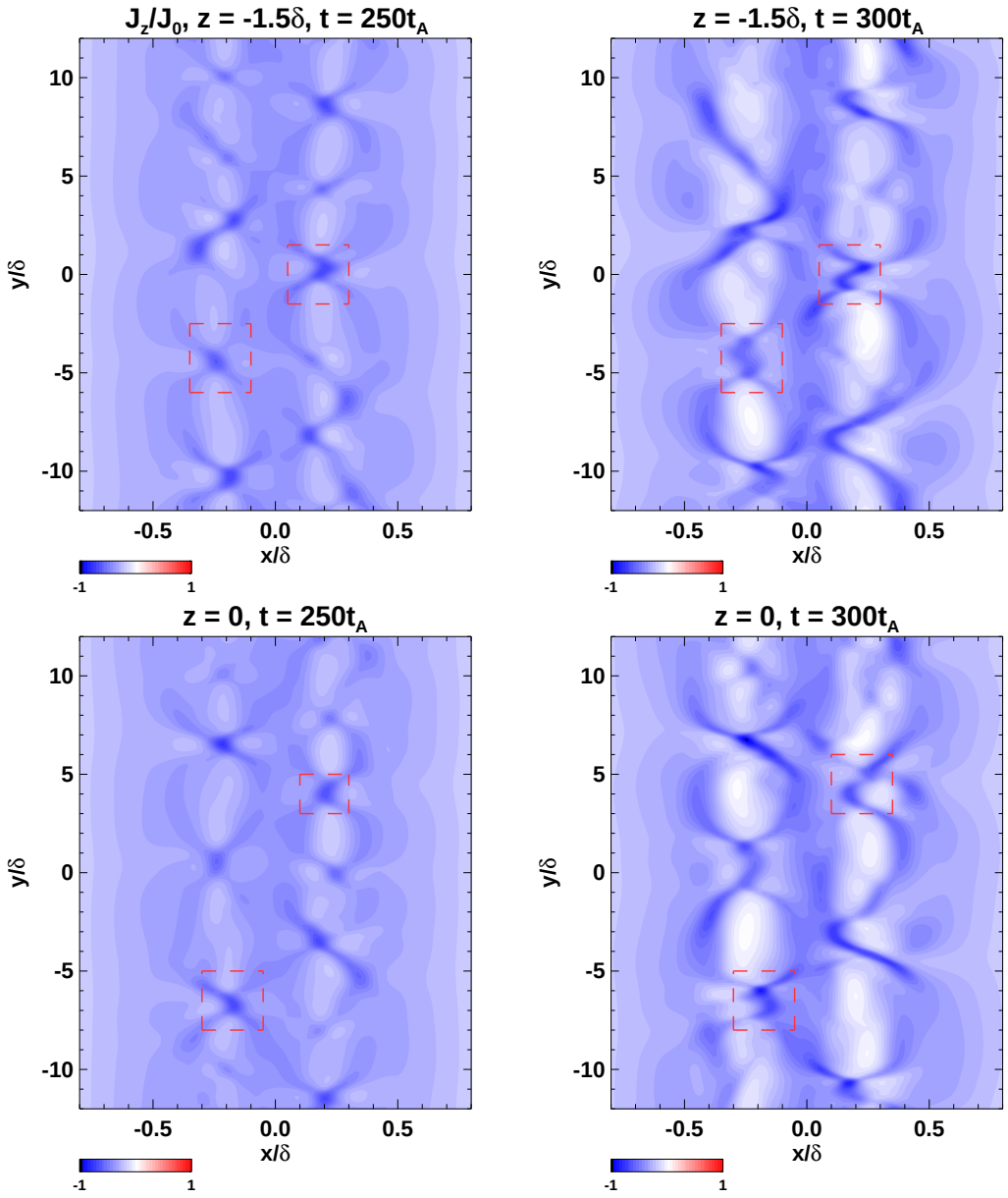

Figure 4.4: Examples of secondary tearing (labeled by red dashed line box) by showing current density J_z contour plot at different times on selected planes.

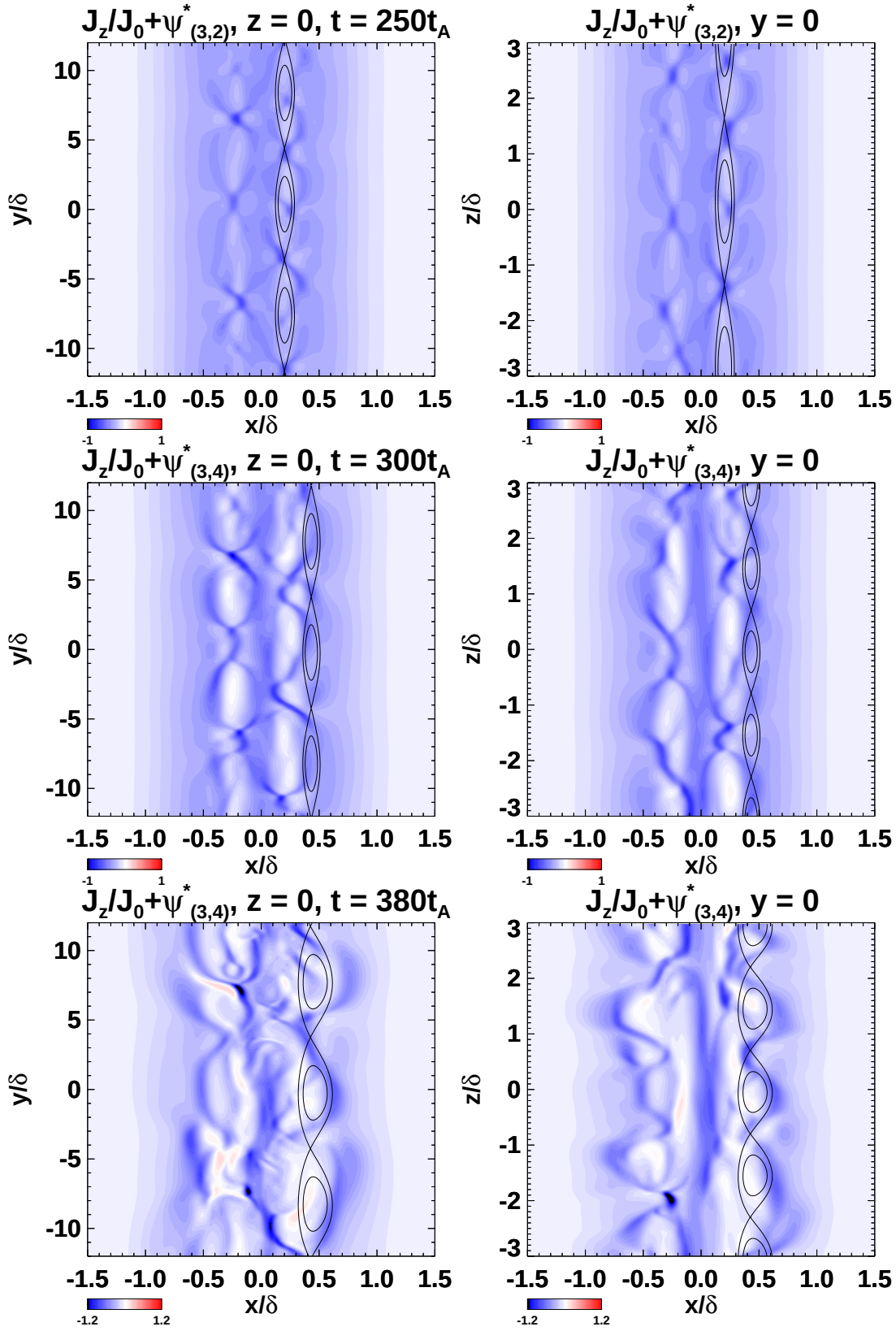

Figure 4.5: Current density J_z contour plot at different times. The left panels are cuts on $z = 0$ plane, while the right panels are cuts on $y = 0$ plane. Pseudo flux functions of modes $(3, 2)$ and $(3, 4)$ are overplotted as black contour lines.

in Chap.3, we find roughly two boosts in the reconnection rate development. The first one starts from $200t_A$ to $500t_A$ and the second one starts from $600t_A$ to $800t_A$. Since asymmetry appears in our system, we will discuss each side independently.

When the first boost initiates, multiple modes on both sides of the current sheet grow strong enough that they start to form the inflow-outflow coupling across the whole current sheet as we described above. Some examples of the inflow-outflow coupling are shown in Fig.4.7. After entering the first boost, a change of mode from $(2, -1)$ to $(2, -4)$, afterwards the lower harmonic $(1, -2)$, are found on the negative x-side. While on the positive x-side, a more complicated energy transfer is found. At first, there is a clear change from mode $(3, 2)$ to $(3, 4)$, as we have shown in Fig.4.5. Afterwards, a new mode $(2, 3)$ grows but is overcome by $(1, 1)$. Around $t = 500t_A$, mode $(2, 5)$ grows over $(1, 1)$ in a short period. In the second boost, $(1, -1)$ exceeds $(1, -2)$ in the negative x-side which shows a reversed trend compared to our previous study. However, an energy transfer path from $(1, 1)$ to $(1, 2)$ and finally $(1, 3)$ is shown in the positive x-side. In general, the energy transfer along the global guide field is a common process that correlates with the global reconnection rate enhancement.

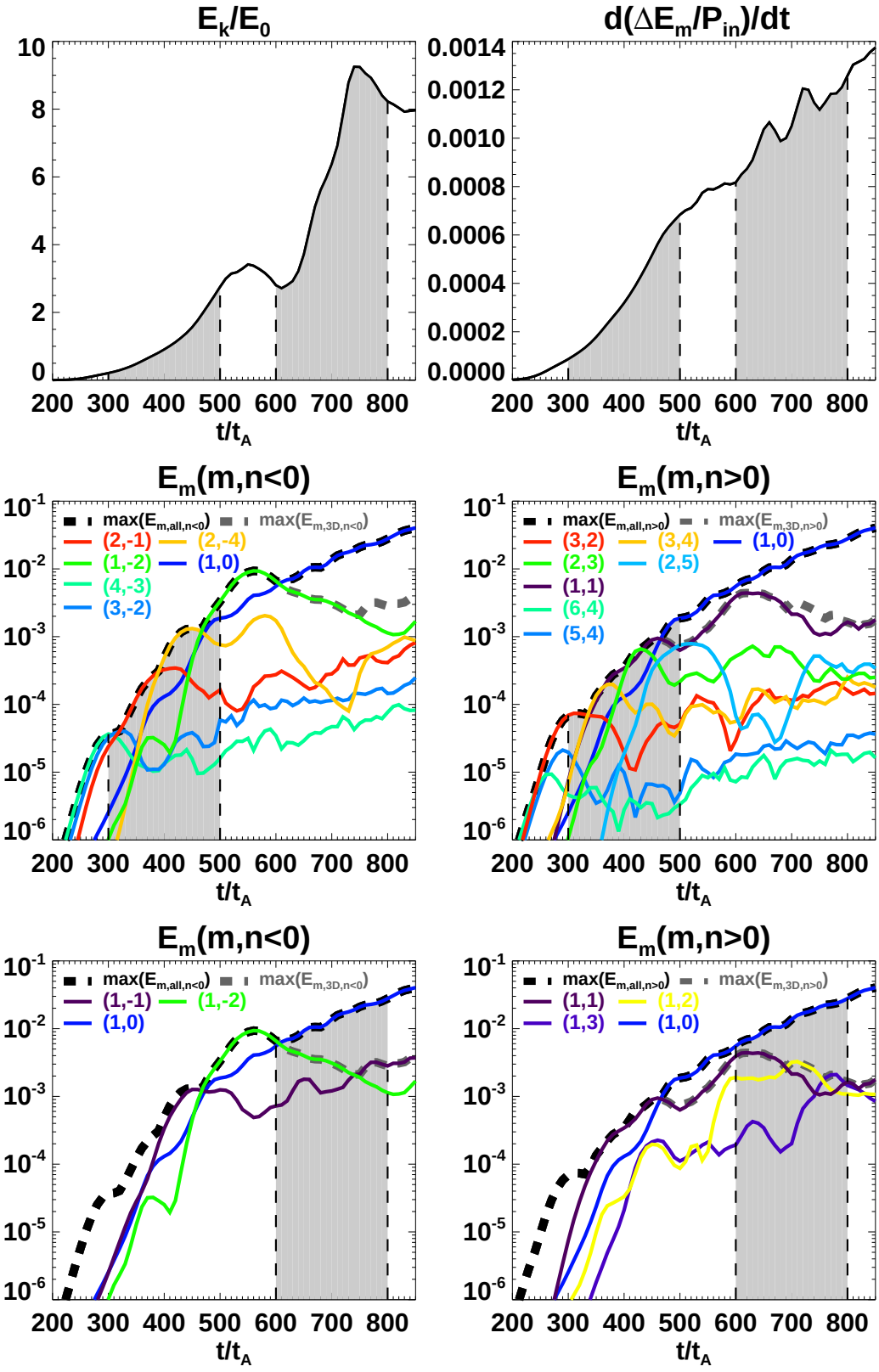

Figure 4.6: Total energy change and mode energy in the random perturbation simulation.

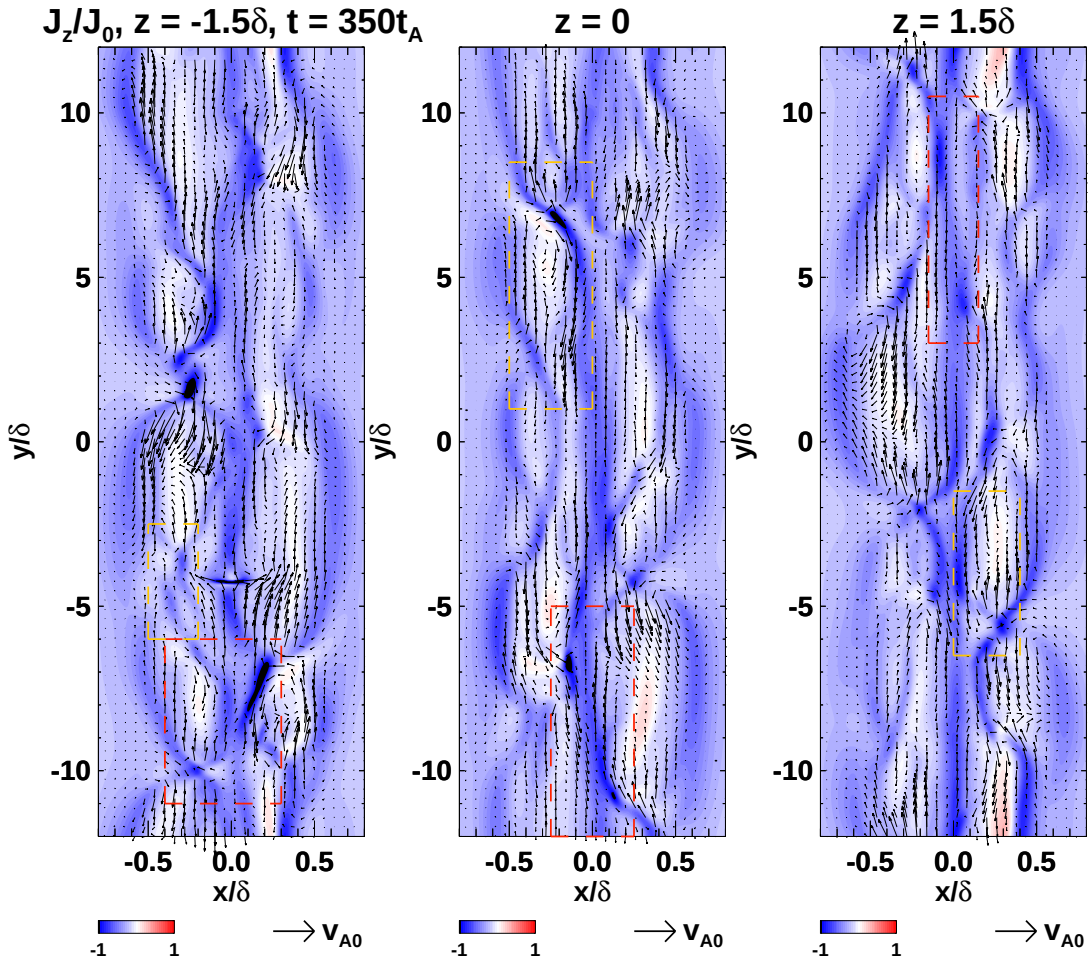

Figure 4.7: Velocity fields overplotted on the current density J_z contour plot as vectors on different z-planes at $t = 350t_A$. The inflow-outflow coupling across the current sheet is labeled by red dashed line boxes, while the coupling on the same side of the current sheet is labeled by orange dashed line boxes. Vector scales are plotted at the bottom.

4.4 Discussion

The loss of symmetry makes the analysis in the random perturbation simulation much more difficult. However, the basic process seems to be consistent with our previous results and arguments in the double-layer simulation. There are several extra comments we want to touch.

First of all, the emerging modes are not what we have found in the linear analysis. After we apply the random perturbation, it takes $50t_A$ for the system to reorganize. Then 3D modes start to grow first while the 2D mode such as $(1, 0)$ starts to grow exponentially after $180t_A$. During the reorganization phase, the background changes thus probably regulates the most unstable tearing modes. On the other hand, the emerging modes are not allowed by the linear theory. The reason is unclear now that further study should be done.

The second issue is the acceleration time of each boost. In the random perturbation simulation, multiple layers (more than 2) emerge and expand roughly from $x = -0.3\delta$ to 0.3δ across the current sheet. The double-layer simulation $(3, \pm 1)$ has only two layers initially and the layers expand from $x = -0.07\delta$ to $x = 0.07\delta$. Regarding this, we were expecting a faster reconnection rate enhancement in the random perturbation simulation than the double-layer simulation, as the layers are widely distributed. By comparing Fig.3.10 and Fig.4.6, we notice that the acceleration of the overall reconnection rate is slower in the random perturbation simulation. The two boosts in the double-layer simulation $(3, \pm 1)$ take $100t_A$ to increase the overall reconnection by ~ 0.0006 and ~ 0.001. The two boosts in the random perturbation simulation take $200t_A$ to increase the overall reconnection by ~ 0.0006 and ~ 0.0004. The final reconnection rate is in the same magnitude for these simulations. One possibility is that the emerging modes in the random perturbation simulation have much smaller wavelength compared to the applied modes in our double-layer simulations. Therefore it takes time to build up an efficient inflow-outflow coupling across the sheet center, although the inflow-outflow coupling on the same side is effective from the start. As we have emphasized in Chap.3, the successive

inflow-outflow coupling that connects the anti-parallel magnetic fields from either side of the current sheet is important to enhance the overall reconnection. So this result seems to be consistent with our argument. We expect that the longer the wave modes emerge in the linear phase, the faster the overall reconnection rate increases. This should be checked with a larger system in the future.

A related issue is the reconnection rate difference in the two boosts. In our double-layer simulation, the second boost gives a higher enhancement of reconnection rate, while it is reversed in the random perturbation case. It is possible that in the second boost of the random perturbation case, only the modes on the positive x-side are transferring the energy into modes closer to the asymptotic field, while the most energetic mode on the negative x-side shrinks back into inner layer (from $(1, -2)$ to $(1, -1)$). In that case, the inflow-outflow coupling does not cover across the whole current sheet, so less acceleration in the overall reconnection rate is obtained.

Finally, we discuss the suppression mechanism of 2D modes under the influence of 3D modes in the random perturbation case. In Fig.4.6, the 2D mode $(1, 0)$ grows faster than that in the double-layer simulation and becomes predominant in the whole current sheet from $600t_A$. This growth seems to contradict to our previous argument in Sec.2.6.2. We plot again the mode energy of $(1, 0)$ in Fig.4.8 and compare it to the mode energy of $(1, 0)$ in a 2D random perturbation simulation where 3D modes cannot grow. The initial perturbation in the 2D random perturbation simulation contains only 2D modes, while the amplitudes and phases of these 2D modes are the same as that in the 3D random perturbation simulation.

From panel A), both 3D and 2D simulations show a re-organization period at the beginning phase. During this phase, the current sheet grows thicker due to the global diffusion. Therefore, the expected growth rate of $(1, 0)$ is smaller than that in the initial current sheet, as the current density becomes weaker. However, $(1, 0)$ grows in the same magnitude as the linear growth rate in the initial current sheet (black dashed line) in the 3D simulation. In comparison, $(1, 0)$ grows much slower in the 2D simulation. As it can

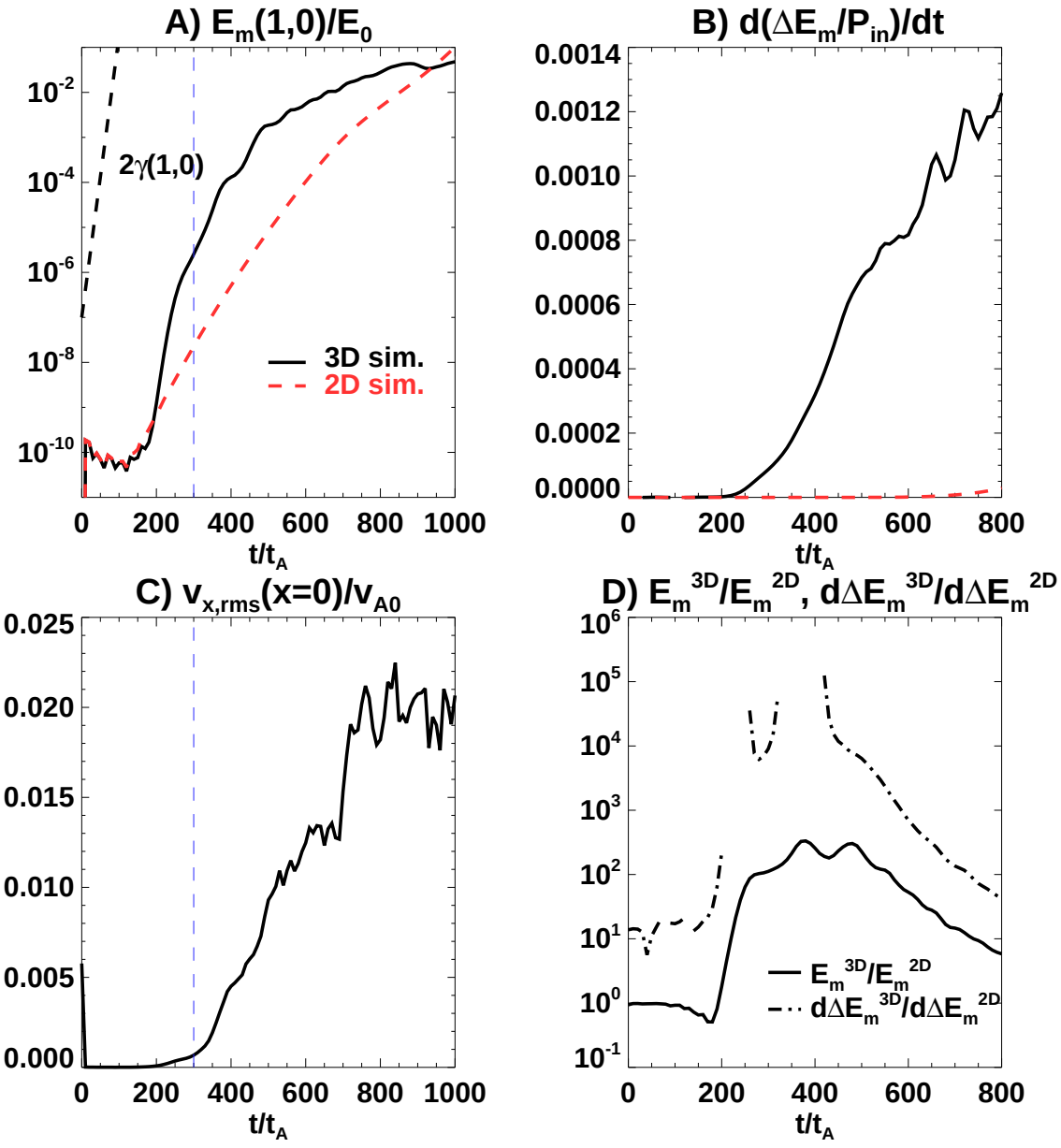

Figure 4.8: Panel A): mode energy of $(1,0)$ in the 3D (black thick line) and the 2D random perturbation simulations (red dashed line). The linear growth rate of $(1,0)$ in the initial current sheet is overplotted as the black dashed line. Panel B): overall magnetic energy conversion rate in the 3D (black thick line) and the 2D random perturbation simulations (red dashed line). Panel C): root-mean-square of v_x on $x = 0$ plane. Panel D): ratio of $(1,0)$ mode energy (solid line) and the magnetic energy conversion rate (dot-dash line) in the 3D and the 2D random perturbation simulations.

be seen in Fig.4.5, in the initial phase of the 3D perturbation, 3D modes are growing on either side of the current sheet rather independently. At this moment (before $t = 300t_A$), the interaction between two sides is very weak, which can be seen from the root-mean-square of v_x right at the current sheet center in panel C). If 3D modes on either side of the current sheet grow strong enough, there should exist a sufficient amount of flow that goes through the sheet center. From panel C), it is shown that it takes hundreds of Alfvén time for $v_{x,rms}$ to grow up to $10^{-3}v_{A0}$. During this phase, 3D modes on either side are coupling by themselves and pour energy into not only 3D modes but also 2D modes due to the nonlinear coupling. Especially that the number of activated modes in the random perturbation is much more than that in the double-layer simulation, the number of energy transfer paths should be much abundant. Therefore, 2D modes are receiving energy from both sides as 3D modes are far apart thus grow rapidly. It explains why $(1, 0)$ is growing faster in the 3D simulation than that in the 2D simulation.

When 3D modes grow large enough, they obtain large amplitude of energy that they eject fast outflow to form local shear flows across the current sheet center, which is observed as a sufficiently large $v_{x,rms}$. Then 3D modes reversely suppress the growth of $(1, 0)$ that the growth rate of $(1, 0)$ decreases roughly from $t = 350t_A$, as we argued in Sec.2.6.2.

The total magnetic energy conversion rate in the 3D simulation is much faster than the 2D case, as shown in panel B). To take a better look, we also plot in panel D) the ratio of the mode energy of $(1, 0)$ in the 3D simulation over that in the 2D simulation and the total magnetic energy conversion rate ratio in the 3D simulation over that in the 2D simulation. There is at least one order of magnitude difference between the energy conversion rate ratio and the mode energy ratio. It means that 3D modes contribute significantly in enhancing the magnetic energy dissipation in the 3D random perturbation case that only 2D modes cannot explain.

4.5 Summary

In this chapter, in order to approach the realistic system in various astronomical events, we change the initial perturbation into random velocity fields to understand how the system develops in an arbitrary reconnection initiation. Multiple layers (more than 2) coexist in the current sheet after applying the random perturbation (Fig.4.1). Since the tearing layers on the same side of the current sheet are much closer than the tearing layers across the current sheet, they couple with each other by either forming an inflow-outflow coupling or degenerate into a single diffusion region (Fig.4.2 and Fig.4.3). The direct result of the tearing mode coupling is the trigger of secondary tearing (Fig.4.4). Secondary tearing changes the local flow and forms new diffusion regions which correspond to the creation of new modes that process reconnection (Fig.4.5). The new modes are having larger wavenumbers along the global guide field direction and they help to boost up the overall reconnection rate (Fig.4.6) by the globally existing coupling (Fig.4.7).

Chapter 5

Result IV: Parameter survey

In this chapter, we investigate the dependence of the inflow-outflow coupling on the distance between adjacent tearing layers and the global guide field for a further generalization of our previous results.

5.1 Introduction

In Chap.2 and Chap.3, one specific double-layer simulation was studied in detail to understand the fast 3D reconnection. Since only one case was examined, how the coupling and the reconnection change with the system are not clear.

In previous studies (Landi et al., 2008; Wang et al., 2015) and also in Chap.4, multiple 3D tearing layers (more than 2) are found in the initial state under a random perturbation. Since the linear theory by far cannot explain why 3D modes emerge faster than the prediction, it is difficult to learn beforehand the distribution of tearing layers for a given system. Therefore, whether the layers always couple in any system remains an open issue. It is straightforward to expect that the inflow-outflow coupling efficiency increases with a decreasing layer distance. A quantitative study on the coupling efficiency is helpful for the prediction of the nonlinear behavior (2D-like or 3D cascade) once the most unstable tearing modes are known.

On the other hand, the guide field strength, which is also arbitrary in the real system,

changes the character of the whole system. When the guide field is large, say 10 times of the anti-parallel asymptotic field, the system is approaching 2D since the perturbation along the guide field will be smoothed out by fast Alfvénic mode. If the guide field reduces to be comparable to (Beresnyak, 2017) or 10% of the anti-parallel asymptotic field (Wang et al., 2015), it is proved that multiple 3D tearing layers emerge. When the guide field shrinks to 0, initially only 2D modes can grow right at the current sheet center. Later, 3D modes disturb the 2D structures (Dahlburg et al., 1992; Dahlburg & Einaudi, 2002) and create a turbulent state (Oishi et al., 2015). Clearly, the emerging modes have a non-monotonic dependence on the guide field. Moreover, when the guide field is larger than 10% of the anti-parallel asymptotic field, well-organized magnetic structures such as shear flux tubes can be identified. On the contrary, it becomes drastically turbulent that no clear coherent structure can be found when no guide field exists. The threshold between different turbulent states is also worth studying. In addition, the universal existence of the inflow-outflow coupling in terms of the guide field strength should be addressed. When the initial perturbation is the same for systems with different guide field strengths, the resonance layers correspond to the perturbation are more packed to the current sheet center in a weaker guide field case. As we have shown in Chap.4, the two layers exhibit the feature of merging when they are close. If the coupling of reconnection layers is missing when $B_{\text{guide}} \to 0$, another theory is required to explain the fast reconnection mechanism in these cases.

In this chapter, we will test our tearing mode coupling model in different systems based on the consideration above for generalization. We first check the reconnection dependence on the distance between initial tearing layers (Sec.5.2), then we check the reconnection dependence on the guide field (Sec.5.3).

5.2 Reconnection dependence on input eigenmodes

In this section, we will study quantitatively the dependence of the inflow-outflow coupling efficiency on the tearing layer distance.

5.2.1 Simulation setup

The simulation setup is the same as that in Sec.2.4. In total, we execute 4 sets of simulations. Each set includes a double-layer simulation and a correspondent single-layer simulation. The applied tearing modes are $(1,1)$, $(2,1)$, $(3,1)$ and $(4,1)$, which are labeled in the left panel of Fig.2.3. From Eq.(2.28), among all double-layer simulations we apply, $(4,\pm1)$ has the smallest distance between two layers while the layers in $(1,\pm1)$ are the furthest. All simulations are applying the same resolution as $(3,\pm1)$ except $(4,\pm1)$ and $(4,1)$ which have a higher resolution that $\Delta x \geqslant 0.004\delta$ and $\Delta y = \Delta z = 0.015\delta$. A smaller box with $L_y = 6\delta$ is applied to save the numerical resource for these two simulations.

5.2.2 Inflow enhancement

We examine the dependence of the inflow enhancement on the layer distance first. In our 4 simulation sets, both the tearing layer position x_s and the wavelength λ change. Because the inflow region size is positively scaled to the wavelength (Steinolfson, 1983), we normalize the layer distance $2x_s$ to λ and define a normalized layer distance A_c as

$$A_c = \frac{2x_s}{\lambda} \sim \frac{2\alpha a n}{L_z}\sqrt{1+\left(\frac{nL_y}{mL_z}\right)^2} \tag{5.1}$$

where x_s is evaluated by Eq.(2.28). We check the inflow enhancement dependence on the value of A_c in the following part. By this definition, the double-layer simulation $(4,\pm1)$ has the smallest A_c value while $(1,\pm1)$ has the largest A_c.

We measure the inflow strength on both sides of a coupled diffusion region in all simulations on the anti-symmetric planes (Sec.2.5), which is shown in Fig.5.1. The inflow from the coupling side (near the current sheet center) increases monotonically in panel A) when the tearing layers approach each other. Moreover, the inflow enhancement from the coupling (inflow ratio between the double-layer simulation and the single-layer simulation) also increases monotonically in panel B) with decreasing layer distance. It is

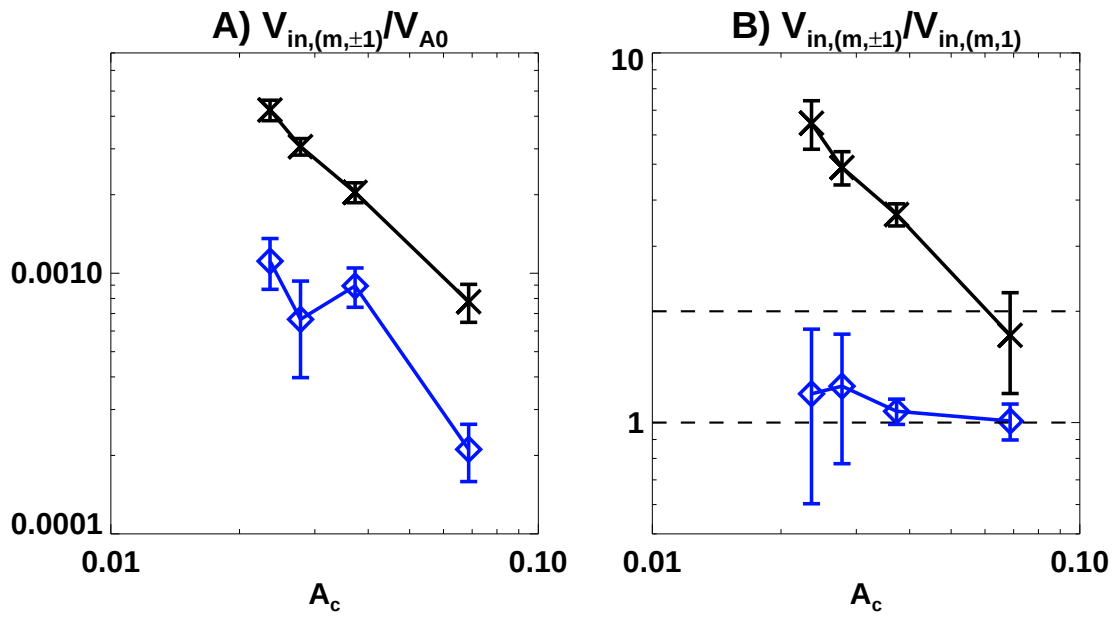

Figure 5.1: A) Averaged inflow of diffusion regions on the anti-symmetric planes in double-layer simulations. B) Averaged inflow ratio of double-layer simulations to their correspondent single-layer simulations. The inflows are detected both from the coupling side (black line with crosses) and the outer side (blue line with diamonds). The detection is averaged along inflow boundary in half of the diffusion region length, then averaged along time until secondary tearing starts to grow. Standard deviations are shown as error bars.

worth pointing out that the inflow ratio for $(1, \pm 1)$ with $A_c \sim 0.07$ is ~ 2. It means that the inflow-outflow coupling is very ineffective that the resultant inflow is roughly the superposition of flows from each layer. With a smaller distance between layers ($m \geq 2$), an effective inflow-outflow coupling is built up that the enhancement value exceeds 2 largely. On the contrary, the inflow in double-layer simulations from the outer side is not effectively changed compared to single-layer simulations even when the inflow-outflow coupling is strong, as the ratio is always around 1 in panel B). The difference in the inflow-outflow coupling efficiency can be directly seen in Fig.5.2. It is obvious that the inflow-outflow coupling is more effective in $(4, \pm 1)$ than that in $(1, \pm 1)$, as the inflow is approaching Alfvénic.

In the double-layer simulation $(3, \pm 1)$, new modes $(3, 3)$ and $(3, 5)$ emerge due to the nonlinear coupling. The wavelength of $(3, 3)$ is one-third of $(1, 1)$ that A_c for $(3, 3)$ is three times of that for $(1, 1)$. So $(3, 3)$ and $(3, -3)$ are incapable to couple across the sheet. As $(3, 5)$ has an even smaller wavelength and a larger layer distance with each other, A_c for $(3, 5)$ is even larger than that for $(3, 3)$. As can be seen in Fig.3.2, neither $(3, 3)$ nor $(3, 5)$ couple with their counterpart, which is consistent with the result above.

5.2.3 Energy cascade and reconnection rate enhancement

In Chap.3, we found that the global reconnection rate increases when new energy modes are activated. These new modes have larger wavenumbers along the global guide field than the original coupled modes. The creation of new diffusion regions comes from the growth of secondary tearing, which is triggered by the piling-up magnetic fields when the inflow-outflow coupling is effective. New diffusion regions form new reconnection layers, which can be understood by the nonlinear coupling between pre-existing modes with their higher order harmonics which have short wavelengths. In this section, we will check whether this is a general character when the coupling is built up.

In Sec.5.2, we have confirmed that $m \geq 2$ modes form the inflow-outflow coupling effectively across the current sheet. So in Fig.5.3, we compare the double-layer simulations

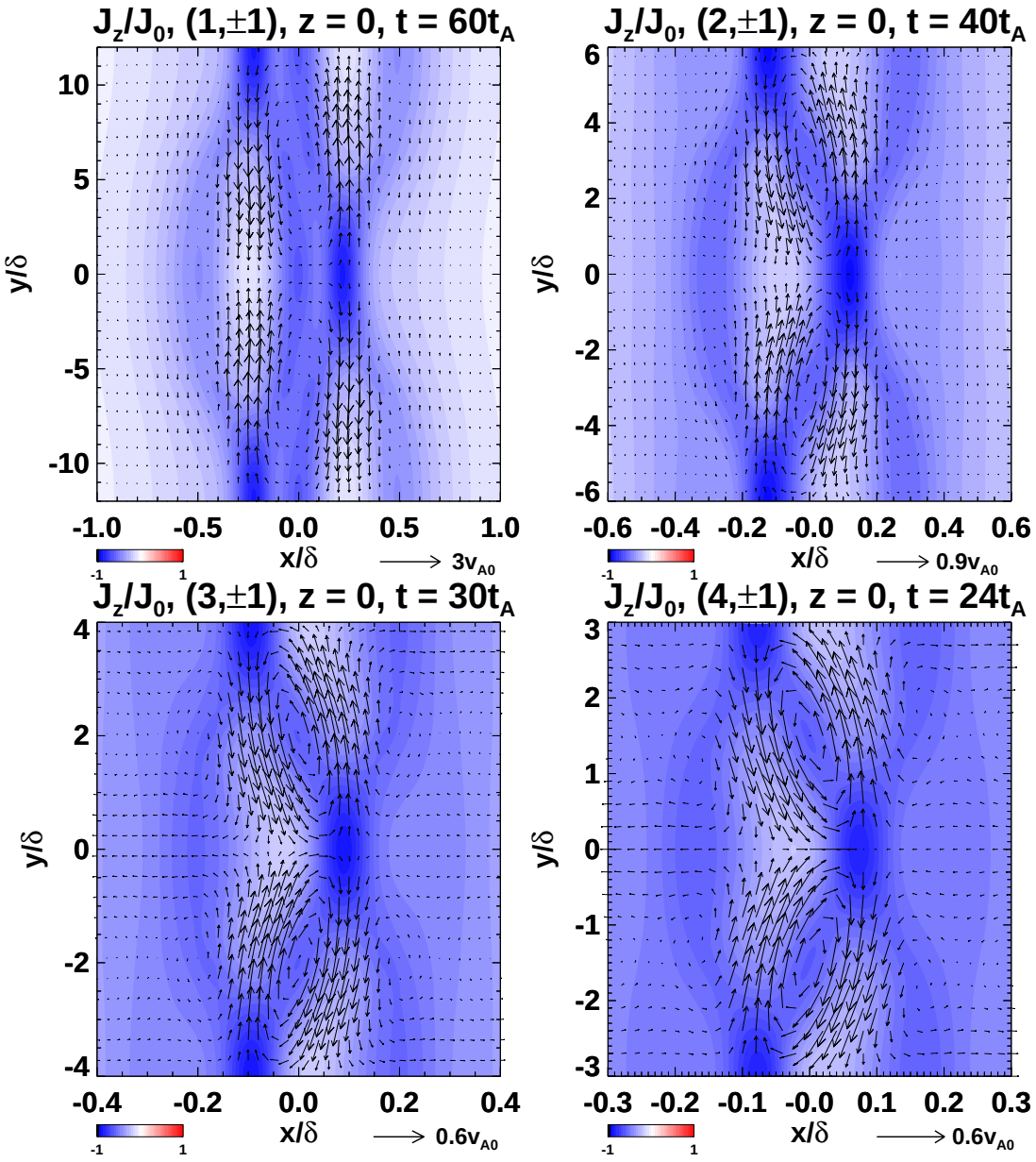

Figure 5.2: Velocity vectors overplotted on the current density J_z contour plot of double-layer simulations at different times on $z = 0$ plane. Vector scales are plotted at the bottom.

$(2, \pm 1)$, $(4, \pm 1)$ and their correspondent single-layer simulations to see the local development of diffusion regions. In the upper panels, it can be seen that $(2, 1)$ is potentially vulnerable to second tearing, while $(4, 1)$ saturates. In double-layer simulations, both of them exhibit the character of secondary tearing. A vertical diffusion region can be seen in both cases, while the overlying diffusion region in $(4, \pm 1)$ grows quickly.

By a careful check, we notice that there exist two kinds of secondary tearing in $(2, \pm 1)$. The one with 4 small diffusion regions along $x \sim 0.25\delta$ are the partitioned diffusion regions of $(2, 1)$. The two partitioned diffusion regions along $x \sim 0.2\delta$, which produce the vertical diffusion region, are originally the separatrix of $(2, -1)$. In this case, $(2, 1)$ and $(2, -1)$ tearing layers are marginally close to each other. So as each mode grows on either side of the current sheet, the potential secondary tearing evolves and separates the diffusion regions from the separatrices. The partitioned diffusion regions and the separatrices couple with each other, while also build up the inflow-outflow coupling with the counterparts on the other side of the current sheet. In comparison, in both $(3, \pm 1)$ (Fig.3.1) and $(4, \pm 1)$ (Fig.5.3), the two initial layers are too close that the separatrices degenerate with the diffusion regions. Thus simpler structures are observed in these two cases.

We next try to confirm the energy cascade path in all double-layer simulations to see the global modes development. In Fig.5.4, the magnetic energy calculated by Eq.(3.2) is shown. In the effective inflow-outflow coupling cases ($m \geq 2$), a clear cascade path along the global guide field (k_z-direction) can be seen. However, in $(1, \pm 1)$, the energy mainly goes along the 2D-like cascade path (yellow dashed line).

Finally, we compare the reconnection efficiency of all simulations. The overall reconnection rate calculated by Eq.(3.21) is shown in Fig.5.5. We consider two different stages. The first stage is the initial coupling stage just before secondary tearing emerges. The second stage is the end of the first cascade. In the understanding of the first stage, we compare the global reconnection rate ratio of double-layer simulations over their correspondent single-layer simulations in panel A), while the values are normalized by the

reconnection rate ratio at $t = 0$. If the value shown in panel A) exceeds 1, it means that the inflow-outflow coupling increases the overall reconnection rate compared to the reconnection in a single tearing layer. We find that although the inflow-outflow coupling becomes more effective with decreasing A_c, the overall reconnection rate ratio exhibits a non-monotonic change with a peak around $A_c \sim 0.035$.

As we have shown in Fig.2.6, magnetic fields pile up in front of the coupled diffusion region due to the effective inflow-outflow coupling. It is possible that when the coupling inflow exceeds a certain threshold, the local reconnection cannot consume all piling-up fields but locally saturates while pouring energy fast to the higher order harmonics (secondary tearing). It also explains why the inflow from the outer side does not increase as much as the inner side (the coupling side) in panel B) of Fig.5.1. Another reason is that the closest pair of the coupling has the shortest wavelength, thus they influence only a limited region near the sheet center. Therefore, the overall reconnection rate does not change much compared to the single-layer simulation. The values of the overall reconnection rate in all double-layer simulations in the first stage is shown in panel B) (blue line with squares). In comparison, the reconnection rate at the second stage (red line with stars) shows that more effective inflow-outflow coupling will result in a higher enhancement of the reconnection rate. On the other hand, all coupled modes are still having smaller overall reconnection rate values than the independently growing $(1, \pm 1)$.

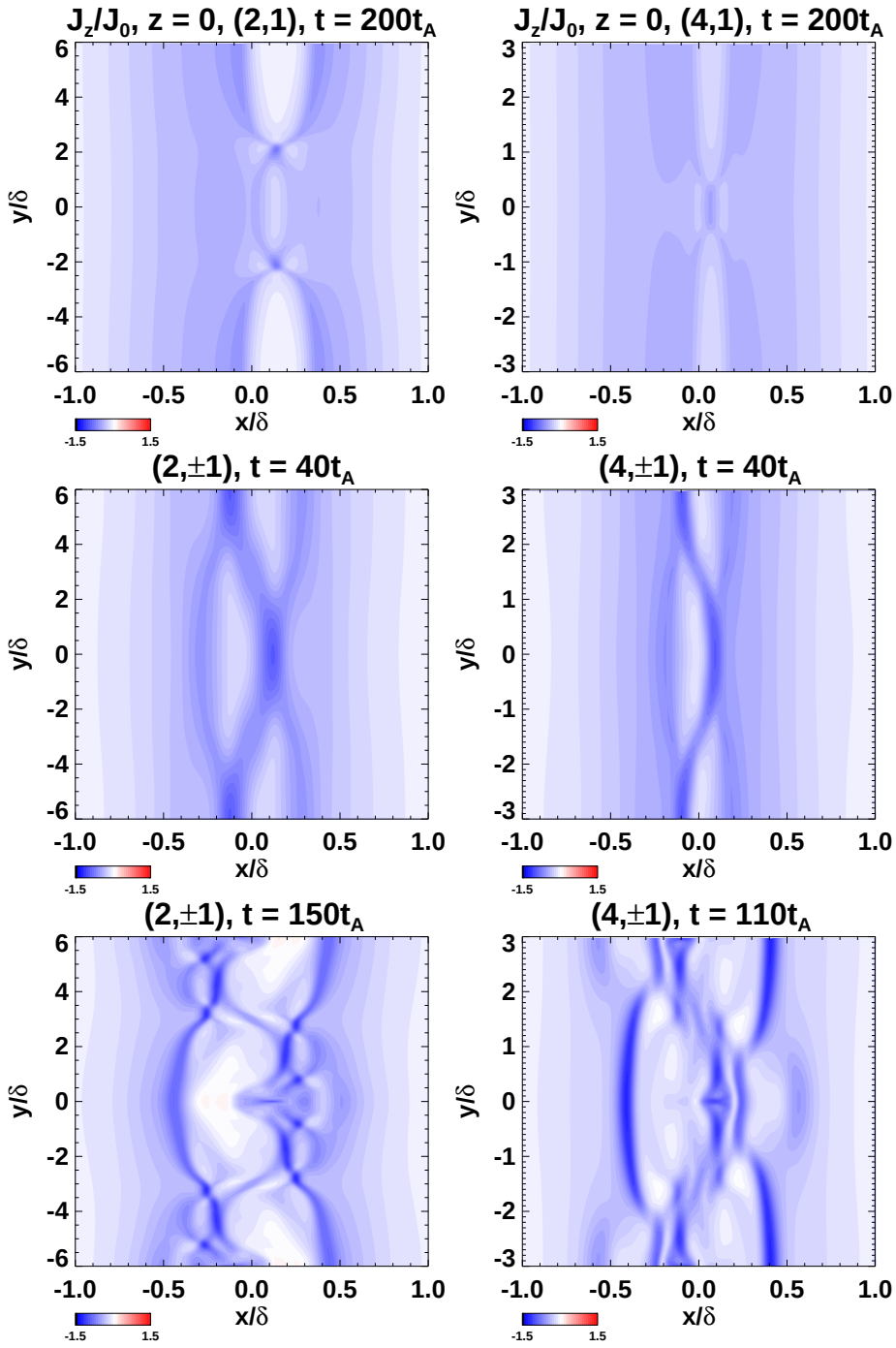

Figure 5.3: Current density J_z contour plot for double-layer simulations $(2, \pm 1)$, $(4, \pm 1)$ and their correspondent single-layer simulations at different times on the anti-symmetric plane $z = 0$.

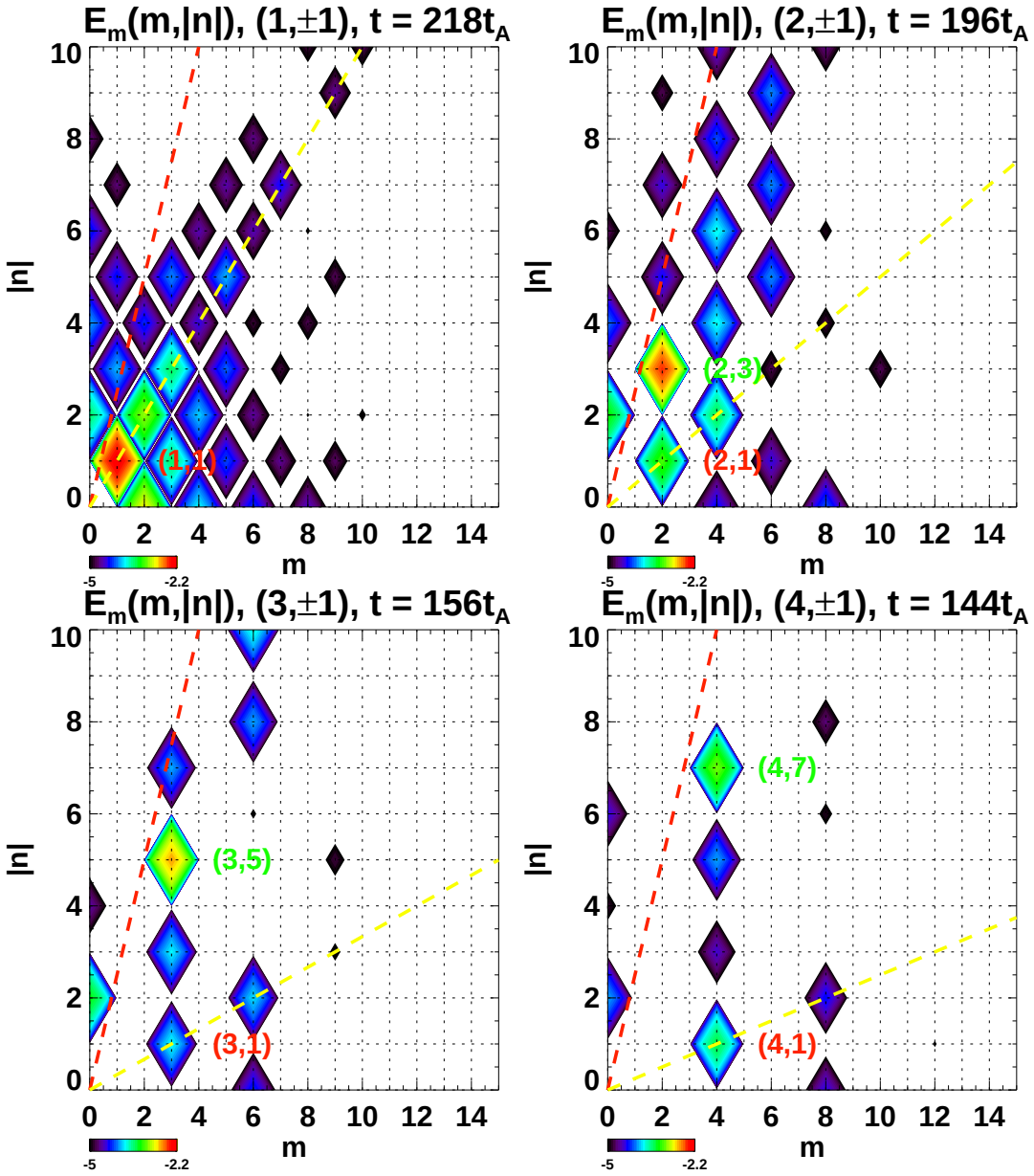

Figure 5.4: Magnetic energy of modes calculated by Eq.(3.2) for all double-layer simulations. The original modes are labeled as red characters, while the green color represents the cascaded mode. The red dashed line is the asymptotic magnetic field orientation. The yellow dashed line is the 2D-like cascade path for initially perturbed modes. The time slice in $(1, \pm 1)$ is chosen at when the reconnection rate reaches the first peak. The others are chosen at when the cascaded modes reach their peaks. Colors are in the logarithmic scale.

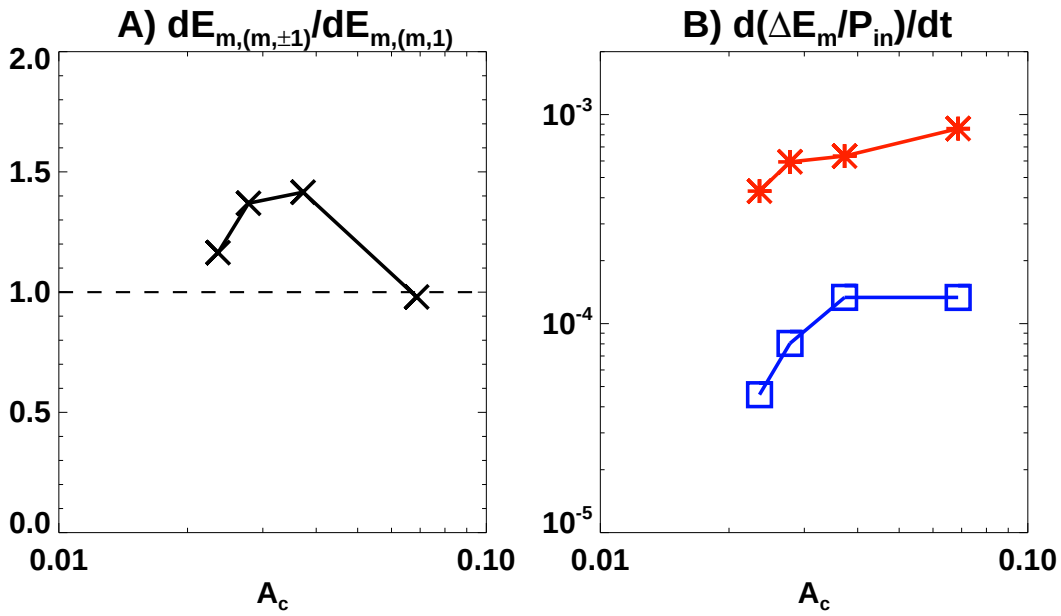

Figure 5.5: A) The reconnection rate ratio of double-layer simulations over their correspondent single-layer simulations during the initial coupling phase before secondary tearing emerges. The values are normalized by the initial reconnection rates. B) Reconnection rate calculated via Eq.(3.21) for double-layer simulations. The blue line with squares is the overall reconnection rate of double-layer simulations before secondary tearing emerges. The red line with stars is the reconnection rate selected at the same times as in Fig.5.4.

5.2.4 Summary and discussion

In this section, we checked the dependence of the inflow-outflow coupling efficiency and its consequences on the initial tearing mode wavelength and position. We notice that the inflow-outflow coupling, which is quantitatively presented by the enhanced inflow from the coupling side, becomes more effective when the distance between the initial tearing modes shrinks (Fig.5.1 and Fig.5.2). Secondary tearing is triggered when the inflow-outflow coupling exists, even for the originally secondary tearing stable modes (Fig.5.3). New modes which are close to the current sheet boundary are gradually activated after secondary tearing develops, so an energy transfer along the global guide field direction rather than a 2D-like cascade is observed in the coupling cases (Fig.5.4). During the initial inflow-outflow coupling phase, the overall reconnection first increases when the inflow-outflow coupling becomes effective but decreases when the coupling flow is too strong (panel A) in Fig.5.5). Although the inflow-outflow coupling also sufficiently enhances the overall reconnection by cascading to new modes, still the longest mode pair gives the faster global reconnection (panel B) in Fig.5.5).

The parameter survey on the wavelength and the layer distance gives a consistent conclusion with Chap.2 and Chap.3. However, two new arguments are raised from the results in this section.

The first argument is that the inflow-outflow coupling seems to have a non-monotonic dependence on the layer distance. It seems that there exists an optimal distance between layers in the inflow-outflow coupling. When layers are much beyond this distance that $A_c \gtrsim 0.06$, no effective inflow-outflow coupling is built. If the layers are too close that $A_c \lesssim 0.02$, it is possible that the overall reconnection in a pair of coupled tearing layers is slower than the reconnection by a single tearing layer.

The other argument regarding our present results is that longer modes participating the coupling are beneficial for a global fast reconnecting system. Although $(1, \pm 1)$ does not exhibit an effective inflow-outflow coupling, it still gives the highest global reconnection rate compared to the other well-coupled modes. It is not only because that $(1, 1)$ is

much closer to the current sheet boundary where magnetic field is abundant, but also because of its extended inflow region, whose size is roughly proportional to its wavelength (Steinolfson, 1983). A larger inflow region indicates a larger reconnecting magnetic field component. So $(1, \pm 1)$ reconnects asymptotic magnetic fields directly on either side of the current sheet. Therefore, once a longer wave mode participates the coupling, it is potential to accelerate the global reconnection more by effective local reconnection compared to a shorter mode.

In Sec.3.4, we found two boosts in the simulation. The second boost has a higher global reconnection rate than the first boost (roughly twice). The coupling coverage in the two boosts are comparable (Fig.3.18), but the reconnecting modes have different wavelengths (Fig.3.7). In the first boost, the outermost mode is $(3, 5)$ which has a wavelength of 1.2δ. In the second boost, the outermost mode is $(1, 3)$ that the wavelength is 2δ, which is about twice longer. Moreover, in the second boost, 3D modes are coupling directly with 2D modes at the current sheet center, which also have long wavelengths (for example, $\lambda_{(6,0)} = 4\delta$). As a whole, they produce faster reconnection than the first boost, in which only short wavelength modes couple.

5.3 Reconnection dependence on the guide field strength

In Sec.5.2, we noticed that when the normalized layer distance $A_c \lesssim 0.035$, the inflow-outflow coupling has a trend to reversely decrease the overall reconnection rate that the coupled tearing layers will be slowly reconnecting compared to their single-layer counterpart. According to Eq.(5.1), A_c is a monotonically decreasing function of guide field strength α. One concern arises from this result is that how the reconnection changes when the guide field changes. When the guide field is weak, the coupling between tearing layers is more likely to fall into the same category as $(4, \pm 1)$ and makes the overall reconnection slow. So in this section, we will try to test whether a pair of coupled tearing modes in a

system with a weak guide field will enhance or suppress the overall reconnection.

5.3.1 Simulation setup

The simulation setup is the same as that in Sec.2.4. We change the guide field strength into $\alpha = 0.01$. The rotational-symmetric double-layer simulation with tearing modes $(2, 1)$ and $(2, \pm 1)$ are executed, since $(2, \pm 1)$ in $\alpha = 0.1$ case has shown the feature of the inflow-outflow coupling. The numerical resolution is $\Delta x \geqslant 0.002\delta$ and $\Delta y = \Delta z = 0.012\delta$. A smaller box with $L_y = 12\delta$ is applied to save the numerical resource.

5.3.2 Result

We concentrate on the global change in the double-layer simulation $(2, \pm 1)$ with $\alpha = 0.01$. We first check the magnetic energy for modes calculated by Eq.(3.2) in the left panel of Fig.5.6. Unlike the cases with $\alpha = 0.1$, the mode $(0, 2)$ and its higher order harmonics (for example $(0, 4)$) along the global guide field becomes overwhelmingly dominant after $t \sim 30t_A$. Meanwhile, the original modes $(2, 1)$ and $(2, -1)$ rapidly decay. Since $(0, 2)$ and its higher order harmonics do not participate reconnection directly, the behavior of these modes indicates a slow global reconnection, which is confirmed in the right panel. By calculating Eq.(3.21), we find that the overall reconnection in the double-layer simulation $(2, \pm 1)$ (black line) is highly suppressed compared to the single-layer simulation $(2, 1)$ (blue line). The maximum reconnection rate of $(2, \pm 1)$ is roughly $1/6$ of $(2, 1)$ and maintains slow until $200t_A$.

We also plot the 2D magnetic energy spectrum of $(2, \pm 1)$ at different times in Fig.5.7 to see the energy cascade path, while one of the possibilities is $(2, -1) + (2, 1) \rightarrow (0, 2)$ that starts from the initial perturbed 3D modes. The left panel shows the initial state ($t = 10t_A$), just before the double-layer simulation decelerates than its single-layer correspondent. At this moment, in addition to the original modes, 2D mode $(4, 0)$ which may come from $(2, -1) + (2, 1) \rightarrow (4, 0)$ starts to grow. The middle panel is close to the reconnection peak of $(2, \pm 1)$ ($t = 60t_A$). Two energy cascade paths along the global guide

field can be identified. The path along $m = 2$, which is similar to our previous results, is only weakly growing. Another path along $m = 0$ dominates and controls the whole system as shown in the left panel of Fig.5.6. At the end of our simulation, all modes energy decreases and the system is still dominated by modes along the global guide field. As we expected, the cascade along the global guide field does not reach sufficiently far enough to reach the asymptotic magnetic field.

In order to understand the overall development, we plot magnetic field lines in the 3D box to make a clear visualization (Fig.5.8). Unlike the well-organized structures in Fig.3.6, the magnetic field lines exhibit a rather chaotic and ephemeral pattern in the simulation. At $t = 10t_A$, the main diffusion regions are existing near the symmetric planes, while the diffusion regions on the anti-symmetric planes almost disappear. This is because that the distance between two initial perturbed modes are too close, so the diffusion regions on the symmetric planes degenerate into one and center at $x = 0$. They completely change the global reconnection pattern that two 2D-like flux tubes are created due to the dominant reconnection in these diffusion regions. Each tube extends only half of the box size. As the plasma and magnetic fields are piling up in the tube region, they try to relax along the z-direction and the fluxes are ejected into the original diffusion region location. The flux shatters the diffusion regions and accumulates there $(t = 60t_A)$. Due to the weak global guide field, the tube suffers from kink-like instability. Afterwards, the tubes seem to untwine ($t = 70t_A$) and four flux tubes are produced in the region of $(y < 0, z < 0)$ and $(y > 0, z > 0)$ ($t = 80t_A$). The tubes move under the push from the flow and collide near $y = 0$ plane ($t = 110t_A$). After the system relaxes ($t = 160t_A$), tubes are created locally again at the center ($t = 180t_A$). Gradually a large tube is produced ($t = 190t_A$). From these observations, small and short flux tubes are created repeatedly here and there at the current sheet center, then destroyed by collision and afterward relaxation. These scattered local reconnection events cannot support a global fast reconnection, as we have shown in Fig.5.6.

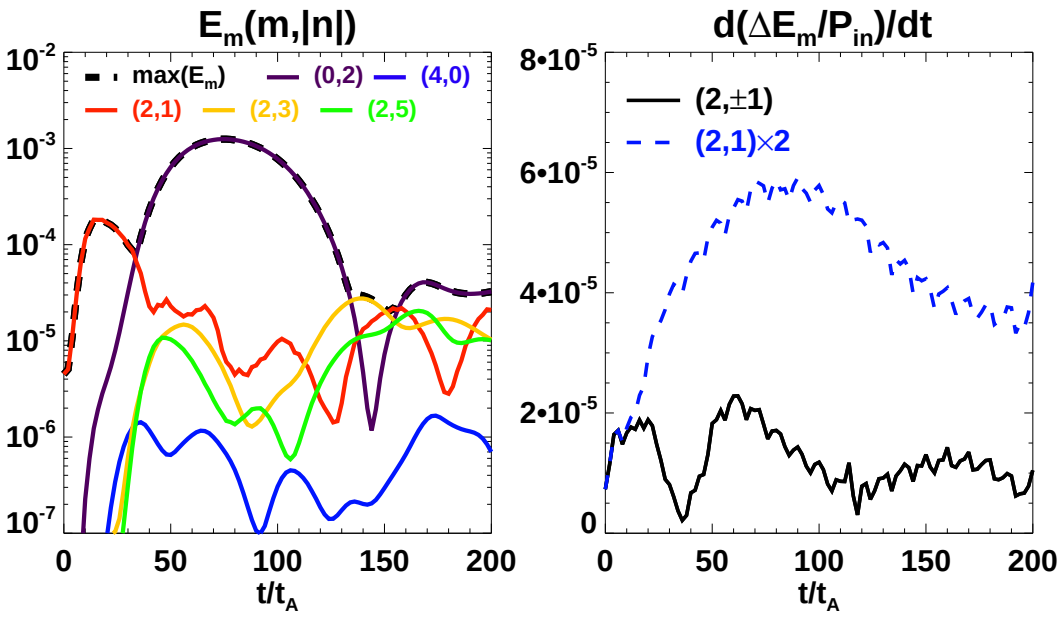

Figure 5.6: Left panel: magnetic energy of selected modes. Black dashed line is the maximum mode energy at each time step. Right panel: total magnetic energy conversion rate in the whole box by Eq.(3.21). The black line is the result of the double-layer simulation $(2, \pm 1)$, while the blue dashed line is double the reconnection rate in the single-layer simulation $(2, 1)$.

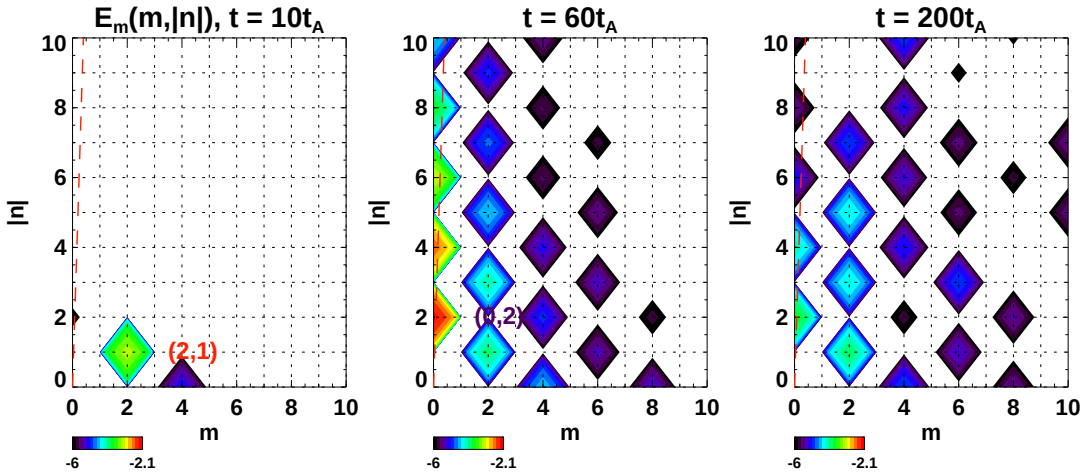

Figure 5.7: Magnetic energy of modes calculated by Eq.(3.2) at different times. The red dashed line is the asymptotic magnetic field. The dominant modes are labeled. Colors are in the logarithmic scale.

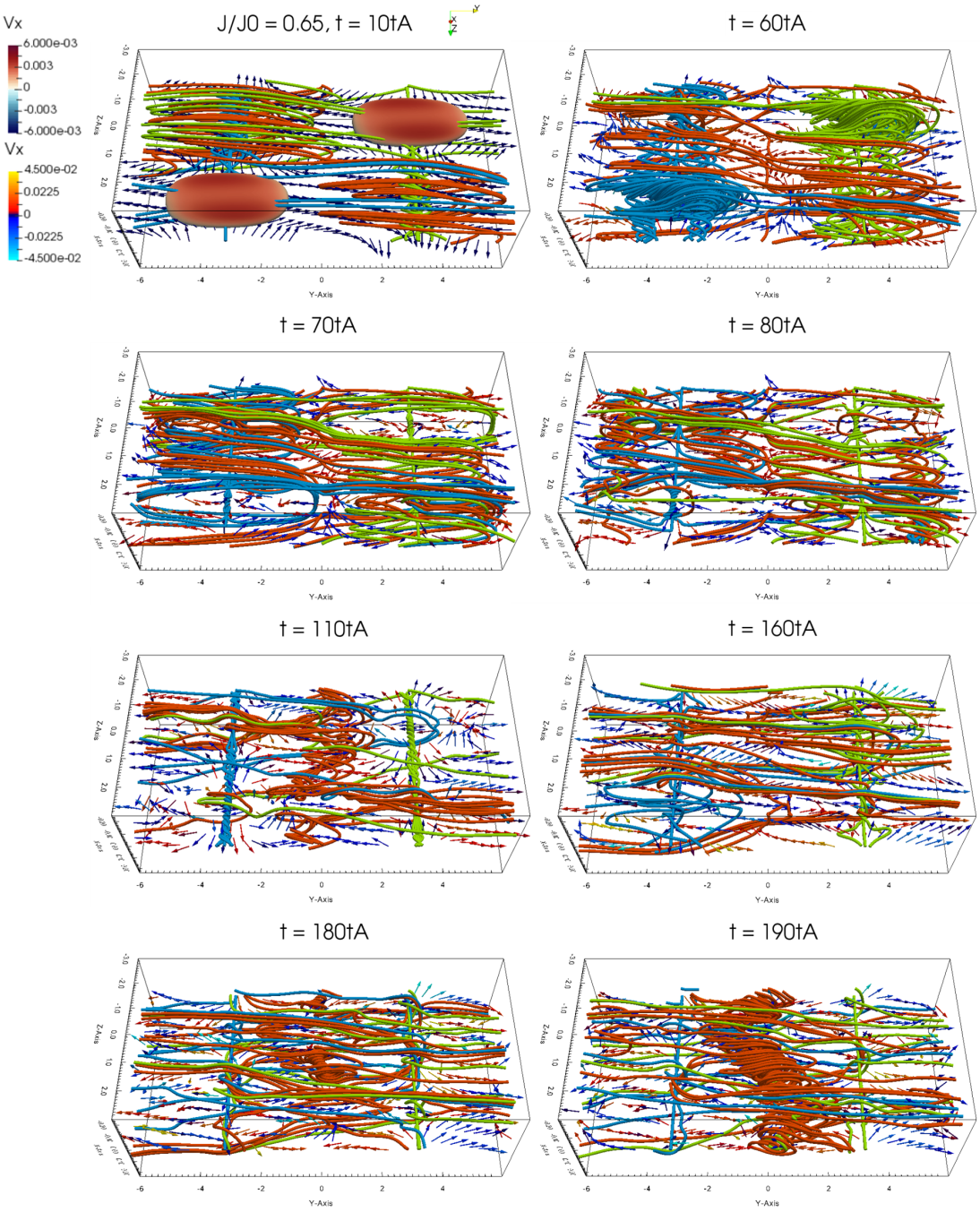

Figure 5.8: Magnetic field lines selected at different times. Orange, blue and green lines correspond to the field lines start from $y = 0, -3\delta, 3\delta$ planes, respectively. The isosurface shows the current density $J/J_0 = 0.65$, while the velocity fields on $x = 0$ plane is overplotted as vectors. The colors of the isosurface and vectors represent v_x strength.

5.3.3 Summary and discussion

We notice that the tearing mode coupling across the current sheet in the weak guide field case ($\alpha = 0.01$) gives a slow overall reconnection (Fig.5.6) while the energy cascade path prefers to be $m = 0$ modes which do not contribute to the reconnection directly (Fig.5.7). Different from the well-organized reconnecting layers in $\alpha = 0.1$ cases, the reconnection events scatter in the box and localize (Fig.5.8).

The modes we applied here have a normalized layer distance $Ac \sim 0.004$, which is far beyond the cases in $\alpha = 0.1$. As the two layers are too close to each other, the available magnetic field is extremely limited as shown in Eq.(2.36). Then the diffusion regions saturate soon on the anti-symmetric planes when no free energy is provided from the inner side. In comparison, on the symmetric planes, the diffusion regions are aligned. They degenerate into one that the system is more likely to produce 2D-like flux tubes rather than 3D tubes. These tubes are easy to kink (Dahlburg et al., 1992; Dahlburg & Einaudi, 2002) since the guide field is weak. Thus the system is disturbed by 3D modes again.

On the other hand, reducing the global guide field increases the plasma β at the current sheet center. As the sound speed is much faster than the local Alfvén speed, the diffusion regions are difficult to survive long when the plasma flow becomes turbulent. The transient reconnection results in slow overall reconnection in the range of our simulation ($t_{\text{end}} = 200t_A$).

As we have found in Sec.5.2, when $A_c \lesssim 0.035$, the inflow-outflow coupling will reversely reduce the overall reconnection during the coupling phase. However, the afterwards energy cascade still gives a faster reconnection. But in the case of the weak guide field with initial layers of $A_c \sim 0.004$, the overall reconnection is slow all along. Therefore, there seems to exist another threshold in addition to the two that we have identified in Sec.5.2. Whether this threshold is related to the global guide field strength α or is a general parameter that can be applied to any slab-like system should be examined in the future.

Although we have identified the energy cascade along the global guide field, the cascading path that starts from the initial perturbed modes is rather weak along $m = 2$ modes. From the 2D energy spectrum (Fig.5.7), a weak guide field makes the asymptotic field to be almost parallel to k_z. It means that it takes many steps of energy transfer along the global guide field to get to the asymptotic field from the initial perturbed layers. During the transfer, the wavenumber increases drastically. Modes with short wavelengths are highly possible to suffer from the restoring tension force so they cannot grow. In this way, the expanding reconnecting system will be stopped on the way to reach to the current sheet boundary and gives only slow reconnection as a whole.

5.4 Summary

In this chapter, we check the generalization of our result from a typical tearing layer coupling simulation in different systems.

For an arbitrary system, the distribution of the initially emerging modes is not well understood. Therefore, understanding the dependence of the inflow-outflow coupling on the layer distance can help to predict the nonlinear behavior of a system once the emerging modes are known (Sec.5.2). We find that although the inflow in the coupling increases with a decreasing layer distance (Fig.5.1), the overall reconnection rate decreases when the distance is too close for a pair of modes that is far from being parallel (Fig.5.5). When the coupling is effective, secondary tearing produces new diffusion regions, while globally they form new reconnection layers that correspond to new modes which have higher wavenumbers along the global guide field than the original modes (Fig.5.4).

As the background magnetic field controls the emerging modes, we then check the inflow-outflow coupling in a pair of rotational-symmetric tearing modes in a current sheet with a weak guide field ($\alpha = 0.01$), as the tearing layers are likely to be packed close to the sheet center that the layers are possible to merge (Sec.5.3). We notice that in this case, the inflow-outflow coupling saturates soon, while the diffusion regions that are aligned with each other degenerate into a single one (Fig.5.8). The whole system is mainly under the

control of the modes that are parallel to the global guide field and results in a very slow reconnection (Fig.5.6). Energy cascades mainly along the global guide field direction, while the cascade starts from the original modes is cut-off on the way to the asymptotic field and remains weak (Fig.5.7).

It seems that when the guide field is moderate, namely around 10% of the asymptotic anti-parallel magnetic field, the successive processes of the inflow-outflow coupling and the nonlinear coupling will produce new reconnection layers, which also participate the inflow-outflow coupling to increase the overall reconnection. So our results in Chap.2 and Chap.3 are shown to validate through the generalization. On the other hand, when the guide field is weak, say less than 1% of the asymptotic anti-parallel magnetic field, the growing 3D modes tune the reconnection into instantaneous events that different theory should be applied for this system.

Chapter 6

Summary and discussion

In this dissertation, we executed different numerical simulations to understand the fast three-dimensional (3D) reconnection in a current sheet with a finite guide field.

6.1 Summary of results

As multiple tearing layers emerge when a random perturbation is applied to a slab-like current sheet with a finite guide field (Landi et al., 2008; Wang et al., 2015), we expected that the coupling between tearing layers are important in the acceleration of 3D reconnection. In order to achieve a fast overall reconnection, successive inflow-outflow couplings that span across the whole current sheet are required. Meanwhile, each reconnection layer must extend along the current sheet and cover a sufficiently large area. We then applied simulations and analysis to confirm our hypothesis on the fast 3D reconnection.

Local analysis of the inflow-outflow coupling in the typical case

First of all, we tried to understand the local properties of the inflow-outflow coupling between two rotational-symmetric 3D tearing modes $(3, 1)$ and $(3, -1)$ growing in a current sheet with a finite global guide field, while the guide field strength is 10% of the anti-parallel asymptotic magnetic field (Chap.2).

The pair of modes exhibits a strong three-dimensionality along the global guide field

direction (Fig.2.4). On some planes, diffusion regions form a zigzag pattern that the outflow from one diffusion region feeds into the inflow of the diffusion region on the other tearing layer (Fig.2.5). On other planes, diffusion regions are aligned with each other across the sheet that no coupling exists. On the coupled plane, due to the inflow-outflow coupling, the inflow in the coupled diffusion region and the local reconnection rate increase, while the reconnecting magnetic field piles up in the coupling region (Fig.2.6) and triggers secondary tearing in the coupled diffusion region (Fig.2.7).

Although the coupled planes cover roughly half of the simulation box along the global guide field direction (Fig.2.9), this initial inflow-outflow coupling has not grown strong enough to influence the whole current sheet. As the turbulent state is still confined near the current sheet center, the overall reconnection rate is not large.

The initial perturbed two tearing modes create Alfvénic shear flows across the current sheet center. It is highly possible that they suppress the growth of 2D modes (Fig.2.10). In order to prove this argument, we executed an extra set of simulations. Each simulation contains two 3D modes as that in the typical double-layer simulation, as well as a selected 2D mode. We compared the growth of 2D and 3D modes in the three-layer simulations and the typical double-layer simulation (Fig.2.11). It is found that the most unstable 2D mode ($(1, 0)$ in our system) in the initial static current sheet is suppressed that the growth rate becomes only half of the growth rate predicted by the linear analysis. The dynamic system-preferred 2D mode ($(6, 0)$ in the typical double-layer simulation) is regulated by the existing 3D modes. It receives energy from 3D modes if the amplitude is small but reversely suppressed when the amplitude becomes large.

Global analysis of the inflow-outflow coupling in the typical case

We then examined the temporal and spatial development of the inflow-outflow coupling and how they relate to the global reconnection rate enhancement in the later phase of the double-layer simulation $(3, \pm 1)$ (Chap.3).

As the inflow-outflow coupling is essentially existing between diffusion regions, we

tracked how and where new diffusion regions are created. As secondary tearing is triggered in the coupled diffusion region, the partitioned diffusion regions open a vent that reconnected field lines are ejected outwardly and collide with free field lines. New diffusion region outside of the original one is formed due to the collision (Fig.3.1 and Fig.3.2). On the planes where no inflow-outflow coupling is built, a new diffusion region is also created outwardly due to the tension force that comes from the non-uniformity of field lines along the global guide field (Fig.3.3 and Fig.3.4). Since the other part of the simulation box possesses both the characters from the coupling planes and the non-coupling planes, the creation of diffusion regions outside of the original diffusion regions are considered to be common in the whole simulation box. Two new sheet-wise extending reconnection layers are found on either side of the current sheet, closer to the asymptotic fields (Fig.3.6). It is noticed that these two layers are the mixture of new energy modes $(3, \pm 3)$ and $(3, \pm 5)$, which have larger wavenumbers along the global guide field direction compared to the initial perturbed modes $(3, \pm 1)$ (Fig.3.7 and Fig.3.8). By studying the energy transfer rate (Fig.3.9), we noticed that new modes are activated by the nonlinear coupling between pre-existing modes with their higher order harmonics, even though these new modes are not preferred by the initial current sheet. When new modes grow over a threshold, they start to grow by themselves by absorbing the energy directly from the background current.

As new modes are created outwardly, the global kinetic energy increases while the magnetic energy is converted fast (Fig.3.10). After the first boost of the magnetic energy conversion rate, there exists a relaxation phase that flux tubes relax and reform into new flux tubes (Fig.3.11). The newly formed flux tubes are growing from inside due to the growth of new modes (Fig.3.12). It starts a second boost of reconnection by activating new modes outwardly (Fig.3.13, Fig.3.14). From the 2D energy spectrum, the processes above can be seen as an energy transfer further to the asymptotic magnetic field then backwards due to the inverse energy cascade, and outwardly again (Fig.3.15). The global dissipation is dominated by 3D modes (Fig.3.16).

As we have confirmed that new reconnection layers which are extending along the whole current sheet are created outwardly from the current sheet center region, the next concern is that whether the inflow-outflow coupling is also working among new and old layers. By tracking the local flow pattern and the resonance layer position, it is confirmed that new reconnection layers couple with old layers, while the inflow-outflow coupling between old layers across the sheet center still remains (Fig.3.17). Meanwhile, the inflow-outflow coupling covers almost the whole simulation box (Fig.3.18), which correlates with an increasing global reconnection. As we have conjectured, the overall reconnection increases when new sheet-wise extending reconnection layers are created outwardly due to nonlinear coupling and sheet-crossing successive inflow-outflow couplings are built.

New reconnection layers are chosen by the non-uniform reconnection system along the global guide field, which comes from the nonlinear coupling of the initial two perturbed modes across the current sheet (Fig.3.20).

The sheet-crossing coupling in the random perturbation simulation

In Chap.2 and Chap.3, we analyzed in detail a reconnecting current sheet perturbed by selected modes. However, this simulation setup is highly specific. In order to generalize the application of our hypothesis, we re-examined the spontaneous reconnection that is initiated by a random perturbation which mimics the waves with arbitrary phases and wave vectors in the universe (Chap.4).

Still, we retrieve the coexistence of 3D tearing layers inside the current sheet after applying a random perturbation on velocity field (Fig.4.1), while the numbers of layers are more than two and symmetry is not held across the sheet. As the tearing layer pair is closer on the same side of the current sheet compared to the tearing layer pair across the current sheet, the coupling on the same side of the current sheet is much more efficient than the coupling across the sheet. The coupling falls into two categories due to the small layer distance. One type of coupling is the inflow-outflow coupling studied in the previous chapters, the other type of coupling is the degeneration of two diffusion regions into a

single one which reconnects fast by itself (Fig.4.2 and Fig.4.3). Secondary instability is triggered in many diffusion regions (Fig.4.4). It changes the local flow and forms new diffusion regions which correspond to the creation of new energy modes (Fig.4.5). Consistent with the results in Chap.3, new modes have larger wavenumbers along the global guide field. The overall reconnection rate boosts up (Fig.4.6) when new modes grow and the inflow-outflow coupling exists globally across the whole sheet (Fig.4.7).

Generalization of the sheet-crossing coupling model

Our sheet-crossing coupling model of 3D reconnection is further generalized by changing simulation setup (Chap.5).

The emergence of multiple tearing layers under a random perturbation seems to contradict the linear theory. Then the dependence of the inflow-outflow coupling on the tearing layer distance is helpful for the nonlinear behavior prediction once the emerging modes are known. Thus we generalize our coupling model in 3D reconnection by processing parameter survey on the tearing layer distance (Sec.5.2). We found two critical normalized layer distance (A_c). When $A_c \lesssim 0.06$, an effective inflow-outflow coupling is built between two tearing layers (Fig.5.1 and Fig.5.2). It triggers secondary tearing and creates diffusion regions outwardly (Fig.5.3). Afterwards, energy cascade along the global guide field is observed that new energy modes with higher wavenumbers are activated (Fig.5.4), which is consistent with Chap.3. When $A_c \lesssim 0.035$, the inflow-outflow coupling does not effectively increase the global reconnection, while the energy cascades fast into shorter modes. Moreover, there seems to show a trend that when $A_c \lesssim 0.02$, the overall reconnection of a pair of coupled tearing layers will be slower than that in a single tearing layer (Fig.5.5). It is also found that long wave modes are beneficial to fast reconnection than short wave modes. It explains why the final reconnection rate in the second boost of double-layer simulation $(3, \pm 1)$ is higher than the first boost.

Because the position of a tearing mode is determined by the background magnetic field, how the inflow-outflow coupling changes with the global guide field strength is

also studied to give a general conclusion (Sec.5.3). When the global guide field becomes weaker, the modes with $n = 1$ near the center has a very small A_c value that it is possible that the mode pair saturates soon. We executed a double-layer simulation $(2, \pm 1)$ in a current sheet with a global guide field that is 1% of the anti-parallel magnetic field. The overall reconnection is always slow (Fig.5.6) while the energy cascades mainly along $n = 0$ modes (Fig.5.7). As the two layers are too close with each other, the diffusion regions from the two modes degenerate into one single diffusion region on the plane where these two modes are in phase and transient flux tubes are created then perish soon (Fig.5.8). The energy cascade path found in Chap.3, Chap.4 and Chap.5 is rather weak in this case. This is probably due to the numerous cascade steps to reach the asymptotic magnetic field. During the cascade, new modes are having smaller and smaller wavelengths that their growth is suppressed by the magnetic field tension force.

6.2 General discussion

In this dissertation, we attacked the long-term remaining problem, namely the fast 3D reconnection problem, from the viewpoint of the diffusion region development, together with the coupling between diffusion regions across the current sheet.

6.2.1 Global reconnection rate

Presently, we mainly argued that how the reconnection rate increases without discussing the final reconnection rate. Unlike the 2D reconnection regime, the reconnection rate is difficult to define in 3D regime, as the magnetic flux surface is not intact anymore. In our analysis, we mainly measured the magnetic energy conversion rate as shown in Eq.(3.21). This measurement includes the contribution from all energy modes, both 2D and 3D, as well as other dynamics such as instabilities and local dynamo. It is in the form of dB^2/dt thus smaller than the classical measurement by dB/dt as the averaged B in the current sheet is always smaller than the asymptotic magnetic field.

simulation	reduced E_m	$d\phi_{\text{MR}}/dt$	$\bar{v}_x$	$d\Delta_{\text{MR}}/dt$
$(3, \pm 1)$	0.0016	0.0045	0.0015	0.0088
random	0.0013	0.0032	0.0027	0.0045

Table 6.1: Table of reconnection rate measured by different methods in the double-layer simulation $(3, \pm 1)$ and the random perturbation simulation.

Since no rigorous definition of 3D reconnection rate exists, we re-examine several different methods, such as measuring the reconnected magnetic flux (Huang & Bhattacharjee, 2016), global inflow (Kowal et al., 2009) and turbulent current sheet width growth rate (Beresnyak, 2017; Kowal et al., 2017), to make a fair comparison.

The reconnection rate measured by the reconnected magnetic flux ϕ_{MR} temporal change is calculated by

$$M_A = \frac{1}{v_{A0} B_{y0}} \frac{d}{dt} \left(\max |\phi_{\text{MR}}(y)| \right) \tag{6.1}$$

where ϕ_{MR} is measured as

$$\phi_{\text{MR}}(y) = \int_0^y \bar{B}_x(x = 0, y') dy' \tag{6.2}$$

and $\bar{B}_x = \int_{-L_z/2}^{L_z/2} B_x(x, y, z) dz / L_z$. By averaging along the global guide field direction (z-direction), Eq.(6.2) mainly measures the reconnected flux by 2D modes near the current sheet center, while the reconnected fluxes by 3D modes cancel out in the integration.

The reconnection rate measured by the maximum global inflow $\bar{v}_x$ is detected in the asymptotic magnetic field region. It is also averaged along the global guide field direction that $\bar{v}_x = \int_{-L_z/2}^{L_z/2} v_x(x, y, z) dz / L_z$. This measurement is similar to the observational method, since the averaging process mimics the line-of-sight effect.

The turbulent current sheet width Δ_{CS} is measured by the spatially averaged total current density $\langle |\mathbf{J}(\mathbf{x})| \rangle$, as that in Sec.3.4. This measurement includes all modes information. Moreover, the flux tubes are also included as they contribute much to the turbulence (Lapenta et al., 2015).

We list out all measurements for the double-layer simulation $(3, \pm 1)$ around $t = 460 t_A$

and the random perturbation simulation around $t = 800t_A$ (end of the second boost) (Table.6.1). The reconnection rate varies with methods and the magnitude covers from 0.001 to 0.01. We first assume that our model is independent of the diffusivity and the box size. The reconnection rates on the reconnected flux measurement are smaller than that in Huang & Bhattacharjee (2016), which is around 0.008. This is because that, in their simulation, a sufficiently grown Sweet-Parker sheet is in the background of the turbulent state. Therefore, a large portion of the reconnection rate (roughly half) comes from 2D modes. The Lundquist number in our simulation is 7×10^4, which corresponds to a Sweet-Parker sheet with a global reconnection rate of 0.0037. If we assume that 3D modes mediate the 2D reconnection, then by adding up the Sweet-Parker reconnection rate, our result approaches their measured value. The measurements on the global inflow are two orders of magnitude smaller than Kowal et al. (2009), in which a driven turbulent flow was implemented at the beginning and sustained for a while. It seems that the driven reconnection (Kowal et al., 2009) is faster than the spontaneous reconnection. On the other hand, the measurements on the current sheet width expansion rate give reconnection rate in the same order of magnitude as that in Kowal et al. (2017); Beresnyak (2017) from $(3, \pm 1)$ but smaller reconnection rate in the random perturbation case. It is probably because that new modes are only created in the positive x-side in the random perturbation case thus the sheet width expands less.

As many observations show that the inflow is roughly $0.1 - 0.001$ of the ambient Alfvén speed (Yokoyama et al., 2001b; Takasao et al., 2012b), reconnection rate $M_A \sim 0.1 - 0.001$ is required for the solar flare case. Whether our result is also true when the diffusivity gets smaller or when the box size gets larger need further study.

In all of our simulations, the time for boosting up the reconnection rate is always in the order of $100t_A$. We estimate the normalization for all variables in the environment of the solar corona by setting up the length scale $\delta \sim 0.05$Mm, the asymptotic Alfvén velocity $v_{A0} \sim 1000$km/s, temperature $T_0 \sim 6 \times 10^6$K and the diffusivity $\tilde{\eta}_0 \sim 5 \times 10^{10}\mathrm{m}^2/\mathrm{s}$. Our current sheet length becomes $L \sim 1.2$Mm, which is only a part of an extended sheet. The

boosting time now becomes 5s. In Kowal et al. (2017), the time it takes to reach a fast global inflow is independent of diffusivity. Therefore, although our estimated diffusivity is $1.5\times10^7\mathrm{m}^2/\mathrm{s}$, which is much larger than that in the solar corona ($\sim 1\mathrm{m}^2/\mathrm{s}$), we assume here that the nonlinear development time does not change substantially even in a weakly diffusing environment. If this argument holds in the solar flare case, the total boosting time, which is several hundreds of Alfvén time in our simulation, will be tens of seconds or minutes. Whether this fast-evolving time can be applied to the eruptive phase of the solar flare should be tested in the future with a larger box and a smaller diffusivity.

6.2.2 2D modes versus 3D modes

Bi-directional outflows and the production of plasma blobs were observed in a sheet-like structure in the solar flare study (Takasao et al., 2012b). Moreover, coronal mass ejection (CME), which is the ejection of the reconnection produced flux tubes, is often related to the solar flares (e.g., Andrews, 2003). As multiple tearing layers emerge in various 3D reconnection simulations in a current sheet with a finite guide field (Landi et al., 2008; Wang et al., 2015; Beresnyak, 2017; Kowal et al., 2017), the question becomes how to grow 2D modes start from a 3D turbulent state.

In Sec.2.6.2, we argued that the shear flow from 3D modes on either side of the current sheet has a potential to suppress the growth of 2D modes right at the current sheet center when 3D modes are close to each other. By comparing the results shown in the three-layer simulations, it seems that this argument is confirmed. On the other hand, when 3D modes are far from each other, as the initial stage of the random perturbation shows (Fig.4.8), 3D modes can reversely cultivate 2D modes or at least make space for 2D modes to grow.

In our typical double-layer case, the strongest 2D mode in the early phase is $(6,0)$ which obtains energy through the nonlinear coupling $(3,1)+(3,-1)$. As it can be observed in Fig.3.15, $(6,0)$ maintains its dominance among all 2D modes until the end of the first boost, although it is still much weaker than 3D modes. Afterwards, there exists a relaxation phase that pre-existing flux tubes seem to coalesce with each other and pro-

duce larger flux tubes (Fig.3.11). As a result, the energy is pouring into 3D modes with longer wavelengths. When $(1, 1)$ mode becomes dominant in the current sheet, longer 2D modes $(4, 0)$ and $(2, 0)$ are activated that the number of diffusion regions on $x = 0$ plane reduces (Fig.3.14). Subsequently, the longest wave mode $(1, 0)$ dominates the whole current sheet (final panel in Fig.3.15). Apparently, there exists an inverse cascade process in the development of 2D modes.

When 2D modes grow strong enough, they are observed to form the inflow-outflow coupling with 3D modes (Fig.3.18 and Fig.4.7). This implies that the reconnection in 2D modes is consuming the magnetic field lines from the tubes in the coupled 3D modes. Then two possibilities are raised. The first one is that the 2D tubes are produced by the reconnection of the 3D flux tubes, that the tube-tube reconnection produces a patchwork tube. The serpent structure of this patchwork tube then relaxes into a straight one and is seen as a 2D tube. The other possibility is that the 2D flux tubes are created by peeling off the field lines from the 3D flux tubes one by one, instead of exchanging tube structures. Which process is true should be checked by both theory and numerical result.

In the tube-tube reconnection scenario, it is found that the reconnection pattern changes with the angle between the tubes and the helicity (Sakai & Koide, 1992; Linton et al., 2001). The flux tubes produced in our system have the same sign of helicity, which corresponds to the slow tube reconnection regime. For the tubes on the same side of the current sheet, the tilting angle between the tubes is small that their reconnection falls into the "merge" category in Linton et al. (2001). In the random perturbation, although several modes grow together with similar strengths on the same side of the current sheet in the initial phase $t \leq 300t_A$, finally only one mode wins and dominates the dynamics (Fig.4.6). It is possible that the modes on the same side coalesce due to the merging of flux tubes. Also, it can explain that why reconnection layers are the mixture of two modes, such as $(3, \pm 3)$ and $(3, \pm 5)$ in Fig.3.8. In contrary, the flux tubes from opposite sides of the current sheet usually have a large tilting angle in between. For example, the two tubes from $(1, 1)$ and $(1, -1)$ have a tilting angle of $5\pi/6$. So the reconnection falls into the "bounce"

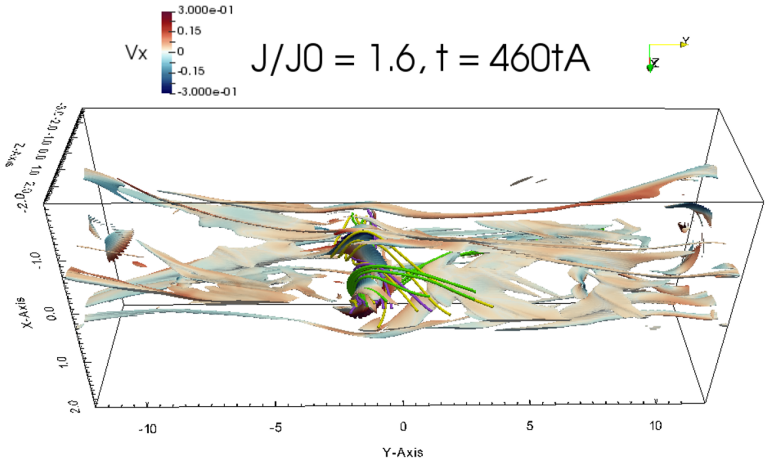

A) diffusion regions with magnetic field lines of 2D tube

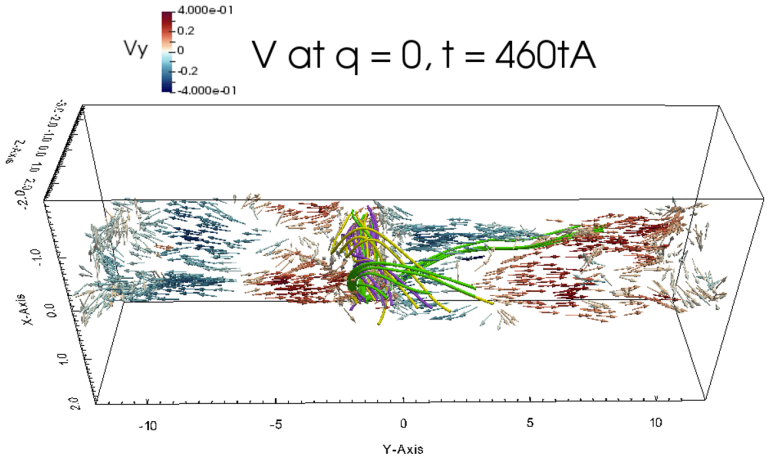

B) plasma flow on $q = 0$ surface with magnetic field lines of 2D tube

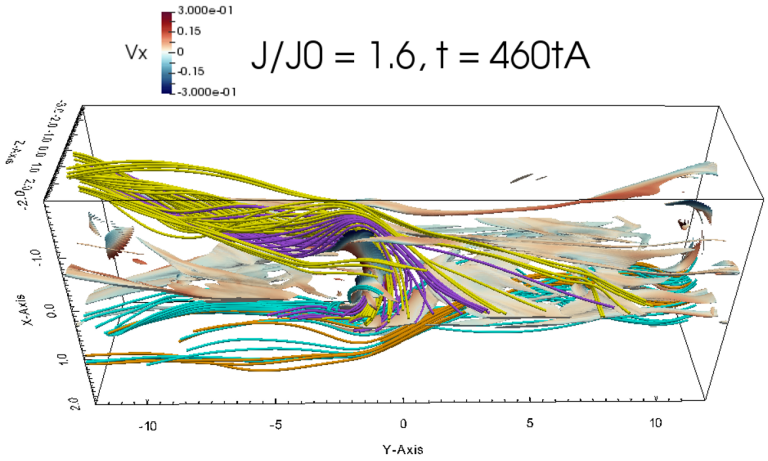

C) diffusion regions with magnetic field lines from (1,1) mode (purple and yellow lines) and $(1, -1)$ mode (cyan and orange lines)

Figure 6.1: Reconnecting field lines producing the 2D flux tube at the sheet center in the double-layer simulation $(3, \pm 1)$. The isosurface of current density J represents diffusion regions and colored by v_x, while velocity fields are plotted by arrows along $q = 0$ and colored by v_y. Purple, yellow and green field lines in panel A) and B) are selected along $q = 0$ plane at $z = -1.5\delta, 0, 1.5\delta$, respectively. Purple and yellow field lines are selected from $(1, 1)$ flux tube, while cyan and orange field lines are selected from $(1, -1)$ flux tube.

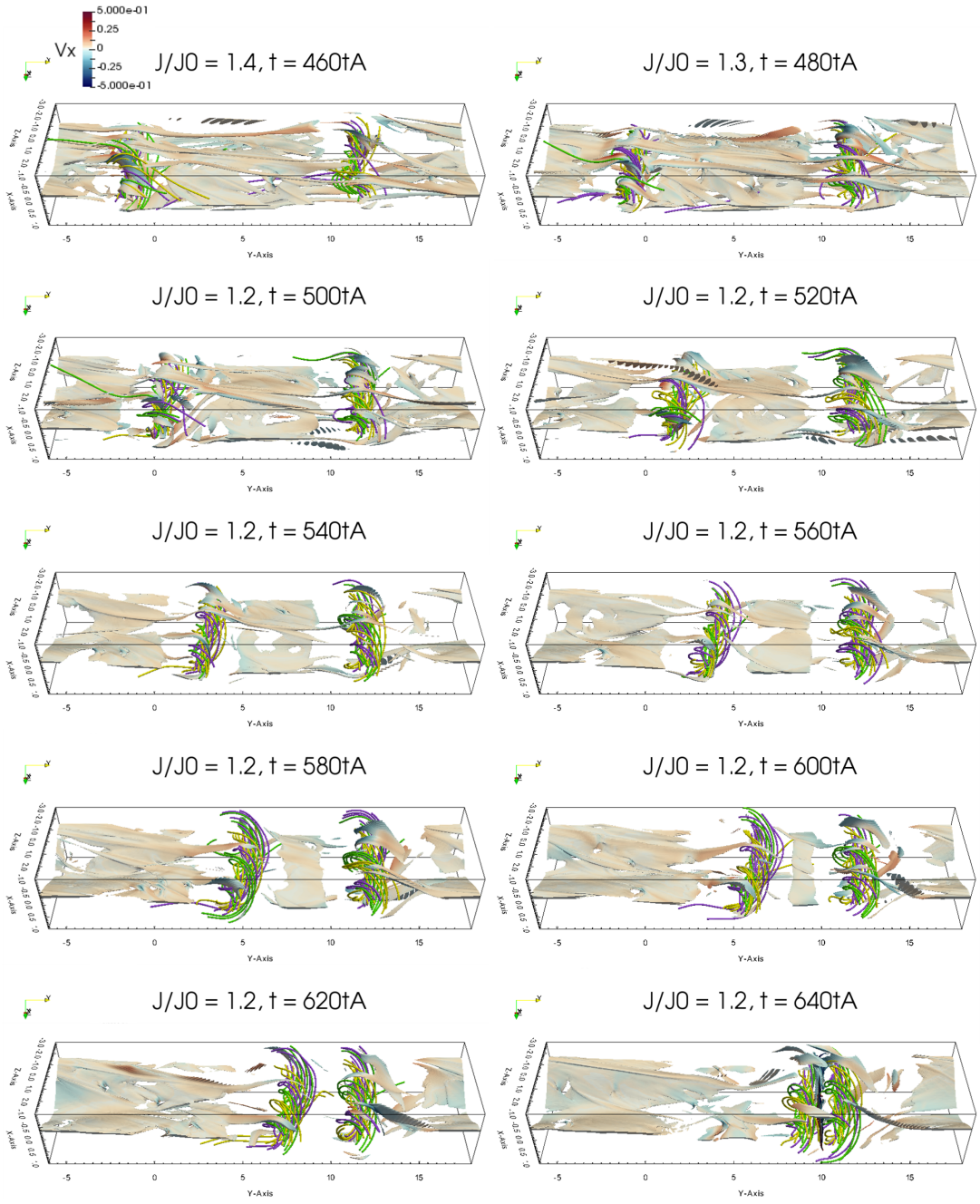

Figure 6.2: Coalescence of 2D flux tubes. Purple, yellow and green lines are selected field lines along $q = 0$ plane at $z = -1.5\delta, 0, 1.5\delta$, respectively. The isosurface of the current density J with color (v_x) represents mainly diffusion regions. The simulation box is shifted by 6δ to the positive y-side.

category that the reconnection between tubes across the sheet is difficult.

As a result, the 2D tubes in our system are likely to be produced by patchy-like reconnection that magnetic field lines reconnect one by one to form a new structure. We select the later phase $t = 460$ in the double-layer simulation $(3, \pm 1)$ to examine this argument. By comparing diffusion regions and outflows v_y in panels A) and B) of Fig.6.1, the reconnection that produces the 2D flux tube seems to proceed in a spatially scattered manner. However, bi-directional outflows are ejected from the high density regions. By checking the magnetic field lines that are producing the 2D tube at the sheet center, we cannot find the tube-tube reconnection but rather the line-line reconnection.

Two 2D flux tubes remain in this phase. The left one is centered at $y \sim -1.5\delta$, the right one is near $y \sim 11.5\delta$. As 2D modes grow, the left tube starts to move to the right and the coalescence of 2D flux tubes is observed (Fig.6.2). So our simulation shows that the 2D tube, which is created by the line-line reconnection of the 3D flux tubes, is produced and bi-directional outflows are formed out of the 3D turbulent state. Afterwards, the longer 2D mode is created by the inverse cascade from short 2D modes.

In the random perturbation simulation, the longest 2D mode $(1, 0)$ maintains its advantage all through the whole process, while $(1, 0)$ is the most unstable mode in our static current sheet. Since our simulation box is supposed to be one part of an extended current sheet, it is possible that if we execute simulation with a large box size along y and z, the initial most energetic 2D modes are smaller than the box size. In that case, the inverse cascade as we observed in $(3, \pm 1)$ might be important to produce large 2D flux tubes and globally bi-directional flow as the observations suggest.

6.2.3 Contribution to the turbulence reconnection model

One global picture of the spontaneous 3D reconnection was given in Beresnyak (2017). This work proposed that turbulence gradually builds up and expands the whole current sheet, finally produces global 2D-like bi-directional inflows and outflows. In our study, we showed in Chap.3 that new energy modes, namely new reconnection layers, are pro-

duced outwardly. It explains the current sheet expansion stage (Sec.6.2.2). Meanwhile, the nonlinear coupling of the pre-existing modes creates new modes and builds up the turbulent state, as more and more energy modes are activated seen from the 2D energy spectrum. The bi-directional flows are shown by the development of 2D modes in Sec.6.2.2. In turbulence reconnection picture (Lazarian & Vishniac, 1999), the field lines are thought to wander around inside the whole current sheet and gradually release the energy by continuous reconnection at different positions. We describe this wandering motion as the inflow-outflow coupling of adjacent reconnection layers, while the inflow-outflow coupling was examined locally in detail. In this sense, we have given a clear physical picture of the turbulence reconnection process, from the viewpoint of the diffusion region development and the interaction between diffusion regions.

The theoretical 3D turbulence reconnection model couples the MHD turbulence theory (Goldreich & Sridhar, 1995) in understanding the fast reconnection in a quasi-steady turbulent state (Lazarian & Vishniac, 1999). In our simulation, we found a dynamic energy ejection scale which corresponds to a new energetic mode. This shifting ejection scale was not explicitly identified in previous studies. In addition, a reorganization stage appears in between two boosts in both double-layer simulation $(3, \pm 1)$ and the random perturbation simulation. During this stage, the outermost layers saturate and disappear, while new energy modes grow from the inner side and evolve into the starting modes for the second boosts. Then whether a quasi-steady turbulent state can last long in spontaneous reconnection remains an open question. If the quasi-steady turbulent state is too short, or even cannot be achieved in the spontaneous reconnection regime, the theoretical turbulence reconnection model is then not sufficient. In comparison, our model based on the dynamical changes and seems to be more general.

The existence of the reorganization stage also implies that the current sheet cannot grow eternally thicker. Although it is possible that this reorganization stage is related to our closed boundary condition along the inflow direction, it can also happen to an open system from the physical point of view. The turbulent current sheet width we measured

in Sec.3.4 and Sec.6.2.1 composes of the outermost reconnecting layers positions and the width of flux tubes on the outermost layer. The reconnection layer position is limited by the initial current sheet width. Flux tubes cannot grow without limitation either. As we have explained in Sec.6.2.2, flux tubes on the same side are easy to coalesce to form a big tube. Therefore the final turbulent current sheet width is likely to be determined by the 3D flux tubes with the longest wavelength that is allowed by this system on either side of the current sheet. It is believed that the highest reconnection rate is 0.2, regardless of the diffusion mechanism (Liu et al., 2017). The aspect ratio of a flux tube width to its length is also limited by this number, by considering the shape of the separatrices. Thus the turbulent current sheet width is unlikely to exceed $\sim 0.2L$ by considering the asymmetry, where L is the system scale that represents the longest available modes in this system.

Although we have studied 1D energy spectrum (Appendix.H), we made an integral across the current sheet direction that the smallest scale is not the dissipation scale (diffusion region width). So no discussion on the 1D energy spectrum was given. The anisotropic energy cascade along and perpendicular to the local magnetic direction is an important issue (Goldreich & Sridhar, 1995). The energy fluctuation formed an elongated shape along the local magnetic field in a current sheet with fully developed turbulence (Huang & Bhattacharjee, 2016). It is reasonable to relate this feature to the reconnection layer since Alfvén waves are produced in the downflow and propagate along $\mathbf{k}$ of that mode. As the field line passes from different reconnection layers, the Alfvén waves produced by reconnection at different positions collide and cascade into new wave modes following the 4-wave resonance (Goldreich & Sridhar, 1995). Our argument on the nonlinear coupling is similar to the 4-wave resonance, but we are considering the energy mode that is growing without propagating. Further understanding of the energy spectrum and how to relate the waves to the reconnection picture are worth studying in the future.

6.2.4 Extension to particle simulation

Our work is in the MHD regime, which lacks the physics in the particle scale. However, the plasma in different astronomical events is not necessary to be always collisional, but collisionless in many cases. Then whether our model is also valid in collisionless plasma is not clear.

Big particle-in-cell (PIC) simulations show that multiple layers exist after the current sheet is perturbed by a random perturbation (Daughton et al., 2011). The turbulent layer expands across the current sheet with time, while energy cascade along the global guide field and flux tubes that are almost parallel to the asymptotic fields are also found (Nakamura et al., 2016). So we believe that a similar story as our model can be achieved even in the particle regime. Whether this argument holds should be checked in the PIC simulations.

6.3 Future prospects

Although we have generalized our results in Chap.4 and Chap.5, there still exist many other aspects that should be considered in future works.

Dependence on the diffusivity

All present simulations are applying much larger diffusivity than the realistic one due to the limitation on the computational resource. In order to understand the development of a system with extremely small diffusivity, one way is to tune down the diffusivity little by little and trace the trend of the change. In 2D reconnection simulation, it is found that when the diffusivity is lower than a certain threshold, the reconnection rate becomes independent of diffusivity under various circumstances (Bhattacharjee et al., 2009; Huang & Bhattacharjee, 2010; Loureiro et al., 2012; Ni et al., 2012a; Shibayama et al., 2015). In 3D reconnection regime, this question still remains (Oishi et al., 2015; Beresnyak, 2017; Kowal et al., 2017).

Let us assume first that the inflow-outflow coupling between diffusion regions is a universal phenomenon. In the 3D reconnection coupling, it takes time for the outflow on the linearly growing tearing layer to grow large enough to start the inflow-outflow coupling effectively across the current sheet. The growth rate of the tearing mode is reversely scaled to the diffusivity (Furth et al., 1963; Coppi et al., 1976), so it is possible that it takes a long time for a system to develop the inflow-outflow coupling when the diffusivity is small. On the other hand, the inflow-outflow coupling changes the spontaneous reconnection into the driven regime locally (Pritchett et al., 1980). Theoretically, the local reconnection is less dependent on the diffusivity in the driven reconnection but rather relies on the inflow electric field ($E_{\rm in} \sim v_{\rm in} B_{\rm in}/c$) (Sato & Hayashi, 1979; Kitabata et al., 1996). Thus it is possible that the 3D reconnection becomes less dependent on the diffusivity due to the local driven reconnection that spreads all over the current sheet. When a current sheet is driven by an external turbulence, it has been shown that the reconnection rate is independent on the diffusivity but dependent on the driving strength (Kowal et al., 2009). How the diffusivity changes the reconnection efficiency in a spontaneous reconnecting system which couples with the self-generated turbulence needs further detailed investigation.

Dependence on the boundary condition

As we described in Sec.2.4, we are considering a part of an extended current sheet. In addition, we are applying periodic boundary condition along all directions. When incoming magnetic fields are depleted in the system due to reconnection, further pouring of field lines are stopped as the magnetic pressure is no longer capable to push the field lines into the current sheet. Since a reorganization period exists in our study but not specifically identified in other studies, whether a step-like increasing reconnection rate can be achieved in other systems should be confirmed.

Meanwhile, the closed outflow region does not only change the possible emerging modes that determine the initial development but also forbids any structure removal from

the system. A closed system will saturate (Taylor, 1974) while an open system is potential to have a more dynamic development (Shibata & Tanuma, 2001). Thus reconnection has a strong reliance on the boundary condition. Whether our story is also feasible in a system with different boundary conditions, such as the half-open system for solar flare, should be examined in the future. Also, the size of the current sheet should be more extended to mimic the large system in most astronomical events. Our box size is in the same size as the most unstable 2D mode. If the box is much more extended, whether a further inverse cascade of 2D modes into longer and longer modes exists is an interesting topic.

Dependence on the global guide field

Although we have tried one simulation with a weak guide field, the initial perturbation was a pair of selected tearing eigenmodes so the generality is limited. It is found that the reconnection in a current sheet with a global guide field in the magnitude of half to double of the anti-parallel magnetic field does not change essentially (Beresnyak, 2017). However, it is still not clear whether the detailed development can be unified as what we expect. Moreover, the current sheet with only anti-parallel magnetic fields should be explained by another theory, as the turbulence becomes isotropic rather than being Alfvénic.

Dependence on the current sheet character

Since the magnetic field structure is quite complicated in the universe, many different parameters can be changed based on the magnetic field itself.

In the original story of the Sweet-Parker reconnection (Sweet, 1958; Parker, 1957), the big diffusion region is created by the slowly approaching dipole fields on the surface of the sun under the footpoint motions. Thus in the last several decades, many studies concentrated on how a large Sweet-Parker sheet changes from slow dynamics into a fast one. The most notable one is the 2D plasmoid instability reconnection model (Bhattacharjee et al., 2009; Huang & Bhattacharjee, 2010; Loureiro et al., 2012; Shibayama et al., 2015).

Recently, the prerequisite of the 2D Sweet-Parker sheet is re-examined. It was found that if a 2D current sheet is created by two approaching magnetic features, the current sheet collapses before the Sweet-Parker sheet is formed (Pucci & Velli, 2014; Comisso et al., 2016; Uzdensky & Loureiro, 2016; Comisso et al., 2017), unless the Lundquist number S is moderately large and the perturbation is weak (Huang et al., 2017).

If the system size is large enough to include the Coppi's regime (Coppi et al., 1976), a plasmoid chain is formed when the current sheet collapses (Uzdensky & Loureiro, 2016) that no bi-directional global outflows are created. If the system size is moderate (moderate S), the current sheet has a chance to be dominated by the longest mode that bi-directional outflows can form. This mode is possible to evolve into a Sweet-Parker type reconnection in the nonlinear stage (Loureiro et al., 2005).

We first consider the sheet collapsing case without the Sweet-Parker type reconnection. In this case, we have to re-estimate the time as the sheet has a potential to collapse before the coupling becomes effective. We assume that the initial potential field formed by two dipole fields in the solar atmosphere has a magnetic scale size of 1Mm on the plane that is perpendicular to the global guide field. A current sheet is eventually created as the anti-parallel magnetic fields approach each other. By applying the scaling law in Uzdensky & Loureiro (2016), the collapsing current sheet width is ~ 0.05Mm, which is the size of our initial current sheet width (Sec.6.2.1), while the collapsing time is 5.4hours. If our boost time ($5s$) is independent on the diffusivity, then the nonlinear coupling is feasible to finish the energy cascade across the sheet. Since the theoretical predictions are all considering the development of one single 2D mode inside a changing current sheet, nonlinear simulations of a developing 3D current sheet are highly required to confirm our arguments.

Next, we consider the case that a global Sweet-Parker type reconnection can be achieved. At the end of our simulation, 2D modes dominate. If the 3D tearing instability starts to grow in the 2D-like current sheet with bi-direction outflow, whether the energy cascade path described in Chap.3, Chap.4 and Chap.5 can be obtained is unclear. Or in another

word, whether our system can reprise in a Sweet-Parker type current sheet is not known. Since 3D modes are found in the Sweet-Parker sheet (Huang & Bhattacharjee, 2016), we believe that they can reappear as long as new fields are provided in the inflow region. On the other hand, as shown in Fig.F.1 in Appendix.F, the field lines in the coupling tangle up with each other. So unless a 3D flux tube is uniformly transported in a certain direction, the tube will be stretched bi-directionally by the bi-directional outflows. The stretching will make the tube to be more parallel to the asymptotic magnetic field. If the stretching makes the local magnetic field on the reconnection layer to be larger than the inflow magnetic field, the reconnection is likely to cease. Whether these arguments are true needs further proof.

In our simulation, the total pressure balance is maintained at the beginning. Another kind of system is the force-free field, which is believed to be important on the solar surface (e.g., Sakurai, 1979). One typical case is the force-free field composed of a gradually rotating magnetic field with the same magnitude. Thus current density also rotates across the current sheet while maintaining the magnitude. Therefore, each layer has an equal possibility to develop tearing instability. In Landi et al. (2008), it is shown that the reconnection in a force-free field is much different from the one with an initial total pressure balance. Then whether multiple layers develop and whether they couple with each other should be checked.

Other effects, such as plasma β (Ni et al., 2012b), ionization level (Murphy & Lukin, 2015; Hillier et al., 2016), thermal conduction and viscosity (Minoshima et al., 2016), gravity (Jelínek et al., 2017), relativity (Sironi et al., 2016) and so on, are also important to the reconnection study and need more detailed understanding.

Chapter 7

Concluding remarks

Since several decades ago, the understanding of magnetic reconnection aroused lots of interests among the plasma physicists. It is one of the most important fundamental processes and believed to support models for various astronomical events. Regarding the observational results on the energy release efficiency, such as the eruptive solar flare, fast reconnection in a three-dimensional (3D) system is required. The fast 3D reconnection problem remained unsolved for a long time. Theoretical model that couple with the turbulence theory is raised, however the basic physics were not sufficiently examined.

We executed three-dimensional (3D) magnetohydrodynamics (MHD) numerical simulation of a current sheet with a finite guide field to understand the development of diffusion regions, which is the essential part in the reconnection. As many previous numerical simulations showed, multiple tearing layers coexist in the current sheet when it is perturbed by random perturbation. We noticed an inflow-outflow coupling mechanism exists once two tearing layers are close to each other. Thus we first applied a pair of rotational-symmetric eigenmodes of the tearing instability to investigate the basic physics and the consequences of the coupling. The schematic plot of our main result is shown in Fig.7.1.

The inflow-outflow coupling is exhibited as the enhancement of the inflow into the diffusion region from the coupling side. We found that when two tearing layers are far apart, no coupling mechanism exists. When two tearing layers are close, the inflow-outflow coupling is effective and piles up magnetic fields in front of the coupled diffusion regions.

Secondary tearing is triggered due to the large piling-up magnetic fields, while higher order harmonics of the existing modes becomes energetic. Secondary tearing opens a vent for the field lines to eject out and collide with the free field lines. Due to the collision, new diffusion regions are formed outwardly. New diffusion regions form new reconnection layers further into the asymptotic magnetic field. These new layers correspond to new energy modes with higher wavenumbers along the global guide field than the original tearing modes, which can be explained by the successive nonlinear coupling among existing modes. Meanwhile, the inflow-outflow coupling is built up between old and new layers, while new layers are absorbing the asymptotic magnetic fields directly. Therefore, the global reconnection rate increases due to this sheet-crossing coupling that spans from one side of the current sheet to the other.

In order to verify that the sheet-crossing coupling is a general behavior, we re-examined the reconnection in a sheared current sheet perturbed by a random velocity field and the same story is retrieved. In comparison, the inflow-outflow coupling in a current sheet with a considerably weak global guide field breaks up very soon. Transient and piece-like reconnection happens that no global coherent structures are formed nor stay long.

Unlike most of the studies on fast 3D reconnection in the turbulent state, we concentrate on the detail of the physical properties. Our model describes how reconnection layers are created and interact with each other to accelerate reconnection in the whole current sheet. Hopefully, our description of reconnection in the turbulent state can be integrated with the MHD turbulence studies and applied to the models for realistic astronomical events in the near future.

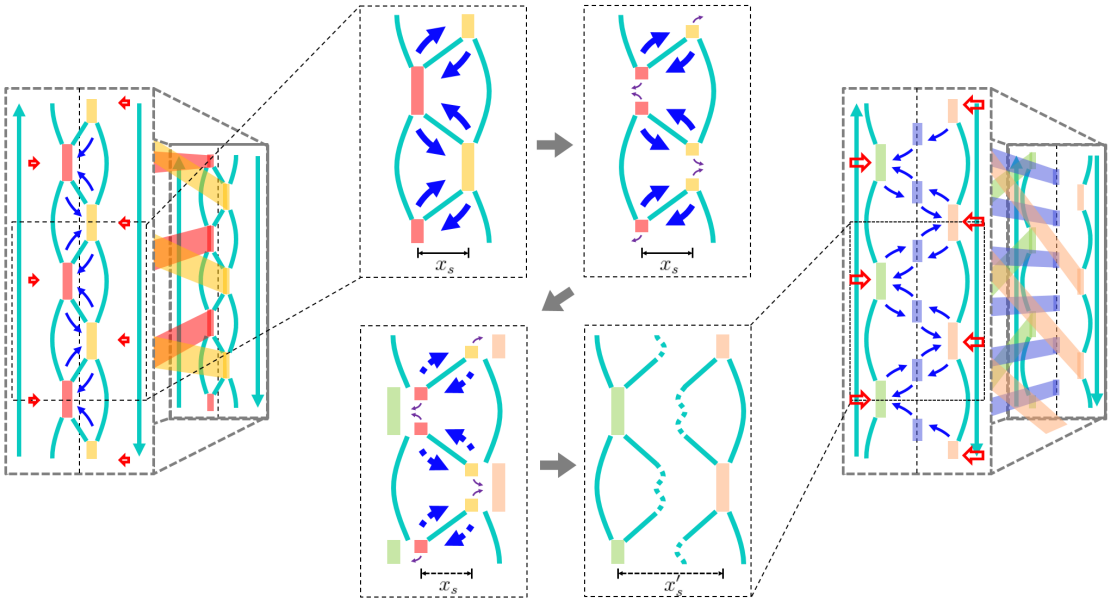

Figure 7.1: Schematic picture of sheet-crossing coupling model for fast 3D reconnection.

Appendix A

Physical understanding of the tearing instability

As shown in Eq.(1.10), the tearing instability grows on the layer where the local magnetic field is perpendicular to the perturbation wave vector $\mathbf{k}$. In this case, all field lines are perturbed in phase along the direction of $\mathbf{k}$ (left panels of Fig.A.1). The newly produced Lorentz force is uniformly acting on the magnetic field lines on this layer and also parallel to the wave vector $\mathbf{k}$. If $\mathbf{k}$ is tilted from $\mathbf{B}$, the magnetic field is locally squeezed as a phase difference is introduced along $\mathbf{B}$ (right panels of Fig.A.1). The Lorentz force (tension force of the bent and locally enhanced magnetic pressure) will transport the perturbation away in the form of Alfvén wave (orange arrows). The perturbation energy is dissipated along $\mathbf{B}$ so it is difficult to nurture instability on this layer.

It is straightforward to expect that the most unstable tearing instability grows right at the current sheet center, where the current density is the strongest. As it can be observed from the left panels of Fig.A.1, the magnetic pressure gradient produced by the perturbation will try to restore the configuration back to its original status. The force that opposes this restoration is the tension force from the newly created plasmoid by reconnection (right panel of Fig.1.3). We compare these terms by implementing the Harris sheet (Harris, 1962) as Eq.(1.16).

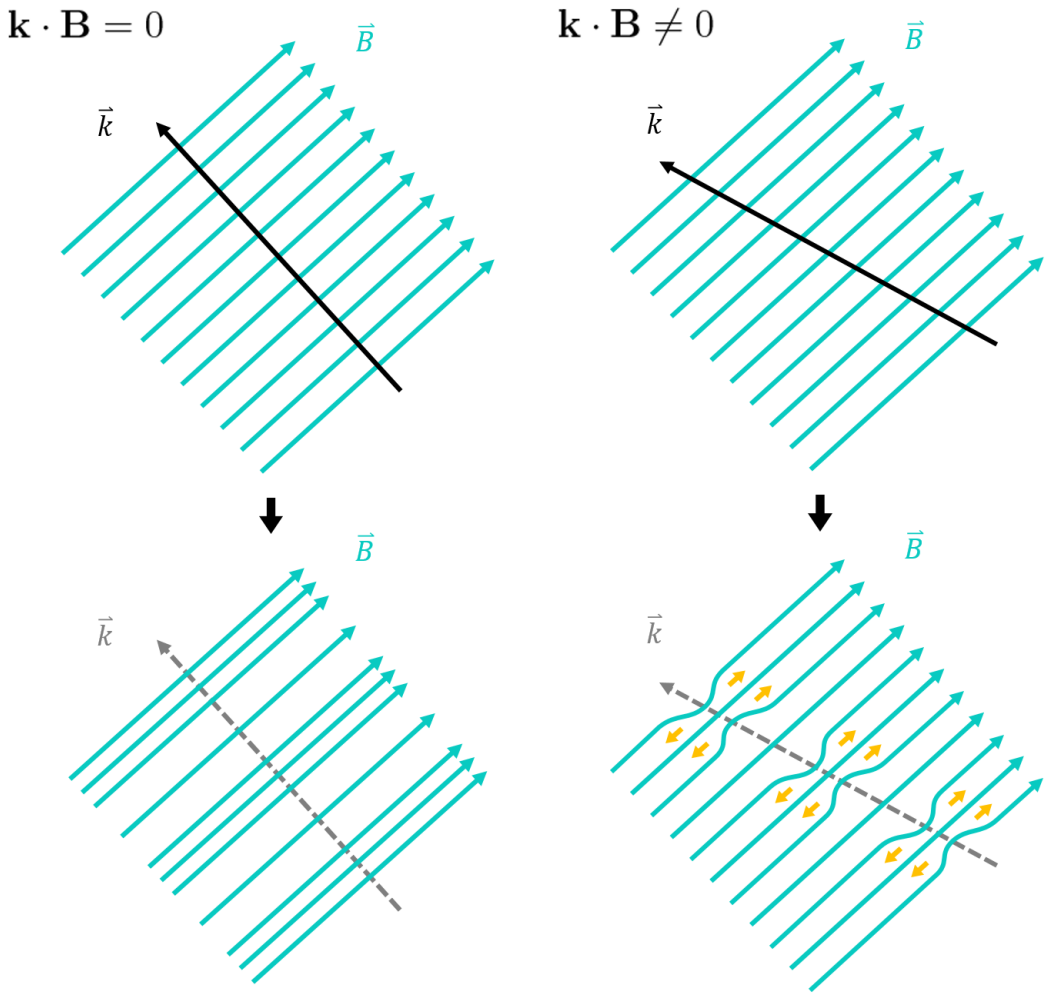

Figure A.1: The physical explanation for the tearing criteria $\mathbf{k} \cdot \mathbf{B} = 0$. Turquoise lines are magnetic field lines. Black solid and grey dashed vectors are perturbation wave vectors. Orange vectors indicate perturbation dissipation direction.

Near the center of the current sheet, the magnetic field can be approximated as

$$B_{\parallel}(x) \sim B_0 \frac{x}{a}. \tag{A.1}$$

In addition, a guide field B_{guide} is added perpendicular to the Harris sheet. The restoring force that corresponds to the tearing instability developing on the plane $x = x_s$ can be estimated from the linear term in the Lorentz force as:

$$J^{[1]}B^{[0]} \sim \frac{\Delta B_p k}{4\pi}\sqrt{B_{\text{guide}}^2 + \left(B_0 \frac{x_s}{a}\right)^2} \tag{A.2}$$

where $f^{[0]}$ and $f^{[1]}$ are the 0th and the 1st order of variables, ΔB_p is the compressed magnetic component on the tearing layer $x = x_s$ inside plasmoid. The whole term of the square root is the strength of the local field $\mathbf{B}^{[0]} = \mathbf{B}^{[0]}(x_s)$, which are shown as straight lines in Fig.A.1. The linear term that represents the plasmoid tension force parallel to the wave vector $\mathbf{k}$ is

$$J^{[0]}B^{[1]} \sim \frac{B_0}{4\pi a}\frac{B_{\text{guide}}}{\sqrt{B_{\text{guide}}^2 + \left(B_0 \frac{x_s}{a}\right)^2}} B_x \tag{A.3}$$

where B_x is the reconnected component. Let's assume that inside the current sheet, diffusion regions (with X-point at the center) and plasmoids are evenly distributed and both of them have a length scale $\sim 1/(2k)$ along $\mathbf{k}$. Reconnection, or the tearing, is happening inside a diffusion layer width $2\delta_\eta$ that is much thinner than the current sheet width $2a$. Due to the flux conservation along the boundary of the diffusion layer,

$$\begin{aligned} \frac{1}{4k}B_x &\sim \delta_\eta \left(\Delta B_\eta^+ - \Delta B_\eta^-\right) \\ B_x &\sim 2\Delta B_\eta \delta_\eta k \end{aligned} \tag{A.4}$$

where $\Delta B_\eta^{\pm}$ is the reconnecting magnetic field on either side of the diffusion layer and we assume symmetry across the diffusion layer for simplicity. Also we assume that the compression in ΔB_p is due to the plasmoid contraction. Just after the reconnection at the

X-point, local field $\mathbf{B}^{[0]}$ maintains its value. But as the plasmoid contracts towards its center, namely the O-point, local field increases inside the plasmoid. During the linear phase, plasmoid width is growing exponentially that $w(t) = w(0)\exp(\gamma t)$. At the same time, one end of the plasmoid travels from X-point to the edge of diffusion region during 1 unit of diffusion time $t_\eta = \delta_\eta^2/\widetilde{\eta}$. Assuming the magnetic flux conserves inside the plasmoid,

$$\begin{aligned} \frac{B(x_s)+\Delta B_p}{2k} w(t_0)\exp(\gamma t_\eta) &\sim \frac{B(x_s)}{k} w(t_0) \\ \Delta B_p &\sim C_0 B(x_s) \end{aligned} \tag{A.5}$$

where $C_0 = 2\exp\left(-\frac{\gamma\delta_\eta^2}{\widetilde{\eta}}\right) - 1$. Integrating all equations from Eq.(A.2) to Eq.(A.5), the ratio between the tension force and the restoring force is

$$\frac{J^{[0]}B^{[1]}}{J^{[1]}B^{[0]}} = \frac{2B_0\delta_\eta\Delta B_\eta}{C_0 a} \frac{B_{\text{guide}}}{\left[B_{\text{guide}}^2 + \left(B_0\frac{x_s}{a}\right)^2\right]^{\frac{3}{2}}}. \tag{A.6}$$

This equation shows that the force ratio is a monotonically decreasing function of the layer position x_s regarding the second term on the R.H.S.. If the first term is also reversely dependent on x_s, then it is proved that 2D modes are always growing faster than 3D modes with the same wavelength in a current sheet with a uniform guide field. Once the first term has an opposite trend, 3D modes can be faster (Baalrud et al., 2012). If we normalize the guide field to the asymptotic anti-parallel field,

$$\alpha = \frac{B_{\text{guide}}}{B_0} \tag{A.7}$$

then Eq.(A.6) can be simplified as

$$\frac{J^{[0]}B^{[1]}}{J^{[1]}B^{[0]}} = \frac{2\delta_\eta}{C_0 a}\frac{\Delta B_\eta}{B_0} \frac{\alpha}{\left[\alpha^2 + \left(\frac{x_s}{a}\right)^2\right]^{\frac{3}{2}}}. \tag{A.8}$$

which is an explicitly monotonically decreasing function of α.

No clear dependence of the tearing growth on the wavelength is shown in Eq.(A.6) or Eq.(A.8). But we are expecting a small δ_η and a large ΔB_η for a long wave mode since they provide strong compression near the tearing layer due to the weak tension force. As we explained above, we believe that they are positively related to the wavelength as a whole, so Eq.(A.8) is larger with a longer wave. Meanwhile, there also should exist an upper limit for the wavelength. When the tearing instability grows, it takes approximately $1/(kv_{\text{out}})$ to reorganize the structure, where v_{out} is the outflow from the X-point. Especially in the early phase of the tearing, v_{out} is considerably small. This time scale gets larger with an increasing perturbation wavelength. When it is longer than the diffusion time $\delta_\eta^2/\widetilde{\eta}$, the outflow cannot carry out the newly reconnected magnetic flux away from the X-point downstream fast enough that the flux will choke down the reconnection in the X-point. So the tearing instability is suppressed. Also when the diffusivity $\widetilde{\eta}$ gets larger, the upper limit of the wavelength is lower that the most unstable tearing mode has a shorter wavelength compared to the case of small diffusivity.

Appendix B

Solving the tearing instability linear equations

We solve the two coupled second-order ordinary differential equations Eq.(2.18) and Eq.(2.19) by second-order overrelaxation method. The solutions are found by relaxing

$$\frac{\partial \phi}{\partial t} = \frac{d^2\phi}{dx^2} - P(\phi, \psi) \tag{B.1}$$

$$\frac{\partial \psi}{\partial t} = \frac{d^2\phi}{dx^2} - Q(\phi, \psi) \tag{B.2}$$

where $P(\phi, \psi)$ and $Q(\phi, \psi)$ are the terms on the R.H.S. of Eq.(2.18) and Eq.(2.19) respectively. We iteratively solve Eq.(B.1) and Eq.(B.2) numerically as

$$\phi_i^{j+1} = \phi_i^j + dt \left[\frac{\phi_{i+1}^j - 2\phi_i^j + \phi_{i-1}^{j+1}}{(dx)^2} - P(\phi_i^j, \psi_i^j) \right] \tag{B.3}$$

$$\psi_i^{j+1} = \psi_i^j + dt \left[\frac{\psi_{i+1}^j - 2\psi_i^j + \psi_{i-1}^{j+1}}{(dx)^2} - Q(\phi_i^j, \psi_i^j) \right] \tag{B.4}$$

where dx is the uniform grid size across the current sheet, dt is the time advance that $dt = 1.8(dx)^2/2$. The lower label i represents the numerical grid number along the x-direction, while the upper label j represents the time step number. Solid boundary condition is applied that $\phi = 0$ and $\psi = 0$. The initial guess of the growth rate γ is estimated from the classical theory Eq.(1.14). The solution convergence is checked by

the following method. We calculate the difference of solutions in one time advance that

$$d\psi_i = \frac{2(\psi_i^{j+1} - \psi_i^j)}{\psi_i^{j+1} + \psi_i^j} \tag{B.5}$$

(following Steinolfson (1983)) for each grid i first. The derivation is calculated by

$$\sigma_{d\psi} = \frac{\sqrt{\sum_i^{N_x} (d\psi_i - \langle d\psi_i \rangle)^2}}{\sqrt{N_x}\langle d\psi_i \rangle} \tag{B.6}$$

where $\langle d\psi_i \rangle$ is the mean of $d\psi_i$ and N_x is the total number of grids. If the maximum $d\psi_i$ is smaller than 0, which means that new solution is not growing, the growth rate γ is reset as 0.995γ. When all $d\psi_i > 0$ and $\sigma_{d\psi} < 0.005$, the relaxed functions of ϕ and ψ, as well as the growth rate will be recorded. The solution of the linear analysis depends on the wavelength. More grids are used with a decreasing wavelength.

Initial functions of ϕ and ψ are estimated as

$$\phi(x, t=0) = \begin{cases} \gamma \exp(kx)/k & , x < 0 \\ \gamma \exp(-kx)/k & , x > 0 \end{cases} \tag{B.7}$$

$$\psi(x, t=0) = \begin{cases} B_{y0}(k_y + \alpha k_z) \exp(kx)/k & , x < 0 \\ B_{y0}(k_y + \alpha k_z) \exp(-kx)/k & , x > 0 \end{cases} \tag{B.8}$$

which depend on the selected mode $\mathbf{k}$.

Examples of eigenfunctions ψ and ϕ are shown in Fig.B.1. The upper panels are eigenfunctions of the 2D mode $(1, 0)$ while the lower panels are eigenfunctions of the 3D mode $(1, 1)$. The eigenfunctions are normalized by the maximum value of ψ along the x-direction.

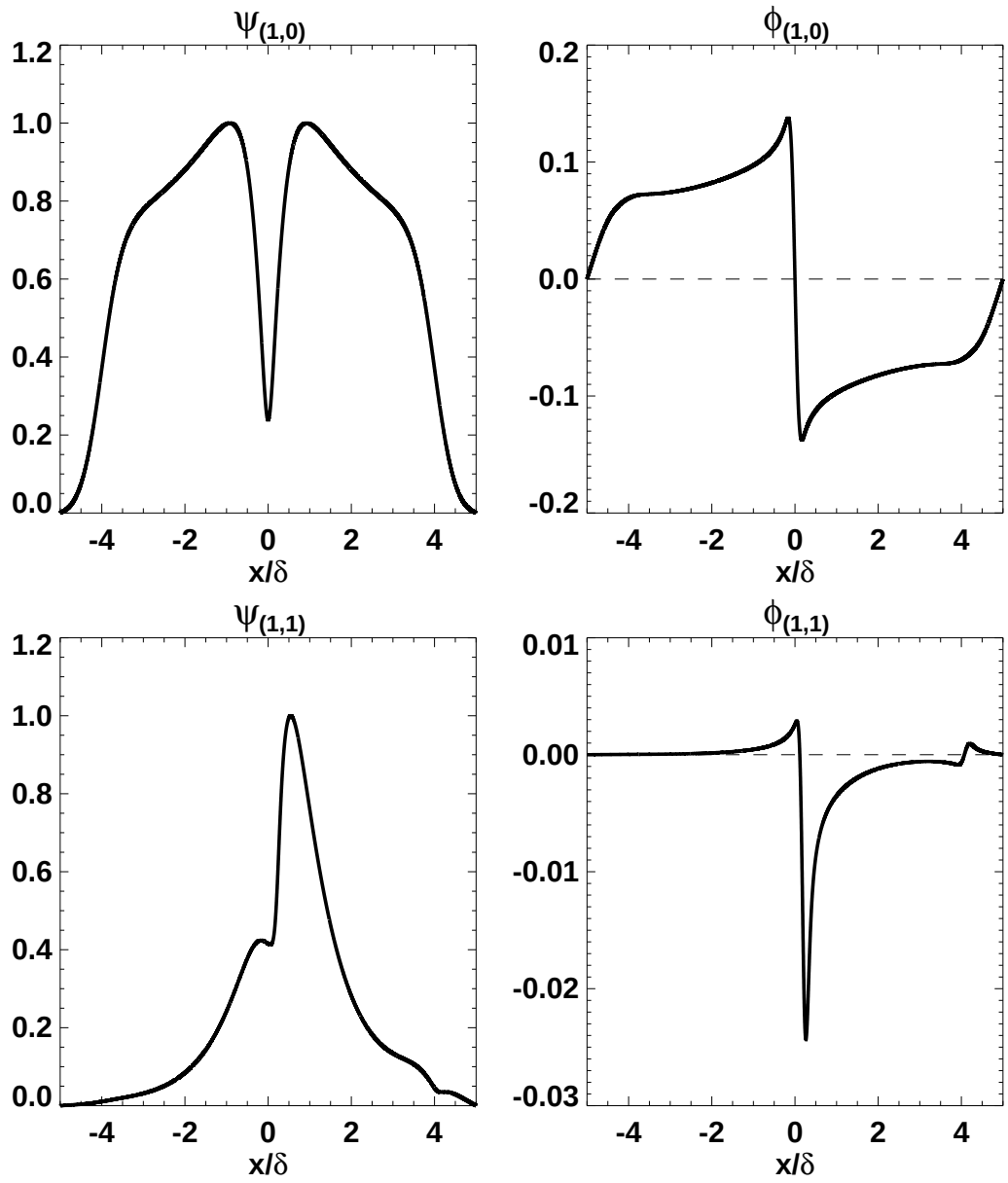

Figure B.1: Examples of normalized eigenfunctions of ψ and ϕ for mode $(1, 0)$ and $(1, 1)$. Dashed lines are $\phi = 0$.

Appendix C

Initial condition for double-layer simulations

The eigenfunctions of ψ and ϕ are converted into the perturbed magnetic and velocity fields in the form of

$$\begin{aligned} B^{[1]}_{x,L}(x,y,z) &= \Re\left\{ik\psi(-x)e^{i(k_y y - k_z z + \pi)}\right\} \\ &= k\psi(-x)\sin(k_y y - k_z z) \\ B^{[1]}_{x,R}(x,y,z) &= \Re\left\{ik\psi(x)e^{i(k_y y + k_z z)}\right\} \\ &= -k\psi(x)\sin(k_y y + k_z z) \end{aligned} \tag{C.1}$$

$$\begin{aligned} B^{[1]}_{y,L}(x,y,z) &= \Re\left\{\frac{k_y}{k}\left.\frac{\partial\psi}{\partial x}\right|_{-x} e^{i(k_y y - k_z z + \pi)}\right\} \\ &= -\frac{k_y}{k}\left.\frac{\partial\psi}{\partial x}\right|_{-x}\cos(k_y y - k_z z) \\ B^{[1]}_{y,R}(x,y,z) &= \Re\left\{-\frac{k_y}{k}\left.\frac{\partial\psi}{\partial x}\right|_{x} e^{i(k_y y + k_z z)}\right\} \\ &= -\frac{k_y}{k}\left.\frac{\partial\psi}{\partial x}\right|_{x}\cos(k_y y + k_z z) \end{aligned} \tag{C.2}$$

$$
\begin{aligned}
B^{[1]}_{z,L}(x,y,z) &= \Re\left\{-\frac{k_z}{k}\left.\frac{\partial\psi}{\partial x}\right|_{-x} e^{i(k_y y - k_z z+\pi)}\right\} \\
&= \left.\frac{k_z}{k}\frac{\partial\psi}{\partial x}\right|_{-x} \cos(k_y y - k_z z) \\
B^{[1]}_{z,R}(x,y,z) &= \Re\left\{-\frac{k_z}{k}\left.\frac{\partial\psi}{\partial x}\right|_{x} e^{i(k_y y + k_z z)}\right\} \\
&= -\left.\frac{k_z}{k}\frac{\partial\psi}{\partial x}\right|_{x} \cos(k_y y + k_z z)
\end{aligned} \tag{C.3}
$$

$$
\begin{aligned}
v^{[1]}_{x,L}(x,y,z) &= \Re\left\{-k\phi(-x)e^{i(k_y y - k_z z+\pi)}\right\} \\
&= k\phi(-x)\cos(k_y y - k_z z) \\
v^{[1]}_{x,R}(x,y,z) &= \Re\left\{k\phi(x)e^{i(k_y y + k_z z)}\right\} \\
&= k\phi(x)\cos(k_y y + k_z z)
\end{aligned} \tag{C.4}
$$

$$
\begin{aligned}
v^{[1]}_{y,L}(x,y,z) &= \Re\left\{i\frac{k_y}{k}\left.\frac{\partial\phi}{\partial x}\right|_{-x} e^{i(k_y y - k_z z+\pi)}\right\} \\
&= \left.\frac{k_y}{k}\frac{\partial\phi}{\partial x}\right|_{-x} \sin(k_y y - k_z z) \\
v^{[1]}_{y,R}(x,y,z) &= \Re\left\{i\frac{k_y}{k}\left.\frac{\partial\phi}{\partial x}\right|_{x} e^{i(k_y y + k_z z)}\right\} \\
&= -\left.\frac{k_y}{k}\frac{\partial\phi}{\partial x}\right|_{x} \sin(k_y y + k_z z)
\end{aligned} \tag{C.5}
$$

$$
\begin{aligned}
v^{[1]}_{z,L}(x,y,z) &= \Re\left\{-i\frac{k_z}{k}\left.\frac{\partial\phi}{\partial x}\right|_{-x} e^{i(k_y y - k_z z+\pi)}\right\} \\
&= -\left.\frac{k_z}{k}\frac{\partial\phi}{\partial x}\right|_{-x} \sin(k_y y - k_z z) \\
v^{[1]}_{z,R}(x,y,z) &= \Re\left\{i\frac{k_z}{k}\left.\frac{\partial\phi}{\partial x}\right|_{x} e^{i(k_y y + k_z z)}\right\} \\
&= -\left.\frac{k_z}{k}\frac{\partial\phi}{\partial x}\right|_{x} \sin(k_y y + k_z z)
\end{aligned} \tag{C.6}
$$

for double-layer simulations, where wavenumbers are taken as positive for convenience. In single-layer simulations, only the mode growing on the positive x-side is applied.

Appendix D

Local reconnection measurement

The diffusion region and its external region are identified by the following method.

The reconnection is proceeding on the plane which is parallel to the local $\mathbf{k}$ of the tearing mode. So we use J_h to identify the diffusion region thus the external region. The external region is determined by finding the local maximum of J_h on either side of the diffusion region, thus $J_{h,\text{maxl}}$ and $J_{h,\text{maxr}}$ are labeled as the characteristic current densities for the external regions. The diffusion region width d is measured by the current density level $J_{h,\text{half}}$ which is calculated by

$$J_{h,\text{half}} = J_{h,\text{min}} + \frac{1}{2}\left(\frac{J_{h,\text{maxl}} + J_{h,\text{maxr}}}{2} - J_{h,\text{min}}\right) \tag{D.1}$$

where $J_{h,\text{min}}$ is the local minimum of the current density J_h, namely the current density at the diffusion region center. We assume that the diffusion dominates in the diffusion region so the cross term $\nabla \times (\mathbf{v} \times \mathbf{B})$ in the induction equation from other modes is neglected. The length of the diffusion region is measured by the distance between positions where locally $J_h = J_{h,\text{half}}$ along $\mathbf{k}$. This straight line of measurement extends from the middle point of the diffusion region center and the right boundary of the diffusion region.

The measurements right on the diffusion region boundary are denoted as v_{in} or B_{in}, while the measurements in the external regions are denoted as v_{e} and B_{e}. We pick up the diffusion region that results from the tearing mode $\mathbf{k}$ on the positive x-side.

The averaged values are used in the context. The variables in the inflow region are averaged along the inflow boundary extends half of the diffusion region length. The variables in the outflow region are averaged along the outflow boundary in the whole diffusion region width.

The reconnection rate can be also evaluated by the electric field difference in X-point and its correspondent O-point. The electric field is perpendicular to the reconnection plane. The reconnection rate for a reconnecting region spreading on x- and k-direction with an infinitesimal width δn along the n-direction can be evaluated by

$$\begin{aligned} M_A &= \frac{t_{A0}}{B_c \delta n L_c} \int_{-\frac{\delta n}{2}}^{\frac{\delta n}{2}} (E_{h,O} - E_{h,X}) dn \\ &\sim \frac{t_{A0}}{B_c L_c} (E_{h,O} - E_{h,X}) \end{aligned} \tag{D.2}$$

where the integration of E_y disappears due to the rotational symmetry (point symmetry) along the integration path that

$$E_y(y, z) = E_y(-y, -z) \tag{D.3}$$

and the normalization ϕ_0 is taken as $B_c \delta n L_c$, where B_c and L_c are characteristic values depending on the purpose. The X-point and O-point are located along the resonance layer of the tearing mode (m, n).

Appendix E

Diffusion region width change

One effect of the inflow-outflow coupling is the thickening of the diffusion region, which is a positive contribution to the local reconnection rate.

The diffusion region width d is measured by the method in Appendix.D. The result is shown in Fig.E.1. It is clear that the diffusion region width gets thicker for a coupled diffusion region. The thickness is approximately as twice thicker as the diffusion region in the single-layer simulation.

The thickening of the diffusion region comes from the bent of the inflow magnetic field lines, as shown in Fig.E.2. The blue and orange lines are magnetic field lines selected in the inflow and the outflow regions with 3D separatrix in between. Translucent isosurface locates the diffusion region, with a purple field line penetrates through the X-point. It is clear that at $t = 50t_A$, the separatrix open angle in the double-layer simulation $(3, \pm 1)$ is wider than that in the single-layer simulation $(3, 1)$. This angle is determined by the inflow and the outflow region characters. As the plasma inflow is enhanced due to the flow coupling near the current sheet center, magnetic field lines have to bend more to decelerate the strong flow, which can be seen by comparing the bent of inflow region lines (blue lines on left). Meanwhile, the closed boundary of the system forbids the removal of flux tubes. The flux tube growth ensures the bent to be enhanced rather than being relaxed. This bent increases the characteristic scale across the current sheet direction, which is depicted as the diffusion region width.

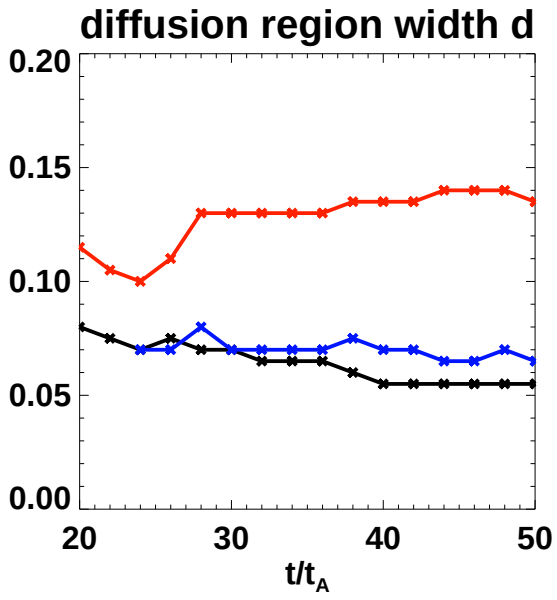

Figure E.1: The diffusion region width measurement. The red line with crosses is the measurement from the anti-symmetric plane in the double-layer simulation $(3, \pm 1)$, the blue line with crosses is the measurement from the symmetric plane in $(3, \pm 1)$ and the black line with crosses is the measurement in the single-layer simulation $(3, 1)$.

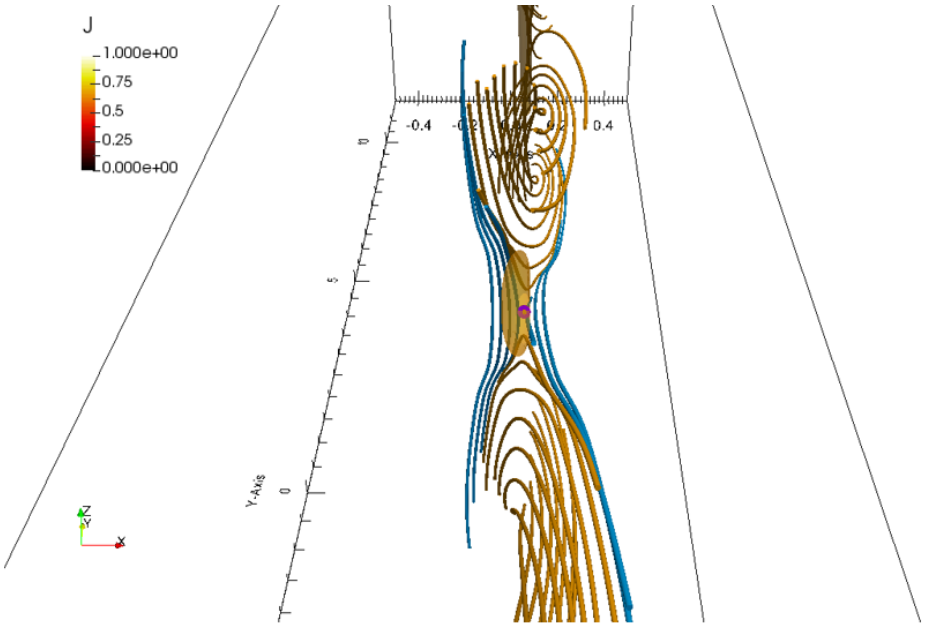

A) diffusion region (translucent isosurface) and selected field lines in X-point (purple line), inflow region (blue lines) and outflow region (orange lines) for $(\mathbf{3}, \mathbf{1})$ single-layer simulation at $t = 50t_A$

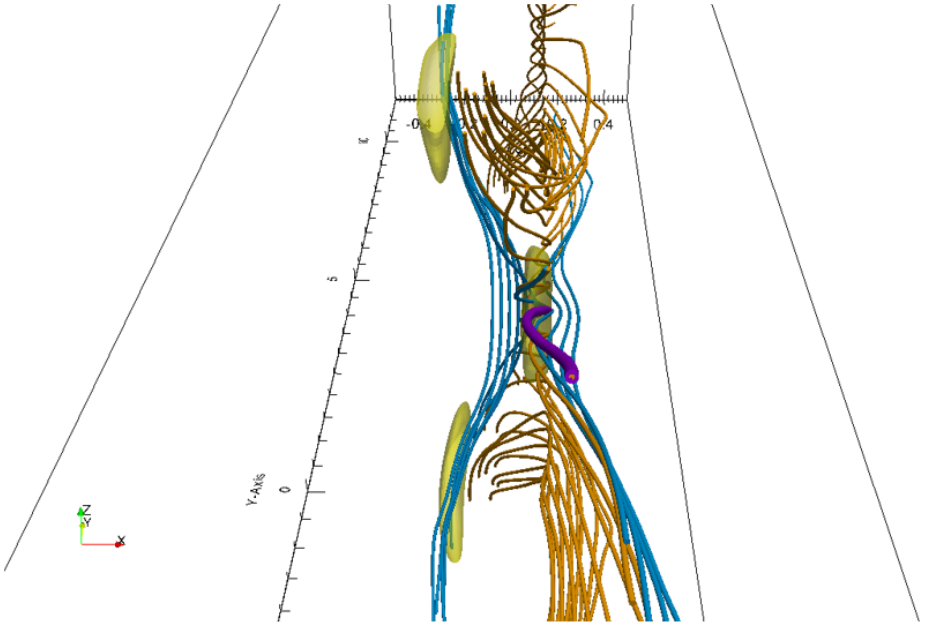

B) diffusion region (translucent isosurface) and selected field lines in X-point (purple line), inflow region (blue lines) and outflow region (orange lines) for $(\mathbf{3}, \pm\mathbf{1})$ double-layer simulation at $t = 50t_A$

Figure E.2: Diffusion regions and selected field lines in $(3, 1)$ and $(3, \pm 1)$ simulations.

Appendix F

Magnetic field lines in secondary tearing

We notice that the opening up of the flow outwardly creates a new diffusion region. This flow originates from the partitioned diffusion regions due to secondary tearing. In 2D reconnection picture, secondary tearing will produce a plasmoid in between the partitioned diffusion regions, instead of creating a vertical diffusion region as shown in our study. Moreover, the position of the new overlying diffusion region corresponds to the separatrix, namely the plasmoid boundary. In order to understand why a new diffusion region is created but not a coherent flux tube (plasmoid in 3D) along the tearing layer, we plot the magnetic field lines near the partitioned diffusion regions, as shown in Fig.F.1 and Fig.F.2.

First, we check the field lines near the partitioned diffusion regions (Fig.F.1). The field lines that are entering the diffusion region are blue and yellow lines. The blue lines are from the flux tube on $(3, -1)$ layer and the twisting feature can be identified from panels B) and C). The yellow lines are free field lines, which are rather straight as in panel C). The reconnected field lines are selected from the diffusion region downflow, labeled by orange and green lines in panel D). Orange lines in $z < 0$ side are ejected into the main flux tube of mode $(3, 1)$, while the lines in $z > 0$ side are in the flux tube of mode $(3, -1)$. So the orange lines connect the flux tubes from either side of the

current sheet by exchanging the line parts in $z > 0$ and $z < 0$ sides. The green lines also connect the field lines from either side, as it can be observed with a sharp turning of the field direction near $z = 0$. But the lines in $z > 0$ side are ejected into the region between the partitioned diffusion regions, instead of the main flux tubes. It means that the green lines are presenting different result compared to orange lines, and the result is the creation of a vertical diffusion region. Rotational symmetry exists across $y = 0$, so the field lines selected in Fig.F.1 for diffusion region in $y > 0$ side has a symmetric set near the diffusion region in $y < 0$ side. The light blue lines in panel D) of Fig.F.2 are the reconnected lines earlier than the green lines in Fig.F.1, while the purple lines are their counterparts in $y < 0$ side. These lines are transported into the vertical diffusion region along $y = 0$ and reconnect. The reconnected field lines are selected at downflow regions as shown by dark blue and red lines in panel D) of Fig.F.2. It is interesting to notice that the red lines are nearly straight lines perpendicular to the mode $(3, 1)$ in panel C), while extra components of B_x is created (a bump along the x-direction in panel B)) under the push by the outflow. Meanwhile, the dark blue lines are basically following the flux tube of mode $(3, -1)$. Shortly speaking, after these successive reconnections, the field lines are returned back. But these field lines maintain their twice reconnection history on $z = 0$ plane as the local braiding of field lines, which can be seen in panel C) near the center of the box. In another word, the helicity of the original field lines is transported and localized in this region. A simple explanation for the missing of secondary flux tube between the partitioned diffusion regions is that no translational invariance exists along any direction near the current sheet center. In order to grow a flux tube, a series of consistent reconnection must proceed simultaneously along a certain direction. At the current sheet center, the modes interact with each other that field lines from both sides are fully entangled. The consistency and simultaneity are lost in this region. So in such a system, the flux tube can only grow along the surface of the current sheet, where free fields lines participate more.

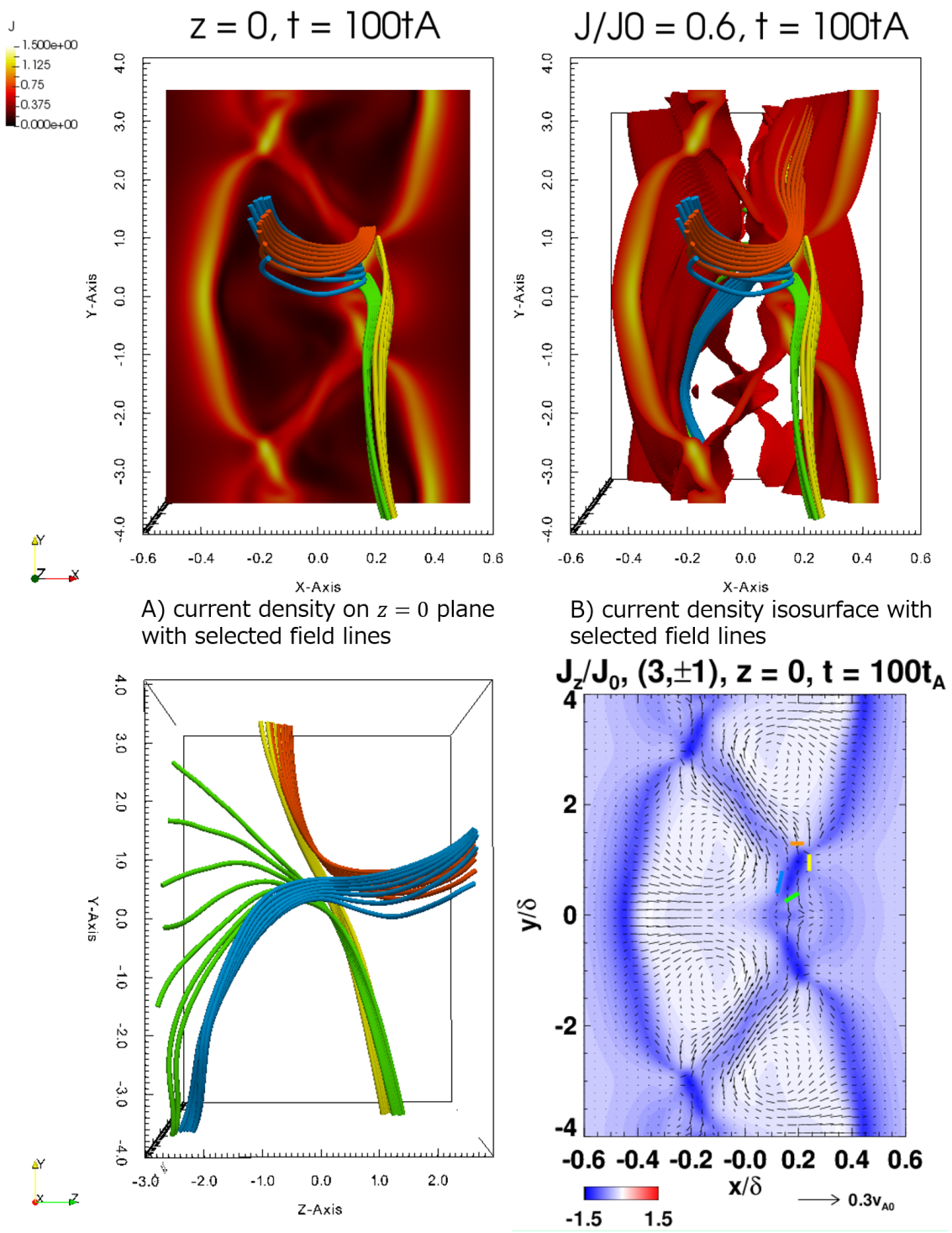

Figure F.1: Current density structure in $(3, \pm 1)$ with selected field lines near the partitioned diffusion regions on $z = 0$ plane at $t = 100t_A$.

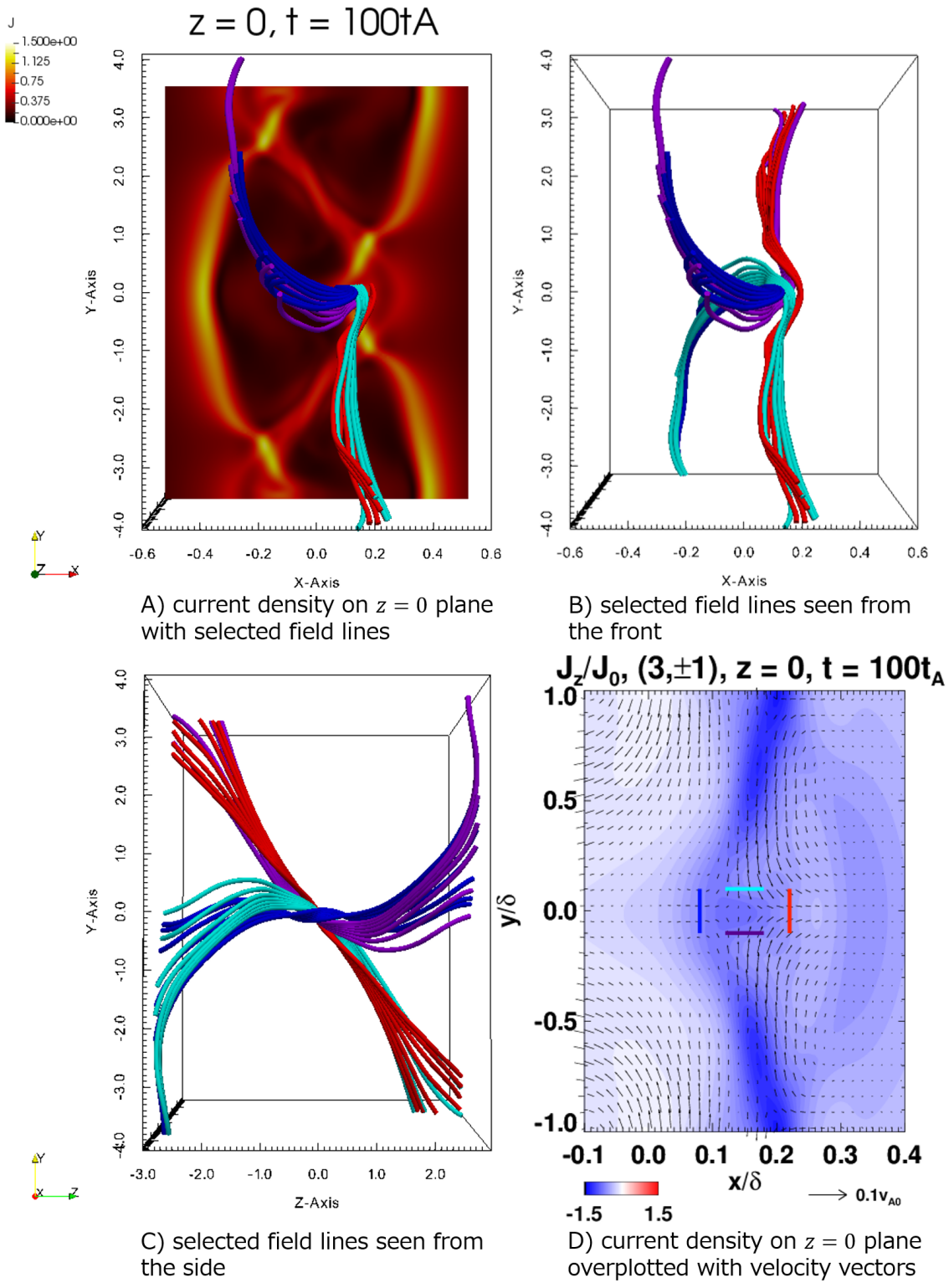

Figure F.2: Current density structure in $(3, \pm 1)$ with selected field lines near the vertical diffusion region on $z = 0$ plane at $t = 100t_A$.

Appendix G

The nonlinear coupling

At the beginning phase of the double-layer simulation, the two tearing layers are expected to grow linearly independently that only first-order terms are important. With the exponential growth of the tearing mode, the second-order terms that come from the cross terms of the first-order terms cannot be ignored, as well as even higher order terms. The growth of the second order terms is referred to as the nonlinear coupling in our study.

In the context of reconnection, the induction equation Eq.(1.1) is the most important equation. So we will only consider the induction equation here for simplicity. Among all variables, we choose the anti-parallel component of magnetic field B_y for discussion, as it is the reconnecting component in our simulation.

All first-order quantities can be written in the form of

$$f^{[1]} = f_L^{[1]} + f_R^{[1]} \tag{G.1}$$

in our double-layer simulation. We can rewrite the induction equation of $B_y^{[2]}$ as

$$\begin{aligned}
\frac{\partial B_y^{[2]}(t+dt)}{\partial t} &= \frac{\partial}{\partial z}\left[\mathbf{v}^{[1]}(t)\times\mathbf{B}^{[1]}(t)\right]_x - \frac{\partial}{\partial x}\left[\mathbf{v}^{[1]}(t)\times\mathbf{B}^{[1]}(t)\right]_z + \widetilde{\eta}\nabla^2 B_y^{[2]}(t) \\
&= \frac{\partial}{\partial z}\left[\left(\mathbf{v_L}^{[1]}+\mathbf{v_R}^{[1]}\right)\times\left(\mathbf{B_L}^{[1]}+\mathbf{B_R}^{[1]}\right)\right]_x \exp(2\gamma t) \\
&\quad -\frac{\partial}{\partial x}\left[\left(\mathbf{v_L}^{[1]}+\mathbf{v_R}^{[1]}\right)\times\left(\mathbf{B_L}^{[1]}+\mathbf{B_R}^{[1]}\right)\right]_z \exp(2\gamma t) \\
&\quad +\widetilde{\eta}\nabla^2 B_y^{[2]}(t).
\end{aligned} \tag{G.2}$$

As the diffusion part in Eq.(G.2) is a linear term that no new mode is created, we check only the advection terms.

The first term on the R.H.S. of Eq.(G.2) can be further expanded by applying Eq.(C.1) to Eq.(C.6). For $B_y^{[2]}$ growing on the positive x-side ($x > 0$), it becomes

$$\begin{aligned}
& \frac{\partial}{\partial z}\left[\left(\mathbf{v_L}^{[1]}+\mathbf{v_R}^{[1]}\right)\times\left(\mathbf{B_L}^{[1]}+\mathbf{B_R}^{[1]}\right)\right]_x \exp(2\gamma t) \\
= & \frac{\partial}{\partial z}\left[v_{y,L}^{[1]}B_{z,R}^{[1]}+v_{y,R}^{[1]}B_{z,L}^{[1]}-v_{z,L}^{[1]}B_{y,R}^{[1]}-v_{z,R}^{[1]}B_{y,L}^{[1]}\right]\exp(2\gamma t) \\
= & \frac{2k_yk_z^2}{k^2}\left(-\left.\frac{\partial\phi}{\partial x}\right|_x\left.\frac{\partial\psi}{\partial x}\right|_{-x}+\left.\frac{\partial\phi}{\partial x}\right|_{-x}\left.\frac{\partial\psi}{\partial x}\right|_x\right)\cos(2k_zz)\exp(2\gamma t) \qquad \text{(G.3)}
\end{aligned}$$

where $\cos(2k_zz)$ corresponds to the mode $(0,2)$. Moreover, Eq.(G.3) is an odd function of x to the center of the current sheet. It produces a sausage-like mode along the guide field direction (z-direction). As we have identified in the main context, $(0,2)$ represents a change of reconnection efficiency along the guide field.

The second term on the R.H.S. of Eq.(G.2) is

$$\begin{aligned}
& -\frac{\partial}{\partial x}\left[\left(\mathbf{v_L}^{[1]}+\mathbf{v_R}^{[1]}\right)\times\left(\mathbf{B_L}^{[1]}+\mathbf{B_R}^{[1]}\right)\right]_z \exp(2\gamma t) \\
= \quad & k_y\left[\left.\frac{\partial\phi}{\partial x}\right|_x\left.\frac{\partial\psi}{\partial x}\right|_x-\left.\frac{\partial\phi}{\partial x}\right|_{-x}\left.\frac{\partial\psi}{\partial x}\right|_{-x}+\frac{1}{2}\phi|_x\left.\frac{\partial^2\psi}{\partial x^2}\right|_x-\frac{1}{2}\phi|_{-x}\left.\frac{\partial^2\psi}{\partial x^2}\right|_{-x}\right. \\
& \quad \left.+\frac{1}{2}\left.\frac{\partial^2\phi}{\partial x^2}\right|_x\psi|_x-\frac{1}{2}\left.\frac{\partial^2\phi}{\partial x^2}\right|_{-x}\psi|_{-x}\right]\exp(2\gamma t) \\
& +\frac{1}{2}k_y\left[\phi|_x\left.\frac{\partial^2\psi}{\partial x^2}\right|_x-\left.\frac{\partial^2\phi}{\partial x^2}\right|_x\psi|_x\right]\cos(2k_yy+2k_zz)\exp(2\gamma t) \\
& -\frac{1}{2}k_y\left[\phi|_{-x}\left.\frac{\partial^2\psi}{\partial x^2}\right|_{-x}-\left.\frac{\partial^2\phi}{\partial x^2}\right|_{-x}\psi|_{-x}\right]\cos(2k_yy-2k_zz)\exp(2\gamma t) \\
& +\frac{1}{2}k_y\left[-\phi|_x\left.\frac{\partial^2\psi}{\partial x^2}\right|_{-x}+\phi|_{-x}\left.\frac{\partial^2\psi}{\partial x^2}\right|_x\right. \\
& \quad \left.+\left.\frac{\partial^2\phi}{\partial x^2}\right|_x\psi|_{-x}-\left.\frac{\partial^2\phi}{\partial x^2}\right|_{-x}\psi|_x\right]\cos(2k_yy)\exp(2\gamma t) \\
& +\frac{1}{2}k_y\left[2\left.\frac{\partial\phi}{\partial x}\right|_x\left.\frac{\partial\psi}{\partial x}\right|_{-x}-2\left.\frac{\partial\phi}{\partial x}\right|_{-x}\left.\frac{\partial\psi}{\partial x}\right|_x\right. \\
& \quad -\phi|_x\left.\frac{\partial^2\psi}{\partial x^2}\right|_{-x}+\phi|_{-x}\left.\frac{\partial^2\psi}{\partial x^2}\right|_x \\
& \quad \left.-\left.\frac{\partial^2\phi}{\partial x^2}\right|_x\psi|_{-x}+\left.\frac{\partial^2\phi}{\partial x^2}\right|_{-x}\psi|_x\right]\cos(2k_zz)\exp(2\gamma t). \qquad \text{(G.4)}
\end{aligned}$$

The first term on the R.H.S. of Eq.(G.4) is a uniform variation along the current sheet, which is an odd function of x. This term is changing the background magnetic field symmetrically across the sheet. The second and the third terms are the second harmonics of the initial perturbed modes. So they represent the 2D-like energy cascade along the initial reconnection layers. The fourth and the fifth terms are also odd functions of x, while the fourth term corresponds to the 2D mode $(2m, 0)$. Since the fourth term exhibits a sausage-like variation along the y-direction across the current sheet center, it implies that this mode is directly contributing to the reconnection.

The chain effect of the nonlinear coupling will produce more and more new modes, while the forms are more complicated than the expressions above. Moreover, the linear growing term $\exp(\gamma t)$ is not applicable as the modes stop to grow exponentially in the nonlinear phase.

Appendix H

Integrated 1D spectrum of the double-layer simulation $(3, \pm 1)$

We integrate the 2D energy spectrum Eq.(2.39) into 1D spectrum that

$$\tilde{E}_m(k) = \int_0^{2\pi} \tilde{E}_m(k_y, k_z) d\Omega \tag{H.1}$$

where Ω is the azimuthal angle on $k_y - k_z$ plane. As shown in Fig.H.1, the most dominant energy mode represents the energy ejection scale. The energy embedded in the background current sheet is extracted out by the tearing mode first then transfers to the other modes due to the coupling. When the new modes grow strong enough, they take the job and extract energy by themselves then transfer the energy to the other modes. As a result, we achieve a 1D spectrum with a shifting energy ejection scale with time. Since we have integrated the x-direction-oriented modes out, no dissipation scale is shown.

The energy transfer is frequently discussed in the turbulence theory. Presently, many self-generated turbulence reconnection theories are considering the spectrum when the turbulence sufficiently grows and obtains a quasi-steady state (Huang & Bhattacharjee, 2016; Kowal et al., 2017). At this stage, the current sheet expands as the turbulence region expands and whirls in new magnetic field lines to participate reconnection (Beresnyak, 2017). In our simulation, we found a reorganization stage in between the two

boosts of reconnection that was not discussed by the other studies. One reason might be our closed boundary condition. The proceeding of reconnection at the center region will gradually deplete the magnetic fields outside of the current sheet and reduce the magnetic pressure there. Therefore, the global current sheet center oriented Lorentz force reduces that the system stops absorbing in the field lines. In the previous study, a step-like increasing reconnection rate is observed in the early phase, while a quasi-steady turbulent state is achieved when the reconnection rate oscillates with a high frequency (Huang & Bhattacharjee, 2016). Whether a continuously expanding current sheet can be achieved in the turbulent state needs further investigation.

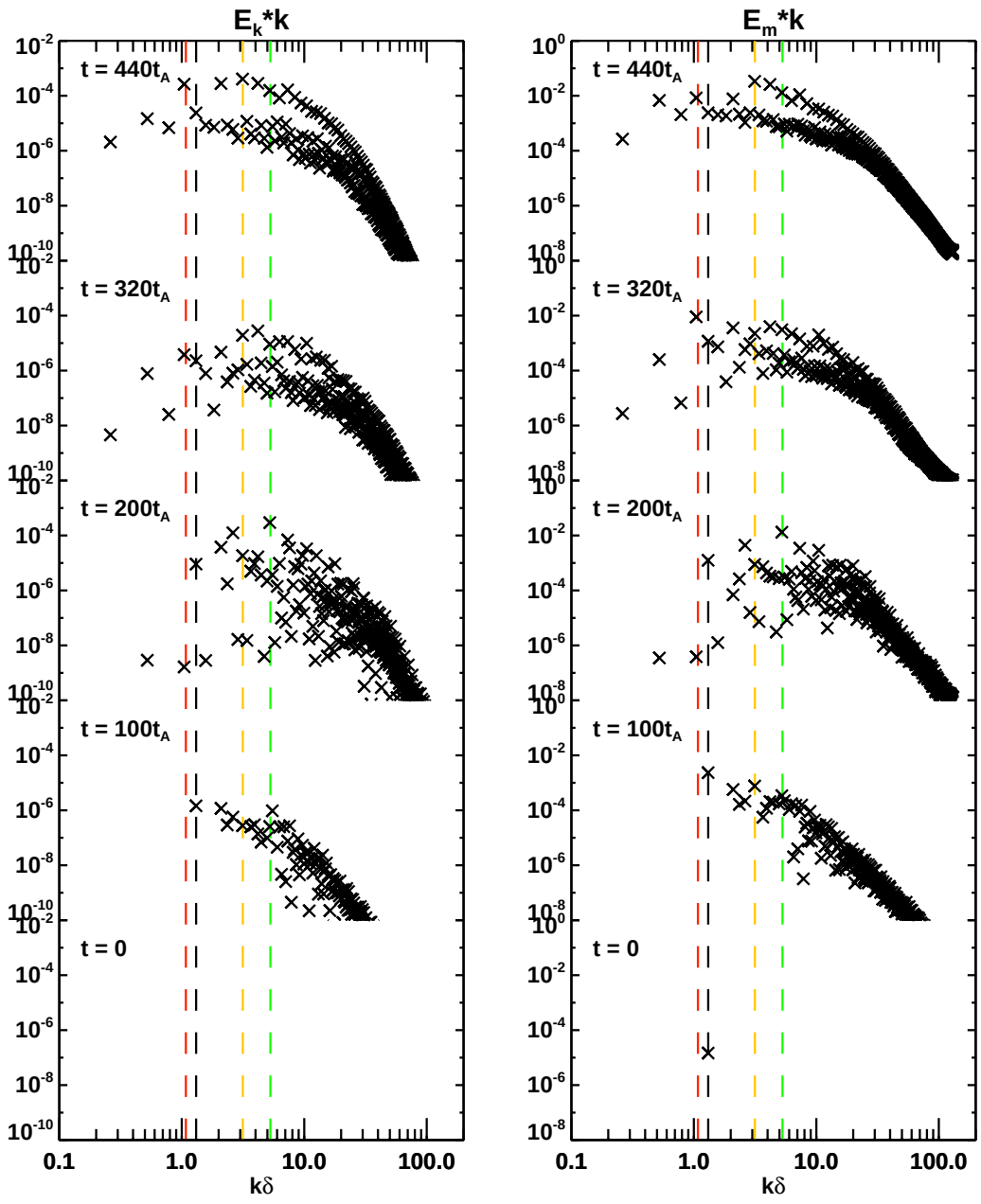

Figure H.1: Integrated 1D kinetic energy (left) and magnetic energy (right) spectrum stack plot in the double-layer simulation $(3, \pm 1)$ selected at times corresponding to the red circles in Fig.3.10. The black, red, orange and green dashed lines are the positions of modes $(3, 1)$, $(1, 1)$, $(1, 3)$ and $(3, 5)$, respectively.

References

Andrews, M. D. 2003, Solar Physics, 218, 261

Aulanier, G., et al. 2007, Science, 318, 1588

Baalrud, S. D., Bhattacharjee, A., & Huang, Y.-M. 2012, Physics of Plasmas, 19, 022101

Bárta, M., Büchner, J., Karlický, M., & Skála, J. 2011, The Astrophysical Journal, 737, 24

Baty, H., Priest, E. R., & Forbes, T. G. 2006, Physics of Plasmas, 13, 022312

Beresnyak, A. 2017, The Astrophysical Journal, 834, 47

Bhattacharjee, A., Huang, Y.-M., Yang, H., & Rogers, B. 2009, Physics of Plasmas, 16, 112102

Biernat, H. K., Heyn, M. F., & Semenov, V. S. 1987, Journal of Geophysical Research, 92, 3392

Birn, J., Nakamura, R., Panov, E. V., & Hesse, M. 2011, Journal of Geophysical Research (Space Physics), 116, A01210

Biskamp, D. 1986, Physics of Fluids, 29, 1520

—. 1997, Nonlinear Magnetohydrodynamics, 392

Boldyrev, S., & Loureiro, N. F. 2017, The Astrophysical Journal, 844, 125

Carmichael, H. 1964, NASA Special Publication, 50, 451

Cassak, P. A., & Shay, M. A. 2007, Physics of Plasmas, 14, 102114

Chen, Q., Otto, A., & Lee, L. C. 1997, Journal of Geophysical Research, 102, 151

Comisso, L., Lingam, M., Huang, Y.-M., & Bhattacharjee, A. 2016, Physics of Plasmas, 23, 100702

—. 2017, The Astrophysical Journal, 850, 142

Coppi, B., Galvao, R., Pellat, R., Rosenbluth, M., & Rutherford, P. 1976, Fizika Plazmy, 2, 961

Dahlburg, R. B., Antiochos, S. K., & Zang, T. A. 1992, Physics of Fluids B, 4, 3902

Dahlburg, R. B., & Einaudi, G. 2002, Physics Letters A, 294, 101

Daughton, W., Roytershteyn, V., Karimabadi, H., Yin, L., Albright, B. J., Bergen, B., & Bowers, K. J. 2011, Nature Physics, 7, 539

Dungey, J. W. 1961, Physical Review Letters, 6, 47

Eastwood, J. P., Phan, T. D., Øieroset, M., & Shay, M. A. 2010, Journal of Geophysical Research (Space Physics), 115, A08215

Fisk, L. A., Schwadron, N. A., & Zurbuchen, T. H. 1999, Journal of Geophysical Research, 104, 19765

Furth, H. P., Killeen, J., & Rosenbluth, M. N. 1963, Physics of Fluids, 6, 459

Galeev, A. A., & Zelenyi, L. M. 1977, ZhETF Pisma Redaktsiiu, 25, 407

Gibson, S. E., et al. 2002, The Astrophysical Journal, 574, 1021

Goldreich, P., & Sridhar, S. 1995, The Astrophysical Journal, 438, 763

Grasso, D., Borgogno, D., & Pegoraro, F. 2007, Physics of Plasmas, 14, 055703

Harris, E. G. 1962, Il Nuovo Cimento, 23, 115

Hassanin, A., & Kliem, B. 2016, The Astrophysical Journal, 832, 106

Hillier, A., Takasao, S., & Nakamura, N. 2016, Astronomy & Astrophysics, 591, A112

Hirayama, T. 1974, Solar Physics, 34, 323

Hoshino, M. 2012, Physical Review Letters, 108, 135003

—. 2015, Physical Review Letters, 114, 061101

Huang, Y.-M., & Bhattacharjee, A. 2010, Physics of Plasmas, 17, 062104

—. 2016, The Astrophysical Journal, 818, 20

Huang, Y.-M., Comisso, L., & Bhattacharjee, A. 2017, The Astrophysical Journal, 849, 75

Hughes, W. J., & Sibeck, D. G. 1987, Geophysical Research Letters, 14, 636

Janvier, M., Aulanier, G., Pariat, E., & Démoulin, P. 2013, Astronomy & Astrophysics, 555, A77

Janvier, M., Kishimoto, Y., & Li, J. Q. 2011, Physical Review Letters, 107, 195001

Jelínek, P., Karlický, M., Van Doorsselaere, T., & Bárta, M. 2017, The Astrophysical Journal, 847, 98

Jemella, B. D., Shay, M. A., Drake, J. F., & Rogers, B. N. 2003, Physical Review Letters, 91, 125002

Jiang, F., Zhang, J., & Yang, S. 2015, Publications of the Astronomical Society of Japan, 67, 78

Kaneko, T., & Yokoyama, T. 2017, The Astrophysical Journal, 845, 12

Kitabata, H., Hayashi, T., Sato, T., & Complexity Group. 1996, Journal of the Physical Society of Japan, 65, 3208

Kopp, R. A., & Pneuman, G. W. 1976, Solar Physics, 50, 85

Kowal, G., Falceta-Gonçalves, D. A., Lazarian, A., & Vishniac, E. T. 2017, The Astrophysical Journal, 838, 91

Kowal, G., Lazarian, A., Vishniac, E. T., & Otmianowska-Mazur, K. 2009, The Astrophysical Journal, 700, 63

Kudoh, T., Shibata, K., & Matsumoto, R. 1999, in Astrophysics and Space Science Library, Vol. 240, Numerical Astrophysics, ed. S. M. Miyama, K. Tomisaka, & T. Hanawa, 203

Kusano, K., Bamba, Y., Yamamoto, T. T., Iida, Y., Toriumi, S., & Asai, A. 2012, The Astrophysical Journal, 760, 31

Kusano, K., & Sato, T. 1987, Nuclear Fusion, 27, 821

Landi, S., Londrillo, P., Velli, M., & Bettarini, L. 2008, Physics of Plasmas, 15, 012302

Lapenta, G. 2008, in European Solar Physics Meeting, Vol. 12, European Solar Physics Meeting, ed. H. Peter, 3.30

Lapenta, G., Markidis, S., Goldman, M. V., & Newman, D. L. 2015, Nature Physics, 11, 690

Lapidus, A. 1967, Journal of Computational Physics, 2, 154

Lazarian, A., & Vishniac, E. T. 1999, The Astrophysical Journal, 517, 700

Lee, L. C., & Fu, Z. F. 1985, Geophysical Research Letters, 12, 105

Linton, M. G., Dahlburg, R. B., & Antiochos, S. K. 2001, The Astrophysical Journal, 553, 905

Linton, M. G., & Longcope, D. W. 2006, The Astrophysical Journal, 642, 1177

Liu, Y.-H., Hesse, M., Guo, F., Daughton, W., Li, H., Cassak, P. A., & Shay, M. A. 2017, Physical Review Letters, 118, 085101

Loureiro, N. F., Cowley, S. C., Dorland, W. D., Haines, M. G., & Schekochihin, A. A. 2005, Physical Review Letters, 95, 235003

Loureiro, N. F., Samtaney, R., Schekochihin, A. A., & Uzdensky, D. A. 2012, Physics of Plasmas, 19, 042303

Mallet, A., Schekochihin, A. A., & Chandran, B. D. G. 2017, Monthly Notices of the Royal Astronomical Society, 468, 4862

Masuda, S., Kosugi, T., Hara, H., Tsuneta, S., & Ogawara, Y. 1994, Nature, 371, 495

Matthaeus, W. H., & Lamkin, S. L. 1985, Physics of Fluids, 28, 303

Minoshima, T., Miyoshi, T., & Imada, S. 2016, Physics of Plasmas, 23, 072122

Moore, R. L., Schmieder, B., Hathaway, D. H., & Tarbell, T. D. 1997, Solar Physics, 176, 153

Murphy, N. A., & Lukin, V. S. 2015, The Astrophysical Journal, 805, 134

Nakamura, N., Shibata, K., & Isobe, H. 2012, The Astrophysical Journal, 761, 87

Nakamura, T. K. M., Nakamura, R., Narita, Y., Baumjohann, W., & Daughton, W. 2016, Physics of Plasmas, 23, 052116

Ni, L., Roussev, I. I., Lin, J., & Ziegler, U. 2012a, The Astrophysical Journal, 758, 20

Ni, L., Ziegler, U., Huang, Y.-M., Lin, J., & Mei, Z. 2012b, Physics of Plasmas, 19, 072902

Oishi, J. S., Mac Low, M.-M., Collins, D. C., & Tamura, M. 2015, The Astrophysical Journal Letters, 806, L12

Onofri, M., Isliker, H., & Vlahos, L. 2006, Physical Review Letters, 96, 151102

Onofri, M., Primavera, L., Malara, F., & Veltri, P. 2004, Physics of Plasmas, 11, 4837

Orszag, S. A., & Patera, A. T. 1983, Journal of Fluid Mechanics, 128, 347

Osman, K. T., Matthaeus, W. H., Gosling, J. T., Greco, A., Servidio, S., Hnat, B., Chapman, S. C., & Phan, T. D. 2014, Physical Review Letters, 112, 215002

Parker, E. N. 1957, Journal of Geophysical Research, 62, 509

—. 1972, The Astrophysical Journal, 174, 499

Petschek, H. E. 1964, NASA Special Publication, 50, 425

Phan, T. D., Gosling, J. T., & Davis, M. S. 2009, Geophysical Research Letters, 36, L09108

Priest, E. R., & Forbes, T. G. 1986, Journal of Geophysical Research, 91, 5579

Priest, E. R., & Pontin, D. I. 2009, Physics of Plasmas, 16, 122101

Pritchett, P. L., Lee, Y. C., & Drake, J. F. 1980, Physics of Fluids, 23, 1368

Pucci, F., & Velli, M. 2014, The Astrophysical Journal Letters, 780, L19

Rutherford, P. H. 1973, Physics of Fluids, 16, 1903

Sakai, J.-I., & Koide, S. 1992, Solar Physics, 142, 399

Sakurai, T. 1976, Astronomical Society of Japan, Publications, 28, 177

—. 1979, Publications of the Astronomical Society of Japan, 31, 209

Sato, T., & Hayashi, T. 1979, Physics of Fluids, 22, 1189

Semenov, V. S., Volkonskaya, N. N., & Biernat, H. K. 1998, Physics of Plasmas, 5, 3242

Shibata, K., Masuda, S., Shimojo, M., Hara, H., Yokoyama, T., Tsuneta, S., Kosugi, T., & Ogawara, Y. 1995, Astrophysical Journal Letters, 451, L83

Shibata, K., & Tanuma, S. 2001, Earth, Planets, and Space, 53, 473

Shibayama, T., Kusano, K., Miyoshi, T., Nakabou, T., & Vekstein, G. 2015, Physics of Plasmas, 22, 100706

Sironi, L., Giannios, D., & Petropoulou, M. 2016, Monthly Notices of the Royal Astronomical Society, 462, 48

Sonnerup, B. U. Ö. 1970, Journal of Plasma Physics, 4, 161

Steinolfson, R. S. 1983, Physics of Fluids, 26, 2590

Sturrock, P. A. 1966, Nature, 211, 695

Sweet, P. A. 1958, in IAU Symposium, Vol. 6, Electromagnetic Phenomena in Cosmical Physics, ed. B. Lehnert, 123

Takasao, S., Asai, A., Isobe, H., & Shibata, K. 2012a, The Astrophysical Journal Letters, 745, L6

—. 2012b, The Astrophysical Journal Letters, 745, L6

Takasao, S., Isobe, H., & Shibata, K. 2013, Publications of the Astronomical Society of Japan, 65, 62

Tanuma, S., Yokoyama, T., Kudoh, T., Matsumoto, R., Shibata, K., & Makishima, K. 1999, Publications of the Astronomical Society of Japan, 51, 161

Taylor, J. B. 1974, Physical Review Letters, 33, 1139

Tsuneta, S., et al. 1991, Solar Physics, 136, 37

Ugai, M., & Tsuda, T. 1977, Journal of Plasma Physics, 17, 337

Uzdensky, D. A., & Loureiro, N. F. 2016, Physical Review Letters, 116, 105003

Uzdensky, D. A., Loureiro, N. F., & Schekochihin, A. A. 2010, Physical Review Letters, 105, 235002

Wang, S., Yokoyama, T., & Isobe, H. 2015, The Astrophysical Journal, 811, 31

Wang, Z. X., Wang, X. G., Dong, J. Q., Lei, Y. A., Long, Y. X., Mou, Z. Z., & Qu, W. X. 2007, Physical Review Letters, 99, 185004

Watanabe, H., Vissers, G., Kitai, R., Rouppe van der Voort, L., & Rutten, R. J. 2011, The Astrophysical Journal, 736, 71

Yamada, M., Kulsrud, R., & Ji, H. 2010, Reviews of Modern Physics, 82, 603

Yan, M., Otto, A., Muzzell, D., & Lee, L. C. 1994, Journal of Geophysical Research, 99, 8657

Yokoyama, T., Akita, K., Morimoto, T., Inoue, K., & Newmark, J. 2001a, The Astrophysical Journal, 546, L69

—. 2001b, The Astrophysical Journal Letters, 546, L69